The Evolution of Massive Disc Galaxies with Environment and Redshift

Steven P. Bamford

The University of Nottingham

Thesis submitted to the University of Nottingham
for the degree of Doctor of Philosophy

May 2006

Supervisor: Dr. Alfonso Aragón-Salamanca

Examiners: Prof. Richard Bower *(University of Durham)*
Dr. Christopher J. Conselice *(University of Nottingham)*

Submitted: 9 December 2005

Examined: 13 February 2006

Final version: 12 May 2006

Contents

List of Figures

List of Tables

Abstract

This thesis examines the evolution of massive disc galaxies as a function of cosmic time and environment by analysing a sample of luminous disc galaxies, located in the field and rich clusters at intermediate redshifts. The data utilised for this study are two-dimensional optical spectra obtained with the FORS2 instrument on the VLT, along with imaging from a variety of sources. From these we measure absolute rest-frame B-band magnitudes, stellar scalelengths ($r_{\mathrm{d,phot}}$), rotation velocities (V_{rot}), emission-line scalelengths ($r_{\mathrm{d,spec}}$) and emission-line equivalent widths, resulting in estimates of gas-phase oxygen abundance, current star formation rate (SFR) and dust extinction.

We investigate evolution of the field Tully-Fisher relation (TFR) using a sample of 89 galaxies covering the redshift range 0.1–1. We find evidence that these luminous ($M_B \lesssim M_B^*$) spiral galaxies are increasingly offset from the local TFR with redshift, reaching a brightening of -1.0 ± 0.5 mag, at a given V_{rot}, by $z \sim 1$. We argue that, due to likely selection effects, this observed evolution represents an upper limit.

Previous studies have used an observed correlation between TFR residuals and V_{rot} to argue that low mass galaxies have evolved significantly more than those with higher mass. However, we demonstrate that such a correlation does not necessarily indicate a physical difference in the evolution of galaxies with different V_{rot}.

Interpreting the luminosity evolution derived from the TFR as due to evolution in the SFR of these luminous spiral galaxies, we find that $\mathrm{SFR}(z) \propto (1+z)^{1.7\pm1.1}$. Although the uncertainties are large, this evolution, which is probably an upper limit, appears to be slower than that derived for the overall field galaxy population. This suggests that the rapid evolution of the SFR density of the universe observed since $z \sim 1$ is not in general driven by the evolution of the SFR in *individual* bright spiral galaxies.

The measured emission-line equivalent widths, diagnostic ratios, oxygen abundances, star formation rates and dust extinctions for a sample of 40 luminous, massive ($V_{\mathrm{rot}} \gtrsim 80$ km s^{-1}), star-forming, field disc galaxies, with redshifts $z = 0.2$–0.8, cover similar ranges to those observed across a large sample of local galaxies. However, at a given galaxy luminosity, many of our galaxies have oxygen abundances significantly lower than local galaxies with similar luminosities. The galaxies in this luminous, metal-poor subsample exhibit physical conditions similar to those of local *faint* and metal-poor star-forming galaxies. Lower-metallicity systems are $\sim$2 mag brighter, and have star formation rates an order of magnitude higher, compared with similar metallicity galaxies today. Oxygen abundances are not found to correlate with the emission scale length size of galaxies, and the rotation velocity–metallicity relation, while perhaps present, is unclear. This suggests that massive field galaxies at intermediate redshifts are diverse in terms of their interstellar gas properties and stellar content.

continued

To examine variations in the TFR with environment, matched samples of 58 field and 22 cluster galaxies are constructed, selected in a homogeneous manner and covering similar ranges in redshift ($0.25 \leq z \leq 1.0$) and luminosity ($M_B \leq -19.5$ mag). The distributions of M_B, $V_{\rm rot}$ and scalelength are found to be comparable for the two samples. However, we find that the TFR of the cluster galaxies is systematically offset with respect to the field sample by -0.7 ± 0.2 mag. This offset is significant at 3σ and persists when we account for an evolution of the field TFR with redshift. Tests are performed to investigate potential differences in the observed emission lines and derived parameters of the cluster and field samples. However, no such differences which could account for the offset are found.

Offsets are also found between cluster and field samples in the relations of M_B and $V_{\rm rot}$ versus $r_{\rm d,phot}$ and $r_{\rm d,spec}$, although these are difficult to interpret. Our cluster galaxies are found to have ratios of emission-line to stellar scalelengths ($r_{\rm d,spec}/r_{\rm d,phot}$) significantly lower than for our field galaxies: 0.88 ± 0.08 versus 1.15 ± 0.05, respectively. This indicates that star formation is more centrally concentrated in the cluster galaxies.

The comparison of interstellar gas properties between 16 bright, star-forming, cluster disc galaxies at intermediate redshifts ($0.3 \lesssim z \lesssim 0.6$, $\langle z \rangle = 0.42$) and their counterparts in the coeval field, reveals that both samples are generally similar. However, on average the cluster galaxies have emission-line equivalent widths that are significantly lower than for the field galaxies. A contrasting fraction of the distant cluster galaxies, though, appears to have much higher emission-line equivalent widths, comparable to the highest seen in the field. This tentatively implies a bimodality in the star formation rates per unit luminosity of distant cluster galaxies, which is not present for our field sample. However we find no substantial difference in the long term star formation histories of these cluster and field galaxies, as indicated by their gas-phase metallicities.

The most likely explanation for the results of our cluster versus field comparison is that spiral galaxies entering intermediate-redshift clusters often experience a short-lived enhancement of their star formation rate, followed by a decline, which we would expect to be accompanied by a transformation to S0 morphology.

Acknowledgements

My foremost thanks go to my wonderful wife, Cally, for her love and companionship, but also for her support and encouragement of both my PhD studies and astronomy career. I am grateful to my parents for their support throughout my long education.

Thanks to my supervisor, Alfonso, for his valuable guidance and encouragement over the past three years, and to Bo, for providing me with such excellent data to work on and a good clue of what to do with it.

I have thoroughly enjoyed my time in the Nottingham astronomy group, mostly due to the great friends I have found here. Thanks to the two students who have made it through the past three years along with me: Helen, for putting up with sharing the same office as me for all that time, and Emma, for always providing the interesting subject of what she's been up to at the weekend for us to talk about during our many extended lunches! Thanks to the various students and postdocs who have made the office (and outside of it) so entertaining (sometimes too much fun given the amount of work I have needed to do recently!). In particular, these include Ian, for helping provide the much needed distractions of snooker, pool, poker and murder mysteries; Kyle, for being one of the most entertaining and likable chaps one could hope to meet, and Seb, along with Helen again, for assisting in the drinking of vast quantities of good red wine!

Thanks to all the Nottingham astronomy group staff, for the provision of drinks at the Staff Club; and for various useful scientific discussions, in particular with Frazer and Omar, whose ideas have had a significant influence on my understanding of galaxy formation and evolution, as presented in this thesis.

I will miss being at Nottingham, but am looking forward to starting my new postdoc position in Portsmouth, and thank the members of the ICG, and in particular my new boss, Bob Nichol, for giving me a job!

I would like to thank those involved for giving me the opportunity to go observing on several occasions during my PhD: to the VLT at Paranal, NTT at La Silla, and 2-meter at Kitt Peak, and the observatory staff who helped these trips go so smoothly. Thanks also to my co-observers on these trips: Bo, Paz and Alejandro.

Thanks to Osamu Nakamura and Asmus Böhm for useful discussions on various specifics of the work contained in this thesis, and Bodo Ziegler for his helpful comments as referee of our cluster Tully-Fisher paper.

My studies were funded by the University of Nottingham, for which I am grateful. I have benefited from the attendance of numerous conferences and workshops thanks to funding from the University, the Graduate School, and the MAGPOP European Research Network.

The work in this thesis was based on observations made with the ESO VLT, under programme IDs 066.A-0376 and 069.A-0312, and also with the NAOJ Subaru Telescope. It also used observations made with the NASA/ESA HST, obtained from the data archive at the Space Telescope Institute.

Published work

Much of the work in this thesis has been previously presented in four papers:

I Bamford S. P., Milvang-Jensen B., Aragón-Salamanca A., Simard L., 2005, "The Tully-Fisher relation of distant cluster galaxies", MNRAS, 361, 109

II Bamford S. P., Aragón-Salamanca A., Milvang-Jensen B., 2006, "The Tully-Fisher relation of distant field galaxies", MNRAS, 366, 308

III Mouhcine M., Bamford S. P., Aragón-Salamanca A., Nakamura O., Milvang-Jensen B., 2006a, "The metallicities of luminous, massive field galaxies at intermediate redshifts", MNRAS in press (astro-ph/0603639)

IV Mouhcine M., Bamford S. P., Aragón-Salamanca A., Nakamura O., Milvang-Jensen B., 2006b, "Star formation rates and chemical abundances of emission line galaxies in intermediate-redshift clusters", MNRAS, 368, 1871

Paper I contains much of the work detailed in chapter 2 and sections 3.1 and 5.2 of this thesis. Paper II describes the work presented in sections 4.2, 4.3, and 4.4. Sections 3.2 and 4.5 feature the analysis presented in Paper III. Finally, Paper IV describes the results covered in section 5.4. In this thesis an attempt has been made to present and discuss the data, analysis, and results from these separate papers in an integrated, coherent fashion.

The vast majority of the work presented in this thesis was performed by the author, with advice from the paper coauthors listed above. Where the material presented is the result of more collaborative work, this is mentioned at the beginning of the relevant chapter.

Chapter 1

Introduction

This thesis investigates the evolution of disc galaxies as a function of cosmic time and environment. We investigate these topics by analysing a set of spatially-resolved spectroscopic and complementary photometric data. The approach used is to observe galaxies in different environments over a fairly wide range of cosmic time, and hence out to large distances. In particular this means that the present study is limited, by current telescope and instrument capabilities, to considering only luminous, star-forming disc galaxies. An alternative approach is to analyse the properties of nearby galaxies and infer their earlier properties, in a manner analogous to archaeology. While this allows the full range of galaxies to be examined, our method has the distinct advantage that it makes use of more reliable direct measurements. The two approaches are thus very complementary.

The initial motivation for the spectroscopic observations employed herein was a comparison of luminous, star-forming, disc galaxies in distant, rich clusters with their counterparts in the coeval field. The motivation and background to this study are presented in section 1.3, the data and their reduction are discussed in chapter 2 and the subsequent analysis is described in chapter 3. The results of various comparisons between our cluster and field samples are presented in chapter 5.

However, our data include a field sample spanning a wide range of cosmic time, from today to when the universe was half its current age. This is useful for investigating evolution in the more general, field disc galaxy population. This field evolution is important to consider, both in itself, and as the background against which environmental effects occur. For this reason the field study is presented before the more specific consideration of cluster effects. The motivation and introduction to the field study is given in section 1.2, and the results, which are based on the same data and analysis as the cluster study, are presented in chapter 4. Finally, the conclusions of this thesis are summarised in chapter 6, and some areas of further work described.

In this thesis the, currently most popular, 'Big Bang' cosmological paradigm is assumed, with cold dark matter (CDM) gravitationally dominating over normal, baryonic matter, and with an appreciable dark energy (Λ) content (e.g., see Narlikar & Padmanabhan 2001for a review). The cosmological parameters used throughout are the concordance values of $\Omega_\Lambda = 0.7$, $\Omega_m = 0.3$ and $H_0 = 70\ \mathrm{km\,s^{-1}\ Mpc^{-1}}$ as supported by e.g., Spergel et al. (2003) (WMAP). All logarithms are base-10.

1.1 Galaxy formation

In order to set the work of this thesis in context, we first briefly present an overview of the current ideas concerning galaxy formation and evolution. Much more detail can be found in, e.g., the recent reviews of early structure formation by Ciardi & Ferrara (2005), and of disc galaxy formation and evolution by Silk (2003).

Our current models of galaxy formation are based upon the structure of the underlying dark matter distribution. This is determined by small inhomogeneities in the density distribution of the very early universe, which have subsequently grown and evolved under gravity. Much theoretical work has been done to understand the formation and evolution of dark matter structure in a cosmological context, including both analytical approaches and numerical simulations.

The analytical approach is generally referred to as Press-Schechter theory, due to Press & Schechter (1974), which derives the overall mass function of dark matter haloes as a function of redshift. This has been extended in a number of ways, including for specific density large-scale environments (Bond et al. 1991), for specific present-day cluster mass (Bower 1991), and in order to determine the halo correlation function (Mo & White 1996). It has also been improved to take into account ellipsoidal, rather than simply spherical, collapse (Sheth et al. 2001). Many of the results from these analytical models are illustrated in Mo & White (2002).

Numerical cosmological simulations have progressed hugely from the early work of, e.g., Efstathiou et al. (1988), to the recent 10^{10} particle 'Millennium Simulation' by Springel et al. (2005). These simulations agree very well with the analytical results, but have the distinct advantage that individual haloes can be tracked, and their internal structure examined, information which is lost in analytical considerations as the systems become non-linear. Analytical results, on the other hand, help generalise the results of simulations based on specific parameter values.

These analytical and simulation studies find that dark matter forms gravitationally-bound haloes in a hierarchical manner, with smaller haloes forming first, which then merge to form more massive haloes (e.g., see Reed et al. 2003). It is expected that the baryonic matter will generally follow the dark matter, except that its detailed distribution will be different within individual haloes due to hydrodynamic effects. This applies particularly to the centres of haloes, where baryonic matter's ability to dissipate energy allows more dense structures to form, i.e. stars and galaxies.

Dark matter-only simulations are now capable of resolving down to dwarf galaxy halo scales in volumes large enough to contain multiple superclusters. While there may be dark matter structure at still smaller scales, this is less important from a galaxy point-of-view, as baryonic physics begin to dominate on these scales. Simulations incorporating the baryonic component, in addition to dark matter, have been widely studied, with rapid recent progress. As modelling hydrodynamics is more computationally demanding, these simulations are necessarily lower resolution, or volume, than the dark matter only models, but much is still being learnt, e.g., the need for feedback to reproduce the observed entropy floor in galaxy clusters (e.g., Ponman et al. 1999; Borgani et al. 2002; Kay et al. 2004).

However, the range of scales involved in star-formation is enormous: from galaxies to molecular clouds, star formation regions, and individual stars. Furthermore, a wide range of physical processes require consideration. This means that simulating even a single galaxy in a consistent hydrodynamical manner is currently infeasible. Consistently simulating star-formation in a cosmological volume is beyond our ability for the foreseeable future.

To make progress with including galaxies in cosmological models, we must therefore resort to simplified ‘recipes’ describing the properties of a galaxy formed in a halo with given parameters, and the evolution of these galaxy properties as the host halo evolves and, in particular, undergoes mergers (e.g., Kauffmann et al. 1993; Cole et al. 1994). These recipes are usually motivated to some extent by the underlying physics, and are calibrated using theoretical models, high resolution simulations of the small scale phenomena, and more often in an iterative manner by comparing cosmological observations with the results of simulations, and altering the recipes to give simultaneous agreement with as many observational tests as possible (e.g., Somerville & Primack 1999; Cole et al. 2000). For this reason, semi-analytic galaxy formation, as it is known, is often regarded as a rather complex fitting procedure, rather than a model with predictive power. It does, however, have some ability to discern which galactic processes are important in determining the overall properties of the galaxy population. Observations can only examine the distribution of dark matter by using the properties of visible galaxies. The semi-analytic technique is thus a valuable aid for comparing dark matter simulations with the real universe.

Historically there are two competing scenarios for galaxy formation. The first of these is monolithic collapse (e.g., Eggen et al. 1962), whereby a galaxy forms by the collapse of a single, massive overdense region, and gains no significant mass thereafter. The alternative, suggested by the results of work on structure formation as described above, is hierarchical galaxy formation. In this scenario, small galaxies form first, in the numerous small haloes that are present at high-redshift. These low-mass galaxies, along with their host haloes, then undergo a series of mergers to gradually form the massive galaxies seen today.

The dark matter haloes produced in simulations tend to rotate, due to the gravitational tidal effect of the surrounding structure (Barnes & Efstathiou 1987; Steinmetz & Bartelmann 1995) and mergers (Vitvitska et al. 2002). Baryonic matter in such a halo, initially heated during the halo’s formation, cools by radiating and falls into a thin, rotating disc (e.g., Fall & Efstathiou 1980). Stars then form in this disc, giving rise to the observed disc components of many galaxies (e.g., Dalcanton et al. 1997). Mergers between two such galaxies result in a relaxed, roughly spheroidal distribution for the stars already present, explaining the formation of elliptical galaxy morphologies. However, any gas that was present in the galaxies prior to their merger, while initially heated, can again cool into a disc, in which further stars may form. The full range of observed galaxy morphologies may be thus produced. This prescription forms the basis of the semi-analytic galaxy formation models mentioned above.

The success of hierarchical dark matter theories in explaining the observed structure of the universe (e.g., Hawkins et al. 2003; Tegmark et al. 2004) obviously supports the hierarchical galaxy formation scenario. However, there are a number of potential problems. Today a proportion of reasonably massive galaxies are late-type spirals, with very little bulge component. These are difficult to produce in a scenario where every massive galaxy has been formed from the merger of several smaller ones. In addition, massive elliptical galaxies in clusters do not appear to change much between $z \sim 1$ and today. These galaxies have old stellar populations, generally with no evidence for star formation since $z \gtrsim 2$, consistent with the monolithic collapse scenario (e.g., Bower et al. 1992). A further related issue is the phenomenon of ‘downsizing’ (Cowie et al. 1997). There are many observations indicating that the main epoch of star-formation activity was earlier for more massive, or luminous, galaxies (e.g., Heavens et al. 2004). Most massive galaxies today are not forming stars at a significant rate, even when it appears there should be an ample supply of fuel, e.g. galaxies in the centres of groups and clusters. On the other hand, there are many dwarf galaxies locally with star formation rates much higher than their past average. This is reflected in the bimodality of the colour and star formation rate distributions and their relations versus magnitude (Balogh et al. 2004), and the variations in the luminosity function with spectral type (Madgwick et al. 2002). In the most straightforward interpretation of the hierachical scenario, small galaxies should have formed first, and the largest galaxies later. This appears to contrast strongly with the observations listed above.

It is likely, though, that these apparently problematic observations can be reconciled with the hierarchical scenario, and that the true difficulty is our understanding of the processes involved in galaxy formation and evolution. It is now becoming apparent that a mechanism is required which delays the formation of stars in small haloes. A good candidate for this is feedback from the first stars which formed in these haloes at early times, the so-called ‘Population III’ stars. These stars are expected to be extremely massive, and hence their supernovae could have produced a large amount of energy in a short space of time (e.g., see the review by Bromm & Larson 2004). This would have heated the gas in the halos, which, due to the low density and low metal-content, would have then taken a long time to cool enough to begin forming stars again. Other possibilities also exist, that could have prevented the gas in low mass haloes from cooling until later times. The formation of galaxies in small haloes can thus be delayed. This also helps account for the appearance of massive disc galaxies with very little bulge component. These can still be built up from the merging of smaller haloes, if these haloes contained mostly gas, with very few stars. Following a number of such mergers, the halo potential would be deep enough for the gas to cool, forming a disc.

A mechanism also appears to be required to stop the formation of stars in massive galaxies, in order to explain the properties of local ellipticals. This is possibly supplied by AGN activity, driven by a central supermassive black hole (SMBH). The masses of central SMBHs are observed to correlate well with the velocity dispersion (and hence mass) of their host stellar spheroid (e.g., Tremaine et al. 2002). This implies that the growth of the SMBH and galaxy are linked. When the SMBH reaches a threshold mass, and hence from the correlation the host galaxy has accumulated a particular mass of stars, the AGN activity due to the SMBH may be powerful enough to heat and/or expel any remaining gas, preventing further star formation (e.g., Wyithe & Loeb 2003; Springel et al. 2005).

Semi-analytic models following the growth of galaxies’ central SMBH, and incorporating AGN feedback, have recently been developed (Bower et al. 2005; Croton et al. 2006). These show reasonable success in solving the over-cooling problems discussed above.

In the hierarchical galaxy formation scenario it is still possible to form large elliptical galaxies early, in a short period of time, analogous to monolithic collapse. At early times, and at the highest peaks in the density distribution (the locations of today’s galaxy clusters), the merger rate was very high, including between haloes massive enough to host high levels of star formation without losing their gas. With some mechanism to truncate star-formation, as discussed above, uniform populations

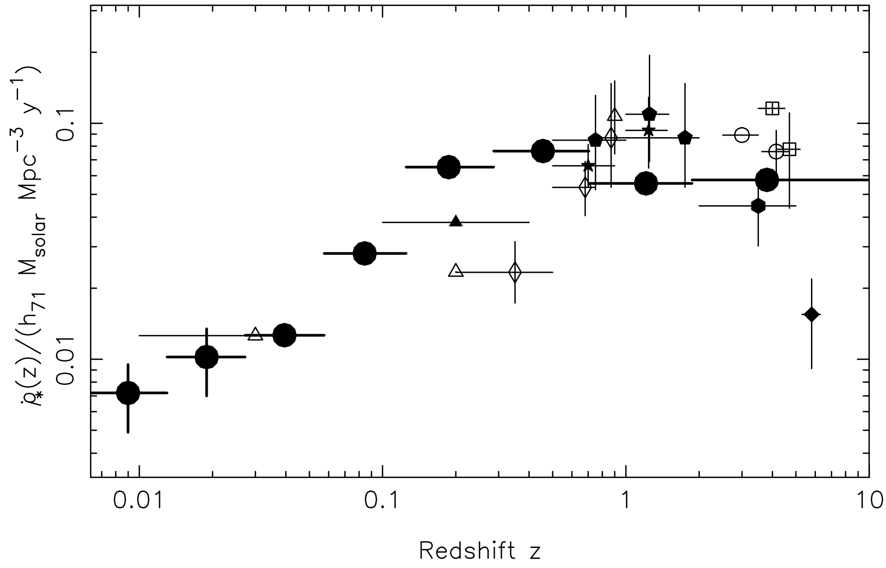

Figure 1.1. The global star formation rate density ($\dot{\rho}_*$) of the universe versus redshift, from a variety of sources, including both direct measurements of the star formation in distant galaxies (small symbols), and star formation histories inferred the stellar populations of local galaxies (large filled circles). This is figure 1 from Heavens et al. (2004); see this paper for more details.

of old, passive ellipticals may be created, matching those seen in present-day clusters.

Hierarchical galaxy formation in a ΛCDM cosmology does appear to provide an excellent framework for understanding the observed universe. Therefore, for at least the near future, the focus must be on improving our knowledge of the physical processes which determine the star formation behaviour of galaxies within this system. This includes topics from examining the formation of individual stars (e.g., Bonnell et al. 2004), to measuring the evolution of the global star-formation rate density (e.g., Heavens et al. 2004). The work in this thesis falls between these extremes, investigating how star formation varies in luminous, disc galaxies as a function of cosmic time (redshift) and environment.

1.2 Galaxy evolution in the field

Overall the star formation rate density of the universe, i.e. how many stars are formed per unit volume per unit time, is found to evolve rapidly from $z \sim 1$ to the present-day (e.g., Lilly et al. 1996; Heavens et al. 2004). This is illustrated in figure 1.1, a so-called Lilly-Madau plot of star formation rate density versus redshift.

Studies of the global star formation rate density of the Universe at low redshift (e.g., Gallego et al. 1995) and as a function of look-back time (see, e.g., Heavens et al. 2004 for a summary) generally indicate a very strong evolution of around a factor of 10 between $z \sim 1$ and today (see Hopkins 2004 for a compilation of measurements). While it is clearly important to know globally when the stars in the universe formed, these studies do not offer much indication of the systems this star formation took place in, or the mechanisms responsible for its evolution.

Bell et al. (2005) determine the star formation rates of individual morphologically-classified galaxies at $z \sim 0.7$ using 24μm Spitzer observations, finding much higher star-formation rates in individual massive galaxies than seen today. In addition, around half of these galaxies have spiral morphologies, and most are undisturbed. They argue that this implies that the rapid evolution of cosmic star formation is not driven by a higher incidence of major mergers at intermediate redshifts.

If the enhanced star formation rate in high-redshift galaxies apparently has no obvious cause, which could be subsequently removed at low redshifts (e.g., a decline of the merger rate), thereby resulting in the star formation decline, then perhaps high star formation rates are the norm, but some mechanisms are at work to suppress star formation at later times.

In addition, it is still an open question whether the star-forming spiral galaxies observed at intermediate-redshift are still star-forming spirals today. Wolf et al. (2003) find, using the COMBO-17 survey, that the number density of red galaxies increases dramatically between $z \sim 1.1$ and today, while blue galaxies decline in abundance and luminosity. This suggests that rather than just a gradual decline in individual galaxy star formation rates, intermediate-redshift blue, star-forming galaxies are being changed into red, passive galaxies by the present-day.

This receives some support from the VIMOS VLT Deep Survey (VVDS), which find similar evolution in the luminosity function of the late-type population, although there may be conflicting results for the red population (Zucca et al. 2005). On the other hand, results from the DEEP2 Redshift Survey only find luminosity evolution for blue galaxies, such that they are ~ 1.3 mag fainter today than at $z \sim 1$, while the red galaxy results are comparable to those of COMBO-17, though less pronounced (Willmer et al. 2005). Combining the DEEP2 and COMBO-17 results (Faber et al. 2005), reinforces the conclusion that since $z \sim 1$, while the red galaxy population has increased by a factor of ~ 4, the blue, and hence star-forming, galaxy population has changed little in number density, but has experienced a moderate decline in luminosity.

Rather than tracing the amount of ongoing star formation in galaxies, through their emission-line or far-infrared luminosity, B-band magnitude, or colours, another approach to investigating the star formation histories of distant galaxies is to measure their stellar mass. Bundy et al. (2005) examine the stellar mass function from $z \approx 0$–1, finding little evolution, at least for the massive galaxies they sample. This latter interpretation implies that such galaxies have not formed significant amounts of stars in the past 8 Gyr, compared with their star formation levels before this time. The K20 survey (Fontana et al. 2004) find mild evolution of the stellar mass function to $z \sim 1$ followed by more rapid evolution to $z \sim 2$ and beyond. However, while broadly consistent, the MUNICS survey (Drory et al. 2004) and Drory et al. (2005), using FDF and GOODS-CDFS data, find a factor of two evolution in the stellar mass function normalisation since $z \sim 1$. Ellipticals dominate the high end of the stellar mass distribution at high redshifts (Fontana et al. 2004; Bundy et al. 2005) and today (e.g., Bell et al. 2003), and become increasing dominant overall with time (Brinchmann & Ellis 2000).

Environment may well play a role in reducing the global star formation rate density, potentially by both fast truncation and more gradual suppression of star formation in individual galaxies. It has recently become clear that even fairly low-density group environments have a significant effect upon their constituent galaxies, both in terms of reducing the star formation rates of star-forming galaxies, and transforming star-forming galaxies into passive types, both locally (Lewis et al. 2002; Gómez et al. 2003; Balogh et al. 2004), and at intermediate-redshift (Poggianti et al. 2006). The mechanism responsible for this is still unclear, and a number of possibilities are discussed in the context of denser environments in section 1.3. However, these do not seem to be effective enough in such low density conditions. Perhaps AGN activity, proposed as a solution to star-formation truncation in individual massive galaxies (e.g., Wyithe & Loeb 2003; Springel et al. 2005), may be capable of influencing entire groups.

The degree of chemical enrichment provides an alternative measure of past star formation in galaxies. This approach reveals star formation rates at $z \approx 1$–2 considerably higher than today (e.g., Pei & Fall 1995), in agreement with direct studies of current SFR at high-z. Analyses of the oxygen abundances of star-forming field galaxies at intermediate redshifts seem to indicate that the luminosity–metallicity relation evolves with redshift, with steeper slope (faster variation in metallicity with luminosity) at earlier cosmic times (Kobulnicky et al. 2003; Maier et al. 2004; Liang et al. 2004; Maier et al. 2006). These studies imply that lower luminosity field galaxies have experienced substantial chemical evolution since $z \sim 1$, while the brightest galaxies have changed little. This, in turn, suggests that luminous galaxies have experienced little star formation since $z \sim 1$, compared with before this time, while fainter galaxies are still in the process of forming their stars.

A putative picture is thus emerging, whereby star formation occurs in more massive disc galaxies at earlier times. This is at some point suppressed by an as yet unconfirmed mechanism, and the galaxies transformed into passive types, potentially with elliptical morphology, e.g., following mergers. Less massive disc galaxies experience their main epoch of star formation at later times, building up their stellar content and metallicity at intermediate redshifts.

Much more work is required to add support and detail to this picture. Fortunately, however, there is considerably more still to be done with the wide variety of local and distant surveys already available. In addition, even more ambitious surveys are in progress or planned, which will add a wealth of information to this field. The biggest difficulty will be interpreting what it all means!

As part of this thesis we investigate the evolution of individual, luminous, massive disc galaxies in the field at $z \approx 0$–1, through their Tully-Fisher relation, star-formation properties and metallicities.

1.2.1 The role of the Tully-Fisher relation

The slope, intercept and scatter of the Tully-Fisher relation (TFR; Tully & Fisher 1977) are key parameters that any successful prescription for galaxy formation and evolution must reproduce.

This observed correlation between the luminosity and rotation velocity of spiral galaxies may be thought of as being comprised of three more fundamental parts. These are: the relation between observed rotation velocity and total galaxy mass, the relation between total and stellar mass distributions, and the mass-to-light ratio of the stellar population. The first of these is dependent upon the degree to which the observed material is rotationally supported, but assuming a negligible non-rotational component the mass within a radius r is simply

$$m_r = \frac{V_{\mathrm{rot}}^2 r}{G_{\mathrm{N}}}, \tag{1.1}$$

where G_{N} is Newton's gravitational constant. The second relation is determined by the galaxy formation process, while the third is dependent on the star formation history and initial stellar mass function. Using the definition of the mean surface brightness within r, I_r, for a (face-on) galaxy with luminosity L_r,

$$L_r = \pi r^2 I_r, \tag{1.2}$$

and combining with equation 1.1, gives

$$L_r = \frac{V_{\mathrm{rot}}^4}{\pi G_{\mathrm{N}}^2 I_r (m/L)_r^2}. \tag{1.3}$$

Taking r to be defined in some way which scales with galaxy size, e.g. the effective radius r_e, and naively assuming the mean surface brightness and total mass-to-light ratio within r, $(m/L)_r$, are constant between different galaxies gives $L_r \propto V_{\mathrm{rot}}^4$. Expressing equation 1.3 in the usual observers form (and dropping the r subscripts) this becomes

$$M = -10 \log V_{\mathrm{rot}} - \mu + 5 \log(m/L) + c_M, \tag{1.4}$$

where $\mu = -2.5 \log I_r$ and c_M is a constant. Much more detailed derivations may be found in, e.g. Aaronson et al. (1979). Essentially, any departure from a slope of 10 indicates a dependency of $\mu - 5\log(m/L)$ on V_{rot} (or equivalently M), and any change in the intercept between two samples reflects differing values of $\mu{-}5\log(m/L)$ between the samples.

The near-infrared K-band TFR is observed to possess a slope of approximately 10 (e.g. Pierini & Tuffs 1999), in reasonable agreement with that derived from the above assumptions. However the slope flattens as one goes to shorter wavelengths, for example Pierce & Tully (1992) find TFR slopes of 9.5, 8.7, 8.2 and 7.5 for the H, I, R and B bands respectively. As the K-band light is dominated by the old stellar population it reflects the long-term, average properties of galaxies, and as such could be expected to be closest to the naive theoretical TFR. The observed flattening of the TFR at bluer wavelengths implies that $\mu - 5\log(m/L)$ decreases (becomes more negative) with V_{rot} (or equivalently with decreasing M) in these bands. Galaxy light at bluer wavelengths is increasingly dominated by young stars, hence this suggests a dependence of star-formation properties on V_{rot} and/or M. This could be a due to a variation in either μ, m/L or both. Note that these quantities could also vary due to a change in the radius within which they are measured, usually defined by the light profile, with respect to a radius which scales with the galaxy mass profile.

In the past decade significant progress has been made toward understanding the astrophysics responsible for the TFR. This involves understanding how the parameters involved conspire to maintain the relation, through some form of self-regulation of star-formation in the disc (Silk 1997), while explaining the variations which lead to its intrinsic scatter. For example, it has been demonstrated that the roles of μ and m/L are more subtle than their simply being individually constant. Rather, they are anti-correlated in such a way as to preserve a TFR slope of approximately 10 in the K-band (Pierini & Tuffs 1999). However, while this anti-correlation remains at shorter wavelengths, it cannot restrain a flattening of the TFR slope (Burstein et al. 1997).

It is now becoming clear that the TFR is a projection of a tighter relation in a higher dimensional parameter space, including a measure of disc size along with the luminosity and rotational velocity (Kodaira 1989; Koda et al. 2000). Furthermore this three-dimensional relation, along with the similar Fundamental Plane for elliptical galaxies, can be understood as a particular case of a general behaviour seen for all self-gravitating, equilibrium stellar systems (Burstein et al. 1997). Modern simulations are able to reproduce the slope and scatter of the I-band TFR (e.g. Koda et al. 2000), respectively identifying these with the natural range of mass and spin parameters for dark matter haloes. However, reproducing the TFR intercept while matching other properties of the galaxy population is currently beyond the abilities of semi-analytic models (Cole et al. 2000).

As well as a goal to understand in its own right, the TFR is particularly useful as a benchmark with which to compare samples of galaxies, in order to examine the differences between them, or changes with respect to another parameter. Using this method, we can gain insight into the evolution of disc galaxies by considering the variation of the TFR with cosmic time.

1.2.2 Distant Tully-Fisher studies

One of the first attempts at measuring reliable, true rotation velocities of distant galaxies, and constructing their Tully-Fisher relation, was performed by Vogt et al. (1996). This studied nine galaxies, five below $z = 0.5$ and four at $z = 0.8$–1.0, mostly from the Deep Extragalactic Evolutionary Probe project (DEEP). Combining all of these galaxies $\langle z \rangle \sim 0.6$, and without any sample selection corrections, an offset of the B-band TFR from the local fit of Pierce & Tully (1992, hereafter PT92) of 0.55 ± 0.16 mag was measured. Vogt et al. (1997) added an additional 8 lower luminosity galaxies to this sample, extending the sample to cover the range $-19 \gtrsim M_B \gtrsim -22$ for 16 galaxies with $z = 0.15$–1.0 ($\langle z \rangle \sim 0.7$). No evidence for a change in the TFR slope from that of PT92 was found. A B-band TFR intercept offset of 0.36 ± 0.13 mag was measured. The size–luminosity relation was also studied, revealing the distant galaxies to be offset from the local relation of de Jong (1996) by $0.59 + -0.13$ mag at a fixed disk scalelength. This was consistent with contemporary studies (e.g., Forbes et al. 1996), particularly when surface brightness selection effects were considered, and in reasonable agreement with the TFR offset. This implies that the observed TFR evolution is primarily due to luminosity evolution.

Further TFR work on the expanding DEEP sample (Vogt et al. 2005) has been periodically announced (e.g., Vogt 1999, 2001; Vogt et al. 2002). With additional data and analysis, this work has converged on the conclusion that, once selection effects are accounted for, the B-band TFR has not changed significantly since $z \sim 1$, except perhaps for the appearance of a population of over-luminous, low-mass galaxies beyond $z \sim 0.5$, with TFR offsets of up to 3 mag. They also report little evolution in the size-luminosity relation, once surface brightness selection effects have been considered. A final paper on this work is expected soon, which will reveal more important details about this analysis.

Several other earlier studies of the Tully-Fisher relation at intermediate redshifts found significant luminosity evolution with redshift, such that the distant galaxies are brighter at a given rotation velocity than seen locally. In a study of 24 faint, blue galaxies ($B \sim -19$, $B - R \sim 1$) at $z \sim 0.25$, Rix et al. (1997) found a TFR offset of ~ 1.5 mag. Note that this study utilised linewidths, in contrast to the resolved emission line fits used by the other studies discussed here. Simard & Pritchet (1998) find a B-band TFR offset of 1.5–2 mag for a sample of 22 star-forming galaxies at $z = 0.25$–0.45, but note that this may be exaggerated by selection effects, particularly on [OII] emission strength.

Dalcanton, Spergel & Summers (1997) and Simard et al. (1999) argue that much, if not all, of the size-luminosity and TFR evolution measured is due to surface brightness selection effects.

More recently, studies by Barden et al. (2003; $\langle z\rangle \sim 0.9$), Böhm et al. (2004; $\langle z\rangle \sim 0.5$), Nakamura et al. (2006; $\langle z\rangle \sim 0.4$) and Böhm & Ziegler (2006; $\langle z\rangle \sim 0.5$) have all found comparable evolution of the B-band TFR intercept of ~ 1 mag per unit redshift, before selection effects are accounted for. With consideration of the surface brightness limits intrinsic to these studies, it is possible that they would find little or no evolution of the TFR intercept.

However, expressing the true evolution of galaxies in the TFR may be complicated by the existence of a bright, low-mass population at intermediate redshift. For instance Vogt (2001) describe the TFR as unchanging with redshift, and fit with the slope fixed to its local value, but note the existence of this additional population. In contrast, Böhm et al. (2004) and Böhm & Ziegler (2006) fit the TFR with a free slope, and find strong evidence for a change in this slope at intermediate redshift. They find that while distant massive galaxies are located similarly in the Tully-Fisher diagram to their local counterparts, lower mass distant galaxies are brighter by 1–2 mag in the B-band at $\langle z\rangle \sim 0.45$. This appears to agree with other (non-TFR) studies which find evidence of this so-called 'down-sizing', as mentioned earlier in this chapter.

So far we have been considering the B-band TFR, which is clearly sensitive to the level of on-going star-formation in the galaxies being considered. As such it is often used to examine star-formation evolution in the galaxy population. However, the TFR is also of use in constraining the build up of both the dark and baryonic matter content of galaxies. These slightly disparate goals can sometimes cause confusion in discussing TFR evolution: has the TFR evolved once star-formation variations have been taken out, or once the cosmological build up of galaxy haloes is accounted for?

To examine the build-up of the dark matter and stellar content of galaxies it is more useful to study the TFR in a red or near-infrared (NIR) band, where recent recent star-formation has less of an effect, and the galaxies' total stellar content is being measured. This can be taken further, to using estimates of stellar mass, usually obtained by correcting a red or infra-red luminosity for the (usually small) effect of recent star-formation through the use of one of more colours (e.g., Bell & de Jong 2001). Recently, NIR imaging has become sufficiently sensitive to allow distant TFR studies in the rest-frame red and infra-red bands, and hence accurate stellar mass estimates.

Conselice et al. (2005) find no significant evolution in either the K-band the baryonic Tully-Fisher relation, i.e., between stellar and total mass, since $z \sim 1$. This result suggests that either these galaxies have not evolved significantly since this time, or that as they have gained stars they have also acquired dark matter in proportion. This implies that the growth of massive disc galaxies since $z \sim 1$ has proceeded in a hierarchical fashion, with mergers bringing in dark matter along with stars, or gas from which stars can subsequently form. However, the explanation for these results could be more complicated. For example, one could speculate that they may also be consistent with a scenario in which the ratio of a galaxy's stellar to total mass is limited, e.g., by AGN feedback. Galaxies in a given mass halo with more than a threshold stellar mass may have been transformed into passive galaxies, and potentially an early-type morphology, by such a mechanism, and therefore no longer appear in a Tully-Fisher sample. Over the same time, galaxies with low stellar-to-total mass ratios, and hence too faint to appear in distant NIR Tully-Fisher samples, could have rapidly formed their stellar content, and moved on to the TFR.

In the past few years spectroscopic integral field units (IFUs) have started to be used for distant TFR studies. Using this technique one can recover a more detailed, two-dimensional velocity field, rather than the one spatial dimension afforded by slit-based spectroscopy. This enables a more accurate characterisation of the velocity field, and hence easier recognition of kinematically peculiar systems.

Following an initial demonstration (Flores et al. 2004), the velocity fields of 35 galaxies at $0.4 < z < 0.75$ have been obtained by Flores et al. (2006) using the multiple deployable IFUs of FLAMES/GIRAFFE at the VLT. They find that 65% of these galaxies show perturbed or complex kinematics. The 11 galaxies displaying regular rotation form a tight K-band TFR, very similar to that observed locally. The baryonic TFR is also very pronounced and compatible with the local relation. These results agree well with those of Conselice et al. (2005).

In the B-band, Flores et al. (2006) again find a strong TFR for galaxies with regularly rotating disks. In this case the relation is brighter than that seen locally by roughly 0.5 mag. The scatter is also dramatically increased, and it appears as though while some of the galaxies lie on the local TFR, approximately one-third have enhanced B0band luminosity. This is interpreted as galaxies undergoing a phase of enhanced star-formation. In both the K and B-bands, the TFR slope defined by the rotating disks is consistent with the local value. However, the sample is limited to bright objects, and covers less than half the magnitude range of the Böhm & Ziegler (2006) study, which finds evidence for a change in slope driven by faint galaxies which are not included in the Flores et al. (2006) sample.

Flores et al. (2006) measure their rotation velocities simply from the maximum gradient of their derived velocity field, with a 20% correction factor derived from simulated observations of normally rotating galaxies. As well as doing this for their observed regularly rotation disks, they also measure these apparent rotation velocities for their galaxies with perturbed and complex kinematics (using the same correction factor). This is intended to mimic the naive value that would be measured by a slit-based study, making the assumption that all the galaxies are regular rotating disks. When plotted on the TFR, these peculiar galaxies have a larger scatter, and are biased to lower rotation velocities for a given luminosity when compared with the regular rotators. This is taken as being due to the measured values being underestimates of the 'true' rotation velocity these systems would display in the absence of an interaction. This produces an apparently flatter slope of the TFR (less luminosity variation with respect to rotation velocity). Flores et al. suggest that this is the reason behind the TFR slope evolution measured by Böhm & Ziegler (2006), i.e., that it is not a real evolution, but due to biases in the measurement of galaxies with peculiar velocity fields, which cannot be identified with only slit-based spectroscopy. However, it is again worth noting that the sample of Flores et al. does not extend to as faint luminosities as that of Böhm et al.

Another interesting development in TFR studies is the use of lensing by clusters to magnify background galaxies and thereby dramatically increase their luminosity and spatial resolution. This method is applied to six $z \sim 1$ galaxies by Swinbank et al. (2006). Four of these are found to have regular rotation curves. These galaxies form I and B-band TFRs with scatter and slopes comparable to the local relations, and offset to brighter magnitudes by < 0.1 mag in I and $\sim$ 0.4–0.5 mag in B, in agreement with much of the work described above.

1.3 Galaxy evolution in clusters

1.3.1 Summary of evidence

The effects of falling into a cluster upon an individual galaxy are important for a complete understanding of galaxy evolution. Despite only a small minority of galaxies being located in rich clusters, even at zero redshift, such environments are naturally very interesting to study as extrema. In particular they are sites of simultaneously both unusually fast and slow galaxy evolution, and hence contain unique galaxy populations. Because of this, they have the potential to provide much insight into a variety of astrophysical processes, not only specific to clusters, but also occurring in the general galaxy population.

A substantial fraction ($\sim$80%) of bright galaxies ($M_b < -19.5$) in local clusters have no significant current star-formation, as judged from Hα emission (Balogh et al. 2004). In addition, clusters predominantly contain galaxies with elliptical and S0 morphology (again $\sim$ 80%; Dressler 1980). Both of these observations are in contrast to the local field, for which the same studies find $\lesssim$ 40% of galaxies to be non-starforming and an early-type fraction of $\sim$20%.

While some galaxies likely formed in dense regions, it is generally considered very difficult to create discs under such conditions, as the cluster environment removes the supply of cold gas from which a disc might form (Gunn & Gott 1972). In addition the structure formation scenario of ΛCDM implies that many galaxies have undergone the transition from field to cluster environment since $z \lesssim 1$ (De Lucia et al. 2004). At least some of these galaxies must have been transformed following their entry into the cluster environment, in order to account for the disparity between the cluster and field galaxy populations seen today.

The fraction of elliptical galaxies in clusters is observed to be fairly constant out to $z \sim 1$ (e.g., Fasano et al. 2000). However, it is well established that the general properties of the disc galaxy population in distant clusters are different to those locally, and that a smooth change in these properties can be traced with redshift, albeit with substantial scatter. There is a larger fraction of blue galaxies at high redshift (Butcher & Oemler 1978), found to be star-forming (Dressler & Gunn 1982, 1992) and typically with spiral morphology (Couch et al. 1998; Postman et al. 2005). This is in contrast with the quiescent S0 galaxies which form a significant fraction of the cluster population at low redshift, and dominate the cores of rich clusters (Dressler et al. 1997).

A possible implication of all this evidence is that star-forming spirals are transformed into passive lenticulars by the cluster environment, and that this is the dominant path for forming such galaxies, at least in clusters. While there is evidence at low redshifts that group environments may be the most important regions for decreasing the *global* star formation rate of the universe (Balogh et al. 2004), for massive galaxies and earlier epochs clusters seem to be more effective. Additional evidence for the reality of the transformation of spirals into S0s is provided by the existence in clusters of two unusual galaxy types. The first is passive spirals, with spiral morphology but no sign of current star-formation. These are found in the outskirts of low-redshift clusters, but not generally in the field, and suggest that some interaction with the cluster environment has recently curtailed their star-formation (Goto et al. 2003). The second type are disc galaxies with spectra indicative of a recent, sudden truncation of their star-formation. Such galaxies have an E+A spectral type (also known as k+a) with features of both an old (> several Gyr; K stars, which define a typical elliptical galaxy spectrum) and intermediate age ($\lesssim$ 1 Gyr; A stars) stellar population, but with no sign of on-going star-formation (Dressler & Gunn 1983; Dressler et al. 1999). Furthermore, many such spectra indicate a star-burst occurred shortly prior to the end of star-formation (Poggianti et al. 1999). E+A galaxies are found over a wide redshift range, but in local clusters most are dwarfs (Poggianti et al. 2004) and in the field they have almost entirely elliptical or irregular morphologies (Yang et al. 2004; Tran et al. 2004). The larger, disky E+As which may form the link between spirals and S0s are preferentially found in clusters at intermediate redshifts, where the relative fraction of spirals and S0s is seen to change most rapidly.

1.3.2 Transformation of spirals to S0s

Several mechanisms have been proposed that could transform spirals to S0s in cluster environments. The favoured options are ram-pressure stripping (Gunn & Gott 1972) and unequal-mass mergers (Bekki 1998; Mihos & Hernquist 1994).

In the ram-pressure stripping scenario, the pressure due to the galaxy's passage through the intra-cluster medium (ICM) removes gas that would have fuelled future star-formation. Depending upon the model one assumes, the gas could be removed from the disc itself, causing a fast truncation of star-formation (Abadi et al. 1999; Quilis et al. 2000), or the gas could merely be removed from the galaxy halo (Bekki et al. 2002). Normally the disc gas consumed in star-formation is replenished by infall from the reservoir of halo gas. This latter alternative thus leads to a gradual decline in star-formation rate (SFR) as the quantity of available disc gas diminishes. Prior to the cessation of star-formation, the increased pressure in the disc gas may actually trigger an initial burst of star-formation, through compression of the galactic molecular clouds (Bekki & Couch 2003). This in turn would cause an increase in the rate of disc gas consumption, and hence reduce the time taken for star-formation to cease. The duration of any star-burst of this form is therefore self-limiting, and necessarily short, with the strongest bursts being the shortest-lived. These alternative star formation histories are illustrated in figure 1.2.

Galaxy mergers may cause an eventual truncation of star-formation by first inducing a star-burst. This enhanced SFR quickly depletes the supply of gas from which future stars could have formed, and thus subsequently halts star-formation. Gas from the outer disc is also tidally stripped, reducing the amount available for star-formation. From simulations, Bekki (1998) find that mergers with a mass ratio of $\sim 3:1$ often result in S0 morphologies. Minor mergers (mass ratio $\gtrsim 10:1$) have a smaller effect on the larger galaxy, the disc is dynamically heated and therefore becomes thicker, but repeated minor mergers may also lead to an S0 appearance. Mergers between galaxies of nearly-equal mass, on the other hand, while also inducing a star-burst and consequent end of star-formation, generally destroy any disc component, resulting in an elliptical morphology.

Both of these mechanisms may well occur, and result in galaxies with roughly S0 morphology and typically corresponding spectral properties. However, we would like to know which has the dominant role, and examine any differences in the form of the transformations, including how E+A galaxies fit into the evolution. In addition there is likely to be a dependence of the S0 formation mechanism on environment, which deserves attention. For example, the high relative velocities in clusters make merging less likely than in groups, while ram-pressure stripping is probably only effective in the dense ICM of large clusters.

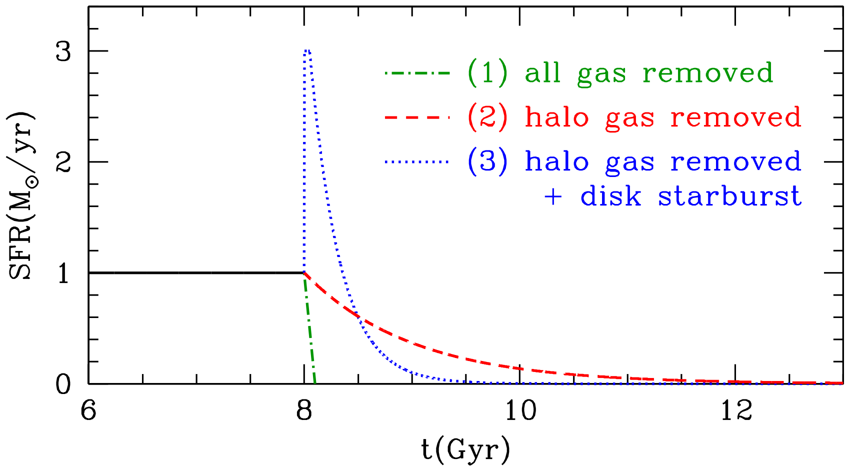

Figure 1.2. A simple illustration of possible alternative star formation histories for galaxies entering the cluster environment. Initially the galaxy is forming stars at a constant rate. Some possibilities upon encountering the cluster environment are: (1) all gas is removed from the galaxy, resulting in a very fast truncation of star formation, (2) only the halo gas is removed, leading to a gradual decline in star formation as the disc gas reservoir is consumed but not replenished, (3) the halo gas is removed, but in addition the interaction causes an initial enhancement of the star formation rate, which uses up the disc gas at a faster rate, producing a subsequent rapid decline.

Another potential effect, present in clusters, is galaxy harassment (Moore et al. 1999). This is caused by the tidal effects of close encounters with other, more massive, galaxies. However, while this may contribute somewhat to a thickening of discs in clusters, it is more important for dwarf galaxies than the giant discs we are considering here. A tidal effect likely to be more significant for the evolution of massive galaxies is the tidal field due to the cluster potential itself. While in the smooth, static case this is judged to only be important close to the cluster core (Henriksen & Byrd 1996), the existence of substructure, and in particular cluster-group and cluster-cluster mergers, may result in a time-varying tidal field with more significant effects (Bekki 1999; Gnedin 2003a,b).

Recently direct observational support for some of these mechanisms has begun to emerge. For example, evidence of ram-pressure stripping at work in a cluster environment is presented statistically by Vogt et al. (2004) and in detailed individual cases by Crowl et al. (2005a,b). On the other hand, Owen et al. (2005) and Ferrari et al. (2005) suggest that tidal interactions due to cluster-cluster mergers are the most likely explanation for their observations of enhanced star-formation in Abell 2125 (at $z = 0.25$) and Abell 3921 (at $z = 0.1$), respectively. Poggianti et al. (2004) find evidence for blue E+A galaxies, hence with recently truncated star formation, to be correlated with the fronts of merging substructures in the local Coma cluster, and suggest ram pressure as the responsible mechanism. More work is clearly necessary before the roles and dominance of the various suggested mechanisms can be established.

A potential key difference between the transformation by ram-pressure stripping and through mergers or tidal effects is that the former is likely to enhance star-formation across the disc (Bekki & Couch 2003), while any star-burst caused by merging or tides is probably centrally concentrated, due to disc gas being driven inward by an induced central bar (Mihos & Hernquist 1994). These differences may be distinguishable, once a luminosity enhancement has been established for a galaxy, by examining colour gradients or more detailed properties of the stellar-populations as a function of radius. For example, if the galaxy centre is bluer than the disc, this implies centrally enhanced star-formation, and therefore possibly that a tidal interaction is responsible. However, such interpretations will require careful comparison with simulations of galaxies' internal responses to the various mechanisms. We do not attempt to examine colour gradients in our present sample, due to the uncertainties that would be caused by the heterogeneous nature of our imaging.

In complement to the examination of stellar-population gradients, differences in the time-scales of the star-burst and subsequent SFR decline may also help to distinguish between the proposed mechanisms. An attempt of this has been made by Nakamura et al. (2006), but without clear results.

To summarise, much evidence has been accrued for the transformation of spirals to S0s by the cluster environment, and a number of plausible mechanisms have been proposed, but there is still little known about its detailed nature and few constraints on which mechanism is actually responsible. This thesis presents a study to address this issue by examining the first stage of this phenomenon, the early effect on spiral galaxies falling into a cluster. By comparing the Tully-Fisher relation (TFR) for field and cluster galaxies, we aim to evaluate the cluster's effect upon the mass-to-light ratio of a galaxy during the period for which it retains spiral morphology and an appreciable star-formation rate. Assuming star-formation is eventually suppressed in cluster galaxies, such galaxies are thus presumably recently arrived from the field. We can therefore investigate the existence and prevalence of luminosity (and hence perhaps star-formation rate) enhancement in the early stages of the spiral to S0 transformation. This is investigated in section 5.2. Relations based on the sizes of galaxies, both stellar and emission line scalelengths, may provide additional information, as considered in section 5.3.

1.3.3 Star formation histories

In the hierarchical picture of galaxy formation, galaxies first form at rare, isolated, high-significance peaks in the dark matter dominated density distribution. These over-densities grow over time, principally by accreting smaller, individual structures which have formed later from lower-significance peaks. The first structures to form have had more time to grow, and through their greater mass have more ability to accrete material. These objects therefore become the largest gravitationally-bound structures seen today: massive galaxy clusters.

This scenario implies that the galaxies seen in clusters formed in a diverse range of environments, and have a wide variety of ages. Some will have formed early in the initial cluster over-density, while others may have formed later in the field and have only recently entered the cluster environment. The variety of ages for these galaxies, and the different environmental circumstances throughout their lifetimes, should be reflected in the properties of their stellar populations.

When looking for evidence of an environmentally-induced galaxy transformation, it is important to judge whether the cluster galaxies under consideration would have the same properties as normal field spiral galaxies in the absence of the transformative mechanism. Otherwise, separating their inherent differences from those due to the putative recent environmental interaction makes the problem considerably more difficult. For example, if the cluster galaxies initially formed in a denser environment or are older than the field galaxies against which they are compared, then their properties may be expected to differ anyway, without the need for any later effect.

As discussed in the previous section, there are a number of lines of evidence that clusters have grown by accreting field galaxies, and that these in-falling galaxies have their star formation suppressed on reasonably short timescales (~ 1 Gyr). In this case, any cluster galaxy with current star formation, and hence displaying emission lines, will be recently arrived from the field. However, it would be very useful to test this assumption further, and reduce our reliance on it.

In considering the Tully-Fisher relation, as described above, we can look for variations in luminosity at a given rotation velocity (a proxy for galaxy mass), which would potentially result from a change in star formation rate in the fairly recent past (upto several Gyrs). Direct measurements of the current star formation rate provide information about the shorter timescale, while the metallicity of the galaxies is sensitive to longer-term, integrated star formation histories. By considering these additional properties we can try to confirm the reality and cause of any variations seen in the TFR, while checking that such variations are not simply due to differences in the ages and formation circumstances of the galaxies. This is addressed in section 5.4, using measurements described in section 3.2.

Chapter 2

Data

2.1 Data overview

This studies presented in this thesis use a collection of spectroscopy and imaging data from a range of sources. The principal data set is multi-slit spectroscopy observed with FORS2 on the VLT in September 2002, by Bo Milvang-Jensen. These data have been entirely reduced and analysed by the author, and the procedure used is briefly described in section 2.3. The 2002 VLT spectroscopy is used by all the studies presented herein.

Multi-slit spectroscopy was also available for one cluster, MS1054, from earlier FORS2/VLT observations taken by Bo Milvang-Jensen in February 2001. These data were reduced, and the Tully-Fisher relation analysed, by Bo Milvang-Jensen, as described in Milvang-Jensen (2003) and Milvang-Jensen et al. (2003). However, in order to increase our sample size, these 2001 VLT MS1054 data were re-analysed in the same manner as our 2002 VLT data and combined with it for all the studies presented in this thesis.

Similar multi-slit spectroscopic data was also obtained using FOCAS on the Subaru telescope in August 2002, again by Bo Milvang-Jensen. These data were reduced separately, and the Tully-Fisher relation analysed, by Osamu Nakamura, as described in Nakamura et al. (2006). The Subaru data were combined with the VLT data for the analysis of the spatially-integrated spectra described in section 3.2.

The basic properties of all the clusters with observations used in this thesis are listed in table 2.1.

The imaging data used in this study is primarily from the HST archive and our own FORS2 *R*-band imaging, which was taken for the purpose of designing the spectroscopic masks. These are supplemented with additional reduced and zero-point calibrated ground-based data, in order to provide colour information. This additional colour information is advantageous for constraining the galaxy spectral energy distribution type (SED) and hence improving the *k*-correction. For the fields observed in the 2002 VLT data this additional data was imaging kindly provided by Dr. Ian Smail. Additional photometry for the Subaru fields was collected from a number of literature sources (see Nakamura et al. 2006).

The following sections outline the target selection, spectroscopic reduction, and imaging analysis for the 2002 VLT data which form the basis of this thesis. The 2001 VLT data of MS1054 and the Subaru data were treated in a similar manner by Milvang-Jensen (2003) and Nakamura et al. (2006), respectively.

Table 2.1. Basic properties of the clusters considered in this thesis. The alternative names are those preferred by Simbad (http://simbad.u-strasbg.fr) at CDS, following IAU recommendations. For each field, galaxies with $z_{\rm cl} - \Delta z_{\rm cl} \leq z \leq z_{\rm cl} + \Delta z_{\rm cl}$ are considered to be cluster members.

Targeted cluster	Full alt. cluster name	RA [J2000] h m s	Dec. [J2000] ° ′ ″	$\sigma_{\rm cl}$ [km s^{-1}]	$z_{\rm cl}$	$\Delta z_{\rm cl}$
2002 VLT observations:						
MS0440 [a]	ClG 0440+02	04 43 09.5	+02 10 30	838	0.197	0.010
AC114 [a]	ACO S 1077	22 58 47.1	−34 47 60	1388	0.315	0.018
A370 [a]	ACO 370	02 39 51.6	−01 34 12	859	0.374	0.012
CL0054 [a]	ClG 0054−27	00 56 56.0	−27 40 32	742	0.560	0.012
MS2053 [b]	ClG 2053−04	20 56 22.4	−04 37 43	817	0.583	0.013
2001 VLT observations:						
MS1054 [a]	ClG 1054−03	10 56 57.3	−03 37 44	1178	0.830	0.022
2002 Subaru observations:						
A2390 [a]	ACO 2390	21 53 36.8	+17 41 32	1294	0.228	0.016
MS1621 [a]	ClG 1621+26	16 23 34.5	+26 34 17	735	0.427	0.010
CL0016 [a]	ClG 0016+16	00 18 33.5	+16 26 03	984	0.549	0.015
MS2053 [b]	ClG 2053+04	20 56 22.4	−04 37 43	817	0.583	0.013

[a] position, z and σ from Girardi & Mezzetti (2001),

[b] position and z from Stocke et al. (1991), σ from Hoekstra et al. (2002).

2.2 Target selection

The selection of targets to be observed for this project was performed prior to the commencement of my PhD studies, by Bo Milvang-Jensen and Alfonso Aragón-Salamanca. This selection plays an important role in the interpretation of our studies' results, however, and is therefore described here. This discussion below is based on the procedure applied for the 2002 VLT data, but is very similar to that used in preparing the earlier MS1054 observations.

The clusters chosen to be studied were simply selected to be rich clusters covering a wide redshift range and with available HST imaging, and therefore do not form a particularly homogeneous sample. Our clusters are generally very massive (see velocity dispersions in table 2.1). However, this is not regarded as a problem for our purposes, as we are primarily seeking to establish the reality of a difference between cluster and field galaxies, and gain a first insight into the nature of any disparity. A more detailed examination with respect to cluster properties, redshift, etc. is left for future, larger, more homogeneous studies such as the ESO Distant Cluster Survey (EDisCS, see section 6.2.2; White et al. 2005).

The galaxies observed within each field were selected by assigning priorities based upon the likelihood of being able to measure a rotation curve. To ascertain this we made use, in part, of previously observed spectral properties from a number of studies (MS0440: Gioia et al. 1998, AC114: Couch & Sharples 1987; Couch et al. 1998, A370: Dressler et al. 1999; Smail et al. 1997, CL0054: Dressler et al. 1999; Smail et al. 1997; P-A Duc private comm., MS1054: van Dokkum et al. 2000).

Initial catalogues were constructed from the R-band FORS2 preimaging, by applying SExtractor (Bertin & Arnouts 1996) to mosaics of these images for each cluster. Each galaxy was initially given a priority of 5 (lowest). The priority level of each galaxy was then decreased by one point for each of the following: disky morphology, favourable inclination ($i \gtrsim 30°$), known emission-line spectrum, and available HST data. A priority level of 5 was assigned to all galaxies close to face-on ($i < 30°$). The galaxies were thus divided into five priority categories from 1 (highest) to 5 (lowest). The aim was to select field and cluster galaxies in as similar a way as feasible, that is while still observing a useful number of galaxies actually in the cluster. To increase the likelihood of observing cluster galaxies priority was also increased by one point if the galaxy was known to be at the cluster redshift and did not already have the highest priority level.

This priority ranking method preferentially selects bright, star-forming disc galaxies, and therefore we are not probing the average spiral population in clusters. However, by selecting field galaxies in the same manner we can perform a fair comparison between the bright, star-forming population in clusters and the corresponding population in the field. We can therefore investigate whether there is any evidence for a brightening or fading of this population in clusters.

For each mask, slits were added in order of priority, and within each priority level in order from brightest to faintest R-band magnitude. The only reason for a particular galaxy not being included was a geometric constraint caused by a galaxy of higher priority level, or a brighter galaxy in the same priority level. Often the vast majority of the mask was filled with slits on galaxies in priority levels 1 and 2, with occasional recourse to lower priority objects in order to fill otherwise unoccupied gaps. The effective magnitude limit in each priority level varies, and is generally limited by either the availability of spectroscopic data or slit positioning constraints.

As the multi-object spectroscopy limits the number and minimum separation of targets, the observed galaxies are rather sparsely sampled. As shown later in figure 5.2, the preference for cluster galaxies does therefore not significantly extend nor bias the parameter space inhabited by the cluster galaxies with respect to that of the field galaxies. It merely means that cluster galaxies are slightly over-represented compared with a purely magnitude limited sample. We can therefore internally evaluate the difference between cluster and field galaxies over a range of redshifts, using galaxies that have been selected, observed and analysed in an essentially identical manner. We have no need to resort to comparisons with other studies, and hence avoid the systematic differences this could potentially involve.

The redshift distributions of our sample galaxies are shown in figures 2.1 and 2.2. Clearly the number of galaxies selected which actually lie in the targeted cluster varies considerably between the observed fields. This is primarily a consequence of variation in the spiral population of the clusters, and differing availability of *a priori* redshifts during the target selection. Note that the shorter exposure time required for MS0440 meant we could use three masks, compared with two for the other clusters. The low numbers of selected cluster galaxies, although unfortunate, does go some way to demonstrate the extent to which we have endeavoured to keep our sample unbiased.

In order to best observe the galaxy kinematics, the slits were individually tilted to align with the major axes of the target galaxies. Tilting the slits reduces the effective spatial resolution, and so multiple masks, with different position angles on the sky, are required to accommodate all galaxy position angles. We generally used two, orthogonally aligned, masks for each field, and thus a nominal limiting slit tilt of 45°. Previous work has found that useful spectra can be obtained using slits tilted up to this limit (e.g., Milvang-Jensen 2003). However, on occasion the 45°

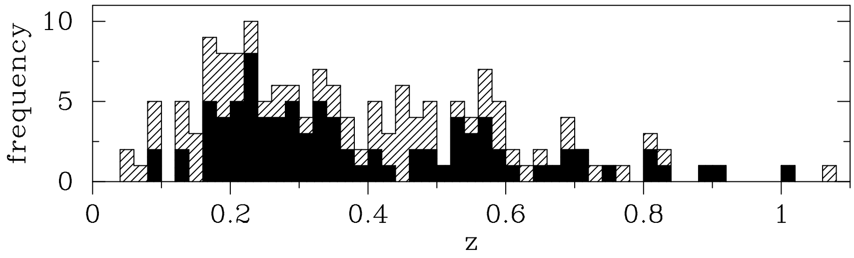

Figure 2.1. The redshift distribution for all of our target galaxies observed with the VLT. The hatched histogram shows the distribution of all field galaxies observed with identifiable emission-lines, and the filled area only those in our final TFR field sample.

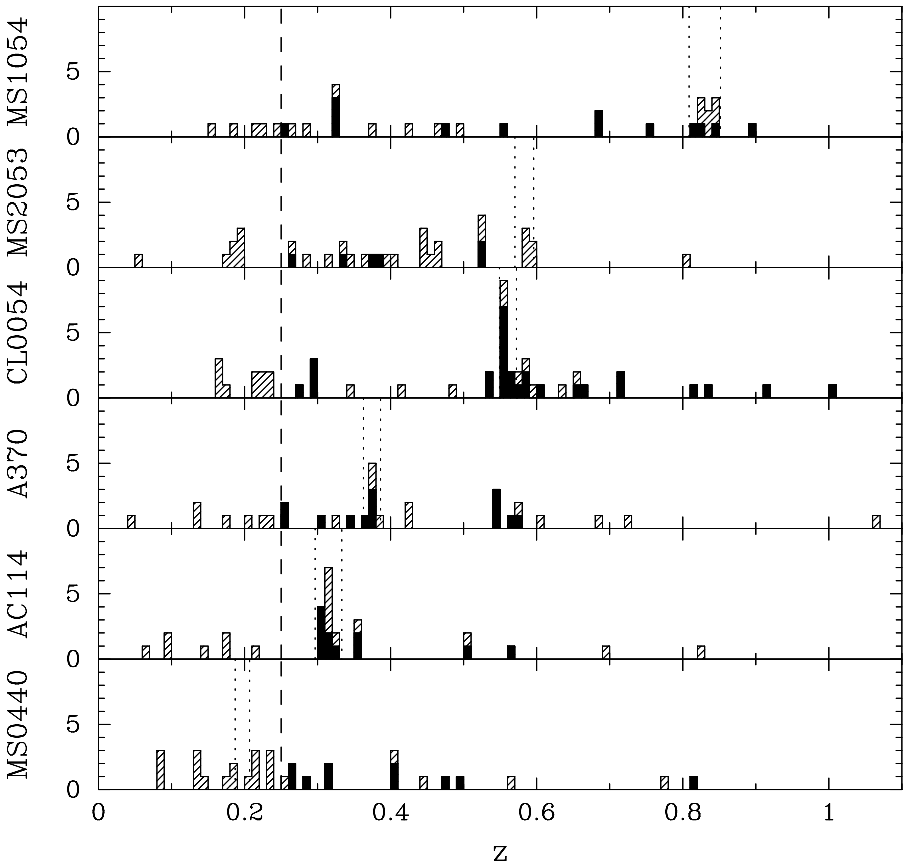

Figure 2.2. The redshift distribution of our VLT target galaxies, shown individually for each field. The hatched histogram gives the distribution of all our observed galaxies with identifiable emission-lines. The filled area shows only those in our final 'matched' TFR sample (see section 5.2). Vertical dotted lines indicate the adopted cluster limits, and the dashed line shows the low redshift cut for the 'matched' sample.

Table 2.2. Summary of the VLT/FORS2 spectroscopic observations.

Cluster-field	No. of masks	Exp. time (mins/mask)
MS0440	3	57, 45, 30
AC114	2	75
A370	2	90
CL0054	2	150
MS2053	2	150
MS1054	2	210

limit was exceeded, principally in order to observe the same object in both masks for comparison. For the three MS0440 masks the same tilt limit was applied to maximise the number of high priority targets which could be fit in the masks. In the completed designs of the 11 masks (not including MS1054), 283 slits were assigned to targets, including 34 stars (roughly three per mask) for the purposes of alignment and measuring the seeing.

2.3 Spectroscopy reduction

The 2002 VLT spectroscopy data, whose reduction is described below, was observed using the MXU mode of FORS2. In this mode slits are cut into a mask which is then placed in the light path. This has significant advantages over the movable slits of MOS mode. Variable slit lengths and tilt angles give increased flexibility for the mask design, increasing the number of objects observable in a single exposure and allowing consistent alignment of the slits with the galaxy major axes.

Our observations are summarized in table 2.2. The seeing, as measured from stellar spectra in the masks, was typically ~ 1 arcsec, and always less than 1.2 arcsec. The setup was similar to that used for the earlier MS1054 observations (an additional 2 masks), the only changes being a larger CCD detector and a different grism (600RI) with a substantially higher throughput. These differences give a wider wavelength coverage, although with a slightly lower spectral resolution, meaning more emission-lines were observed for each galaxy in the present study.

The reduction of multi-slit spectroscopic CCD data requires a number of steps, each of which require careful consideration and adaptation to the specific properties of the data set. The overall process is rather standarised, and so too much description is unnecessary. However, some details are necessary to give the reader an appreciation of the data characteristics. The various steps applied to reduce the data are therefore briefly summarised in this section, with particular attention to aspects of the process particular to this data set.

Most of the reduction was performed using standard IRAF tasks, generally scripted using PYRAF[1], an interface to IRAF for the PYTHON programming language.

2.3.1 Bias subtraction

After inspection to reject any problem images, 20 good bias images were available from the observing run. These were combined to produce a 'master' bias by taking a 3-sigma clipped mean, using the 'avsigclip' mode of the IRAF task IMCOMBINE, to

---

[1] PYRAF is a product of the Space Telescope Science Institute, which is operated by AURA for NASA. See http://www.stsci.edu/resources/software_hardware/pyraf.

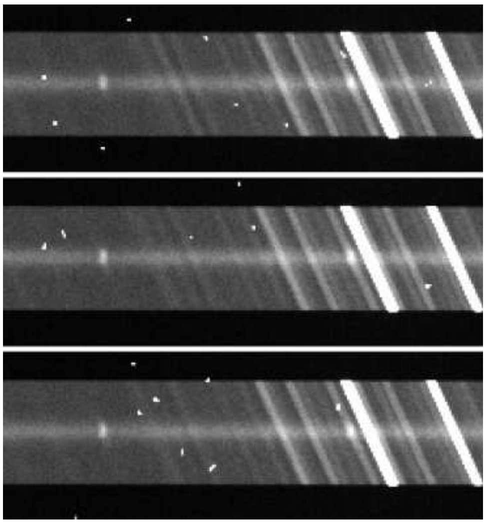

(a) Individual exposures

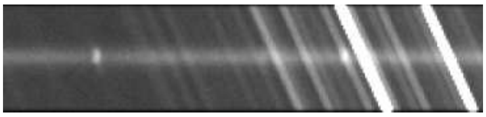

(b) After combining

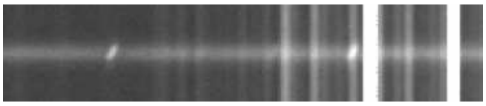

(c) After wavelength calibration

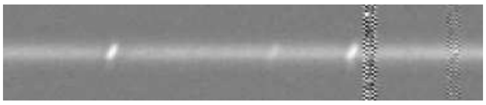

(d) After sky subtraction

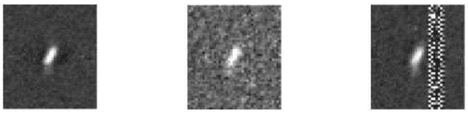

(f) Final 'postage stamp' images

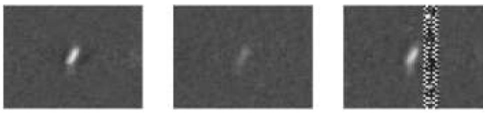

(e) After continuum subtraction

Figure 2.3. An illustration of the various steps applied in reducing the spectroscopic data used in this thesis. Each panel shows the same region of the two-dimensional spectrum for the redshift 0.256 galaxy A370_751, featuring the Hβ and [OIII]λ4959, λ5007 emission-lines. The two bright skylines are due to atomic oxygen, and lie at wavelengths of 6300 and 6364Å.

remove the $\sim$ 30 pixels per image which were affected by cosmic rays (see section 2.3.2).[2]

Variations of upto 3 ADU in the bias level between different images were noticed. To account for this, the biases were additively scaled to have zero mean in their overscan regions prior to combining. The bias was then removed from all images by first subtracting the mean overscan value of each image, and then subtracting the zero normalised master bias. In this way the best estimate of the bias level for each image was used to remove the constant level, while the master bias was used to remove the residual spatial structure seen in the bias.

2.3.2 Combining exposures

Science images

Multiple exposures were taken for each target mask, partly in order to combat the problem of cosmic rays, but also to break the execution time of the observations into more manageable pieces. These have been combined in such a way as to exclude pixels which were affected by cosmic rays, thereby producing a single, higher signal-to-noise, 'clean' image. This, and subsequent reduction steps, are illustrated in figure 2.3. The two detector chips were treated separately.

If the probability of an individual pixel in one exposure being affected by a cosmic

---

[2] Note that while the exposure time for a bias image is approximately zero, cosmic ray hits can accumulate during the time the detector is being reset and read-out, typically $\sim$30 seconds.

ray is p, then the probability of a given pixel being affected by cosmic rays in c of n multiple exposures is given by the binomial distribution,

$$P(c\,|n) = \frac{n!}{c\,!\,(n-c)!}\, p^{c}\, (1-p)^{n-c}\ . \tag{2.1}$$

From inspection of flat regions of the science images we find a typical rate of 1–2 × 10^{-6} cosmic ray incidences per pixel per second. For a single pixel in a science exposure (with integration time 600–1800 seconds) the chance of a cosmic ray hit is $\sim$0.3%, corresponding to $\sim$6000 of the $\sim 2 \times 10^{6}$ pixels in each image.

The number of individual exposures taken for each target mask, and hence which may be combined together, is five for most masks, but only three for those of A370. For a total of five exposures $P(0\,|5) = 0.985$, $P(1\,|5) = 0.015$, $P(2\,|5) = 8.9 \times 10^{-5}$, $P(3\,|5) = 2.7 \times 10^{-7}$. So $\sim$ 31000 pixels per image are affected in one or more exposures, $\sim$180 are affected in two or more exposures, and $\lesssim 1$ pixel is affected in three or more exposures. For a total of three exposures $P(0\,|3) = 0.991$, $P(1\,|3) = 0.0089$, $P(2\,|3) = 2.7 \times 10^{-5}$. So $\sim$ 19000 pixels per image are affected in one or more exposures, and $\sim$ 60 are affected in two or more exposures. With regard to the fraction of pixels affected by cosmic rays, combining by taking a median over all the exposures is equivalent to rejecting the highest two pixels in five exposures, or one pixel in three exposures. The fraction of pixels affected by cosmics in the final median combined image would thus be 3×10^{-7} and 3×10^{-5}, for a total of five and three exposures, respectively. This is excellent in the case of five exposures, and acceptable for three exposures. However, taking a median discards information for every pixel in the image, not just those affected by cosmics, lowering the overall image signal-to-noise by a factor of $\sqrt{2}$ with respect to a mean combined image.

In order to preserve the signal-to-noise, while efficiently rejecting pixels affected by cosmics, we used an adaptive method, based on that of Milvang-Jensen (2003). For each pixel this approach combines exposures by taking the mean, after rejecting any values that are significantly larger than expected. Determining which values should be rejected requires estimates, in the absence of any cosmic ray contamination, for the expected value of the pixel and the expected variation of that pixel value between exposures. The expected value of the pixel is well estimated by the median, which is largely robust to the presence of cosmics, as shown above. The expected variation in the pixel value from exposure to exposure, in the absence of any cosmics, is harder to estimate. Ideally one would like to know the standard deviation of the pixel value, and then reject values that are more than a certain number of standard deviations higher than the expected pixel value (estimated by the median). Values that are greater than three standard deviations from the median are expected to occur with a probability of only 0.001, and thus most pixel values rejected in this manner will be artificially high due to being affected by cosmic rays.

In order to implement this method of combining the images, we need to estimate the standard deviation between exposures for each pixel. A first approach is to consider the CCD noise model, which gives the expected standard deviation due to the combination of Poisson ('shot-noise', or counting) error on the number of electrons in the pixels potential well, and the noise introduced during the read-out of the detector (read-noise). This gives the expected standard deviation as

$$\sigma_{\rm CCD} = G\sqrt{v/G + r^{2}}\ , \tag{2.2}$$

where v is the pixel value in ADU, G is the gain in ADU/electrons, and r is the read noise in electrons. However, while this is gives the correct error on the pixel values in an individual exposure, there is an additional source of variation between exposures which must be accounted for: changes in the level of continuum and, in particular, line emission from the atmosphere. Substantial fluctuations in the sky background can occur on timescales of minutes, due to variations in the temperature and water content of the atmosphere through which the observations are being made. Therefore, σ_{CCD} only provides a minimum to the expected variation between exposures, and its use would lead to the rejection of many pixels located on even fairly weak sky-lines. To avoid this one must estimate the variation between exposures directly from the data.

To estimate the normal variation of each pixel between exposures we required a method which is robust in the presence of pixels affected by cosmic rays and reliable when used with a small number of values. From the calculations above it is far more unlikely (by a factor of $\gtrsim 100$) for the same pixel to be affected by cosmic rays twice in a series of multiple exposures, than for just one of the exposures to be affected. A first step is therefore to base the standard deviation estimate on only the $n-1$ lowest values from the n exposures for each pixel. Note that this introduces a bias which should be corrected for. Secondly, to minimise the overestimation of the standard deviation when two cosmic ray affected values are present, an estimator should be used which is relatively unsensitive to outliers. The canonical standard deviation is based on squared residuals from the mean, and is therefore quite sensitive to outliers. A more robust option is the mean absolute deviation (MAD) defined as

$$\mathrm{MAD}(v_0, \ldots, v_i, \ldots, v_n) = \frac{\sum_i^n |v_i - \overline{v}|}{n}, \text{ where } \quad \overline{v} = \frac{\sum_i^n v_i}{n}. \tag{2.3}$$

However, this estimator is biased with respect to the standard deviation.

The biases on the estimate of the true pixel value standard deviation between exposures, due to using only the $(n-1)$ lowest values from the n exposures and using the MAD estimator rather than the standard deviation, can be approximately determined by simulations. These were performed with a range of realistic properties for the level of sky-line features and their variation.

The entire procedure for combining the multiple science exposures for each target mask was as follows.

- Sort the pixel values, v_i, from the n multiple exposures and calculate $\langle v \rangle$, the median calculated from all n values, and $\mathrm{MAD}_{(n-1)}$, the mean absolute deviation calculated from the lowest $(n-1)$ values.
- Correct $\mathrm{MAD}_{(n-1)}$ to an estimate of the standard deviation variation between exposures, σ_{MAD}, using the relevant bias factor derived from simulations.
- Calculate σ_{CCD}, the lower limit standard deviation due to Poisson statistics and read-noise, using $\max(\langle v \rangle, 0)$ as the estimate of the pixel value.
- Produce the test estimate of the standard deviation variation between exposures, $\sigma_{\mathrm{test}} = \max(\sigma_{\mathrm{MAD}}, \sigma_{\mathrm{CCD}})$.
- Calculate the normalised residual for the pixel value from each exposure, $(v_i - \langle v \rangle)/\sigma_{\mathrm{test}}$.

- Count the number of exposures, n_{inc}, for which the pixel value's residual is less than the predetermined sigma-limit, and which are therefore likely free of cosmic ray contamination and hence to be included in the calculation of the final pixel value.
- Take the mean of the n_{inc} reliable values to produce the final combined value for each pixel.

An error image was created for the combined science images by using the CCD noise model with the pixel values in the combined image. This is the correct approach, as the variation in the skylines between exposures does not actually lead to any additional uncertainty in the signal in the combined images.

Screen-flat images

The screen-flat images have exposure times of several seconds, and are thus not severely affected by cosmic rays. They have at least five exposures for each target mask, which can be combined to remove the affected pixels. This was done in the same manner as the bias images, by taking a 3-sigma clipped mean.

2.3.3 Distortion correction

At this stage all the images contain a small distortion caused by the instrument's optical system. This distortion has the effect of misaligning the dispersion axis of the grism with respect to the CCD rows. This is a problem for two reasons. In the long-term, at the end of the reduction we desire two-dimensional spectra for which each row gives the spectrum for a particular position along the slit. In the short-term, this distortion needs to be corrected at this stage of the reduction, before we can flat-field the images. In order to create the pixel-to-pixel flat-field image (see section section 2.3.4), we must remove the smooth, wavelength-dependent variation along the dispersion axis. This is complicated if the dispersion axis is not aligned with the image pixel rows.

In order to correct for the distortions we first mapped them by measuring the positions along the edges of slit apertures in the screen-flat images. This was done on images of the aperture edges, created by taking the gradient of screen-flat images in the direction perpendicular to the dispersion axis, i.e. convolving by the kernel $\binom{-1}{+1}$, and taking absolute pixel values. An example is shown in figure 2.4, which clearly shows the distortion.

In order to measure the positions of the aperture edges, trace them across the width of the image, fit a 2-dimensional function to these measurements, and undistort the images by transforming them by the inverse of this function, we used the the IRAF package TWODSPEC, which provides the tasks IDENTIFY, REIDENTIFY, FITCOORDS, and TRANSFORM. These tasks are intended for use in the wavelength calibration of spectra, and are used for this purpose later in the reduction (see section 2.3.6). The two CCD chips are considered separately in all of this process.

The form of the distortion is that horizontal lines that should be aligned with the pixel rows curve up slightly at the edges, forming a $\cup$-shaped curve, at the top of the field-of-view. This curvature decreases toward the centre of the field, becoming flat by the lower region of chip 1. The lines then begin to curve in the opposite sense, becoming increasingly $\cap$-shaped toward the lower edge of the field-of-view. A suitable two-dimensional polynomial which describes this behaviour is second-order

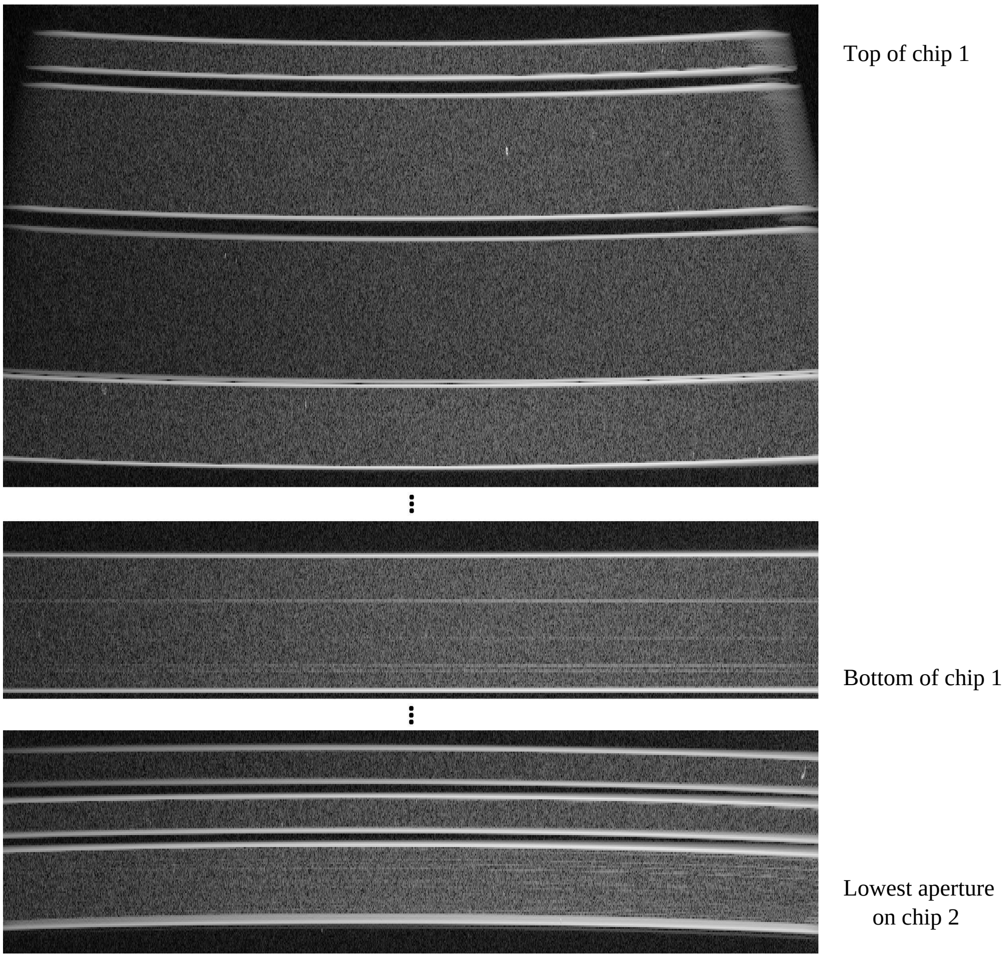

Figure 2.4. Example sections from a screen-flat edge image. The vertical scale has been expanded by a factor of four to better show the geometric distortion caused by the instrument's optical system. Bright features in this image correspond to high gradients in the original screen-flat image, and thus mark the edges of the apertures. The apertures themselves appear slightly lighter than the gaps between the apertures, because of their higher level, and hence larger absolute variations due to Poisson noise, in the screen-flat.

in the dispersion direction and third-order in the orthogonal direction. Fitting this function resulted in acceptably small residuals of $\lesssim 0.1$ pixels.

As a check, the transformation to correct for the optical distortion was first applied to the screen-flat aperture-edge images which were used to determine it, with excellent results. The same transformation was therefore applied to all the combined science, screen-flat, sky-flat and arc-lamp images. The error image for the science observations was also transformed, squaring the pixel values beforehand, and square-rooting afterwards so that the interpolations were done in quadrature.

2.3.4 Flat-fielding

As with all astronomical instruments, the sensitivity of the FORS2 CCD detector and transmission of the FORS2+VLT optical system vary as a function of position in the field of view. In addition, both the detector sensitivity and transmission of the optics depend upon the wavelength of the incident light.

Both screen-flats and sky-flats were taken for most of the target masks. Screen-flats have the advantages of higher signal-to-noise and a spectrum containing no emission-lines. However, perfectly even illumination cannot be guaranteed by screen-flats, while sky-flats, if correctly taken and processed, have perfectly even illumination.

Smooth variations in sensitivity in the spatial direction are not a concern for our purposes, except for on the scale of individual apertures. These are anyway flattened during the slit profile correction, using the sky-flats, described in section 2.3.7.

The smooth variation in response in the dispersion direction (along each CCD row) is inseparable from the spectrum of the lamp or night sky in flat-field images. This can be corrected at a later stage of the reduction using observations of standard stars, but this was not necessary for our aims.

More important for our purposes are the pixel-to-pixel variations in detector sensitivity. Pixel-to-pixel flat-fields were created by fitting a smooth function to each image row, in order to create a smoothed image of the screen-flat, and then dividing the original flats by this smoothed image. Following a series of tests, a 20-piece cubic spline function was chosen. This was the minimum number of pieces required to fit the data without leaving structures in the fit residuals, and removes variations on a scale of $\gtrsim 100$ pixels.

One important consideration in performing these fits was to account for the effect of the vignetting seen in the upper corners of chip1. The suddenness of the level cut-off in these regions cannot be fit by the 20-piece cubic spline function, and introduces ‘ringing’ into the fit, i.e. spurious waves, or wobbles, in the fitted function extending far beyond the vignetted region. One solution would be to increase the number of spline pieces (to around 50), but this would result in quite small features being fit, compromising the creation of an accurate pixel-to-pixel flat-field. The best option was to disregard these vignetted regions from the fit, and all further analysis, as they contain no useful data anyway.

All the science, science error, and arc-lamp images were divided by the pixel-to-pixel flat-field image, to correct for the small-scale sensitivity variations.

2.3.5 Aperture extraction

After the above steps were completed, the individual apertures were cut out and worked on separately. To find the edges of the apertures, the distortion-corrected aperture edge images, produced earlier (see section 2.3.3), were summed in the dispersion direction, to produce one-dimensional images with peaks marking the edges of each aperture.

2.3.6 Wavelength calibration

In order to determine the mapping of pixel positions to wavelength, we used arc-lamp calibration images, taken using simultaneous NeAr and HgCd lamps. The prototype arc-lamp spectral plot used in this reduction was provided by the FORS2 manual (ESO 2002).

The TWODSPEC package of IRAF was used to perform the wavelength calibration. This followed the traditional procedure, except that in order to speed the operation slightly, a near-automated process was developed to establish an initial approximate wavelength solution. A script was written to identify the unique feature of two strong lines close together in the TWODSPEC database, which indicates they must at $\lambda = 7032, 7065$Å. The script was then able to edit the database to specify the wavelength of these and upto six of the other strong lines, allowing a reasonable wavelength solution to be quickly established. This solution was subsequently refined interactively.

The function used to fit the wavelength solution was a two-dimensional Chebychev polynomial, which was always fifth-order in the wavelength direction, and usually first-order in the spatial direction. However, in about one-third of cases, particularly for apertures at the top and bottom of the field of view, a second-order, or occasionally higher, function in the spatial direction gave a significantly better fit and was thus used instead.

To first check the accuracy of the calibration, the arc-lamp images themselves were transformed and inspected. Following the success of this test, the science, error,[3] screen-flat and sky-flat aperture images were wavelength-calibrated by applying the same transformation. The average dispersion of the spectra prior to wavelength calibration was 1.64Å/pixel, and the same dispersion (now constant for all apertures and wavelengths) was thus imposed on the wavelength-calibrated images. Linear interpolation and a flux-conserving algorithm were used for the transformation. The result of wavelength calibration is illustrated by figure 2.3(c).

2.3.7 Slit profile correction

The slit profile for each aperture was determined by median collapsing the wavelength-corrected sky-flats in the dispersion direction, over a wavelength range unaffected by chip-edge effects, then normalising to unit mean. All the apertures were then corrected by dividing by the slit profile, correcting for CCD sensitivity gradients in the spatial direction, and for illumination gradients and irregularities in the width of the slits.

2.3.8 Sky subtraction

In order to estimate the sky spectrum, regions of sky free of signal from astronomical objects were identified. This was achieved by first applying a specially written automatic algorithm, which finds suitable regions by examining the gradient and level in median-collapsed spatial profiles of the science apertures. The selected sky-regions were then inspected and fine-tuned manually.

The sky was then removed from each science aperture by fitting a linear function to each spatial column, using only data in the selected sky-regions, and subtracting the fits from the data.

Note that the noise in the sky-subtracted spectra is obviously higher in regions where strong sky-lines have been removed (see figure 2.3(d)). This is accounted for in the analyses described later by the use of an accurate error image. Furthermore, some structure is seen in the skyline residuals. This is because the skyline profiles are undersampled by the pixel scale. This can be avoided by creating a better sampled sky spectrum, using all of the sky data from an image, rather than from just each aperture, and making use of the fact that tilted slits and optical distortions produce different wavelength samplings in different CCD rows (Kelson 2003). This oversampled sky information is lost during the re-binning which is inherent to the traditional reduction method. However, this novel technique is rather complicated,

---

[3] The error image was again squared prior to the transformation and square-rooted afterwards, so any interpolation was performed in quadrature

and was still in development at the time these data were reduced. The traditional method was thus considered sufficient for our needs.

2.3.9 Emission-line identification and redshifts

One-dimensional spectra were created from the central regions of the two-dimensional spectra, and both of these inspected to identify and measure the wavelength of all visible emission-lines. The main emission-lines observed were [OII]λ3727, Hβ and [OIII]λ4959, λ5007, with Hα but no [OII]λ3727 for nearby galaxies. The wavelengths of multiple lines were checked for consistency, and redshifts determined.

In the 283 slits (not including the MS1054 observations), 303 separate spectra were identified. Of these 177 are identifiable as galaxies with emission-lines.

2.3.10 Emission-line 'postage stamps'

The final stage in the reduction before the analysis of the extended emission lines (described in section 3.1) was to prepare continuum-subtracted 'postage stamp' images of each emission-line. First, sections of each aperture 60 pixels (≈ 97Å) wide in the wavelength direction were cut out around each identified emission-line. The continuum emission was removed from these sections by calculating the mean of each row, rejecting pixels more than two-sigma from the mean in an iterative manner to exclude the emission-line, and then subtracting this mean.

These sections were then trimmed further to a width of ~ 20 pixels (≈ 32Å), and the emission-lines centred both spatially and spectrally. The spatial centre for each emission-line was determined from the median-collapsed spatial profiles of the science apertures, which were created during the sky-subtraction stage. The spectral centre was determined from the line position measured on the central one-dimensional spectra used in section 2.3.9

A region of one two-dimensional spectrum, featuring the Hβ and [OIII]λ4959, λ5007 lines for a redshift 0.256 galaxy (A370_751), is shown at various stages of the reduction process in figure 2.3.

2.3.11 Spatially-integrated spectra

For analysis of the spatially-integrated spectral properties of the galaxies, as described in section 3.2, the sky-subtracted two-dimensional spectra were averaged in the spatial direction to produce one-dimensional spectra. The spatial region used for each spectrum was selected to contain most of the galaxy light. This was determined by averaging the 2d spectrum in the wavelength direction, fitting a symmetrical (Voigt) profile, and calculating the distance from the fit centre to where the profile falls to approximately 1% of its peak value.

2.4 Imaging

This section describes the preparation and analysis of the imaging for the fields observed in the 2002 VLT spectroscopic data. In order to consistently combine the earlier 2001 VLT MS1054 observations with this dataset, the imaging data for MS1054 were reanalysed following the same procedure. Imaging for the Subaru data was analysed separately, as described in Nakamura et al. (2006).

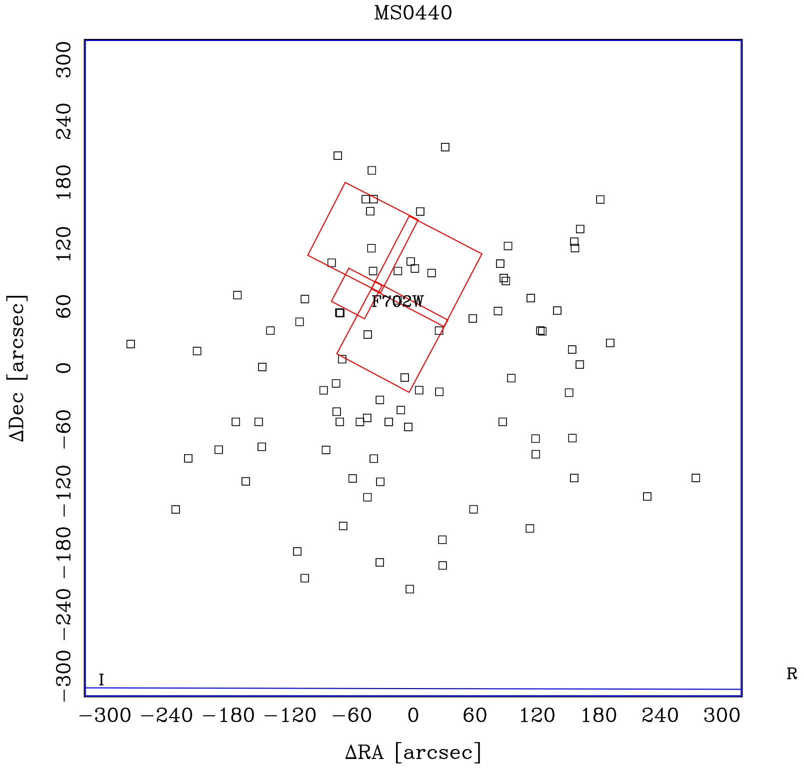

Figure 2.5. Imaging coverage for each of the 2002 VLT spectroscopic fields. The points mark the positions of the spectroscopic slit centres (approximately the position of the objects). Outlines of the available HST/WFPC2 (red) and ground based (blue) imaging are shown, and labelled by their band.

The coverage in the different photometric bands for each field of the 2002 VLT data is illustrated by figure 2.5. All of the 2001 VLT MS1054 targets are covered by both $F606W$ and $F814W$ HST/WFPC2 imaging.

2.4.1 Photometry

The photometric zero-points for our R-band imaging were established by matching the magnitudes of point-sources with those measured on the overlapping $\sim R$-band ($F675W$ or $F702W$) HST/WFPC2 images. In one case (CL0054) no $\sim R$-band HST data were available, and an interpolation between $F555W$ and $F814W$ magnitudes was calibrated using synthetic SEDs and used instead. This was also checked using V and I-band ground-based data, which gives a consistent zero-point. The mean zero-point error on the R-band magnitudes is 0.08 mag, adequate for our purposes. The zero-point errors are included in the overall magnitude errors. Table 2.3 gives the bands in which magnitudes were measured for each galaxy in our full TFR sample (as defined later).

The galaxy magnitudes were measured using SExtractor (Bertin & Arnouts 1996). The AUTO (Kron-style) aperture was used to measure magnitudes on the original images, while colours were determined from 3 arcsec diameter aperture magnitudes measured on images which had been degraded to match the worst seeing for each field. Magnitudes and colours were corrected for Galactic extinction using the maps and conversions of Schlegel, Finkbeiner & Davis (1998).

The conversion from apparent magnitudes to absolute rest-frame B-band was

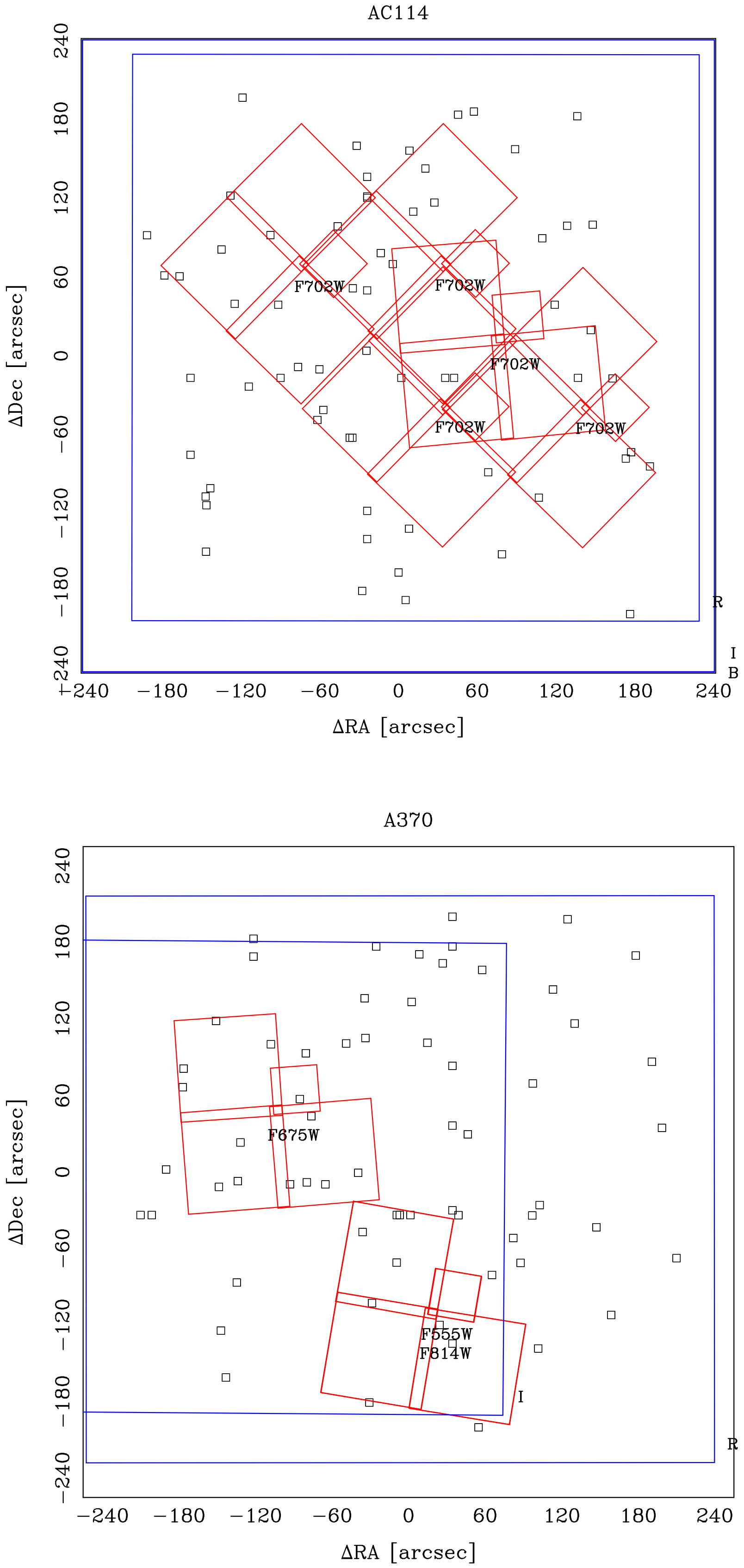

Figure 2.5. continued

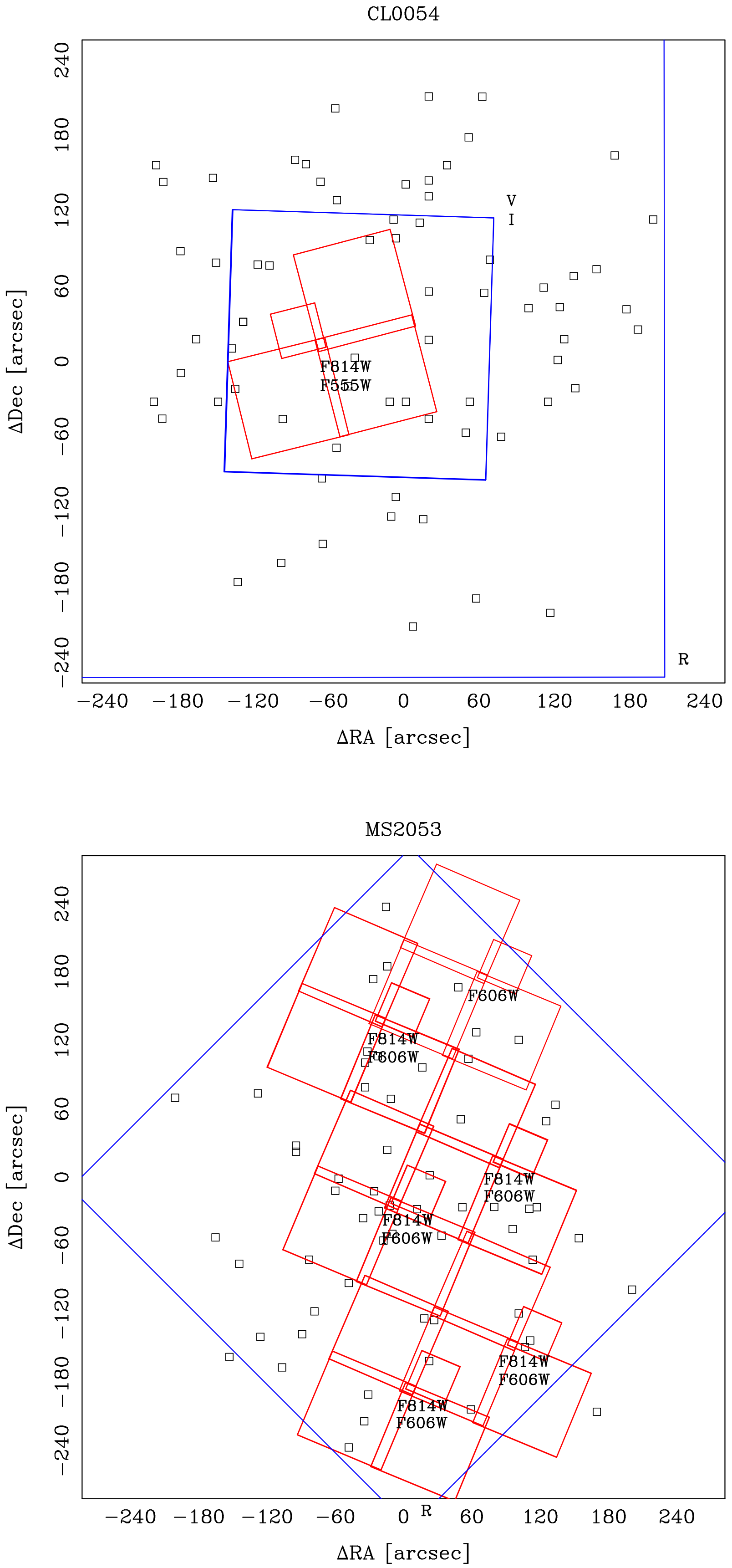

Figure 2.5. continued

achieved by the following procedure. First all colour information was used to find the best fitting SED from a grid of 26, spanning types E/S0 to Sdm. These were formed by interpolating the SEDs of Aragón-Salamanca et al. (1993) and redshifting appropriately. The SEDs are denoted by numbers, with E/S0 = 0.0, Sab = 1.0, Sbc = 2.0, Scd = 3.0 and Sdm = 4.0. Intermediate values indicate linear interpolations of the two bracketing SEDs, thus an SED value of 2.3 corresponds to $0.3\mathrm{Sbc} + 0.7\mathrm{Scd}$. A confidence interval on the SED was also determined by examining the χ^2 of the colour fits. In cases where no colour information was available an average value and confidence interval were adopted for the SED, determined from those galaxies with available colours, $(2.5^{+1.0}_{-1.2})$. The magnitude in the observed band closest to rest-frame B was then adjusted by a colour- and k-correction calculated from the best-fitting SED. The observed band used as the basis for the conversion is indicated in table 2.3. Errors were assigned to this correction corresponding to the SEDs bounding the confidence interval determined above. Finally this magnitude was adjusted by the distance modulus of the galaxy assuming the concordance cosmology.

The magnitudes were additionally corrected for internal extinction (including face-on extinction of 0.27 mag), following the prescription of Tully & Fouque (1985), to give the corrected absolute rest-frame B-band magnitudes, M_B, used in the following analysis.

Note that both the cosmology and internal extinction correction prescription were chosen to allow straightforward comparison with other recent studies.

Because of the varying imaging available for each galaxy, we need to address concerns that M_B for our cluster galaxies may be systematically biased with respect to the field galaxies; for example, due to different colours being available to determine the SED. Our additional imaging tends to be centred on the cluster and, particularly for the HST imaging, often has a smaller field-of-view than the R-band images from which we selected the targets. Cluster galaxies will tend to be located towards the centre of the field-of-view (although this may not be so true for the star-forming spirals in our sample, particularly given that we are confined to a clustercentric radius of $\lesssim 1$ Mpc). We might thus expect cluster galaxies to have imaging available in more bands. However, on average we have a magnitude measured in 2.2 and 2.1 bands for cluster and field galaxies respectively, so there is no evidence for a difference in the number of colours available. Another concern may be that the apparent magnitude used as a basis for M_B is measured on HST images more often for cluster galaxies than for field galaxies. The opposite is actually the case, $(14 \pm 8)\%$ of cluster galaxies have M_B based on HST imaging, compared with $(29 \pm 6)\%$ of field galaxies. However, this is not especially significant, given the Poisson errors. These tests imply that any significant difference measured between the cluster and field samples cannot be attributed to the heterogeneity of the imaging.

A plot of M_B versus redshift for our field galaxies is shown in figure 2.6. Notice how our sample is limited to brighter magnitudes with increasing redshift. We can assess how much of the typical galaxy population we sample by comparing with the M^* luminosity function parameter. Norberg et al. (2002) use data from the 2dF Galaxy Redshift Survey to measure the local b_J-band luminosity function, finding $M^*_{b_J} - 5\log(h) = -19.66 \pm 0.07$ mag. We can transform this into the B-band using the conversion suggested by Norberg et al. (2002), $b_J = B - 0.28(B - V)$, and the colour of a typical galaxy in our sample (estimated from the best-fitting SEDs), $(B - V) = 0.52$. With $H_0 = 70\ \mathrm{km\,s^{-1}\ Mpc^{-1}}$, we therefore have $M^*_B \simeq -20.3$

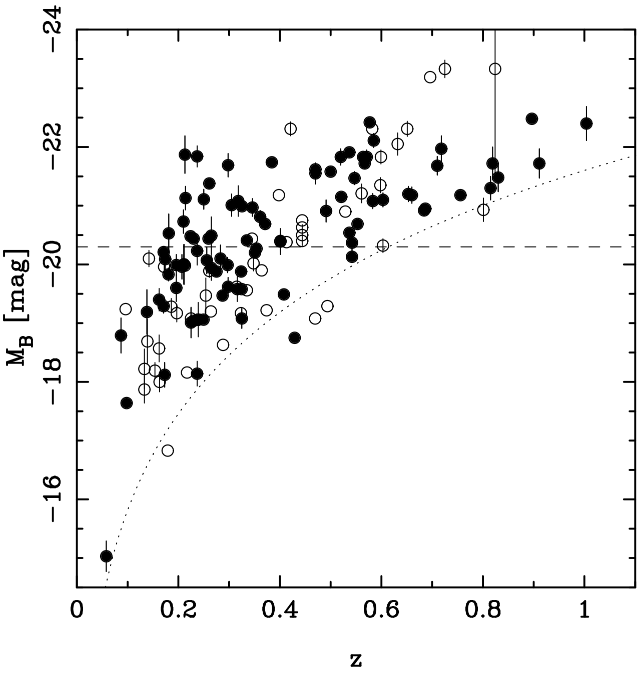

Figure 2.6. Absolute rest-frame B-band magnitude versus redshift for all our field galaxies with identifiable emission-lines. Galaxies in our final field TFR sample are shown by filled points, while open points indicate those for which no emission lines pass our quality control criteria (see section 3.1.1). The dashed line indicates M_B^* as calculated in the text. The dotted line shows the absolute magnitude corresponding to an apparent rest-frame B-band magnitude of 22.5 mag, as a function of redshift in our adopted cosmology.

mag. This is shown by the dashed line in figure 2.6. At $z \sim 0.2$ we sample a range $\sim$2 mag either side of M_B^*. By $z \sim 0.5$ this has reduced to $(M_B^* - 2) \lesssim M_B \lesssim M_B^*$ mag, and at $z \sim 0.8$ we are limited to $M_B \lesssim (M_B^* - 1)$ mag. We therefore sample most of the giant spiral population below $z \sim 0.5$, but beyond this we are limited to only the brightest galaxies in this class. Note that this effect is less serious than in conventional magnitude limited studies as our galaxies at high redshifts have, on average, been observed with longer spectroscopic integrations. This is because the majority of our high-redshift galaxies are from masks targeting our more distant clusters, and thus with longer exposure times (see section 2.3).

2.4.2 Structural parameters

Inclinations (i) and photometric scalelengths ($r_{\mathrm{d,phot}}$) for the disc components of the observed galaxies were measured in bands close to R, preferentially in the HST images (bands F606W, F675W or F702W), and primarily using GIM2D (Simard et al. 2002). GIM2D was used to perform bulge + disk model fits (de Vaucouleurs + exponential profiles). Reliable HST inclination (scalelength) measurements were available for 47 (39) per cent of the galaxies; for the remainder inclination (scalelength) was measured on the ground-based R-band imaging, again usually by GIM2D. These measurements are therefore separated from the bulge component and corrected for the effect of seeing. Typical errors on the inclinations measured using GIM2D on both HST and ground-based imaging are illustrated in figure 2.7. The mean errors are 1.9 and 5.6 degrees for HST and ground-based inclinations, respectively. The same is shown for the photometric scalelengths in figure 2.9. The mean errors are

0.09 and 0.23 arcsec for HST and ground-based $r_{\mathrm{d,spec}}$, respectively.

For a small number of galaxies the GIM2D fit was unreliable. In these cases the SExtractor axial ratio was used to estimate the inclination, assuming an infinitely thin disc (as does GIM2D). These inclinations were corrected by a factor determined from an empirical comparison of SExtractor and GIM2D based inclinations. One factor was used for all ground-based measurements, and another for the HST measurements. The derivation of these factors is illustrated by figure 2.8, which plots SExtractor versus GIM2D and HST versus ground-based inclinations. The corrections applied to SExtractor inclinations were derived from the 3σ-clipped least-squares fits in these plots: $i = 1.3\, i_{\mathrm{SE,ground}}$ and $i = 1.05\, i_{\mathrm{SE,HST}}$. A very small correction was also applied to the ground-based GIM2D inclinations: $i = 1.02\, i_{\mathrm{GIM2D,ground}}$. HST-based GIM2D inclinations were taken as being correct. Representative inclination errors for SExtractor measurements were deduced from the scatter in these plots less the above mean GIM2D errors, in quadrature. This gives 7.3 and 9.9 degrees for HST and ground-based images, respectively.

A comparison of $r_{\mathrm{d,phot}}$ measured on HST and ground-based imaging is shown in figure 2.10. This indicates a possible bias, such that the ground-based measurements are on average ~ 15 larger than those from HST imaging. While a concern, which was discovered only late in the preparation of this thesis, this bias is unlikely to seriously affect any of the discussion herein.

In order to further evaluate our selection function, we measure effective radii, r_{eff}, of circular apertures containing half the galaxy light. These were obtained from our FORS2 R-band imaging, the only band which is available for nearly all of our galaxies,[4] using SExtractor's FLUX_RADIUS output. Plots of $r_{\mathrm{d,phot}}$ and r_{eff} versus redshift for our field galaxies are shown in figure 2.11. Both of these plots include a dotted curve indicating the physical size, in kpc, corresponding to an observed angle of 1 arcsec, as a function of redshift. The seeing in the R-band imaging is roughly 1 arcsec FWHM, but for comparison with r_{eff} one must convert this to a half-light radius. A Gaussian profile with 1 arcsec FWHM has a half-light radius of ~ 0.6 arcsec. The measured r_{eff} are thus all larger than the seeing, but from the correlation of the lower bound of the points r_{eff} distribution with redshift, the seeing is often dominating the measurement.

In order to compare the seeing scale with $r_{\mathrm{d,phot}}$ one can note that if the exponential scalelength of a point source, with a Gaussian seeing profile, were measured, the result would be close to the radius at which a Gaussian profile reaches $1/e$ of its peak value. This occurs at a radius of 0.6 times the FWHM. However, this comparison is complicated by the inclusion of a bulge component in the fit surface brightness model. To some extent, though, the fact that the $r_{\mathrm{d,phot}}$ distribution extends below the seeing scale, and shows little variation in its lower limit with redshift, indicates that $r_{\mathrm{d,phot}}$ is rather more independent of the seeing.

However, due to the similarity of the galaxy sizes to the seeing scale, and in particular the impact of limited resolution on the bulge-disc decomposition, our disc scalelengths are potentially unreliable. This problem becomes worse for both higher redshift and intrinsically smaller galaxies, and should be borne in mind when considering these measurements.

---

[4] Note that, due to full two-band *HST* coverage, FORS2 R-band imaging was not used by the study of MS1054 by Milvang-Jensen (2003). We supplement our data set with these earlier observations, as described later, but do not have R-band effective radii or surface brightness measurements for these additional galaxies.

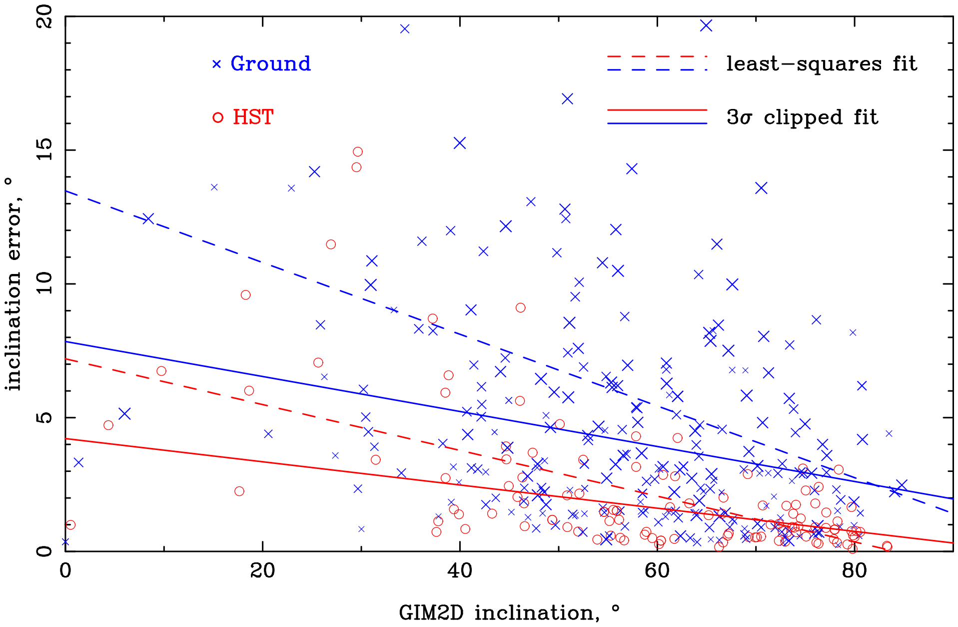

Figure 2.7. Inclination uncertainty plotted as a function of inclination, as given by GIM2D fits on both HST (red circles) and ground-based (blue crosses) imaging. For ground-based data, the size of the crosses are proportional to the seeing. An inclination of 90°corresponds to edge-on. While the scatter is large, due to other factors important to the GIM2D fit quality, e.g., apparent magnitude, this plot provides an indication of our typical inclination errors. Simple illustrative fits to the data are shown, though the inclination dependence is clearly not strong.

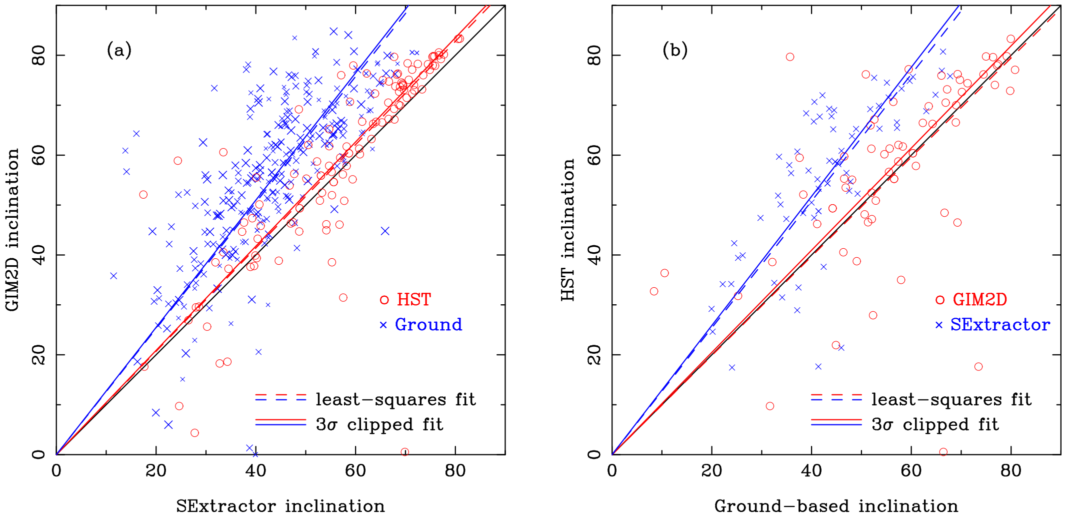

Figure 2.8. Plots comparing inclination measurements performed using GIM2D and SExtractor on HST and ground-based imaging. Panel (a) plots GIM2D versus SExtractor derived inclinations measured on the same HST (red circles) or ground-based (blue crosses) images. Panel (b) plots inclinations measured on HST versus ground-based imaging. In this case the inclinations are averaged over the number of HST or ground-based images available for each galaxy.

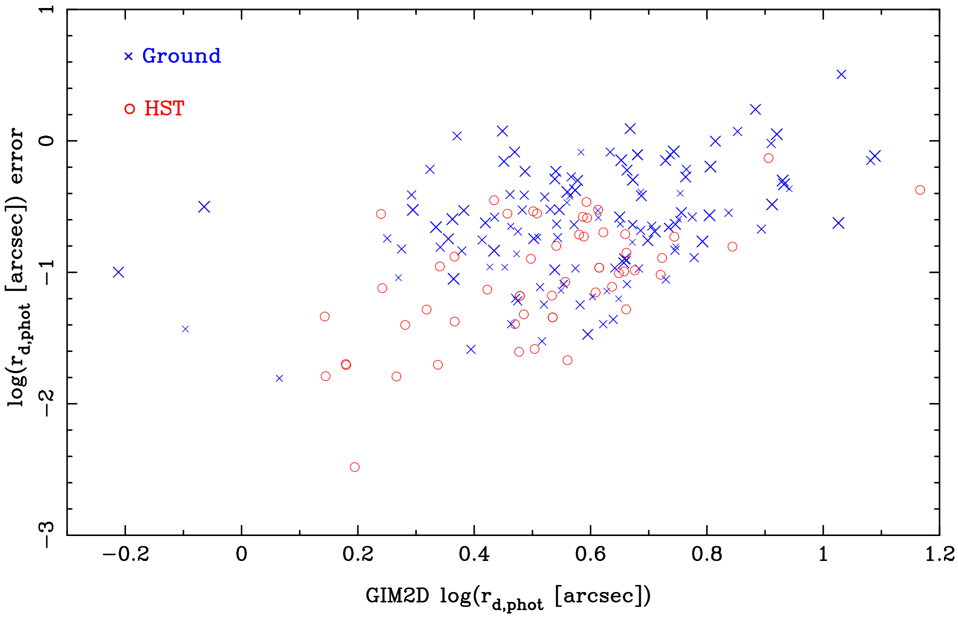

Figure 2.9. A plot of $log(r_{\mathrm{d,phot}})$ uncertainty as a function of $log(r_{\mathrm{d,phot}})$, as given by GIM2D fits on both HST (red circles) and ground-based (blue crosses) imaging. Logarithms are used for clarity. For ground-based data, the size of the crosses are proportional to the seeing. HST imaging can successfully resolve smaller objects. The excess of large ground-based objects is probably simply due to the wider coverage.

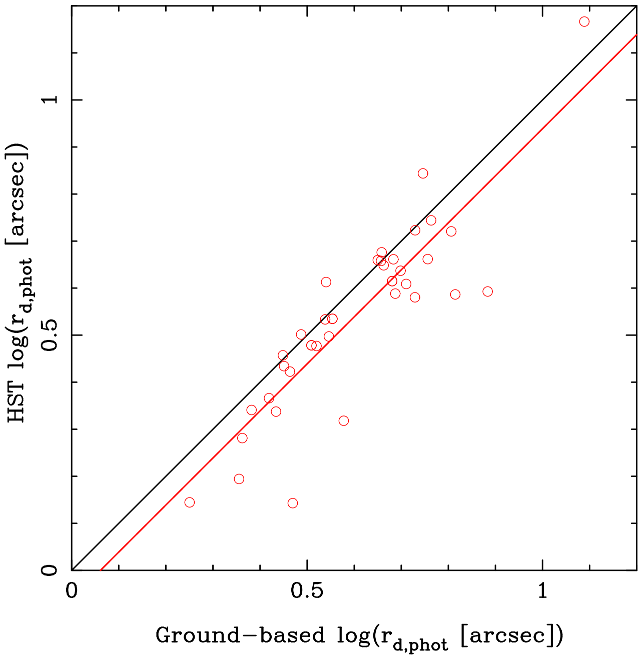

Figure 2.10. Plots comparing $r_{\mathrm{d,phot}}$ measurements performed using GIM2D on HST versus ground-based imaging. The ground-based $r_{\mathrm{d,phot}}$ are measured in R, while the HST-based values are averaged over measurements in whichever of the near R-band HST images (F606W, F675W and F702W) are available for each galaxy.

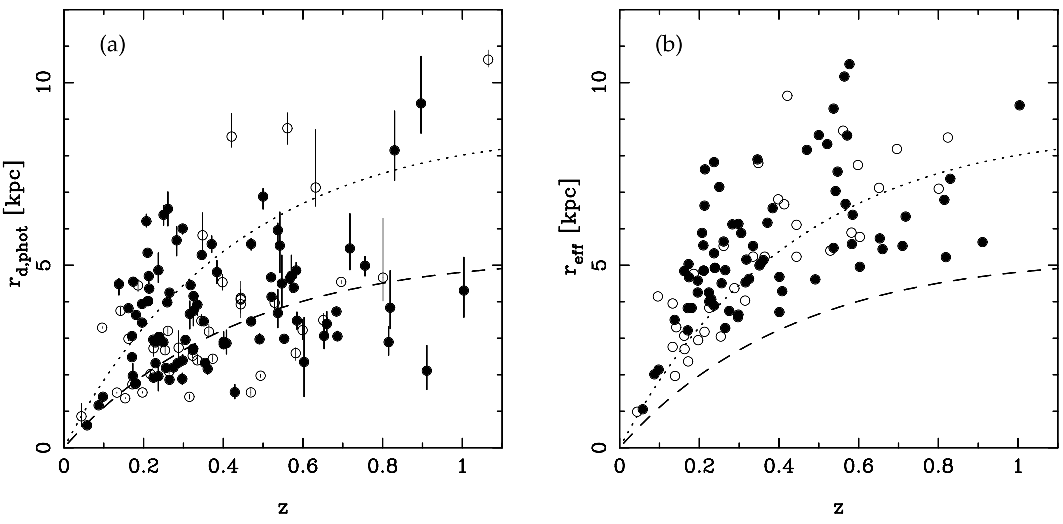

Figure 2.11. Plots against redshift of (a) photometric disc scalelength, $r_{\mathrm{d,spec}}$ and (b) effective (half-light) radius, r_{eff}, both in kpc, for all our field galaxies with identifiable emission-lines (excluding the supplementary MS1054 field in panel (b)). Galaxies in our final field TFR sample are shown by filled points, while open points indicate those for which no emission lines pass our quality control criteria (see section 3.1.1). The dotted line indicates the physical size subtended by an angle of 1 arcsec, as a function of redshift in our adopted cosmology. The dashed line shows the same for an angle of 0.6 arcsec, approximately equal to both the half-light radius and exponential scalelength of a Gaussian with 1 arcsec FWHM.

Another tool to examine our sample selection is provided by the surface brightness of our galaxies. We calculate the apparent R-band average surface brightness within r_{eff}, which we denote $\mu_{R,\mathrm{eff,app}}$, using $\mu_{R,\mathrm{eff,app}} = R_{\mathrm{eff}} + 2.5 \log 2\pi r_{\mathrm{eff}}^2$, where $R_{\mathrm{eff}} = R + 2.5 \log 2$ is the apparent magnitude within r_{eff} by the definition of the half-light radius, with total magnitude, R. This, converted into an absolute observed-frame R-band surface brightness using the distance modulus for our adopted cosmology (denoted $\mu_{R,\mathrm{eff,abs}}$), is plotted for our field galaxies in figure 2.12.

A comparison of figures 2.6 and 2.12 reveals the two plots to show very similar behaviour. This, along with the apparent lack of any redshift-dependent selection on $r_{\mathrm{d,phot}}$ demonstrated by figure 2.11(a), and the simple explanation that the correlation in figure 2.11(b) is due to seeing affecting the r_{eff} measurement, rather than any selection effect, implies that the surface brightness distribution is largely a result of a magnitude-limited selection, rather than any selection on galaxy size.

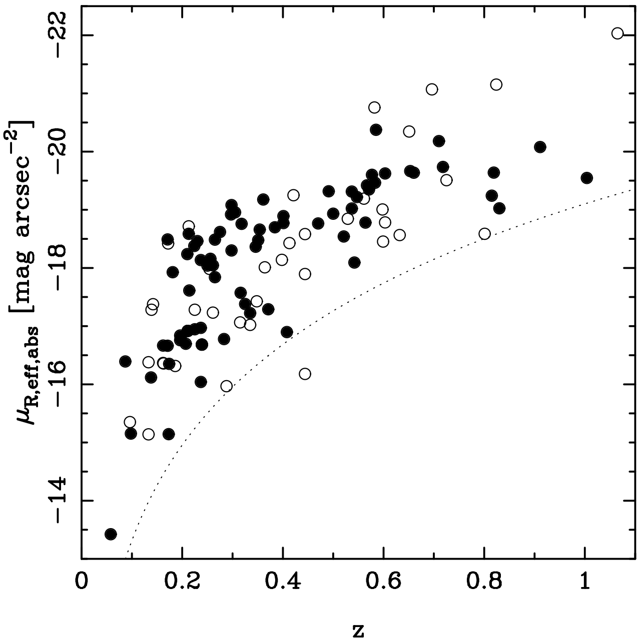

Figure 2.12. Plot against redshift of the absolute observed-frame R-band surface brightness within r_{eff}, for all our field galaxies with identifiable emission-lines (excluding the supplementary MS1054 field). Galaxies in our final field TFR sample are shown by filled points, while open points indicate those for which no emission lines pass our quality control criteria (see section 3.1.1). The dotted line indicates the absolute surface brightness corresponding to an observed apparent surface brightness of 25 mag arcsec^{-1}, according to our adopted cosmology.

Table 2.3. Details of the imaging availability for each galaxy in our full TFR sample. The symbols in columns headed by a photometric band designation indicate the bands in which we were able to measure magnitudes. Numerical band designations correspond to HST/WFPC2 filters, e.g. $F555W$. The symbol • indicates that magnitude information in this band was available, and ⋆ additionally specifies the band which formed the basis for the conversion to rest-frame B-band magnitude. The columns headed 'i' and 'r_d' indicate whether the inclinations and photometric scalelengths are based on HST (•) or ground-based (○) imaging.

			Bands with magnitude available									HST	
ID	z	Mem.	B	555	V	606	R	675	702	I	814	i	r_d
MS0440_101	0.819	F	–	–	–	–	⋆	–	–	–	–	○	○
MS0440_140	0.316	F	–	–	–	–	⋆	–	–	–	–	○	○
MS0440_188	0.491	F	–	–	–	–	⋆	–	–	–	–	○	○
MS0440_207	0.087	F	–	–	–	–	⋆	–	–	–	–	○	○
MS0440_273	0.283	F	–	–	–	–	⋆	–	–	–	–	○	○
MS0440_311	0.470	F	–	–	–	–	⋆	–	–	•	–	○	○
MS0440_319	0.138	F	–	–	–	–	⋆	–	–	•	–	○	○
MS0440_538	0.213	F	–	–	–	–	⋆	–	–	•	–	○	○
MS0440_616	0.211	F	–	–	–	–	⋆	–	–	•	–	○	○
MS0440_627	0.265	F	–	–	–	–	⋆	–	–	•	–	○	○
MS0440_635	0.237	F	–	–	–	–	⋆	–	–	–	–	○	○
MS0440_657	0.265	F	–	–	–	–	⋆	–	–	–	–	○	○
MS0440_735	0.181	F	–	–	–	–	⋆	–	•	•	–	•	•
MS0440_849	0.401	F	–	–	–	–	⋆	–	–	•	–	○	○
MS0440_1109	0.239	F	–	–	–	–	⋆	–	•	•	–	•	•
MS0440_1131	0.318	F	–	–	–	–	⋆	–	–	•	–	○	○
MS0440_1157	0.401	F	–	–	–	–	⋆	–	–	•	–	○	○
AC114_115	0.500	F	•	–	–	–	⋆	–	–	•	–	○	○
AC114_264	0.098	F	⋆	–	–	–	•	–	•	•	–	•	•
AC114_391	0.567	F	•	–	–	–	•	–	⋆	•	–	•	•
AC114_553	0.210	F	–	–	–	–	⋆	–	•	–	–	○	○
AC114_700	0.351	F	•	–	–	–	⋆	–	•	•	–	•	•
AC114_810	0.354	F	•	–	–	–	⋆	–	•	•	–	•	•
AC114_875	0.171	F	⋆	–	–	–	•	–	•	•	–	•	•
A370_39	0.325	F	–	–	–	–	⋆	–	–	–	–	○	○
A370_119	0.564	F	–	•	–	–	⋆	–	–	•	•	•	○
A370_157	0.542	F	–	–	–	–	⋆	–	–	•	–	○	○
A370_183	0.361	F	–	•	–	–	⋆	–	–	•	•	•	○
A370_210	0.230	F	–	⋆	–	–	•	–	–	•	•	•	○
A370_292	0.542	F	–	•	–	–	–	–	–	⋆	•	•	○
A370_319	0.305	F	–	–	–	–	⋆	•	–	•	–	•	•
A370_401	0.346	F	–	–	–	–	⋆	•	–	•	–	•	•
A370_406	0.571	F	–	–	–	–	⋆	–	–	–	–	○	○
A370_540	0.173	F	–	–	–	–	⋆	–	–	–	–	○	○
A370_582	0.207	F	–	–	–	–	⋆	–	–	–	–	○	○
A370_620	0.250	F	–	–	–	–	⋆	–	–	–	–	○	○
A370_630	0.225	F	–	–	–	–	⋆	•	–	•	–	•	•
A370_650	0.547	F	–	–	–	–	⋆	–	–	•	–	○	○
A370_751	0.256	F	–	–	–	–	⋆	•	–	•	–	•	•

continued

Table 2.3 continued

			Bands with magnitude available									HST	
ID	z	Mem.	B	555	V	606	R	675	702	I	814	i	r_d
CL0054_62	0.537	F	–	–	–	–	⋆	–	–	–	–	○	○
CL0054_83	0.718	F	–	–	–	–	⋆	–	–	–	–	○	○
CL0054_89	0.537	F	–	–	–	–	⋆	–	–	–	–	○	○
CL0054_126	0.237	F	–	–	–	–	⋆	–	–	–	–	○	○
CL0054_137	0.297	F	–	–	–	–	⋆	–	–	–	–	○	○
CL0054_138	0.237	F	–	–	–	–	⋆	–	–	–	–	○	○
CL0054_284	0.815	F	–	–	–	–	⋆	–	–	–	–	○	○
CL0054_354	0.224	F	–	–	⋆	–	●	–	–	●	–	○	○
CL0054_407	0.275	F	–	●	⋆	–	●	–	–	●	●	●	○
CL0054_454	0.298	F	–	–	–	–	⋆	–	–	–	–	○	○
CL0054_579	0.577	F	–	–	–	–	⋆	–	–	–	–	○	○
CL0054_588	0.911	F	–	–	–	–	⋆	–	–	–	–	○	○
CL0054_686	0.710	F	–	–	–	–	⋆	–	–	–	–	○	○
CL0054_688	0.298	F	–	–	–	–	⋆	–	–	–	–	○	○
CL0054_779	1.004	F	–	–	–	–	⋆	–	–	–	–	○	○
CL0054_803	0.162	F	–	–	–	–	⋆	–	–	–	–	○	○
CL0054_827	0.583	F	–	–	–	–	⋆	–	–	–	–	○	○
CL0054_892	0.585	F	–	–	●	–	⋆	–	–	●	–	○	○
CL0054_927	0.653	F	–	–	–	–	⋆	–	–	–	–	○	○
CL0054_937	0.603	F	–	●	●	–	⋆	–	–	●	●	●	○
CL0054_979	0.660	F	–	–	–	–	⋆	–	–	–	–	○	○
CL0054_993	0.214	F	–	–	–	–	⋆	–	–	–	–	○	○
CL0054_1011	0.171	F	–	⋆	●	–	●	–	–	●	●	●	○
CL0054_1054	0.830	F	–	–	–	–	⋆	–	–	–	–	○	○
MS2053_86	0.196	F	–	–	–	–	⋆	–	–	–	–	○	○
MS2053_371	0.521	F	–	–	–	●	⋆	–	–	–	●	●	●
MS2053_404	0.384	F	–	–	–	⋆	●	–	–	–	●	●	●
MS2053_435	0.520	F	–	–	–	⋆	–	–	–	–	●	●	●
MS2053_455	0.174	F	–	–	–	⋆	●	–	–	–	●	●	●
MS2053_470	0.371	F	–	–	–	⋆	●	–	–	–	●	●	●
MS2053_741	0.335	F	–	–	–	⋆	●	–	–	–	–	●	●
MS2053_856	0.261	F	–	–	–	⋆	●	–	–	–	–	●	●
MS2053_998	0.196	F	–	–	–	⋆	●	–	–	–	●	●	●
MS2053_1105	0.408	F	–	–	–	⋆	●	–	–	–	●	●	●
MS2053_1296	0.058	F	–	–	–	–	⋆	–	–	–	–	○	○

continued

Table 2.3 continued

			Bands with magnitude available									HST	
ID	z	Mem.	B	555	V	606	R	675	702	I	814	i	$r_{\rm d}$
MS1054_F02	0.180	F	–	–	–	⋆	–	–	–	–	●	●	●
MS1054_F04	0.230	F	–	–	–	⋆	–	–	–	–	●	●	●
MS1054_F05	0.249	F	–	–	–	⋆	–	–	–	–	●	●	●
MS1054_F06	0.259	F	–	–	–	⋆	–	–	–	–	●	●	●
MS1054_F08	0.287	F	–	–	–	⋆	–	–	–	–	●	●	●
MS1054_F10	0.324	F	–	–	–	⋆	–	–	–	–	●	●	●
MS1054_F11	0.325	F	–	–	–	⋆	–	–	–	–	●	●	●
MS1054_F12	0.325	F	–	–	–	⋆	–	–	–	–	●	●	●
MS1054_F14	0.429	F	–	–	–	⋆	–	–	–	–	–	●	●
MS1054_F16	0.470	F	–	–	–	⋆	–	–	–	–	●	●	●
MS1054_F18	0.553	F	–	–	–	⋆	–	–	–	–	●	●	●
MS1054_F19	0.684	F	–	–	–	●	–	–	–	–	⋆	●	●
MS1054_F20	0.686	F	–	–	–	●	–	–	–	–	⋆	●	●
MS1054_F21	0.756	F	–	–	–	●	–	–	–	–	⋆	●	●
MS1054_F22	0.896	F	–	–	–	●	–	–	–	–	⋆	●	●
AC114_18	0.306	C	●	–	–	–	⋆	–	–	●	–	○	○
AC114_142	0.325	C	●	–	–	–	⋆	–	–	●	–	○	○
AC114_193	0.307	C	●	–	–	–	⋆	–	●	●	–	●	●
AC114_768	0.314	C	●	–	–	–	⋆	–	–	●	–	○	○
AC114_930	0.306	C	●	–	–	–	⋆	–	●	●	–	●	●
AC114_959	0.313	C	●	–	–	–	⋆	–	●	●	–	●	●
AC114_1001	0.307	C	●	–	–	–	⋆	–	–	●	–	○	○
A370_532	0.374	C	–	–	–	–	⋆	–	–	●	–	○	○
A370_538	0.373	C	–	–	–	–	⋆	–	–	●	–	○	○
A370_555	0.378	C	–	–	–	–	⋆	–	–	–	–	○	○
CL0054_358	0.564	C	–	–	●	–	⋆	–	–	●	–	○	○
CL0054_609	0.558	C	–	–	–	–	⋆	–	–	–	–	○	○
CL0054_643	0.558	C	–	–	–	–	⋆	–	–	–	–	○	○
CL0054_714	0.562	C	–	–	–	–	⋆	–	–	–	–	○	○
CL0054_725	0.557	C	–	–	–	–	⋆	–	–	–	–	○	○
CL0054_799	0.554	C	–	–	–	–	⋆	–	–	–	–	○	○
CL0054_860	0.559	C	–	–	●	–	⋆	–	–	●	–	○	○
CL0054_918	0.557	C	–	–	–	–	⋆	–	–	–	–	○	○
CL0054_966	0.559	C	–	–	–	–	⋆	–	–	–	–	○	○
MS1054_C01	0.828	C	–	–	–	●	–	–	–	–	⋆	●	●
MS1054_1403	0.813	C	–	–	–	●	–	–	–	–	⋆	●	●
MS1054_2011	0.841	C	–	–	–	●	–	–	–	–	⋆	●	●

Chapter 3

Spectroscopy analysis

The analysis described in this chapter is also discussed, in a briefer form, in the papers which make use of it. These are Bamford et al. (2005, 2006), for the extended emission-line fitting, and Mouhcine et al. (2006a,b) for the spatially integrated spectral measurements. All of the work involved in fitting the extended emission-lines and measuring the equivalent widths was performed by the author of this thesis, with advice from the coauthors of these papers. The quantities derived from the emission-line equivalent widths and fluxes are those tabulated in Mouhcine et al. (2006b), as calculated by Mustapha Mouhcine, which are in close agreement with the same quantities calculated by the author. The internal reddening estimates and extinction corrected quantities are due to Mustapha Mouhcine.

3.1 Extended emission-line fitting

Several techniques are available to measure the rotation velocity of nearby disc galaxies (e.g., see Sofue & Rubin 2001for a review). Radio observations may be used to trace atomic hydrogen via its 21-cm emission (e.g., Haynes et al. 1997), while optical spectroscopy can trace either stellar absorption lines (e.g., Mathieu et al. 2002), or emission regions in a spatially integrated (e.g., Dale et al. 1997) or individual (e.g., Douglas et al. 2000) manner.

The choice of techniques is more limited for distant galaxies. Radio telescopes are not yet sensitive enough to detect HI emission beyond $z \sim 0.2$, and are unlikely to able to reach $z \sim 1$, particularly with the resolution required to measure a rotation curve, rather than simply a velocity width, for well over a decade, until the construction of the Square Kilometre Array (SKA; Carilli & Rawlings 2004). Individual HII regions and planetary nebulae can only be detected and resolved for very nearby objects ($z < 0.01$). This leaves spectroscopy of the unresolved, spatially continuous optical (or near-infrared) light as the only available method. For galaxies with no current star formation, stellar absorption lines must be used. This is difficult due to to the low signal inherent in such observations, and the need for additional modelling to account for the intrinsic stellar spectra and the significant velocity dispersion of old stellar populations. Rotation velocities for non-star-forming galaxies can therefore currently only be obtained at low redshifts (e.g., Mathieu et al. 2002), although spatially unresolved, overall velocity dispersions can be obtained to $z \lesssim 1$ (e.g., Gebhardt et al. 2003). For star-forming galaxies, bright emission-lines can be used, allowing rotation velocities to be measured for galaxies as distant as $z \sim 1$ (e.g., Vogt et al. 1996). The analysis in this thesis is restricted to star-forming, emission-line galaxies.

However, obtaining rotation velocities for distant, star-forming galaxies using optical spectroscopy still has its difficulties, particularly due to the restricted spatial resolution. Nearby galaxies are so large and bright that a relatively narrow spectroscopy slit can be used. The resulting spectrum is therefore only based on light from the major axis, and a rotation curve can thus be directly measured. In contrast, galaxies at intermediate redshift ($z \sim 0.5$) are typically a few arcsec in diameter. A typical good seeing for an 8-m class telescope is ~ 1 arcsec FWHM, and correspondingly ~ 1 arcsec wide slits are used for the observations. This means that the resultant spectrum includes light integrated over a significant fraction of the width of the target galaxy, and thus with varying rotation velocity components. The spatial resolution along the slit is also limited to the seeing scale. To measure rotation velocities and other parameters, one must model and account for these effects. The method we employ is described in detail below. Note that an alternative to slit-based spectroscopy is the use of integral field units (IFUs). This technique is not used in this study, but will be discussed later in section 6.2.

In order to measure the rotation velocity ($V_{\rm rot}$) and emission scale length ($r_{\rm d,spec}$) we fit each emission-line independently using a synthetic rotation curve method based on ELFIT2D by Simard & Pritchet (1998, 1999), and dubbed ELFIT2PY. In this technique model emission-lines are created for particular sets of parameters, and compared to the data to assess their goodness-of fit. The model emission-lines are created assuming a form for the intrinsic rotation curve, an exponential surface-brightness profile, and given the galaxy inclination, seeing and instrumental profile. The intrinsic rotation curve assumed here is the 'universal rotation curve' (URC) of Persic & Salucci (1991), with a slope weakly parametrized by the absolute B-band magnitude, M_B. Adopting a flat rotation curve leads to values of $V_{\rm rot} \sim 10$ km s^{-1} lower, but does not affect the conclusions of this study. As well as $V_{\rm rot}$ and $r_{\rm d,spec}$, the emission-line flux, constant background level and, in the case of [OII]λ3727, the doublet line ratio, are simultaneously fit.

A Metropolis algorithm (Metropolis et al. 1953, as described by Saha & Williams 1994) is used to search the parameter space to find those which best fit the data, and to determine confidence intervals on these parameters. Images of model lines with the best-fitting parameters are also produced for comparison with the data.

The main differences between the method of Simard & Pritchet (1999) (ELFIT2D) and that used here (ELFIT2PY) are a 4× spectral oversampling to reduce the velocity 'quantisation' found by Milvang-Jensen (2003), the use of an error image rather than a constant noise level, improving performance in the vicinity of skyline residuals, and the addition of a test to judge when convergence has been achieved.

While there may be some concerns about the Metropolis algorithm finding a local, rather than global, minimum, inspection of the time series of accepted points in the Metropolis search shows that the $V_{\rm rot}$ and $r_{\rm d,spec}$ parameters converge fairly quickly to their final values, and are usually stable around these values for the remainder of the sampling iterations. This implies fairly deep and smooth global minima in chi-squared space, with few local minima.

In contrast, the less well constrained, but also less critical, parameters of background level and doublet ratio show more frequent jumps between semi-stable values. While this reveals the existence of local minima, it also demonstrates the algorithm's ability to move out of such regions when they exist. The final error in the measured parameter thus includes the uncertainty due to the multiplicity of chi-squared minima. The variations in these subsidiary parameters are rarely accompanied by any significant shift in the stable $V_{\rm rot}$ and $r_{\rm d,spec}$ parameter values. The sky and continuum background has been subtracted prior to the creation of the postage stamp images which are fitted by ELFIT2PY. The mean background level has thus already been determined with more precision than is available from the information provided to ELFIT2PY. The background level is therefore constrained to vary by no more than ±1 ADU. The background noise is typically ~ 12 ADU, and each postage stamp image contains ~ 1000 pixels, therefore these limits correspond to approximately $\pm 2.5\sigma$. Often these limits are not encountered, but in some cases, particularly for lines with absorption wings, the limits prevent the background level from varying excessively. Allowing the background level to vary in this way was done, following ELFIT2D, to improve the fit. The background level appears to have little impact on the fitted values of $V_{\rm rot}$ and $r_{\rm d,spec}$. However, given the above considerations, in hindsight it seems more sensible to hold the background fixed at zero, which will be done in future studies. An even better solution would be to include the presence of stellar absorption in the models, and this possibility will be investigated in the future.

The behaviour of the various parameters during the Metropolis search are illustrated by the examples in figures 3.1 and 3.2 for galaxies with low and high $V_{\rm rot}$ uncertainties, respectively.

Two of the emission-line galaxies do not have absolute B-band magnitudes from the photometry, and a further four have no lines suitable for fitting (i.e. the lines were so faint that the mean flux across the postage stamp was negative due to the noise). An additional 17 galaxies were discarded due to their inclinations being deemed highly uncertain. For the remaining 153 objects, a mean of 3.3 suitable lines per galaxy were fit by the procedure described above.

The principal results of the rotation curve fitting are measurements of $V_{\rm rot}$ and $r_{\rm d,spec}$ with estimates of their error for, in general, several emission-lines per galaxy. (Actually $V_{\rm rot}\sin i$ is measured, which is converted to $V_{\rm rot}$, using the inclinations obtained as described in section 2.4.2, once an average value of $V_{\rm rot}\sin i$ has been determined for each galaxy.) In order to produce a single value of $V_{\rm rot}$ and $r_{\rm d,spec}$ for each galaxy the values for the individual lines (labelled by j below) are combined by a weighted mean. Upper and lower errors $(+,-)$ on these average parameters are determined as the maximum of (a) a weighted combination of the individual errors estimated by ELFIT2PY, and (b) the standard error of the weighted mean determined from the individual measurements. For example, with weights

$$w_j = \frac{2}{({\sigma^{+}_{V_{\rm rot},j}}^2 + {\sigma^{-}_{V_{\rm rot},j}}^2)}, \tag{3.1}$$

the computed upper error on the average $V_{\rm rot}$ is the square-root of

$$\begin{aligned} {\sigma^{+}_{V_{\rm rot}}}^2 = \max \Bigg[& \sum_j w_j^2 \, {\sigma^{+}_{V_{\rm rot},j}}^2 \Big/ \Big(\sum_j w_j\Big)^2 , \\ & \sum_j w_j \left(V_{{\rm rot},j} - \overline{V_{\rm rot}}\right)^2 \Big/ \Big(n \sum_j w_j\Big) \Bigg] \end{aligned} \tag{3.2}$$

where n is the number of measurements contributing to the average. The first term in the max function corresponds to case (a) above, and the second to case (b). The lower error $\sigma^{-}_{V_{\rm rot}}$ is computed similarly.

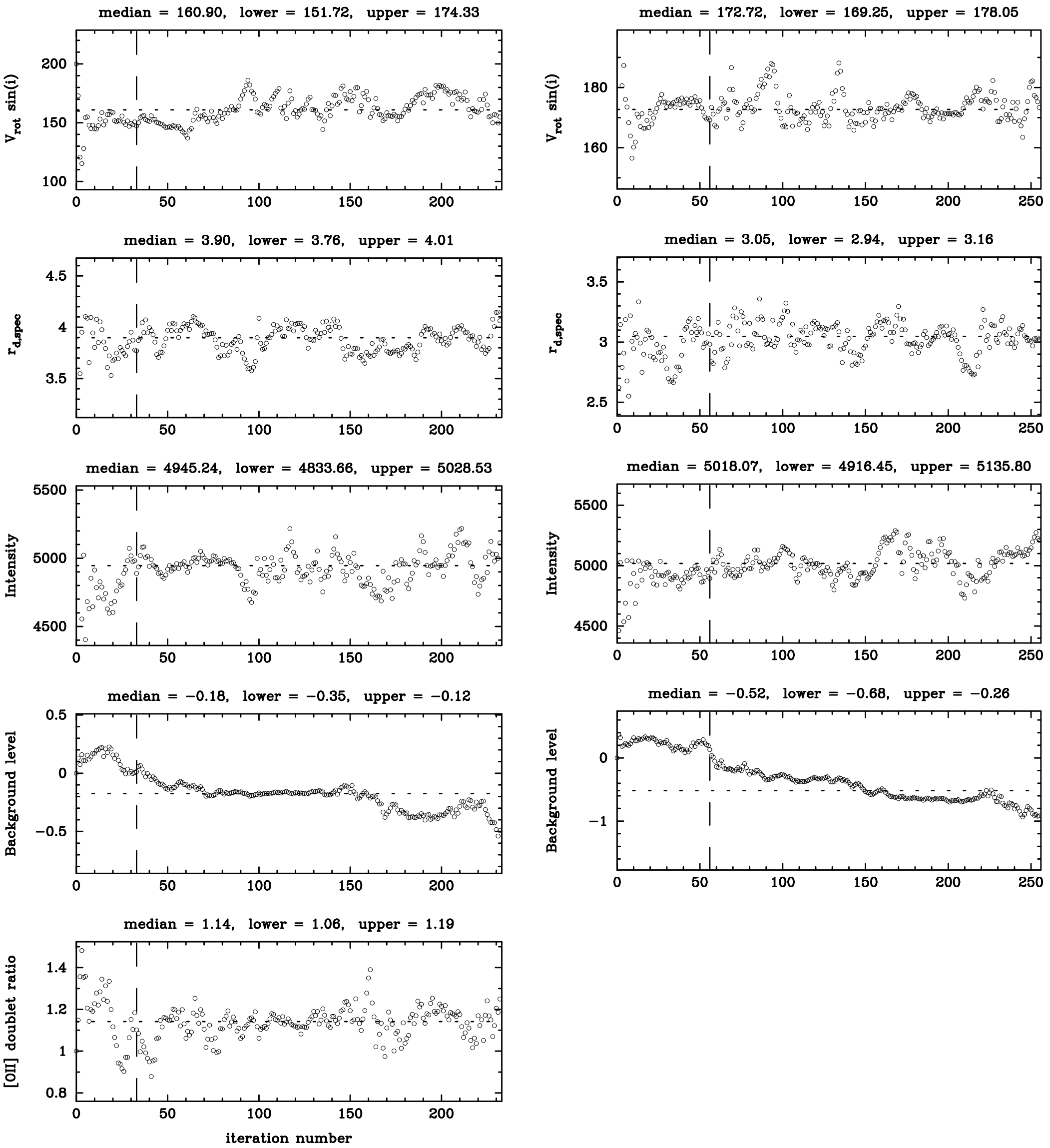

Figure 3.1. Example parameter series during the ELFIT2PY Metropolis search for the (left column) [OII]λ3727 and (right column) Hβ emission-lines of the galaxy MS2053_435. This galaxy has a small $V_{\rm rot}$ error in comparison with the majority analysed in this thesis. The points give the parameter values at each accepted iteration. The panels show, from top to bottom, $V_{\rm rot} \sin i$ (km s^{-1}), $r_{\rm d,spec}$ (kpc, but in a different cosmology to that used elsewhere in this thesis), total line intensity (ADU, relative units), the background level and the [OII]λ3727 doublet ratio where appropriate. The iteration at which the Metropolis search was judged to have converged is marked by the vertical dashed line. The median and 68% lower and upper confidence interval boundaries of the converged points are given above each panel. Note the scales when comparing: the vertical scale of each plot is centred on this median value (marked by the horizontal dotted line), and on either side extends to five times the average of the lower and upper uncertainties.

The $V_{\rm rot} \sin i$ are consistent for the two lines, and thus the weighted average, used as the final value, was assigned an error calculated from the uncertainties provided by ELFIT2PY. On the otherhand, the $r_{\rm d,spec}$ are in some disagreement, as is not unexpected given the differences in the production of the two lines. In this case the uncertainty on the weighted average was estimated from the standard error of the multiple values. Note that while the background level does not appear to converge, it does not appear to significantly affect the other parameters.

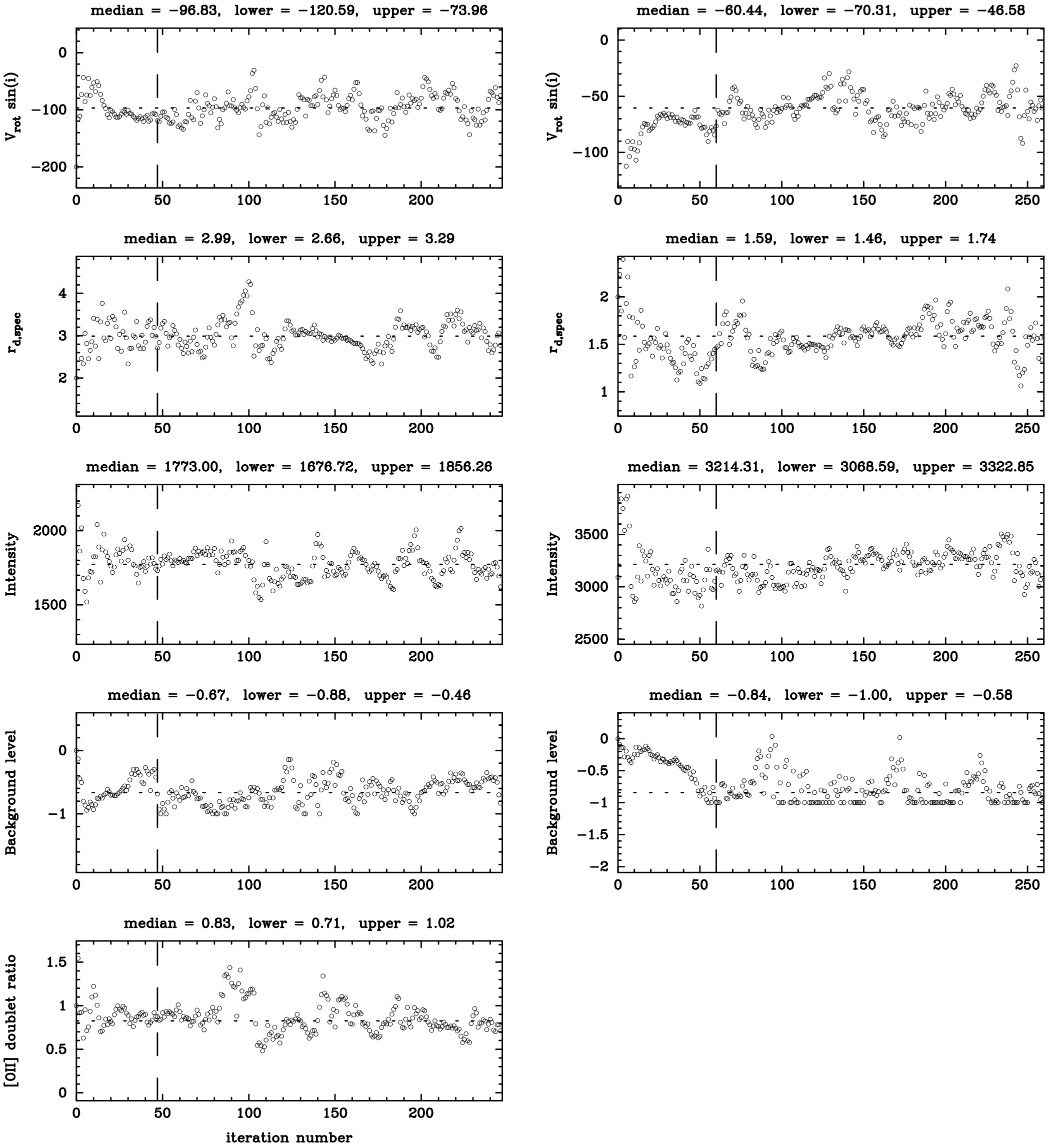

Figure 3.2. Same as figure 3.1, but for the galaxy AC114_959, with a large $V_{\rm rot}$ error in comparison with most of the galaxies analysed in this thesis.

Here both the $V_{\rm rot} \sin i$ are slightly inconsistent for the two lines ($> 1\sigma$), while the $r_{\rm d,spec}$ are more so. For both, therfore, the weighted averages used were asigned an uncertainty estimated from the standard error of the multiple values.

As the sky and continuum background have already been subtracted from the postage stamp images which were fit, the background level was only allowed to vary slightly, by ±1 ADU. This can be seen in the plot for Hβ, in the right column. The Balmer line fits often attempted to move to negative background levels, due to stellar absorption either side of the emission-line, but were prevented by this constraint.

For most galaxies the error calculated from those given by ELFIT2PY is close to that inferred from the standard error of the data, and hence case (a) applies, or case (b) causes a negligible increase in the error. However, for galaxies where there is inconsistency between values from different lines, and no way of determining which lines should be preferred, case (a) would underestimate the true uncertainty. In these situations case (b) provides a more realistic estimate of the error. This test is obviously not possible for galaxies with only one observed (and accepted by the quality control procedure) emission-line, and therefore will cause formally inconsistent errors. However, this is judged to be a minor problem when compared with the elimination of occasional situations where the uncertainty would otherwise be seriously underestimated.

3.1.1 Data quality tests

A significant fraction of the emission-lines identified display dominant nuclear emission, or asymmetries in intensity, spatial extent or kinematics. In severe cases these departures from the assumed surface brightness profile and intrinsic rotation curve mean that the best-fitting model is not a true good fit to the data. A similar situation can occur for very low signal-to-noise (S/N) lines, where an artifact of the noise overly influences the fit. More concerning is the case of very compact lines, where the number of pixels is on the order of the number of degrees of freedom in the model, and hence an apparently good fit is obtained despite a potentially substantial departure from the assumed surface brightness profile.

In order to eliminate such ‘bad’ fits a number of quality tests are imposed, based on a measure of the median S/N (per pixel over the region where the model line has significant flux), and a robust reduced-χ^2 goodness-of-fit estimate ($\chi^2_{\rm r}$). The cuts on these quantities were set following a detailed simultaneous inspection of the data, model line and best-fitting parameters. Firstly, for each line a lower limit in S/N is applied, followed by an upper limit on $\chi^2_{\rm r}$. As an initial attempt at excluding sources too compact to fit reliably, lines were also rejected if the best-fitting scalelength of the emission was consistent with zero within the 1σ confidence interval derived by ELFIT2PY.

These cuts alone were deemed too inefficient, i.e. cuts rejecting all obviously ‘bad’ fits resulted in an excessive number of clearly ‘good’ fits being discarded. Ideally we would prefer an entirely quantitative method, and therefore a number of additional quantities were calculated to assist the quality judgement. The line was fit by a Gaussian in each spatial row using the IRAF/STSDAS task NGAUSSFIT, with the errors on each Gaussian fit determined by repeated simulations with different noise realisations corresponding to the error image. It was found that for the [OII]λ3727 doublet (actually [OII]$\lambda3726, \lambda3728$), fitting a single Gaussian was more robust than attempting to simultaneously fit both components. Through inspection of the parameters and their errors quantitative criteria were developed for judging whether the fit position is reliable. The emission-line was thus ‘traced’ and the region determined for which the trace is reliable.

The distance from the continuum centre to where the line could no longer be reliably detected above the noise we term the *extent* ($r_{\rm extent}$). This quantity is dependent on the properties of the data, e.g. pixel size and seeing, and is thus not suitable for comparison between studies. However, it is useful for the internal investigation of differences between various subsets of our own data set. Note that ELFIT2PY uses all the pixels simultaneously, and therefore successfully uses information further out than $r_{\rm extent}$ when fitting a model line. Indeed, reasonable fits can be obtained even with lines for which $r_{\rm extent}$ is zero.

Additional quantities describing the asymmetry, in terms of extent and kinematics, and the flatness of the line at maximum extent were also formulated. However, a satisfactory set of criteria based on these quantities could not be found. Therefore, with the above cuts on S/N and $\chi^2_{\rm r}$ established all of the model lines were reviewed by eye, along with the galaxy images, observed emission-line, model parameters and the various quantities just described. From this inspection lists were compiled of those lines to be unconditionally excluded or included in the calculation of $V_{\rm rot}$. The main occasions where such action was necessary was to exclude lines which were clearly due to very central emission, judged in combination with the ratios $r_{\rm d,spec}/r_{\rm d,phot}$ and $r_{\rm extent}/r_{\rm d,phot}$, but where $\chi^2_{\rm r}$ was low enough to make the adopted cut.

Also unconditionally excluded were lines which made the $\chi^2_{\rm r}$ and S/N cuts, but were obviously incorrect or clearly inconsistent with other lines available for the galaxy, particularly when this was for an obvious reason such as low S/N or interference from skyline residuals. The primary cases for unconditional inclusion were where slight asymmetries and/or absorption wings caused a high $\chi^2_{\rm r}$ value, but the fit was clearly well matched to a high S/N line with large $r_{\rm extent}/r_{\rm d,spec}$ and $r_{\rm d,spec} \gtrsim r_{\rm d,phot}$.

After the application of these visual exclusions and inclusions, any galaxy with an average $V_{\rm rot}$ consistent with zero rotation, within the errors given by equation 3.2, was discarded from the sample. While this is not ideal, it is very useful to remove galaxies for which the emitting region is probably not rotationally supported. The above line selections were then re-applied with the additional constraint that individual lines were also rejected if their best-fitting $V_{\rm rot}$ was consistent with zero within the 1σ confidence interval derived by ELFIT2PY.

The ratio $r_{\rm d,spec}/r_{\rm d,phot}$ is plotted versus $\Delta M_B{}^{\rm TF}$ and $V_{\rm rot}$ in figure 3.3, for our data both before and after the application of the quality control criteria. This ratio compares the extent of the current star formation activity with the size of the galaxy as defined by its stars. Our quality control procedure preferentially rejects galaxies with low rotation velocities and large TF offsets, and also those with low $r_{\rm d,spec}/r_{\rm d,phot}$. In addition, there are a higher proportion of cluster galaxies with $r_{\rm d,spec}/r_{\rm d,phot} \lesssim 0.5$ (see also the results in section 5.3). However, no significant correlation of $r_{\rm d,spec}/r_{\rm d,phot}$ with $V_{\rm rot}$ or $\Delta M_B{}^{\rm TF}$ is seen, and the $r_{\rm d,spec}/r_{\rm d,phot}$ distribution is otherwise consistent for rejected and accepted galaxies. Galaxies with low $r_{\rm d,spec}/r_{\rm d,phot}$, and hence centrally concentrated current star formation, therefore do not appear to cause a bias in our results.

In five cases there are two spectra corresponding to the same galaxy, both intentionally, for comparison purposes, and coincidentally. In one case the second observation is with a slit at a ~30° angle to the major axis of the galaxy and thus of much lower quality. This observation was therefore discarded. The remaining four galaxies have reasonably consistent measured parameters from their duplicated spectra and thus weighted averages of the fit parameters are adopted.

3.1.2 Full Tully-Fisher sample

After the rigorous line quality-control procedure, 93 galaxies remain. These comprise the TFR sample of the five cluster fields observed for this study. Note that from the 20 serendipitously observed galaxies, only 2 field galaxies that happened to be

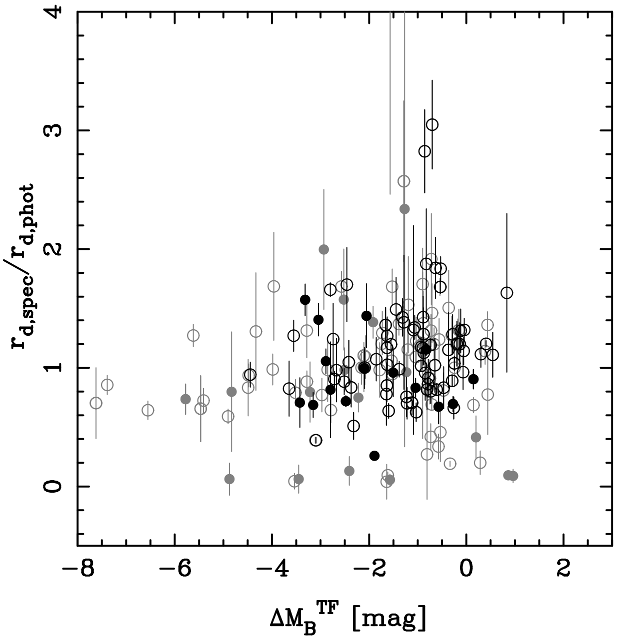

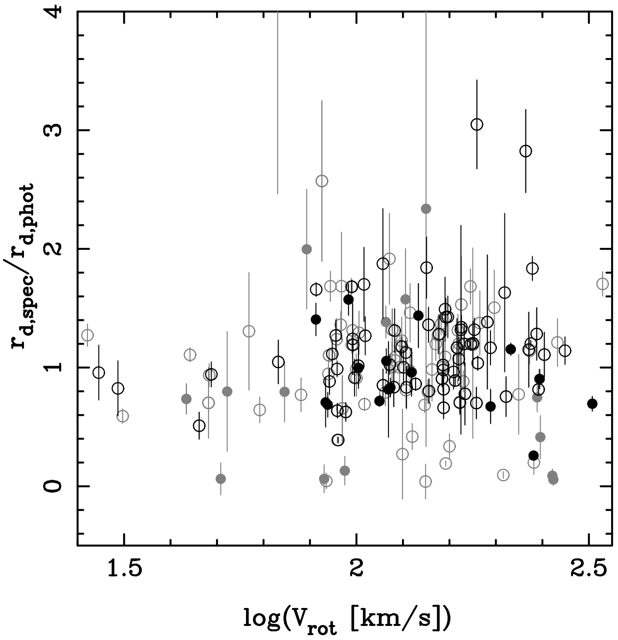

Figure 3.3. Plots of $r_{\rm d,spec}/r_{\rm d,phot}$ versus *(top)* $\Delta M_B{}^{\rm TF}$ and *(bottom)* $V_{\rm rot}$. Open points correspond to field galaxies, filled points denote cluster galaxies. Results with no emission-line quality control criteria applied are shown by the grey points, while the black points give the results for galaxies which make the final TFR sample, determined using only lines which pass the quality checks.

well aligned with the slit, and met all the other criteria, have been included in the TFR study. In order to consistently combine the MS1054 data with this sample, the emission-line postage stamps for the MS1054 galaxies have been re-fit using ELFIT2PY and the same line quality criteria applied. Of the 31 galaxies with emission in the MS1054 observations, 18 remain after applying the line quality criteria. These are added to the sample described above, giving a total of 111 galaxies, with a mean of 2.3 lines contributing to the measurements for each galaxy. The basic properties, photometric data, and results of the extended emission-line fitting procedure, are listed for all TFR sample galaxies in table 3.1.

Figures 2.6, 2.11 and 2.12 show the distributions of M_B, $r_{\mathrm{d,phot}}$, r_{eff} and $\mu_{R,\mathrm{eff,abs}}$ versus redshift for all field emission-line galaxies observed. Those in our final TFR sample are marked by filled points, while those which are not, i.e., for which none of the emission-line fits passed our quality criteria, are shown by open points. There is no noticeable difference between the distributions of selected and rejected galaxies in these plots. This indicates that our quality selection criteria are not biasing our sample from the point of view of the galaxies' broadband photometric properties, beyond those biases inherent to our initial spectroscopy observational selection procedure.

3.2 Spatially-integrated spectral measurements

3.2.1 Emission-line equivalent widths and fluxes

The 2002 VLT data are binned to a dispersion of 1.62 Å pixel^{-1}, the mean dispersion prior to wavelength calibration, and have a spectral resolution of 5.8Å FWHM (roughly constant over the whole wavelength range). For the 2001 VLT data the dispersion is 1.075 Å pixel^{-1} sampling a spectral resolution of 4.2Å, and for the Subaru data the corresponding numbers are 1.4 Å pixel^{-1} and 6.3Å (again the resolution FWHM is roughly constant over the whole wavelength range). These dispersions and resolutions were judged to be similar enough to not require any further homogenisation through rebinning or smoothing, which would increase the covariance between neighbouring pixels and complicate the line-fitting process.

All lines were fit with Gaussians using the IRAF/STSDAS task NGAUSSFIT. This task fits the data with a combination of Gaussians, with specified initial conditions, using an iterative AMOEBA minimization algorithm to find the minimum of the chi-square between the fitting-function and the data, taking into account the uncertainities on each pixel through the error image. Once the best-fitting parameters (i.e. continuum level, position, amplitude and FWHM for a single line) are found, uncertainties on them are estimated through a Monte-Carlo resampling technique. In this, twenty synthetic data realisations are created from the best-fitting function, with random noise added to each pixel corresponding to the provided error image. These synthetic spectra are then fit in the same manner as the true data, and the standard deviations of the resultant parameters are used to estimate the uncertainties on the best-fitting parameters for the true data.

From the best-fitting Gaussian parameters, rest-frame equivalent widths, in units of Å, were calculated using

$$W = \frac{F_{\mathrm{line}}}{F_{\mathrm{cont}}} \frac{d}{1+z} \tag{3.3}$$

where F_{line} is the (continuum-subtracted) flux in the emission-line, in ADU, calcu-

Table 3.1. The photometric and emission-line fit data for our full field and cluster TFR samples. The columns are: (1) ID assigned in this study, (2) R.A. and (3) Dec., (4) redshift, (5) cluster or field membership, (6) inclination (90° ≡ edge-on), (7) internal extinction correction (including 0.27 mag of face-on extinction), (8) best-fitting spectral energy distribution (SED: E/S0 = 0.0, Sab = 1.0, Sbc = 2.0, Scd = 3.0 and Sdm = 4.0), (9) absolute rest-frame B-band magnitude (for $\Omega_\Lambda = 0.7$, $\Omega_m = 0.3$, $H_0 = 70$ km s^{-1} Mpc^{-1} cosmology), (10) rotation velocity, (11) photometric scalelength (12) spectroscopic scalelength (13) weight in TFR fits.

ID	R.A. [J2000]	Dec. [J2000]	z	Mem.	i [deg]	$A^{\rm i}$ [mag]	SED	M_B [mag]	$\log V_{\rm rot}$ [dex]	$r_{\rm d,phot}$ [kpc]	$r_{\rm d,spec}$ [kpc]	$w_{\rm TF}$
MS0440_101	04 43 14.6	02 05 49	0.819	F	66	0.59 ± 0.10	$2.5^{+1.0}_{-1.2}$	-21.72 ± 0.28	$2.23^{+0.03}_{-0.05}$	$3.84^{+1.01}_{-0.57}$	$2.99^{+0.31}_{-0.31}$	0.017
MS0440_140	04 43 09.0	02 06 13	0.316	F	55	0.45 ± 0.05	$2.5^{+1.0}_{-1.2}$	-19.58 ± 0.21	$2.06^{+0.06}_{-0.07}$	$3.67^{+0.35}_{-0.41}$	$6.87^{+0.98}_{-0.96}$	0.014
MS0440_188	04 43 19.3	02 06 42	0.491	F	53	0.43 ± 0.05	$2.5^{+1.0}_{-1.2}$	-20.91 ± 0.19	$2.02^{+0.20}_{-0.21}$	$2.97^{+0.15}_{-0.12}$	$5.05^{+0.53}_{-0.69}$	0.004
MS0440_207	04 43 16.8	02 07 01	0.087	F	51	0.41 ± 0.08	$2.5^{+1.0}_{-1.2}$	-18.79 ± 0.30	$1.99^{+0.06}_{-0.06}$	$1.16^{+0.01}_{-0.02}$	$1.95^{+0.03}_{-0.04}$	–
MS0440_273	04 43 16.4	02 07 31	0.283	F	79	0.96 ± 0.10	$2.5^{+1.0}_{-1.2}$	-20.10 ± 0.23	$2.02^{+0.03}_{-0.04}$	$5.68^{+0.38}_{-0.42}$	$7.20^{+0.42}_{-0.39}$	0.018
MS0440_311	04 43 06.2	02 07 51	0.470	F	39	0.34 ± 0.02	$2.6^{+1.4}_{-2.6}$	-21.55 ± 0.18	$1.96^{+0.09}_{-0.10}$	$5.58^{+0.15}_{-0.16}$	$7.09^{+0.44}_{-0.51}$	0.011
MS0440_319	04 43 07.8	02 08 06	0.138	F	82	0.96 ± 0.07	$1.4^{+2.6}_{-1.4}$	-19.19 ± 0.38	$1.98^{+0.03}_{-0.03}$	$4.48^{+0.15}_{-0.30}$	$2.81^{+0.20}_{-0.21}$	–
MS0440_538	04 43 18.1	02 09 43	0.213	F	59	0.49 ± 0.07	$1.4^{+2.6}_{-1.4}$	-21.87 ± 0.32	$2.39^{+0.02}_{-0.03}$	$4.70^{+0.13}_{-0.20}$	$3.83^{+0.09}_{-0.09}$	–
MS0440_616	04 42 58.8	02 09 37	0.211	F	76	0.84 ± 0.14	$1.8^{+2.2}_{-1.8}$	-20.00 ± 0.34	$2.11^{+0.05}_{-0.05}$	$4.02^{+0.07}_{-0.06}$	$4.52^{+0.28}_{-0.27}$	–
MS0440_627	04 43 14.9	02 09 33	0.265	F	74	0.76 ± 0.17	$1.8^{+2.2}_{-1.8}$	-20.49 ± 0.32	$2.07^{+0.02}_{-0.02}$	$4.25^{+0.07}_{-0.07}$	$4.36^{+0.24}_{-0.24}$	0.019
MS0440_635	04 43 27.2	02 09 43	0.237	F	80	0.96 ± 0.10	$2.5^{+1.0}_{-1.2}$	-20.23 ± 0.24	$2.16^{+0.01}_{-0.01}$	$4.86^{+0.47}_{-0.33}$	$3.90^{+0.14}_{-0.13}$	–
MS0440_657	04 42 50.5	02 09 45	0.265	F	40	0.34 ± 0.03	$2.5^{+1.0}_{-1.2}$	-19.94 ± 0.21	$2.18^{+0.06}_{-0.07}$	$1.86^{+0.11}_{-0.06}$	$2.39^{+0.18}_{-0.19}$	0.014
MS0440_735	04 43 07.2	02 10 21	0.181	F	79	0.95 ± 0.04	$0.0^{+4.0}_{-0.0}$	-20.53 ± 0.33	$2.26^{+0.01}_{-0.01}$	$3.64^{+0.02}_{-0.02}$	$3.77^{+0.16}_{-0.16}$	–
MS0440_849	04 43 14.4	02 10 30	0.401	F	67	0.60 ± 0.11	$4.0^{+0.0}_{-3.0}$	-20.39 ± 0.22	$2.06^{+0.05}_{-0.05}$	$2.90^{+0.27}_{-0.16}$	$2.47^{+0.21}_{-0.20}$	0.016
MS0440_1109	04 43 05.9	02 10 45	0.239	F	49	0.39 ± 0.01	$1.4^{+2.6}_{-1.4}$	-19.06 ± 0.29	$2.08^{+0.04}_{-0.04}$	$3.04^{+0.05}_{-0.05}$	$3.98^{+0.38}_{-0.40}$	–
MS0440_1131	04 43 06.7	02 12 15	0.318	F	67	0.60 ± 0.10	$1.4^{+2.6}_{-1.4}$	-21.08 ± 0.26	$2.23^{+0.03}_{-0.03}$	$4.45^{+0.04}_{-0.08}$	$5.97^{+0.28}_{-0.33}$	0.018
MS0440_1157	04 43 10.9	02 11 32	0.401	F	48	0.39 ± 0.04	$0.0^{+1.8}_{-0.0}$	-20.40 ± 0.18	$2.25^{+0.04}_{-0.05}$	$2.84^{+0.10}_{-0.12}$	$3.41^{+0.40}_{-0.30}$	0.017
AC114_115	22 58 59.7	-34 50 52	0.500	F	65	0.57 ± 0.09	$3.4^{+0.6}_{-0.8}$	-21.58 ± 0.10	$2.22^{+0.02}_{-0.02}$	$6.88^{+0.22}_{-0.34}$	$8.03^{+1.13}_{-1.15}$	0.020
AC114_264	22 58 55.1	-34 49 49	0.098	F	58	0.48 ± 0.02	$3.6^{+0.4}_{-1.4}$	-17.64 ± 0.07	$1.95^{+0.06}_{-0.08}$	$1.40^{+0.02}_{-0.02}$	$1.56^{+0.09}_{-0.12}$	–
AC114_391	22 58 45.6	-34 49 03	0.567	F	59	0.48 ± 0.02	$2.6^{+0.8}_{-0.8}$	-21.72 ± 0.03	$2.25^{+0.02}_{-0.01}$	$4.63^{+0.07}_{-0.07}$	$5.55^{+0.16}_{-0.16}$	0.021
AC114_553	22 58 56.7	-34 48 18	0.210	F	71	0.68 ± 0.14	$0.0^{+1.8}_{-0.0}$	-20.73 ± 0.20	$2.38^{+0.01}_{-0.01}$	$5.34^{+0.03}_{-0.03}$	$6.42^{+0.09}_{-0.09}$	–
AC114_700	22 58 33.7	-34 47 43	0.351	F	60	0.49 ± 0.02	$2.6^{+0.8}_{-0.8}$	-20.20 ± 0.06	$2.23^{+0.04}_{-0.04}$	$3.47^{+0.05}_{-0.05}$	$4.16^{+0.48}_{-0.38}$	0.019
AC114_810	22 58 46.1	-34 46 00	0.354	F	39	0.34 ± 0.03	$3.4^{+0.6}_{-0.8}$	-20.27 ± 0.06	$2.25^{+0.07}_{-0.08}$	$2.33^{+0.04}_{-0.04}$	$3.07^{+0.18}_{-0.12}$	0.014
AC114_875	22 58 51.2	-34 46 21	0.171	F	67	0.59 ± 0.03	$2.2^{+1.2}_{-0.6}$	-19.29 ± 0.12	$2.00^{+0.03}_{-0.03}$	$3.06^{+0.05}_{-0.05}$	$3.11^{+0.08}_{-0.08}$	–

continued

Table 3.1 continued

ID	R.A. [J2000]	Dec. [J2000]	z	Mem.	i [deg]	A^{i} [mag]	SED	M_B [mag]	$\log V_{\mathrm{rot}}$ [dex]	$r_{\mathrm{d,phot}}$ [kpc]	$r_{\mathrm{d,spec}}$ [kpc]	w_{TF}
A370_39	02 39 48.1	-01 38 16	0.325	F	61	0.51 ± 0.13	$2.5^{+1.0}_{-1.2}$	-19.08 ± 0.17	$2.00^{+0.05}_{-0.05}$	$3.75^{+0.44}_{-0.40}$	$3.43^{+0.15}_{-0.15}$	–
A370_119	02 40 02.5	-01 37 13	0.564	F	66	0.58 ± 0.03	$2.0^{+1.4}_{-0.8}$	-21.83 ± 0.10	$2.38^{+0.04}_{-0.03}$	–	$11.03^{+0.84}_{-0.61}$	0.019
A370_157	02 39 55.5	-01 36 59	0.542	F	69	0.64 ± 0.12	$3.4^{+0.6}_{-2.2}$	-20.37 ± 0.17	$2.19^{+0.04}_{-0.04}$	$5.54^{+0.92}_{-0.74}$	$5.65^{+0.23}_{-0.29}$	0.018
A370_183	02 40 00.4	-01 36 38	0.361	F	49	0.40 ± 0.05	$1.6^{+1.4}_{-0.8}$	-20.81 ± 0.11	$2.40^{+0.05}_{-0.05}$	$2.16^{+0.28}_{-0.14}$	$2.40^{+0.17}_{-0.13}$	0.017
A370_210	02 40 00.9	-01 36 16	0.230	F	55	0.44 ± 0.02	$2.0^{+2.0}_{-0.8}$	-20.44 ± 0.03	$1.69^{+0.05}_{-0.06}$	$2.32^{+0.10}_{-0.07}$	$2.18^{+0.14}_{-0.16}$	–
A370_292	02 39 57.8	-01 35 49	0.542	F	72	0.72 ± 0.05	$3.8^{+0.2}_{-1.0}$	-20.13 ± 0.09	$1.84^{+0.07}_{-0.08}$	–	$2.27^{+0.12}_{-0.10}$	0.013
A370_319	02 39 51.8	-01 35 21	0.305	F	46	0.38 ± 0.01	$1.4^{+2.6}_{-1.4}$	-21.01 ± 0.19	$1.99^{+0.15}_{-0.08}$	$2.96^{+0.04}_{-0.04}$	$3.67^{+0.62}_{-0.63}$	0.008
A370_401	02 39 54.5	-01 35 04	0.346	F	50	0.41 ± 0.01	$1.4^{+2.6}_{-1.4}$	-20.97 ± 0.15	$2.26^{+0.04}_{-0.04}$	$5.28^{+0.12}_{-0.12}$	$16.10^{+0.35}_{-1.87}$	0.018
A370_406	02 40 13.9	-01 35 05	0.571	F	49	0.40 ± 0.07	$2.5^{+1.0}_{-1.2}$	-21.83 ± 0.12	$2.22^{+0.06}_{-0.07}$	$4.71^{+0.56}_{-0.44}$	$5.05^{+0.28}_{-0.28}$	0.015
A370_540	02 40 09.7	-01 32 05	0.173	F	68	0.63 ± 0.12	$2.5^{+1.0}_{-1.2}$	-18.12 ± 0.21	$1.66^{+0.04}_{-0.04}$	$1.97^{+0.33}_{-0.26}$	$1.01^{+0.03}_{-0.05}$	–
A370_582	02 40 10.5	-01 33 29	0.207	F	77	0.88 ± 0.13	$2.5^{+1.0}_{-1.2}$	-19.96 ± 0.21	$2.21^{+0.04}_{-0.04}$	$6.21^{+0.19}_{-0.15}$	$5.97^{+0.63}_{-0.61}$	–
A370_620	02 40 04.3	-01 32 59	0.250	F	65	0.57 ± 0.09	$2.5^{+1.0}_{-1.2}$	-21.11 ± 0.17	$2.22^{+0.02}_{-0.02}$	$6.38^{+0.26}_{-0.29}$	$4.49^{+0.40}_{-0.40}$	0.020
A370_630	02 39 50.3	-01 34 22	0.225	F	75	0.78 ± 0.06	$1.6^{+2.4}_{-1.6}$	-19.01 ± 0.26	$1.99^{+0.01}_{-0.01}$	$1.92^{+0.04}_{-0.04}$	$2.29^{+0.06}_{-0.06}$	–
A370_650	02 39 57.8	-01 33 10	0.547	F	40	0.35 ± 0.03	$1.0^{+2.2}_{-1.0}$	-21.47 ± 0.11	$2.37^{+0.06}_{-0.08}$	$4.50^{+0.77}_{-0.65}$	$5.17^{+0.59}_{-0.57}$	0.014
A370_751	02 39 57.5	-01 34 32	0.256	F	56	0.45 ± 0.02	$2.4^{+1.6}_{-2.4}$	-20.07 ± 0.23	$2.13^{+0.01}_{-0.01}$	$2.19^{+0.05}_{-0.05}$	$1.88^{+0.08}_{-0.06}$	0.020
CL0054_62	00 57 00.9	-27 44 18	0.537	F	42	0.36 ± 0.03	$2.5^{+1.0}_{-1.2}$	-21.91 ± 0.09	$2.36^{+0.05}_{-0.05}$	$5.96^{+0.19}_{-0.32}$	$16.82^{+1.26}_{-1.28}$	0.017
CL0054_83	00 56 52.4	-27 44 06	0.718	F	75	0.80 ± 0.16	$2.5^{+1.0}_{-1.2}$	-21.97 ± 0.22	$2.32^{+0.01}_{-0.02}$	$5.46^{+0.95}_{-0.58}$	$4.12^{+0.27}_{-0.25}$	0.020
CL0054_89	00 56 52.4	-27 44 04	0.537	F	53	0.43 ± 0.05	$2.5^{+1.0}_{-1.2}$	-20.54 ± 0.10	$2.19^{+0.05}_{-0.06}$	$3.69^{+0.64}_{-0.40}$	$3.01^{+0.10}_{-0.10}$	0.017
CL0054_126	00 56 59.3	-27 43 41	0.237	F	77	0.87 ± 0.13	$2.5^{+1.0}_{-1.2}$	-18.14 ± 0.21	$1.49^{+0.07}_{-0.07}$	$1.96^{+0.38}_{-0.40}$	$1.62^{+0.03}_{-0.03}$	–
CL0054_137	00 56 55.7	-27 43 25	0.297	F	43	0.36 ± 0.03	$2.5^{+1.0}_{-1.2}$	-19.99 ± 0.13	$2.19^{+0.06}_{-0.06}$	$1.89^{+0.16}_{-0.14}$	$1.25^{+0.06}_{-0.08}$	0.016
CL0054_138	00 56 46.3	-27 42 50	0.237	F	84	0.96 ± 0.09	$2.5^{+1.0}_{-1.2}$	-21.84 ± 0.18	$2.36^{+0.02}_{-0.02}$	–	$11.79^{+0.48}_{-0.48}$	–
CL0054_284	00 56 55.7	-27 42 17	0.815	F	50	0.41 ± 0.04	$2.5^{+1.0}_{-1.2}$	-21.30 ± 0.20	$2.08^{+0.04}_{-0.05}$	$2.90^{+0.42}_{-0.36}$	$2.42^{+0.05}_{-0.11}$	0.017
CL0054_354	00 57 02.3	-27 41 31	0.224	F	46	0.38 ± 0.03	$4.0^{+0.0}_{-1.6}$	-20.48 ± 0.05	$1.91^{+0.04}_{-0.04}$	$2.96^{+0.06}_{-0.06}$	$4.91^{+0.06}_{-0.06}$	–
CL0054_407	00 57 00.7	-27 41 05	0.275	F	38	0.34 ± 0.01	$1.8^{+1.4}_{-0.8}$	-19.88 ± 0.05	$2.32^{+0.06}_{-0.07}$	$2.20^{+0.18}_{-0.13}$	$3.58^{+1.06}_{-0.95}$	0.015
CL0054_454	00 57 09.9	-27 40 44	0.298	F	73	0.73 ± 0.16	$2.5^{+1.0}_{-1.2}$	-21.69 ± 0.20	$2.38^{+0.02}_{-0.02}$	$6.00^{+0.11}_{-0.15}$	$11.01^{+0.31}_{-0.40}$	0.020
CL0054_579	00 57 12.3	-27 40 14	0.577	F	34	0.32 ± 0.02	$2.5^{+1.0}_{-1.2}$	-22.42 ± 0.10	$2.18^{+0.06}_{-0.07}$	$4.39^{+0.12}_{-0.10}$	$3.97^{+0.17}_{-0.19}$	0.015
CL0054_588	00 57 09.1	-27 40 27	0.911	F	29	0.31 ± 0.02	$2.5^{+1.0}_{-1.2}$	-21.72 ± 0.25	$2.28^{+0.07}_{-0.08}$	$2.11^{+0.69}_{-0.51}$	$2.92^{+0.06}_{-0.06}$	0.013
CL0054_686	00 56 50.9	-27 38 01	0.710	F	44	0.37 ± 0.06	$2.5^{+1.0}_{-1.2}$	-21.68 ± 0.16	$2.25^{+0.09}_{-0.11}$	–	$3.16^{+0.13}_{-0.13}$	0.010
CL0054_688	00 56 53.8	-27 37 14	0.298	F	65	0.57 ± 0.09	$2.5^{+1.0}_{-1.2}$	-19.62 ± 0.16	$1.96^{+0.02}_{-0.02}$	$2.39^{+0.16}_{-0.13}$	$1.52^{+0.05}_{-0.05}$	0.020

continued

Table 3.1 continued

ID	R.A. [J2000]	Dec. [J2000]	z	Mem.	i [deg]	$A^{\rm i}$ [mag]	SED	M_B [mag]	$\log V_{\rm rot}$ [dex]	$r_{\rm d,phot}$ [kpc]	$r_{\rm d,spec}$ [kpc]	$w_{\rm TF}$
CL0054_779	00 57 14.5	-27 38 04	1.004	F	38	0.34 ± 0.02	$2.5\,^{+1.0}_{-1.2}$	-22.40 ± 0.29	$2.19\,^{+0.05}_{-0.06}$	$4.31\,^{+0.91}_{-0.73}$	$4.22\,^{+0.11}_{-0.09}$	0.015
CL0054_803	00 56 57.6	-27 38 24	0.162	F	50	0.40 ± 0.04	$2.5\,^{+1.0}_{-1.2}$	-19.40 ± 0.19	$1.96\,^{+0.03}_{-0.04}$	$3.82\,^{+0.06}_{-0.05}$	$3.77\,^{+0.17}_{-0.17}$	–
CL0054_827	00 57 09.1	-27 38 36	0.583	F	60	0.49 ± 0.07	$2.5\,^{+1.0}_{-1.2}$	-21.08 ± 0.13	$2.19\,^{+0.04}_{-0.04}$	$4.86\,^{+0.22}_{-0.20}$	$6.91\,^{+0.47}_{-0.44}$	0.019
CL0054_892	00 56 55.6	-27 39 08	0.585	F	32	0.32 ± 0.03	$2.2\,^{+1.6}_{-1.0}$	-22.11 ± 0.12	$2.39\,^{+0.10}_{-0.14}$	$3.48\,^{+0.23}_{-0.23}$	$4.47\,^{+0.46}_{-0.46}$	0.008
CL0054_927	00 57 07.9	-27 39 28	0.653	F	39	0.34 ± 0.02	$2.5\,^{+1.0}_{-1.2}$	-21.20 ± 0.13	$2.19\,^{+0.05}_{-0.06}$	$3.06\,^{+0.42}_{-0.35}$	$4.57\,^{+0.14}_{-0.05}$	0.016
CL0054_937	00 56 56.8	-27 39 34	0.603	F	65	0.57 ± 0.03	$1.8\,^{+1.4}_{-0.8}$	-21.10 ± 0.12	$2.22\,^{+0.08}_{-0.05}$	$2.35\,^{+1.22}_{-0.95}$	$3.09\,^{+0.19}_{-0.32}$	0.015
CL0054_979	00 56 47.2	-27 38 33	0.660	F	57	0.47 ± 0.06	$2.5\,^{+1.0}_{-1.2}$	-21.18 ± 0.14	$2.10\,^{+0.03}_{-0.03}$	$3.39\,^{+0.33}_{-0.26}$	$3.40\,^{+0.18}_{-0.16}$	0.019
CL0054_993	00 57 11.4	-27 39 46	0.214	F	70	0.66 ± 0.13	$2.5\,^{+1.0}_{-1.2}$	-21.13 ± 0.20	$1.96\,^{+0.02}_{-0.02}$	$4.36\,^{+0.04}_{-0.04}$	$1.70\,^{+0.08}_{-0.06}$	–
CL0054_1011	00 56 58.9	-27 40 20	0.171	F	66	0.58 ± 0.03	$1.4\,^{+0.8}_{-1.4}$	-20.21 ± 0.07	$2.21\,^{+0.01}_{-0.01}$	$2.48\,^{+0.03}_{-0.02}$	$2.21\,^{+0.08}_{-0.08}$	–
CL0054_1054	00 56 59.8	-27 38 08	0.830	F	67	0.61 ± 0.11	$2.5\,^{+1.0}_{-1.2}$	-21.48 ± 0.24	$2.26\,^{+0.03}_{-0.04}$	$8.15\,^{+1.07}_{-0.82}$	$5.71\,^{+0.33}_{-0.40}$	0.018
MS2053_86	20 56 12.4	-04 38 26	0.196	F	74	0.78 ± 0.16	$2.5\,^{+1.0}_{-1.2}$	-19.60 ± 0.23	$2.11\,^{+0.01}_{-0.01}$	$3.94\,^{+0.02}_{-0.04}$	$3.28\,^{+0.50}_{-0.48}$	–
MS2053_371	20 56 17.8	-04 38 01	0.521	F	55	0.44 ± 0.02	$3.2\,^{+0.8}_{-1.8}$	-21.15 ± 0.07	$2.15\,^{+0.05}_{-0.05}$	$4.13\,^{+0.06}_{-0.06}$	$5.62\,^{+0.43}_{-0.42}$	0.017
MS2053_404	20 56 18.7	-04 37 07	0.384	F	69	0.65 ± 0.04	$1.0\,^{+0.8}_{-1.0}$	-21.74 ± 0.05	$2.45\,^{+0.01}_{-0.01}$	$4.81\,^{+0.31}_{-0.31}$	$5.49\,^{+0.17}_{-0.17}$	0.022
MS2053_435	20 56 18.9	-04 40 04	0.520	F	53	0.43 ± 0.02	$1.6\,^{+2.2}_{-1.0}$	-21.83 ± 0.14	$2.33\,^{+0.02}_{-0.01}$	$4.67\,^{+0.07}_{-0.07}$	$5.87\,^{+0.52}_{-0.52}$	0.021
MS2053_455	20 56 20.0	-04 35 54	0.174	F	79	0.95 ± 0.04	$1.4\,^{+1.8}_{-1.4}$	-20.09 ± 0.18	$2.15\,^{+0.02}_{-0.02}$	$4.55\,^{+0.12}_{-0.10}$	$8.37\,^{+0.80}_{-0.80}$	–
MS2053_470	20 56 19.5	-04 38 47	0.371	F	77	0.88 ± 0.07	$2.8\,^{+1.2}_{-1.6}$	-20.69 ± 0.08	$2.20\,^{+0.03}_{-0.03}$	$5.58\,^{+0.22}_{-0.23}$	$7.95\,^{+0.55}_{-0.68}$	0.020
MS2053_741	20 56 23.2	-04 34 41	0.335	F	77	0.85 ± 0.07	$4.0\,^{+0.0}_{-0.8}$	-20.41 ± 0.07	$1.94\,^{+0.04}_{-0.04}$	$3.92\,^{+0.28}_{-0.28}$	$3.46\,^{+0.18}_{-0.18}$	0.019
MS2053_856	20 56 24.8	-04 35 34	0.261	F	70	0.66 ± 0.04	$4.0\,^{+0.0}_{-1.6}$	-21.38 ± 0.06	$2.29\,^{+0.02}_{-0.02}$	$6.54\,^{+0.46}_{-0.46}$	$7.63\,^{+0.42}_{-0.37}$	0.021
MS2053_998	20 56 22.6	-04 41 32	0.196	F	72	0.71 ± 0.05	$1.6\,^{+2.0}_{-1.6}$	-19.99 ± 0.18	$2.10\,^{+0.02}_{-0.02}$	$3.43\,^{+0.01}_{-0.01}$	$4.03\,^{+0.20}_{-0.20}$	–
MS2053_1105	20 56 29.6	-04 38 08	0.408	F	77	0.85 ± 0.07	$3.4\,^{+0.6}_{-1.8}$	-19.49 ± 0.09	$1.83\,^{+0.03}_{-0.03}$	$2.86\,^{+0.36}_{-0.29}$	$3.00\,^{+0.15}_{-0.15}$	–
MS2053_1296	20 56 34.2	-04 38 02	0.058	F	57	0.46 ± 0.06	$2.5\,^{+1.0}_{-1.2}$	-15.03 ± 0.26	$1.45\,^{+0.12}_{-0.16}$	$0.61\,^{+0.12}_{-0.07}$	$0.59\,^{+0.03}_{-0.03}$	–
MS1054_F02	10 56 48.3	-03 37 33	0.180	F	66	0.58 ± 0.03	$2.2\,^{+1.6}_{-0.6}$	-19.83 ± 0.11	$2.00\,^{+0.01}_{-0.01}$	$1.76\,^{+0.11}_{-0.03}$	$1.88\,^{+0.14}_{-0.14}$	–
MS1054_F04	10 56 56.0	-03 37 28	0.230	F	80	0.96 ± 0.03	$4.0\,^{+0.0}_{-1.6}$	-19.04 ± 0.06	$1.73\,^{+0.09}_{-0.07}$	$2.89\,^{+0.08}_{-0.07}$	$8.87\,^{+2.02}_{-1.69}$	–
MS1054_F05	10 57 01.3	-03 35 44	0.249	F	79	0.96 ± 0.04	$2.2\,^{+1.6}_{-0.6}$	-19.06 ± 0.08	$2.06\,^{+0.02}_{-0.03}$	$2.89\,^{+0.03}_{-0.03}$	$2.69\,^{+0.25}_{-0.25}$	–
MS1054_F06	10 56 53.0	-03 38 41	0.259	F	78	0.91 ± 0.06	$2.6\,^{+1.4}_{-0.8}$	-20.44 ± 0.08	$2.07\,^{+0.02}_{-0.01}$	$3.98\,^{+0.14}_{-0.05}$	$2.60\,^{+0.13}_{-0.10}$	0.021
MS1054_F08	10 57 08.2	-03 37 34	0.287	F	69	0.65 ± 0.04	$2.0\,^{+1.4}_{-0.6}$	-19.47 ± 0.06	$2.02\,^{+0.03}_{-0.03}$	$2.33\,^{+0.07}_{-0.07}$	$2.52\,^{+0.27}_{-0.29}$	–
MS1054_F10	10 57 12.3	-03 37 17	0.324	F	68	0.63 ± 0.04	$1.8\,^{+1.2}_{-0.6}$	-19.88 ± 0.05	$1.99\,^{+0.03}_{-0.04}$	$2.67\,^{+0.06}_{-0.05}$	$4.93\,^{+0.42}_{-0.36}$	0.019
MS1054_F11	10 57 08.2	-03 36 42	0.325	F	45	0.37 ± 0.01	$4.0\,^{+0.0}_{-1.2}$	-19.58 ± 0.02	$2.02\,^{+0.02}_{-0.02}$	$2.71\,^{+0.12}_{-0.10}$	$3.20\,^{+0.25}_{-0.25}$	0.021
MS1054_F12	10 57 11.5	-03 36 44	0.325	F	64	0.55 ± 0.03	$1.4\,^{+0.4}_{-1.2}$	-20.99 ± 0.04	$2.42\,^{+0.02}_{-0.02}$	$4.16\,^{+0.04}_{-0.04}$	$6.53\,^{+1.73}_{-1.57}$	0.021

continued

Table 3.1 continued

ID	R.A. [J2000]	Dec. [J2000]	z	Mem.	i [deg]	$A^{\rm i}$ [mag]	SED	M_B [mag]	$\log V_{\rm rot}$ [dex]	$r_{\rm d,phot}$ [kpc]	$r_{\rm d,spec}$ [kpc]	$w_{\rm TF}$
MS1054_F14	10 56 54.7	-03 39 00	0.429	F	77	0.86 ± 0.07	$2.5^{+1.0}_{-1.2}$	-18.75 ± 0.09	$1.86^{+0.04}_{-0.05}$	$1.52^{+0.21}_{-0.18}$	$1.06^{+0.10}_{-0.10}$	–
MS1054_F16	10 57 01.2	-03 34 20	0.470	F	38	0.34 ± 0.01	$3.8^{+0.2}_{-1.2}$	-21.62 ± 0.04	$2.26^{+0.02}_{-0.02}$	$3.46^{+0.04}_{-0.04}$	$3.95^{+0.41}_{-0.39}$	0.021
MS1054_F18	10 57 03.7	-03 38 33	0.553	F	58	0.47 ± 0.02	$4.0^{+0.0}_{-1.0}$	-20.69 ± 0.06	$2.17^{+0.02}_{-0.02}$	$2.99^{+0.08}_{-0.07}$	$3.70^{+0.16}_{-0.10}$	0.021
MS1054_F19	10 56 50.7	-03 35 39	0.684	F	76	0.84 ± 0.07	$3.8^{+0.2}_{-1.8}$	-20.92 ± 0.08	$2.19^{+0.02}_{-0.04}$	$3.73^{+0.12}_{-0.12}$	$3.88^{+0.25}_{-0.34}$	0.019
MS1054_F20	10 57 05.7	-03 36 26	0.686	F	81	0.96 ± 0.01	$1.8^{+1.4}_{-0.6}$	-20.95 ± 0.06	$2.12^{+0.02}_{-0.03}$	$3.05^{+0.13}_{-0.12}$	$3.47^{+0.18}_{-0.13}$	0.020
MS1054_F21	10 56 48.6	-03 35 42	0.756	F	50	0.41 ± 0.01	$3.4^{+0.6}_{-0.8}$	-21.18 ± 0.04	$2.27^{+0.03}_{-0.04}$	$4.99^{+0.25}_{-0.28}$	$5.62^{+0.89}_{-0.58}$	0.019
MS1054_F22	10 57 07.8	-03 37 04	0.896	F	69	0.63 ± 0.04	$2.6^{+0.8}_{-1.0}$	-22.48 ± 0.06	$2.38^{+0.01}_{-0.01}$	$9.43^{+1.29}_{-0.81}$	$14.83^{+2.04}_{-0.89}$	0.022
AC114_18	22 58 48.5	-34 51 39	0.306	C	72	0.72 ± 0.22	$2.4^{+0.8}_{-0.6}$	-21.44 ± 0.23	$2.16^{+0.02}_{-0.02}$	–	$1.54^{+0.05}_{-0.05}$	0.048
AC114_142	22 58 52.0	-34 50 42	0.325	C	43	0.36 ± 0.03	$4.0^{+0.0}_{-0.4}$	-19.92 ± 0.05	$2.07^{+0.04}_{-0.05}$	$3.26^{+0.08}_{-0.07}$	$2.71^{+0.16}_{-0.18}$	0.047
AC114_193	22 58 58.9	-34 50 20	0.307	C	78	0.89 ± 0.07	$4.0^{+0.0}_{-0.2}$	-21.18 ± 0.08	$2.05^{+0.01}_{-0.01}$	$2.85^{+0.08}_{-0.08}$	$2.05^{+0.08}_{-0.06}$	0.053
AC114_768	22 58 35.8	-34 45 47	0.314	C	59	0.49 ± 0.07	$1.4^{+0.4}_{-0.4}$	-22.28 ± 0.10	$2.41^{+0.03}_{-0.04}$	–	$2.70^{+0.16}_{-0.15}$	0.049
AC114_930	22 58 34.0	-34 46 52	0.306	C	60	0.49 ± 0.02	$1.8^{+1.0}_{-0.4}$	-20.72 ± 0.08	$1.91^{+0.08}_{-0.14}$	$3.05^{+0.08}_{-0.08}$	$4.29^{+0.32}_{-0.21}$	0.028
AC114_959	22 58 49.3	-34 47 01	0.313	C	52	0.42 ± 0.02	$1.6^{+0.8}_{-0.4}$	-21.26 ± 0.08	$1.93^{+0.06}_{-0.08}$	$4.19^{+0.28}_{-0.06}$	$2.96^{+0.60}_{-0.60}$	0.039
AC114_1001	22 58 30.1	-34 47 21	0.307	C	50	0.40 ± 0.04	$3.2^{+0.6}_{-1.0}$	-21.02 ± 0.07	$1.94^{+0.09}_{-0.08}$	$4.19^{+0.05}_{-0.03}$	$2.87^{+0.29}_{-0.32}$	0.036
A370_532	02 39 51.0	-01 32 12	0.374	C	82	0.96 ± 0.12	$1.4^{+2.4}_{-1.4}$	-22.31 ± 0.18	$2.27^{+0.01}_{-0.01}$	–	$2.55^{+0.07}_{-0.07}$	0.051
A370_538	02 39 58.2	-01 32 32	0.373	C	68	0.62 ± 0.11	$1.8^{+2.2}_{-1.8}$	-21.64 ± 0.17	$2.07^{+0.02}_{-0.02}$	$8.18^{+0.38}_{-0.27}$	$6.67^{+2.30}_{-2.32}$	0.050
A370_555	02 39 46.4	-01 32 17	0.378	C	71	0.69 ± 0.14	$2.5^{+1.0}_{-1.2}$	-21.13 ± 0.17	$2.39^{+0.02}_{-0.02}$	$8.57^{+0.52}_{-0.41}$	$7.74^{+0.27}_{-0.25}$	0.050
CL0054_358	00 57 04.5	-27 41 30	0.564	C	41	0.35 ± 0.03	$2.5^{+1.0}_{-1.2}$	-21.70 ± 0.10	$2.06^{+0.08}_{-0.09}$	$5.08^{+0.18}_{-0.26}$	$5.35^{+0.24}_{-0.33}$	0.037
CL0054_609	00 56 45.2	-27 38 08	0.558	C	59	0.49 ± 0.07	$2.5^{+1.0}_{-1.2}$	-21.52 ± 0.12	$1.98^{+0.03}_{-0.04}$	$4.71^{+0.26}_{-0.20}$	$7.40^{+0.26}_{-0.24}$	0.049
CL0054_643	00 56 45.4	-27 38 06	0.558	C	51	0.41 ± 0.08	$2.5^{+1.0}_{-1.2}$	-20.72 ± 0.13	$2.12^{+0.06}_{-0.08}$	$3.32^{+0.39}_{-0.36}$	$3.19^{+0.40}_{-0.17}$	0.040
CL0054_714	00 56 46.2	-27 37 23	0.562	C	45	0.37 ± 0.03	$2.5^{+1.0}_{-1.2}$	-20.46 ± 0.11	$2.00^{+0.05}_{-0.07}$	$3.04^{+0.34}_{-0.25}$	$3.03^{+0.21}_{-0.24}$	0.044
CL0054_725	00 56 44.8	-27 37 46	0.557	C	63	0.53 ± 0.08	$2.5^{+1.0}_{-1.2}$	-21.64 ± 0.13	$2.33^{+0.02}_{-0.02}$	$5.57^{+0.13}_{-0.16}$	$6.42^{+0.12}_{-0.10}$	0.051
CL0054_799	00 56 56.4	-27 38 22	0.554	C	60	0.50 ± 0.07	$2.5^{+1.0}_{-1.2}$	-22.40 ± 0.12	$2.51^{+0.03}_{-0.04}$	$7.84^{+0.18}_{-0.24}$	$5.44^{+0.33}_{-0.30}$	0.049
CL0054_860	00 56 49.6	-27 38 51	0.559	C	53	0.43 ± 0.05	$2.5^{+1.0}_{-1.2}$	-21.38 ± 0.11	$2.13^{+0.03}_{-0.04}$	$5.43^{+0.21}_{-0.23}$	$7.80^{+0.97}_{-0.99}$	0.049
CL0054_918	00 57 05.5	-27 40 04	0.557	C	47	0.38 ± 0.04	$2.5^{+1.0}_{-1.2}$	-23.07 ± 0.11	$2.38^{+0.05}_{-0.06}$	$12.07^{+0.54}_{-0.85}$	$3.11^{+0.24}_{-0.26}$	0.044
CL0054_966	00 56 48.4	-27 40 03	0.559	C	57	0.46 ± 0.06	$2.5^{+1.0}_{-1.2}$	-21.06 ± 0.12	$2.29^{+0.07}_{-0.09}$	$3.73^{+0.26}_{-0.20}$	$2.51^{+0.35}_{-0.35}$	0.037
MS1054_C01	10 57 12.0	-03 36 50	0.828	C	80	0.96 ± 0.03	$4.0^{+0.0}_{-0.4}$	-21.29 ± 0.05	$2.10^{+0.03}_{-0.03}$	$4.75^{+0.58}_{-0.41}$	$4.38^{+0.17}_{-0.17}$	0.050
MS1054_1403	10 57 03.8	-03 37 43	0.813	C	70	0.66 ± 0.04	$2.6^{+0.8}_{-0.8}$	-23.02 ± 0.05	$2.45^{+0.01}_{-0.01}$	$6.26^{+0.25}_{-0.22}$	$6.31^{+0.51}_{-0.38}$	0.053
MS1054_2011	10 57 07.1	-03 35 40	0.841	C	53	0.42 ± 0.02	$3.8^{+0.2}_{-0.8}$	-20.86 ± 0.03	$2.05^{+0.03}_{-0.05}$	$1.88^{+0.21}_{-0.14}$	$1.38^{+0.20}_{-0.15}$	0.048

lated from the area of the best-fitting Gaussian ($1.0645\,A\,\Delta\lambda$ given the normalisation of NGAUSSFIT's function, with amplitude A and FWHM $\Delta\lambda$). $F_{\rm cont}$ is the flux in the continuum, in ADU/pixel. In the second term d is the dispersion in Å/pixel, thus $d/(1+z)$ is the galaxy rest-frame wavelength interval per pixel. The uncertainty on W is calculated as

$$\sigma_W = \sqrt{\frac{\sigma^2_{F,{\rm line}}}{F^2_{\rm line}} + \frac{\sigma^2_{F,{\rm cont}}}{F^2_{\rm cont}}} \cdot W, \tag{3.4}$$

where

$$\sigma_{F,{\rm line}} = \sqrt{\frac{\sigma^2_A}{A^2} + \frac{\sigma^2_{\Delta\lambda}}{\Delta\lambda^2}} \cdot F_{\rm line}. \tag{3.5}$$

Fits were attempted for all of the following lines which were included in each spectra's wavelength range: [OII]λ3727, [OIII]λ4959, [OIII]λ5007, Hδ, Hγ, Hβ and Hα. Single Gaussian fits were attempted for all lines. In addition, for the Balmer lines Hδ, Hγ and Hβ, fits with two Gaussians simultaneously, one in absorption and another in emission, were attempted. Hα and its flanking [NII] doublet were simultaneously fit with three Gaussians in emission, but with no Hα absorption component because of the difficulties in fitting this due to the presence of the [NII] emission-lines. Note that [OII]λ3727 is actually a doublet ([OII]λ3726, λ3728), but is barely resolved in our data, particularly in the spatially integrated data, and so is better fit by a single Gaussian. Most studies are unable consider the doublet components separately.

It was found that using initial parameters already close to the true best-fit for the line greatly increased the reliability of the fits. These initial parameters were therefore determined by automatic examination of the region containing the line. The region considered for each fit was ±58Å, i.e. ±10 times the spectral resolution for the 2002 VLT data. For example, the initial continuum level was set using the median pixel value over this region. A more complex algorithm was used to determine the initial amplitude, in order to reduce the effect of nearby skyline residuals.

Lines with observed wavelengths in the range 7580–7700Å, that were thus affected by the strong telluric absorption feature in this region, were rejected. This amounted to, e.g. 1, 3, 2 and 6% of lines for [OII]λ3727, [OIII]λ4959, [OIII]λ5007 and Hβ respectively.

The signal-to-noise ratio, S/N, was estimated from the median pixel value, in regions between 29–58Å (5–10 spectral resolution elements for the 2002 VLT data) away from the line on both sides, divided by the median value of the error image in the same region.

Due to the automatic nature of the fitting process, there were times when the best-fitting function was clearly physically inaccurate. In order to discard such fits the following checks were performed: $\Delta\lambda$ is required to be less than 10 (20) times the spectral resolution for emission (absorption) lines, and greater than 0.5 times the spectral resoltion for all lines; in two-component fits $\Delta\lambda$ for the absorption component must be greater than that for the emission component; the continuum level must be positive; forbidden-lines ([OII], [OIII]) are required to be in emission. These checks were first applied to the two-component fits, and if any were not passed the fit was discarded and the one-component fit was preferred. The one-component fits were then tested. Again, if a fit failed any of the above checks it was rejected.

The rejection rates due to these criteria are, e.g. 18% (11%) for two-component (one-component) fits to Hβ, 6% for fits to [OIII]λ5007 and as low as 1% for fits

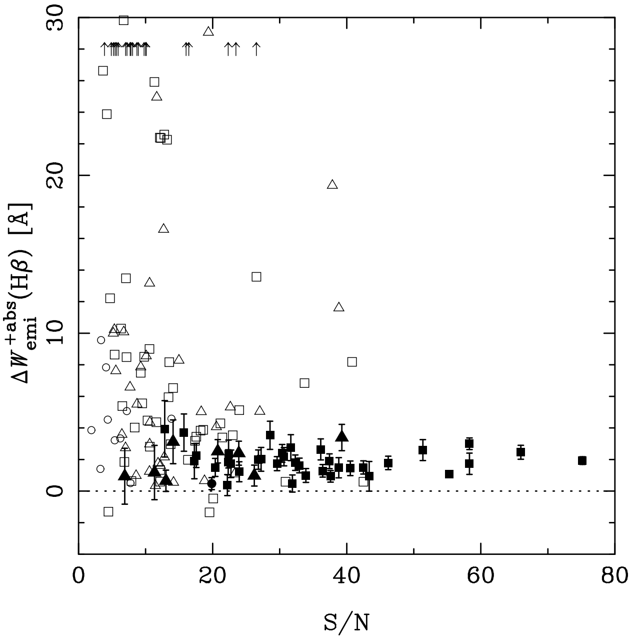

Figure 3.4. The Hβ absorption correction, $\Delta W_{\rm emi}^{+\rm abs}({\rm H}\beta)$, determined from the difference between the emission-line equivalent width measurements of two-component and one-component fits, plotted versus the signal-to-noise in the adjacent continuum, S/N. The filled points are those which have robust two-component fits, as judged by the cuts described in the text and indicated in figure 3.5. Error bars are omitted from the open points for clarity.

to [OII]λ3727. They are thus related to the effects of nearby continuum features influencing the fit.

The two-component fits to the Balmer lines were found to be not generally reliable, particularly for low S/N data. Figure 3.4 shows the difference in the emission-line equivalent width (EW) measured from the two- and one-component fits ($W_{\rm emi}^{(2)}$ and $W_{\rm emi}^{(1)}$ respectively). This quantity is effectively the correction, $\Delta W_{\rm emi}^{+\rm abs}({\rm H}\beta)$, one would need to apply to the one-component fit emission line EWs to obtain the true EW in the absence of stellar absorption,

$$\Delta W_{\rm emi}^{+\rm abs}({\rm H}\beta) = W_{\rm emi}^{(2)} - W_{\rm emi}^{(1)}. \tag{3.6}$$

The one-component fits should slightly underestimate the EW in cases where Balmer line absorption is additionally present, due to missing the lower part of the line. The correction introduced by including this effect, namely through a two-component fit, typically amounts to ~ 2Å (e.g. Kobulnicky & Phillips 2003). It can be seen that there is a ridge around $\Delta W_{\rm emi}^{+\rm abs}({\rm H}\beta)$ at high S/N, and very large scatter at low S/N. However, highly deviant points continue to be present upto fairly high S/N. Virtually all of these outlying points are due to a failure of the two-component fit, because of the difficulties in simultaneously fitting two similar functions with opposing sign.

The nature of the two-component fit makes it prone to fitting noise features either side of the emission-line using a very deep absorption line, and hence requiring an overly-large emission component to still fit the central emission line. However, when attempting to fit noise features the best-fitting parameters naturally have high

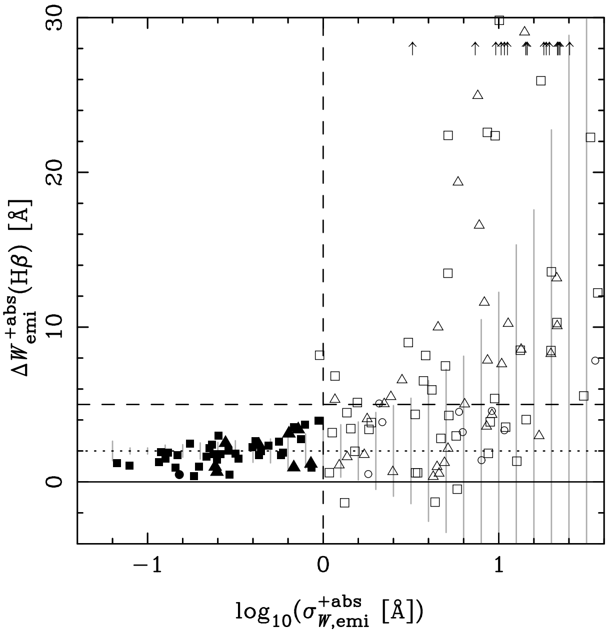

Figure 3.5. The Hβ absorption correction, $\Delta W^{+\mathrm{abs}}_{\mathrm{emi}}(\mathrm{H}\beta)$, determined from the difference between the emission-line equivalent width measurements of two-component and one-component fits, plotted versus an estimate the additional error introduced into the EW measurement by the inclusion of the absorption component, $\sigma^{+\mathrm{abs}}_{\mathrm{EW,emi}}$. Measurements from the 2002 VLT data are plotted with squares, the 2001 VLT data are plotted with circles, and Subaru data are plotted using triangles. Dashed lines show the cuts adopted in selecting the reliable sample of two-component fits. Those points which pass these cuts are filled, while those rejected are open. The mean $\Delta W^{+\mathrm{abs}}_{\mathrm{emi}}(\mathrm{H}\beta)$ of the reliable points, used to correct the one-component Hβ fits for the effects of stellar absorption, is indicated by the dotted line. The gray vertical lines indicate the average error on the data points, in bins of 0.1 dex in $\sigma^{+\mathrm{abs}}_{\mathrm{EW,emi}}$.

uncertainties, which are reliably estimated by the resampling technique described above. In order to identify unreliable two-component fits we estimate the additional error introduced into the EW measurement by the inclusion of the absorption component as

$$\sigma^{+\mathrm{abs}}_{W,\mathrm{emi}} = \sqrt{\sigma^{(2)}_{W,\mathrm{emi}}{}^{2} - \sigma^{(1)}_{W,\mathrm{emi}}{}^{2}}. \tag{3.7}$$

A plot of $\Delta W^{+\mathrm{abs}}_{\mathrm{emi}}(\mathrm{H}\beta)$ versus $\sigma^{+\mathrm{abs}}_{W,\mathrm{emi}}$ does a considerably better job of separating points with reasonable $\Delta W^{+\mathrm{abs}}_{\mathrm{emi}}(\mathrm{H}\beta)$ values from those with unrealistically high $\Delta W^{+\mathrm{abs}}_{\mathrm{emi}}(\mathrm{H}\beta)$, as can be seen in figure 3.5.

From examining figure 3.5, it is clear that points with $\sigma^{+\mathrm{abs}}_{\mathrm{EW,emi}} < 1.0$Å nearly all lie around the expected value of ~ 2Å. For $\sigma^{+\mathrm{abs}}_{\mathrm{EW,emi}}$ above this value there is a striking increase in both the scatter, and the number of unrealistically discrepant points. Note that $\sigma^{+\mathrm{abs}}_{\mathrm{EW,emi}} < 1.0$Å corresponds to where the uncertainty contributed by the inclusion of an absorption component in the fit is less than half the expected size of the correction. i.e. at $\sigma^{+\mathrm{abs}}_{\mathrm{EW,emi}} > 1.0$Å we would expect $> 10\%$ of points to lie further from the true value of the correction than the size of the correction itself, simply due to the measurement uncertainty. It therefore seems reasonable to only consider two-component fits for which $\sigma^{+\mathrm{abs}}_{\mathrm{EW,emi}} < 1.0$Å. In addition, a cut on $\Delta W^{+\mathrm{abs}}_{\mathrm{emi}}(\mathrm{H}\beta)$ is also useful in order to discard clearly discrepant points with

$\Delta W_{\mathrm{emi}}^{+\mathrm{abs}}(\mathrm{H}\beta) > 5$Å. These cuts are indicated in figure 3.5.

With these cuts, 40 galaxies were judged to have both reliable two- and one-component fits to Hβ. The mean of these points is 1.9Å, with scatter 0.9Å. Accounting for measurement uncertainties leaves an intrinsic scatter about the mean of $\sim$0.6Å.

For galaxies with reliable two-component Balmer fits we use the emission equivalent width determined from this fit. For all other galaxies we use the result of the one-component fit, corrected for the effect of stellar absorption. For this correction we adopt the mean of that determined for the two-component fits, $\left\langle \Delta W_{\mathrm{emi}}^{+\mathrm{abs}}(\mathrm{H}\beta) \right\rangle =$ 1.9Å, and include an additional uncertainty of 0.6Å in quaderature. The one-component fits for Hγ and Hδ are corrected for the effect of stellar absorption in the same way, with corrections of 1.8Å and 1.6Å respectively. The same additional uncertainty as determined for Hβ (0.6Å) is included in the Hγ and Hδ corrections.

Our entire sample of field (cluster) galaxies with identifiable emission-lines contains 212 (72) galaxies, and spans the redshift range 0.04–1.22 (0.2–0.84) with a median of 0.36 (0.55). This spectroscopic sample was searched for galaxies with emission-lines suitable for chemical analysis. Only galaxies for which it was possible to measure [OII], Hβ, and [OIII]λ5007 emission-lines were retained, i.e., the lines needed to determine the ionizing source and to measure the oxygen abundance. After applying these selection criteria the sample size drops to 60 (22). For reliable oxygen abundance determinations, only galaxies for which Hβ emission-line is well detected are retained. This was judged by requiring the S/N, estimated from the median pixel value in regions 29–58Å away from the line on both sides, divided by the median value of the error image in the same region, to be larger than 8. An additional 16 (5) objects were excluded from the sample due to the weak detection of Hβ. The final sample contains 44 (17) emission-line galaxies in the redshift range 0.2–0.8 (0.3–0.6), with a median of 0.45 (0.42). Twenty-one (seven) of the sample galaxies have securely measured rotation velocities and emission scale lengths.[1] Hereafter this will be referred to as the EW sample, to differentiate it from the TFR samples considered elsewhere in this thesis. The basic information for galaxies in this sample, i.e., redshift, cluster membership, rest-frame absolute B-band magnitude, rotation velocity and emission scalelength, along with emission-line rest-frame equivalent widths for [OII]λ3727, Hβ and [OIII]λ5007, are given in table 3.2.

3.2.2 [OII] and Hβ emission-line luminosities

The spectra used in this thesis have not been flux-calibrated, but the luminosity of the [OII] and Hβ lines can be calculated from their equivalent-widths (W) and the rest-frame absolute B-band magnitude (M_B), obtained as described in section 3.2.1 and section 2.4.1 respectively.

For [OII] we estimate the continuum flux at the position of the [OII] line from M_B and the SED which best fits the available colours, which was used to determine M_B from the observed magnitudes in the first place.

The absolute continuum flux at the effective wavelength of the B-band ($\sim$4450Å) was calculated from the rest-frame absolute B-band magnitudes using the conversion

---

[1] These numbers reduce to 40 (16) galaxies with oxygen abundances, of which 20 (6) have measured V_{rot} & $r_{\mathrm{d,spec}}$, after we reject several galaxies due to difficulties in measuring their metallicity, and 39 (15) galaxies with star formation rates and internal dust reddenings, 20 (6) with V_{rot} & $r_{\mathrm{d,spec}}$, after we reject galaxies with no magnitude measurement.

given by Fukugita et al. (1995):

$$F_{\mathrm{cont},B} = 6.19 \times 10^{-9} \times 10^{-0.4 M_B} \ \mathrm{erg\ s^{-1}\ cm^{-2}\ \AA^{-1}}. \tag{3.8}$$

Using the SEDs of Aragón-Salamanca et al. (1993), which were used in the determination of the VLT M_B and are similar in the range of interest to those used for the Subaru M_B (Fukugita et al. 1995), the ratios of the continuum flux at [OII] ($F_{\mathrm{cont,[OII]}}$) to that at the B-band effective wavelength ($F_{\mathrm{cont},B}$) are 0.45, 0.53, 0.67, 0.74, and 0.83 for types E/S0, Sab, Sbc, Scd, and Sdm respectively (Milvang-Jensen 2003). An approximate conversion was used to convert the types used for the Subaru data onto the system used for the VLT data. The ratio was interpolated between the listed values for intermediate types.

The absolute flux in the [OII] line is thus simply

$$F_{\mathrm{[OII]}} = W(\mathrm{[OII]}) \times F_{\mathrm{cont,[OII]}}, \tag{3.9}$$

and by geometry the [OII] luminosity is therefore

$$L_{\mathrm{[OII]}} = 1.20 \times 10^{40} \, F_{\mathrm{[OII]}} \ \mathrm{erg\ s^{-1}}. \tag{3.10}$$

For Hβ a conversion from $W(\mathrm{H}\beta)$ and M_B to Hβ luminosity may be derived in a similar manner to the method outlined for [OII] above. However, the central wavelength of the B band is very close to Hβ, 4433Å and 4861Å, respectively, and thus the conversion is mostly independent of the galaxy SED. We apply the conversion of Kobulnicky & Kewley (2004):

$$L_{\mathrm{H}\beta} = 5.49 \times 10^{31} \times 2.5^{-M_B} \, W(\mathrm{H}\beta) \ \mathrm{erg\ s^{-1}}. \tag{3.11}$$

3.2.3 Metallicities and ionisation conditions

The emission-lines observed in galaxy spectra are produced by the radiative decay of ionised gas from excited electronic states. The gas is ionised by UV photons, which may be from either hot stars or from an active galactic nucleus (AGN). The energy to excite the gas can be provided either by the photon field, which ionises the gas further, followed by recombination and subsequent radiative decay, or through inelastic collisions between the species and free electrons (producing the so called 'forbidden lines'), again resulting in line emission through radiative decay. Hot stars, of types O and B, are massive and thus short lived, and therefore associated with regions of star formation.

We wish to determine the properties of the gas throughout our galaxies, rather than just in the nuclear region, and will be using diagnostics calibrated on star-forming HII-regions. Therefore, we must first check that the observed emission is a result of star-formation, rather than AGN activity. The classical diagnostic used to distinguish AGN from star-forming galaxies is the ratio of two pairs of relatively strong emission-lines, i.e., [OIII]λ5007/Hβ versus [NII]λ6584/Hα, and/or [OIII]λ5007/Hβ versus [SII]$\lambda 6717, \lambda 6731$/H$\alpha$ (Baldwin et al. 1981; Veilleux & Osterbrock 1987). However, many of these lines are not available in optical spectra for objects at $z \gtrsim 0.3$. As a solution to this Rola et al. (1997) investigated the location of starbursts and AGNs in diagnostic diagrams involving blue emission-lines only, i.e. [OII]λ3727, Hβ, and [OIII]$\lambda 4959, \lambda 5007$ (see also Dessauges-Zavadsky et al.

Table 3.2. Basic properties and emission-line rest-frame equivalent widths for the galaxies in our EW sample. Columns are: ID, redshift, cluster or field membership, rotation velocity, emission scalelength, and [OII]λ3727, Hβ and [OIII]λ5007 emission-line rest-frame equivalent widths.

ID	z	Mem.	M_B [mag]	$V_{\rm rot}$ [km s^{-1}]	$r_{\rm d,spec}$ [kpc]	W([OII]) [Å]	W(Hβ) [Å]	W([OIII]) [Å]
A370_679	0.373	C	-22.03 ± 0.13	–	–	16.6 ± 0.5	12.8 ± 0.3	1.0 ± 0.2
A370_650	0.547	F	-21.47 ± 0.11	235^{+38}_{-38}	$5.2^{+0.6}_{-0.6}$	12.6 ± 1.7	6.1 ± 1.0	4.7 ± 0.8
A370_555	0.378	C	-21.13 ± 0.17	248^{+11}_{-11}	$7.7^{+0.3}_{-0.3}$	30.3 ± 1.8	5.1 ± 0.9	4.9 ± 0.7
A370_319	0.305	F	-21.01 ± 0.19	98^{+41}_{-17}	$3.7^{+0.6}_{-0.6}$	8.7 ± 0.9	4.4 ± 0.3	1.1 ± 0.2
A370_39	0.325	F	-19.08 ± 0.17	99^{+12}_{-12}	$3.4^{+0.2}_{-0.2}$	54.4 ± 4.1	9.2 ± 1.0	10.1 ± 1.0
A370_50	0.682	F	-21.59 ± 0.04	–	–	48.0 ± 2.2	15.9 ± 1.0	15.3 ± 1.6
A370_401	0.346	F	-20.97 ± 0.15	182^{+19}_{-14}	$16.1^{+0.4}_{-1.9}$	17.0 ± 1.8	4.3 ± 0.8	1.6 ± 0.6
A370_210	0.230	F	-20.44 ± 0.03	49^{+6}_{-6}	$2.2^{+0.1}_{-0.2}$	36.9 ± 1.5	13.8 ± 0.4	6.7 ± 0.3
A370_283	0.421	F	-21.14 ± 0.08	–	–	47.3 ± 1.8	11.7 ± 0.8	31.6 ± 0.5
A370_400	0.384	C	-20.46 ± 0.10	–	–	26.8 ± 1.5	6.3 ± 0.6	7.2 ± 0.6
AC114_700	0.351	F	-20.20 ± 0.06	171^{+15}_{-14}	$4.2^{+0.5}_{-0.4}$	21.5 ± 2.1	5.9 ± 0.9	1.3 ± 0.8
AC114_930	0.306	C	-20.72 ± 0.08	82^{+17}_{-23}	$4.3^{+0.3}_{-0.2}$	13.7 ± 0.9	2.1 ± 0.3	1.6 ± 0.4
AC114_994	0.313	C	–	–	–	19.6 ± 1.8	7.4 ± 1.0	5.6 ± 0.8
AC114_1008	0.500	F	-23.02 ± 0.04	–	–	55.0 ± 2.1	16.6 ± 1.1	15.8 ± 0.6
AC114_906	0.312	C	-21.09 ± 0.08	–	–	12.2 ± 0.6	3.5 ± 0.2	4.8 ± 0.2
AC114_959	0.313	C	-21.26 ± 0.08	86^{+13}_{-15}	$3.0^{+0.6}_{-0.6}$	6.7 ± 0.9	4.4 ± 0.6	4.3 ± 0.2
CL0054_470	0.598	F	-21.35 ± 0.13	–	–	15.2 ± 1.9	5.1 ± 1.4	14.5 ± 0.7
CL0054_575	0.348	F	-20.02 ± 0.13	–	–	32.9 ± 2.8	4.6 ± 1.1	4.4 ± 0.7
CL0054_964	0.225	F	-19.08 ± 0.18	–	–	55.7 ± 2.4	9.9 ± 0.9	29.7 ± 0.6
CL0054_104	0.651	F	-22.31 ± 0.13	–	–	52.7 ± 0.9	19.0 ± 0.5	18.5 ± 0.3
CL0054_138	0.237	F	-21.84 ± 0.18	228^{+12}_{-12}	$11.8^{+0.5}_{-0.5}$	16.6 ± 1.1	2.4 ± 0.9	2.2 ± 0.3
CL0054_686	0.710	F	-21.68 ± 0.16	177^{+41}_{-41}	$3.2^{+0.1}_{-0.1}$	51.9 ± 2.5	15.0 ± 1.0	12.9 ± 0.6
CL0054_966	0.559	C	-21.06 ± 0.12	194^{+36}_{-36}	$2.5^{+0.4}_{-0.4}$	26.2 ± 1.8	22.7 ± 1.5	3.5 ± 1.6
CL0054_979	0.660	F	-21.18 ± 0.14	126^{+10}_{-9}	$3.4^{+0.2}_{-0.2}$	38.0 ± 1.9	9.9 ± 0.9	11.3 ± 1.1
CL0054_892	0.585	F	-22.11 ± 0.12	244^{+66}_{-66}	$4.5^{+0.5}_{-0.5}$	20.6 ± 0.9	9.8 ± 0.7	4.6 ± 0.3
CL0054_992	0.487	F	–	–	–	38.6 ± 0.5	19.6 ± 0.6	74.5 ± 2.5
CL0054_927	0.653	F	-21.20 ± 0.13	155^{+20}_{-20}	$4.6^{+0.1}_{-0.1}$	58.7 ± 1.8	21.1 ± 1.1	16.7 ± 1.4
MS0440_1131	0.318	F	-21.08 ± 0.26	168^{+11}_{-13}	$6.0^{+0.3}_{-0.3}$	35.2 ± 3.0	9.8 ± 1.0	7.6 ± 0.8
MS0440_849	0.401	F	-20.39 ± 0.22	114^{+14}_{-12}	$2.5^{+0.2}_{-0.2}$	75.7 ± 7.0	16.9 ± 1.2	34.8 ± 1.6

continued

Table 3.2 continued

ID	z	Mem.	M_B [mag]	$V_{\rm rot}$ [km s^{-1}]	$r_{\rm d,spec}$ [kpc]	W([OII]) [Å]	W(Hβ) [Å]	W([OIII]) [Å]
MS2053_735	0.588	C	-20.38 ± 0.10	–	–	63.8 ± 3.8	25.6 ± 2.7	16.2 ± 1.7
MS2053_741	0.335	F	-20.41 ± 0.07	$88\ ^{+7}_{-7}$	$3.5\ ^{+0.2}_{-0.2}$	45.4 ± 3.3	12.0 ± 1.0	10.3 ± 0.8
MS2053_675	0.460	F	-20.53 ± 0.06	–	–	56.8 ± 1.7	16.3 ± 0.8	20.7 ± 0.7
MS2053_534	0.599	F	-21.83 ± 0.12	–	–	12.6 ± 0.9	7.2 ± 1.0	1.1 ± 0.9
MS2053_998	0.196	F	-19.99 ± 0.18	$125\ ^{+5}_{-5}$	$4.0\ ^{+0.2}_{-0.2}$	42.0 ± 2.0	8.2 ± 0.4	9.5 ± 0.3
MS2053_844	0.335	F	-19.56 ± 0.04	–	–	63.7 ± 3.3	16.8 ± 1.0	19.8 ± 0.7
MS1054_F16	0.470	F	-21.62 ± 0.04	$180\ ^{+8}_{-8}$	$4.0\ ^{+0.4}_{-0.4}$	33.1 ± 1.0	12.1 ± 0.7	5.9 ± 0.4
C0016_P1_c1_05_A	0.551	C	-21.34 ± 0.10	–	–	12.0 ± 1.3	3.2 ± 1.0	4.1 ± 0.9
C0016_P1_c1_09_A	0.655	F	-21.79 ± 0.08	–	–	3.7 ± 4.2	2.7 ± 1.7	3.3 ± 3.7
C0016_P1_c2_00_A	0.286	F	-20.02 ± 0.17	–	–	4.9 ± 1.7	0.8 ± 0.5	1.1 ± 0.8
C0016_P1_c2_03_A	0.302	F	-19.61 ± 0.06	–	–	23.3 ± 2.7	4.3 ± 3.2	3.1 ± 1.0
C0016_P1_c2_07_A	0.658	F	-21.67 ± 0.13	–	–	30.5 ± 0.9	17.5 ± 1.1	9.3 ± 1.2
C0016_P2_c1_02_A	0.447	F	-21.26 ± 0.07	–	–	52.4 ± 1.0	15.3 ± 0.6	25.8 ± 0.8
C0016_P2_c1_04_A	0.388	F	-20.16 ± 0.08	–	–	13.4 ± 1.1	8.4 ± 0.8	2.2 ± 0.9
C0016_P2_c1_05_A	0.387	F	-20.22 ± 0.07	$149\ ^{+10}_{-11}$	$4.5\ ^{+0.3}_{-0.3}$	52.7 ± 2.0	14.3 ± 1.2	32.7 ± 1.4
C0016_P2_c1_09_A	0.554	C	-20.90 ± 0.09	–	–	7.6 ± 2.9	5.2 ± 1.3	3.2 ± 1.6
C0016_P2_c1_17_A	0.447	F	-20.14 ± 0.08	$210\ ^{+22}_{-20}$	$2.7\ ^{+0.1}_{-0.1}$	39.9 ± 2.3	13.7 ± 1.3	11.1 ± 3.1
C0016_P2_c1_19_A	0.350	F	-20.11 ± 0.09	–	–	46.4 ± 1.2	13.0 ± 0.8	17.0 ± 0.5
C0016_P2_c2_00_A	0.549	C	-22.28 ± 0.08	–	–	24.0 ± 0.9	4.1 ± 0.8	2.2 ± 0.5
C0016_P2_c2_13_A	0.550	C	-20.44 ± 0.11	$137\ ^{+37}_{-49}$	$4.6\ ^{+0.4}_{-0.5}$	19.6 ± 1.9	6.9 ± 1.2	5.3 ± 2.5
C0016_P2_c2_18_A	0.397	F	-20.97 ± 0.07	–	–	19.9 ± 0.7	10.2 ± 0.7	3.4 ± 0.3
M1621_P1_c1_01_A	0.476	F	-21.51 ± 0.07	–	–	28.4 ± 1.2	10.1 ± 0.6	7.3 ± 0.6
M1621_P1_c1_03_A	0.424	C	-21.15 ± 0.07	$213\ ^{+7}_{-8}$	$2.7\ ^{+0.2}_{-0.1}$	10.5 ± 1.0	4.9 ± 0.8	5.4 ± 0.4
M1621_P1_c2_09_A	0.345	F	-19.73 ± 0.06	–	–	21.7 ± 4.0	4.4 ± 3.2	1.9 ± 0.7
M1621_P2_c1_07_A	0.370	F	-20.15 ± 0.09	$144\ ^{+17}_{-15}$	$4.1\ ^{+0.3}_{-0.3}$	39.3 ± 2.8	9.4 ± 1.2	14.8 ± 1.3
M1621_P2_c2_04_A	0.422	C	-20.93 ± 0.09	–	–	63.2 ± 1.6	21.7 ± 1.0	19.6 ± 0.7
M1621_P2_c2_06_A	0.421	C	-20.75 ± 0.08	$216\ ^{+17}_{-20}$	$3.2\ ^{+0.3}_{-0.3}$	24.5 ± 1.6	7.9 ± 0.9	6.9 ± 0.7
M1621_P2_c2_11_A	0.429	C	-19.97 ± 0.08	–	–	14.1 ± 2.7	6.2 ± 1.5	3.3 ± 1.3
M2053_P1_c1_07_A	0.371	F	-20.56 ± 0.05	$188\ ^{+19}_{-20}$	$8.7\ ^{+0.8}_{-1.2}$	22.1 ± 1.9	5.1 ± 1.1	9.1 ± 1.1
M2053_P1_c1_10_A	0.464	F	-20.32 ± 0.14	–	–	13.1 ± 1.9	6.4 ± 1.0	3.4 ± 1.1
M2053_P1_c2_03_A	0.444	F	-21.12 ± 0.20	–	–	27.4 ± 1.2	10.1 ± 0.8	7.7 ± 0.6
M2053_P1_c2_09_A	0.397	F	-20.03 ± 0.08	$196\ ^{+10}_{-13}$	$4.2\ ^{+0.2}_{-0.3}$	14.3 ± 2.1	5.5 ± 1.2	2.2 ± 0.8

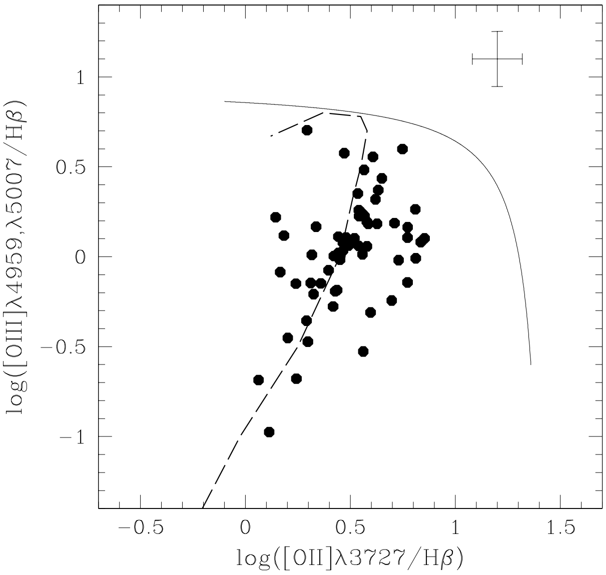

Figure 3.6. Diagnostic diagram of [OIII]/Hβ versus [OII]/Hβ for our EW sample of intermediate-redshift emission-line galaxies. The solid line shows the separation between starburst galaxies and AGNs proposed by Lamareille et al. (2004). The dashed line indicates the theoretical sequence of McCall et al. (1985), which fits local HII regions with metallicity increasing from right to left.

2000). A much larger study of these diagnostics has been performed recently by Lamareille et al. (2004), using emission-line galaxies drawn from the Two Degree Field Galaxy Redshift Survey (2dFGRS). We we use the equivalent width ratios of [OIII]/Hβ and [OII]/Hβ, as parametrized by Lamareille et al. (2004), to check for the presence of AGNs in our sample. Figure 3.6 shows the distribution of our EW sample of intermediate-redshift galaxies in this diagnostic diagram. The solid curve shows the demarcation line, separating starburst galaxies from AGN, of Lamareille et al. (2004). All the objects in our EW sample fall within the zone where starburst galaxies are located, indicating that in all of them the dominant source ionizing the interstellar gas is an episode of star formation.

The dashed line in figure 3.6 shows the theoretical sequence of McCall et al. (1985) for line ratios of HII galaxies as a function of metallicity, which provides a good fit to measurements of local HII galaxies. The track is interpreted as a metallicity-excitation sequence; along the track the metallicity is high at the lower left, i.e., for low excitation systems, and low at the upper right, i.e., for high excitation systems. Our intermediate-redshift emission-line galaxies define a continuous sequence, very consistent with that defined by local HII galaxies. Our sample contains objects with a wide variety of excitation levels, extending from those observed for local luminous galaxies to levels observed for faint and metal-poor dwarf galaxies at the present epoch. This also suggests that our sample contains both low- and high-metallicity systems. The agreement between our intermediate-redshift galaxies and local galaxies in this diagram suggests that other locally calibrated diagnostics, and physical quantities derived from them, will be valid for use with our sample. Note, however, that Shapley et al. (2005) find that this may not be the case for even more distant ($z \gtrsim 1$) galaxies.

To examine the chemical evolutionary status of our EW sample galaxies we can use an estimate of the metal content (metallicity) of their interstellar gas. Oxygen is the easiest metal to observe in the gas-phase, and traces the general metal content well. The abundance of oxygen species, relative to hydrogen, is traditionally expressed in the form $12 + \log(\mathrm{O/H})$.

The most reliable method of deriving the gas-phase oxygen abundances of galaxies requires an estimate of the electronic temperature and density of the ionized gas (Osterbrock 1989). However, an accurate determination of these parameters requires reliable measurements of temperature-sensitive auroral lines, usually the [OIII]λ4363 emission-line. The spectra considered here do not have sufficient signal-to-noise to measure these weak lines. However, by making a series of reasonable assumptions it is possible to obtain an accurate estimate of the oxygen abundance simply from measurements of [OII]λ3727, [OIII]λ4959, λ5007, and Hβ, as shown by Pagel et al. (1979). Furthermore, a combination of the [OII]λ3727 and [OIII]λ4959, λ5007 indicators is found to be rather insensitive to the geometry of the emitting region. This commonly used diagnostic ratio is defined as

$$\mathrm{R}_{23} = \frac{[\mathrm{OIII}]\lambda4959, \lambda5007 + [\mathrm{OII}]\lambda3727}{\mathrm{H}\beta}. \qquad (3.12)$$

At low-metallicities ($12 + \log(\mathrm{O/H}) \lesssim 8.2$) R_{23} increases with oxygen abundance, simply because the number of oxygen ions available to emit increases. However, by radiating the energy from collisions between the oxygen ions and free electrons, increased oxygen abundance enables the gas to cool more efficiently. This cooling reduces the rate of ion-electron collisions and consequent production of excited states, leading to a lower level of emission than would otherwise be expected from the number density of oxygen ions. The oxygen abundance has little effect on the number density of photons capable of ionising hydrogen, and thus Hβ is unaffected. For high-metallicities ($12 + \log(\mathrm{O/H}) \gtrsim 8.4$) R_{23} therefore decreases with increasing oxygen abundance. These two degenerate regimes are referred to as the metal-poor and metal-rich branches of the $12 + \log(\mathrm{O/H})$–R_{23} relation, which is illustrated in figure 3.7. At intermediate-metallicities ($8.2 \lesssim 12 + \log(\mathrm{O/H}) \lesssim 8.4$), galaxies may have a large range of metallicities for a narrow range of R_{23}. The uncertainties in this metallicity domain, i.e. whether an object with a given R_{23} parameter lies on the metal-poor branch or on the metal-rich branch of the relation, are therefore high. Note that the solar oxygen abundance is $12 + \log(\mathrm{O/H}) = 8.69$ (Allende Prieto et al. 2001).

A variety of abundance indicators may be used to break the $12 + \log(\mathrm{O/H})$–R_{23} degeneracy, e.g. [NII]/[OIII]λ4959 (Alloin et al. 1979), [NII]/[OII]λ3727 (McGaugh 1994), [NII]/Hα (van Zee et al. 1998; Denicoló et al. 2002). However, for our intermediate-redshift data we generally do not have Hα and [NII] in our spectral range. However, other studies have found that the majority of intermediate-redshift star-forming galaxies with $M_B \lesssim -20$, for which the R_{23}–$12 + \log(\mathrm{O/H})$ degeneracy has been broken, lie on the metal-rich branch of the $12 + \log(\mathrm{O/H})$–R_{23} calibration (Kobulnicky et al. 2003; Lilly et al. 2003; Kobulnicky & Kewley 2004; Maier et al. 2005). We therefore make the reasonable assumption that the luminous, star-forming intermediate-redshift galaxies in our sample also lie on the metal-rich branch. The alternative, that they lie on the metal-poor branch of the relation, would suggest improbably large evolutionary changes in the metallicities of massive galaxies since $z \sim 0.5$–1.0 (see Lilly et al. 2003; Ellison et al. 2005).

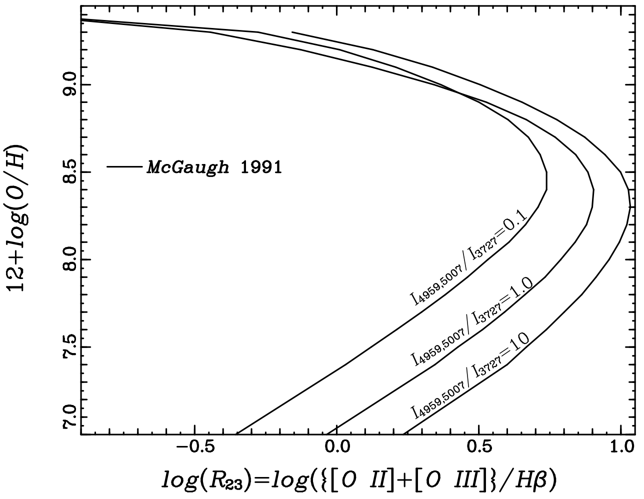

Figure 3.7. Oxygen abundance, $12 + \log(\mathrm{O/H})$, as a function of the logarithm of the parameter $\mathrm{R}_{23} = ([\mathrm{OIII}]\lambda4959, \lambda5007 + [\mathrm{OII}]\lambda3727) \,/\, \mathrm{H}\beta$, as calibrated by McGaugh (1991). Note that the relationship is double-valued, with a given R_{23} indicating two potential oxygen abundances. The dependence on the ionisation of the emitting gas, evalated using the ratio $\mathrm{O}_{32} = [\mathrm{OIII}]\lambda4959, \lambda5007 \,/\, [\mathrm{OII}]\lambda3727$ (denoted $I_{4959,5007}/I_{3727}$ in the plot), is illustrated by the multiple lines. This figure is adapted from Kobulnicky et al. (1999) figure 8.

Extensive studies have been dedicated to calibrating the relation between R_{23} and oxygen abundance (e.g., McCall et al. 1985; Pilyugin 2001), and now strong-line ratios can reliably estimate the oxygen abundance to within the accuracy of the model calibrations, approximately ±0.15 dex. As well as oxygen abundance, the R_{23} parameter is sensitive to the ionization of the emitting gas (e.g., Kewley & Dopita 2002), as this affects the number density of oxygen species with the appropriate ionisation level for emitting in the lines being considered, particularly at low metallicities. The correction of the ionisation dependence of R_{23} is usually done using the ionization-sensitive diagnostic ratio O_{32} (e.g., McGaugh 1991; Kewley & Dopita 2002), defined as

$$\mathrm{O}_{32} = \frac{[\mathrm{OIII}]\lambda4959, \lambda5007}{[\mathrm{OII}]\lambda3727}. \tag{3.13}$$

The dependence of the $12 + \log(\mathrm{O/H})$–R_{23} calibration on O_{32} is illustrated in figure 3.7.

While there may be some concerns about systematic errors in the use of R_{23} to measure oxygen abundances (e.g., Kennicutt et al. 2003), this is not a serious concern for our analysis, as our aim is to study *relative* changes in the oxygen abundance of star-forming galaxies with redshift and environment. The galaxy spectra analysed here are not flux-calibrated, so we use emission line equivalent widths to estimate both the R_{23} and O_{32} parameters, following the prescription of Kobulnicky & Phillips (2003). Using emission-line equivalent widths rather than fluxes has the advantage of being independent of the reddening correction, to first order. Generally the $[\mathrm{OIII}]\lambda4959$ emission-line is of low signal-to-noise. We thus use the theoretical ratio $[\mathrm{OIII}]\lambda5007/[\mathrm{OIII}]\lambda4959 = 3$ to estimate the $[\mathrm{OIII}]\lambda4959$ equivalent width (Osterbrock 1989). The oxygen abundace is then determined using the calibration of McGaugh (1991), as found in Kobulnicky et al. (1999). For the lower metallicity branch this calibration is,

$$\begin{aligned} 12 + \log(\mathrm{O/H}) = {} & 12 - 4.944 + 0.767x + 0.602x^2 \\ & - y\,(0.29 + 0.332x - 0.331x^2), \end{aligned} \tag{3.14}$$

and for the upper metallicity branch,

$$\begin{aligned} 12 + \log(\mathrm{O/H}) = {} & 12 - 2.939 - 0.2x - 0.237x^2 - 0.305x^3 - 0.0283x^4 \\ & - y\,(0.0047 - 0.0221x - 0.102x^2 - 0.0817x^3 - 0.00717x^4), \end{aligned} \tag{3.15}$$

where $x = \log \mathrm{R}_{23}$ and $y = \log \mathrm{O}_{32}$.

For four (one) of the field (cluster) galaxies in our intermediate-redshift EW sample, the oxygen abundance estimated using the metal-poor branch of the calibration was larger than the one derived using the metal-rich branch. Such an inconsistency may occur when R_{23} is larger than the maximum value predicted by the model grid used to calibrated the relation. These galaxies have been excluded from the sample. The oxygen abundances for the remaining galaxies are listed in table 3.3.

3.2.4 Star formation rates and extinctions

Observed star formation rates

The preferred indicator of star formation rate, at optical wavelengths, is Hα emission luminosity, as it is related to the star formation rate in a fairly straightforward manner, and usually very strong. However, at intermediate redshifts this line moves into the near-infrared. Therefore, for the galaxies in our intermediate-redshift EW sample, Hα is not available. The primary alternatives in the optical are Hβ and [OII]λ3727, both of which have additional complications. The measurement of Hβ emission is more significantly affected by the underlying stellar absorption line than is Hα, while [OII] displays a more complex behaviour as a function of the properties of the emitting gas. [OII] is generally brighter, and more easily measured, and so is used more often than Hβ at high-redshifts.

For the intermediate-redshift galaxies in our EW sample, we have sufficient signal-to-noise to measure both the Hβ and [OII]λ3727 lines. In addition, we have enough resolution to simultaneously fit the Hβ emission and absorption components for a subsample of the galaxies. This somewhat reduces the uncertainty due to this correction. We also have measurements of [OII], Hβ and [OIII], for all the galaxies, which allows us to account for metallicity variations in the [OII] star formation rate estimate.

The star formation rates of the galaxies in our sample can thus be measured using the luminosities of either the [OII]λ3727 or Hβ emission-lines, as determined in section 3.2.2.

The star formation rates from Hβ were calculated following the Hα calibration of Kennicutt et al. (1994), as advocated in Kennicutt (1998). Following Kobulnicky & Kewley (2004), we use the ratio $L_{\mathrm{H}\alpha}/L_{\mathrm{H}\beta} = 2.8$ (determined by Hummer & Storey 1987[2]), corresponding to the case B (Baker & Menzel 1938) recombination with a

---

[2] usefully summarised by D. L. DePoy at http://www-astronomy.mps.ohio-state.edu/~depoy/research/observing/hline.html

temperature of $T = 10^4$K and a density of $n_\mathrm{e} \sim 10^2$–$10^4\mathrm{cm}^{-2}$:

$$\mathrm{SFR}(\mathrm{H}\beta)_\mathrm{obs} = \frac{2.8\,L_{\mathrm{H}\beta}}{1.26\times 10^{41}}\ \mathrm{M}_\odot\,\mathrm{yr}^{-1}. \tag{3.16}$$

This calibration is usually applied assuming it is free from any dependence on metallicity or ionisation conditions (and hence gas temperature and electron density) over the range of conditions considered (e.g., Kobulnicky & Kewley 2004). It will, however, be affected by extinction due to dust within the observed galaxy, and hence be an underestimate of the true star formation rate. This extinction-uncorrected star-formation rate estimate is listed for the galaxies in our sample in table 3.3.

For star-forming galaxies with gas conditions similar to what is observed for our intermediate-redshift sample, the locally observed variation in the [OII]/Hα flux ratio is dependent upon extinction and metallicity, with little dependence on the ionisation conditions of the gas (Kewley et al. 2004; Mouhcine et al. 2005).

The star formation rate from [OII] was estimated using the calibration:

$$\mathrm{SFR}([\mathrm{OII}])_\mathrm{obs}\ (\mathrm{M}_\odot\,\mathrm{yr}^{-1}) = 7.9\times 10^{-42} L_{[\mathrm{OII}]}\ (\mathrm{erg\ s}^{-1})\times \mathrm{f(O/H)} \tag{3.17}$$

where $L_{[\mathrm{OII}]}$ is the observed [OII] luminosity, and f(O/H) is a correction factor introduced by Kewley et al. (2004) to account for the effect of metallicity on the [OII]/Hα flux ratio, $\mathrm{f(O/H)} = 1/\big[-2.29\big(12+\log(\mathrm{O/H})\big)+21.21\big]$. Again, this star formation rate determination is an underestimate of the true star formation rate, as it has not yet been corrected for extinction.

Reddening and extinction corrections

The standard way to determine the amount of extinction affecting emission-line luminosity measurements, and thus star formation rate estimates, is to use the Balmer decrement, i.e. the ratio of $L_{\mathrm{H}\alpha}/L_{\mathrm{H}\beta}$ in excess of that expected given atomic physics and the estimated temperature and electron density of the emitting gas. However, we do not have Hα available for the galaxies in our intermediate-redshift sample, so cannot apply this method.

An alternative, suggested by Mustapha Mouhcine, is to compare the energy balance between the luminosities of two different star formation indicators that are free from systematic effects other than dust reddening, i.e., that do not depend on metallicity or ionisation conditions of the emitting gas. These indicators are provided by the extinction uncorrected star formation rates from Hβ and [OII], as derived above. The colour excess $E(B-V)$ can then be estimated using the relation:

$$E(B-V) = \frac{2.5}{\kappa(\mathrm{H}\beta)-\kappa([\mathrm{OII}])}\log\left(\frac{\mathrm{SFR}([\mathrm{OII}])_\mathrm{obs}}{\mathrm{SFR}(\mathrm{H}\beta)_\mathrm{obs}}\right) \tag{3.18}$$

where $\kappa(\lambda)$ is the absolute extinction per unit colour excess at wavelength λ.

The colour excess so determined can be converted into an extinction at a given wavelength, $A(\lambda)$, using $A(\lambda) = \kappa(\lambda)\ E(B-V)$. For both of these steps $\kappa(\lambda)$ is derived from the extinction law of Cardelli et al. (1989), with $\kappa(V) = R_V = 3.1$, as observed for the Milky Way's diffuse interstellar medium. Since a negative colour excess is unphysical, we assume that galaxy properties that give rise to $E(B-V) < 0$ correspond to zero extinction. The estimated colour excess for our intermediate redshift star-forming galaxies are listed in the last column of table 3.3.

The observed star formation rates described above can now be corrected for extinction, using

$$\mathrm{SFR(H\beta)_{cor}} = \mathrm{SFR(H\beta)_{obs}} \times 10^{0.4\,E(B-V)\,\kappa(\mathrm{H}\beta)}, \tag{3.19}$$

where $\kappa(\mathrm{H}\beta) = 3.61$ from equation 3 of Cardelli et al. (1989).

Table 3.3. Quantities derived from emission-line measurements for galaxies in our EW sample. Columns are ID, ionisation sensitive parameter (O_{32}), metallicity sensitivity parameter (R_{23}), oxygen abundance ($12 + \log(O/H)$), observed star formation rate derived from Hβ ($SFR(H\beta)_{obs}$), and colour excess ($E(B-V)$.

ID	O_{32}	R_{23}	$12 + \log(O/H)$	$SFR(H\beta)_{obs}$	$E(B-V)$ [mag]
A370_679	0.08 ± 0.02	1.40 ± 0.05	9.024 ± 0.004	9.23 ± 0.23	0.12 ± 0.04
A370_650	0.48 ± 0.10	3.08 ± 0.59	8.857 ± 0.059	2.62 ± 0.42	0.44 ± 0.25
A370_555	0.21 ± 0.03	7.17 ± 1.28	8.414 ± 0.212	1.62 ± 0.28	0.00 ± 0.31
A370_319	0.17 ± 0.03	2.31 ± 0.25	8.925 ± 0.019	1.24 ± 0.08	0.23 ± 0.13
A370_39	0.24 ± 0.03	7.35 ± 0.93	8.404 ± 0.151	0.44 ± 0.05	0.00 ± 0.22
A370_50	0.41 ± 0.05	4.26 ± 0.34	8.733 ± 0.046	7.68 ± 0.50	0.00 ± 0.12
A370_401	0.12 ± 0.05	4.42 ± 0.94	8.677 ± 0.156	1.18 ± 0.22	0.09 ± 0.34
A370_210	0.23 ± 0.01	3.31 ± 0.16	8.819 ± 0.020	2.32 ± 0.07	0.07 ± 0.07
A370_283	0.87 ± 0.04	7.56 ± 0.52	8.469 ± 0.071	3.73 ± 0.24	0.21 ± 0.12
A370_400	0.35 ± 0.04	5.73 ± 0.61	8.582 ± 0.093	1.08 ± 0.10	0.00 ± 0.18
AC114_700	0.08 ± 0.04	3.93 ± 0.70	8.722 ± 0.119	0.79 ± 0.12	0.00 ± 0.28
AC114_930	0.15 ± 0.04	7.44 ± 1.29	–	–	–
AC114_994	0.37 ± 0.06	3.62 ± 0.55	8.795 ± 0.069	–	–
AC114_1008	0.37 ± 0.02	4.55 ± 0.32	8.701 ± 0.045	9.68 ± 1.89	0.00 ± 0.11
AC114_906	0.51 ± 0.03	5.25 ± 0.29	8.645 ± 0.041	1.07 ± 0.05	0.14 ± 0.09
AC114_959	0.84 ± 0.12	2.81 ± 0.46	8.892 ± 0.036	1.56 ± 0.23	0.51 ± 0.22
CL0054_470	1.24 ± 0.16	6.64 ± 1.88	8.566 ± 0.239	1.99 ± 0.55	0.62 ± 0.46
CL0054_575	0.17 ± 0.03	8.38 ± 2.11	–	–	–
CL0054_964	0.69 ± 0.03	9.48 ± 0.86	–	–	–
CL0054_104	0.46 ± 0.01	4.04 ± 0.12	8.759 ± 0.015	7.71 ± 0.46	0.11 ± 0.04
CL0054_138	0.17 ± 0.02	8.03 ± 3.02	–	–	–
CL0054_686	0.32 ± 0.02	4.59 ± 0.35	8.692 ± 0.051	7.84 ± 0.53	0.02 ± 0.12
CL0054_966	0.17 ± 0.08	1.36 ± 0.15	9.029 ± 0.013	6.74 ± 0.44	0.21 ± 0.11
CL0054_979	0.39 ± 0.04	5.34 ± 0.52	8.624 ± 0.078	3.26 ± 0.29	0.03 ± 0.16
CL0054_892	0.29 ± 0.02	2.72 ± 0.21	8.887 ± 0.020	7.59 ± 0.53	0.12 ± 0.10
CL0054_992	2.51 ± 0.09	6.91 ± 0.28	8.587 ± 0.032	–	–
CL0054_927	0.37 ± 0.03	3.80 ± 0.23	8.777 ± 0.030	7.13 ± 0.37	0.08 ± 0.09
MS0440_1131	0.28 ± 0.04	4.62 ± 0.58	8.684 ± 0.086	2.95 ± 0.30	0.17 ± 0.20
MS0440_849	0.60 ± 0.06	7.14 ± 0.67	8.481 ± 0.097	2.72 ± 0.19	0.00 ± 0.17

continued

Table 3.3 continued

ID	O_{32}	R_{23}	$12 + \log(O/H)$	$SFR(H\beta)_{obs}$	$E(B-V)$ [mag]
MS2053_735	0.33 ± 0.04	3.31 ± 0.39	8.825 ± 0.046	4.07 ± 0.43	0.00 ± 0.16
MS2053_741	0.29 ± 0.03	4.91 ± 0.50	8.655 ± 0.075	1.96 ± 0.16	0.00 ± 0.17
MS2053_675	0.47 ± 0.02	5.13 ± 0.26	8.653 ± 0.037	2.98 ± 0.14	0.01 ± 0.08
MS2053_534	0.12 ± 0.09	1.95 ± 0.34	8.963 ± 0.016	4.33 ± 0.59	0.14 ± 0.17
MS2053_998	0.29 ± 0.02	6.63 ± 0.40	8.485 ± 0.063	0.91 ± 0.04	0.08 ± 0.11
MS2053_844	0.40 ± 0.02	5.32 ± 0.36	8.628 ± 0.053	1.26 ± 0.07	0.05 ± 0.11
MS1054_F16	0.23 ± 0.02	3.37 ± 0.21	8.812 ± 0.026	5.99 ± 0.34	0.00 ± 0.09
C0016_P1_c1_05_A	0.45 ± 0.11	5.34 ± 1.78	8.630 ± 0.257	1.24 ± 0.39	0.21 ± 0.53
C0016_P1_c1_09_A	1.16 ± 1.85	3.01 ± 3.07	8.878 ± 0.253	1.53 ± 0.98	0.83 ± 1.45
C0016_P1_c2_00_A	0.28 ± 0.23	8.24 ± 5.78	–	–	–
C0016_P1_c2_03_A	0.17 ± 0.06	6.31 ± 4.68	8.489 ± 0.787	0.34 ± 0.25	0.00 ± 1.26
C0016_P1_c2_07_A	0.40 ± 0.05	2.43 ± 0.18	8.921 ± 0.013	9.08 ± 0.56	0.11 ± 0.08
C0016_P2_c1_02_A	0.64 ± 0.02	5.63 ± 0.24	8.619 ± 0.034	5.44 ± 0.22	0.03 ± 0.07
C0016_P2_c1_04_A	0.22 ± 0.08	1.94 ± 0.26	8.968 ± 0.008	1.09 ± 0.10	0.14 ± 0.13
C0016_P2_c1_05_A	0.81 ± 0.04	6.65 ± 0.57	8.541 ± 0.077	1.97 ± 0.16	0.05 ± 0.14
C0016_P2_c1_09_A	0.55 ± 0.34	2.27 ± 0.88	8.940 ± 0.045	1.32 ± 0.33	0.69 ± 0.47
C0016_P2_c1_17_A	0.36 ± 0.10	3.98 ± 0.51	8.758 ± 0.070	1.75 ± 0.17	0.00 ± 0.18
C0016_P2_c1_19_A	0.48 ± 0.02	5.29 ± 0.34	8.638 ± 0.049	1.61 ± 0.10	0.00 ± 0.10
C0016_P2_c2_00_A	0.12 ± 0.03	6.62 ± 1.34	8.434 ± 0.240	3.67 ± 0.73	0.00 ± 0.35
C0016_P2_c2_13_A	0.35 ± 0.17	3.83 ± 0.85	8.773 ± 0.114	1.16 ± 0.20	0.10 ± 0.30
C0016_P2_c2_18_A	0.22 ± 0.02	2.39 ± 0.17	8.919 ± 0.013	2.78 ± 0.18	0.12 ± 0.08
M1621_P1_c1_01_A	0.33 ± 0.03	3.77 ± 0.25	8.778 ± 0.033	4.50 ± 0.25	0.09 ± 0.09
M1621_P1_c1_03_A	0.66 ± 0.08	3.61 ± 0.64	8.811 ± 0.071	1.56 ± 0.26	0.49 ± 0.25
M1621_P1_c2_09_A	0.11 ± 0.05	5.54 ± 4.22	8.549 ± 0.738	0.38 ± 0.28	0.15 ± 1.29
M1621_P2_c1_07_A	0.49 ± 0.05	6.21 ± 0.89	8.553 ± 0.130	1.21 ± 0.16	0.24 ± 0.24
M1621_P2_c2_04_A	0.40 ± 0.02	4.09 ± 0.20	8.750 ± 0.026	5.71 ± 0.25	0.00 ± 0.07
M1621_P2_c2_06_A	0.36 ± 0.04	4.23 ± 0.55	8.733 ± 0.075	1.76 ± 0.21	0.09 ± 0.19
M1621_P2_c2_11_A	0.30 ± 0.13	2.98 ± 0.87	8.859 ± 0.093	0.67 ± 0.16	0.09 ± 0.38
M2053_P1_c1_07_A	0.53 ± 0.08	6.59 ± 1.47	8.523 ± 0.213	0.96 ± 0.20	0.19 ± 0.37
M2053_P1_c1_10_A	0.34 ± 0.12	2.75 ± 0.56	8.886 ± 0.052	0.96 ± 0.15	0.13 ± 0.25
M2053_P1_c2_03_A	0.37 ± 0.03	3.70 ± 0.34	8.787 ± 0.043	3.17 ± 0.26	0.14 ± 0.13
M2053_P1_c2_09_A	0.20 ± 0.08	3.14 ± 0.81	8.835 ± 0.099	0.63 ± 0.14	0.03 ± 0.35

Chapter 4

Field results

The analysis and results described in this chapter which relate to the Tully-Fisher relation have been presented previously in Bamford et al. (2006). Most of this work was directly performed by the author, with advice from Alfonso Aragón-Salamanca and Bo Milvang-Jensen. Ideas and technical assistance in determining the implications of our results for the star formation evolution of massive star-forming galaxies were provided by Alfonso Aragón-Salamanca.

The work based on the spatially integrated spectral measurements is presented in Mouhcine et al. (2006b), and was principally done in collaboration with Mustapha Mouhcine. Note that despite not being first author of Mouhcine et al. (2006b), the author of this thesis played a very significant role in determining the content of this paper.

4.1 Overview

The data used in this thesis was primarily observed in order to examine the differences between cluster and field galaxies at intermediate redshift, particularly using the Tully-Fisher relation. However, the field sample, which was observed for comparison with the cluster sample, is useful by itself for investigating the evolution of bright, star-forming, field galaxies with redshift. We investigate this in two ways: using the Tully-Fisher relation to measure changes in luminosity at a given rotation velocity, and by comparing the distribution of various spectral diagnostics, including metallicity and star formation rate, to a local sample.

Through these studies we aim to shed further light on the picture described in section 1.2 of the introduction. In particular, by using the Tully-Fisher relation to trace changes in the luminosity of galaxies as a function of rotation velocity, a proxy for mass, we aim to determine the degree of luminosity, and hence star formation, evolution in individual star-forming disc galaxies since $z \sim 1$. This can improve our understanding of the mechanisms responsible for the observed rapid decline in star-formation since this time (e.g., Lilly et al. 1996; Heavens et al. 2004).

By considering the star formation properties and metallicities of these galaxies, we can gain further insight into their star formation histories. In addition, as our sample is known to be mostly comprised of massive, large galaxies, we can test whether the wide variety of properties observed for distant galaxies by, e.g., Lilly et al. (2003) and Maier et al. (2005), are due to variations over a range of masses or differences between galaxies of similar mass.

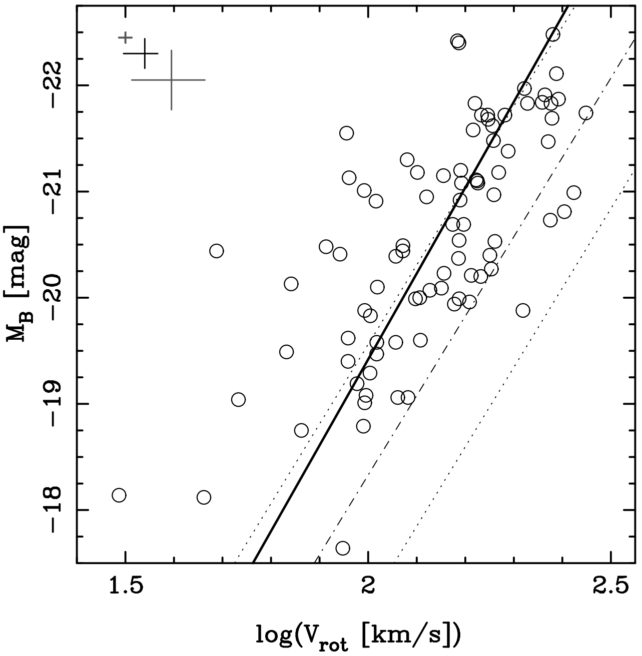

Figure 4.1. The Tully-Fisher relation for our full field TFR sample. The fiducial local relation of Pierce & Tully (1992) is marked by the dot-dashed line, with its 3σ intrinsic scatter delimited by dotted lines. A weighted least-squares fit to all the points is shown by the solid line, see the text for details. The error bars in the top left corner indicate the 10th-, 50th- and 90th-percentiles of the (broadly unimodal) distribution of uncertainties on the displayed points.

4.2 Tully-Fisher relation

4.2.1 Basic fit

The Tully-Fisher relation for our sample of 89 distant field galaxies is shown in figure 4.1. The solid line is an 'inverse' fit to the data,

$$\log V_{\rm rot} = a + bM_B \tag{4.1}$$

found by minimising the weighted squared deviations in $\log V_{\rm rot}$. The weights applied to each point are

$$w_i = 1/\sigma_i^2 \quad \text{, where} \quad \sigma_i^2 = \sigma_{\log V_{\rm rot},i}^2 + b^2\sigma_{M_B,i}^2 + \sigma_{\rm int}^2. \tag{4.2}$$

Here $\sigma_{\log V_{\rm rot},i}$ and $\sigma_{M_B,i}$ are the errors on each point derived from the reduction process, and $\sigma_{\rm int}$ is the intrinsic scatter of the TFR, which is allowed to vary such that the reduced chi-squared statistic, $\chi_{\rm r}^2$, is unity. This was achieved by iteration, each time recalculating the weights using the new value of b, and $\sigma_{\rm int}$ determined via the recurrence relation

$$\sigma_{{\rm int},j+1}^2 = \sigma_{{\rm int},j}^2\, \chi_{\rm r}^{2\alpha} \; ; \quad \text{with } \alpha > 0, \tag{4.3}$$

where, as usual for two degrees of freedom, the reduced-chi-squared statistic is

$$\chi_{\mathrm{r}}^2 = \frac{\chi^2}{n-2}, \quad \chi^2 = \sum_i \left(\frac{\log V_{\mathrm{rot}i} - a - bM_{B,i}}{\sigma_i} \right)^2 . \tag{4.4}$$

The (weighted) total scatter, σ_{total}, is calculated by

$$\sigma_{\mathrm{total}}^2 = \sum_i w_i \left(\log V_{\mathrm{rot}i} - a - bM_{B,i}\right)^2 \Bigg/ \sum_i w_i \; . \tag{4.5}$$

Notice that when χ_{r}^2 is at the desired value of unity, the σ_{int}^2 recurrence relation (equation 4.3) reduces to $\sigma_{\mathrm{int},j+1}^2 = \sigma_{\mathrm{int},j}^2$, as we would want. When $\chi_{\mathrm{r}}^2 > 1$ this implies σ_{int}^2 is too small, and thus it is increased for the next iteration. Alternatively, when $\chi_{\mathrm{r}}^2 < 1$ this implies σ_{int}^2 is too large, and it is therefore decreased for the next iteration. The value of α may be tuned to minimise the number of iterations before convergence is achieved; $\alpha = \frac{2}{3}$ was found to work well.

The fit converges in ~ 4 iterations to give the TFR (converted back into the more traditional 'forward' form):

$$M_B = (-8.1 \pm 0.8) \cdot \log V_{\mathrm{rot}} \; + \; (-3.2 \pm 2.0) \tag{4.6}$$

with $\sigma_{\mathrm{total}} = 1.0$ mag and $\sigma_{\mathrm{int}} = 0.9$ mag.

The 'inverse' fit is often used to avoid a potential bias because of the apparent magnitude-limited nature of a TFR sample. At faint apparent magnitudes, points are preferentially selected above the real TFR. For samples over a narrow range of distance moduli, e.g., in local cluster studies, the nature of this bias is to cause an apparent flattening of the TFR slope. While the dependence of V_{rot} on M_B still causes an effect, Willick (1994) has shown that using an 'inverse' fit reduces the bias by a factor of five compared with the conventional 'forward' fit. As this study covers a wide range of distance moduli, apparently faint galaxies are found over the whole range of absolute magnitude, depending on their redshift. Any bias on the best-fitting TFR should therefore be weakened, and take the form of an intercept shift rather than a flattening of the slope. This is particularly true given the more random priority-based, rather than magnitude-based, selection. However, to minimise any such effect, and allow us to confidently use the same fitting method to compare differently selected samples, we choose to work with the 'inverse' fit.

We weight our fit to make full use of the data, and avoid the influence of unreliable points, while the inclusion of an intrinsic scatter term prevents points with small errors from dominating the fit, and allows us to estimate this useful parameter.

The thin lines in figure 4.1 indicate a fiducial local field TFR. This is derived from the TFR of Pierce & Tully (1992, hereafter PT92), with a zero-point adjustment because PT92, while otherwise using the internal extinction correction of Tully & Fouque (1985), do not include the 0.27 mag of face-on extinction that is applied to our data. The fiducial PT92 TFR, adapted to our internal extinction correction, is thus:

$$M_B^{\mathrm{PT92}}(V_{\mathrm{rot}}) = -7.48 \log V_{\mathrm{rot}} - 3.37 \; . \tag{4.7}$$

PT92 obtained this relation by an 'inverse' least-squares fit, minimising the residuals in rotation velocity. This is the same method we have used to fit our TFR, except that our fit is weighted and includes the intrinsic scatter in these weights. The weighting should not cause any bias, and hence our fitting method is comparable to that used to produce the fiducial TFR of PT92.

There is clearly a significant offset between the TFRs of PT92 and this study. This may not be entirely an evolutionary effect, and some part of it is likely due to the different manner in which we measure the rotation velocities and magnitudes compared with PT92. Note that in generating the fiducial relation we have assumed that $V_{\mathrm{rot}} = 0.5W_R^i$, where W_R^i is the fully-corrected HI velocity width measured by PT92.

A further issue is whether or not the absolute calibration of the PT92 TFR is correct. This is based upon Cepheid and RR Lyrae distances to six local calibrator galaxies, and hence dependent upon the calibration of the whole extra-galactic distance scale at the time. There is also the issue of how representative this small number of local calibrator galaxies are compared with the whole PT92 TFR sample. Pierce (1994, hereafter P94) uses the PT92 TFR to calibrate supernovae distances and derive $H_0 = 86 \pm 7\ \mathrm{km\,s^{-1}\ Mpc^{-1}}$. If, as is suggested, the primary cause of uncertainty in this value is the absolute TFR calibration, then we could potentially use the modern, significantly more accurate, value of H_0 to correct this. We could therefore derive a more accurate TFR absolute calibration by using our cosmologically measured H_0, a reversal of the traditional method.

The current best estimate of H_0 is provided by a combination of data from WMAP and a number of other surveys: $H_0 = 71\,^{+4}_{-3}\ \mathrm{km\,s^{-1}\ Mpc^{-1}}$ (Spergel et al. 2003). The difference in distance modulus between this H_0 and that derived by P94 is 0.5 ± 0.1 mag, in the sense of moving the TFR to brighter magnitudes. The errors given only include those on the WMAP H_0 measurement, as the P94 errors are dominated by the uncertainty on the distance scale, which we are replacing. It can therefore be argued that a correction of -0.5 mag should be applied to the intercept of the PT92 TFR.

Fortunately in this study the uncertainty on the intercept of the fiducial local TFR is of little concern. Our sample covers a wide range in redshift, selected and analysed in a homogeneous manner. We can therefore examine the TFR evolution using only this study's data, without recourse to external work.

In future studies it may be wise to consider using the more recent B-band TFR of Tully & Pierce (2000) as a comparison. This relation has an absolute calibration based on Cepheid distances to 24 galaxies and implies a value of $H_0 = 77 \pm 8$, more consistent with the WMAP result. The work of Verheijen (2001) provides another more recent local comparison TFR, which has already been used by some groups. However, these studies use the internal extinction correction scheme of Tully et al. (1998), which has a strong dependency upon galaxy luminosity (or alternatively V_{rot}). While this form of the internal extinction should be more accurate, it will require care as the dependency on luminosity (or V_{rot}) is calibrated locally, and may not be valid for distant galaxies.

The internal scatter we measure, $\sigma_{\mathrm{int}} = 0.90$ mag, is considerably larger than the ~ 0.4 mag generally found for local samples (e.g., Pierce & Tully 1992; Dale et al. 1999). However, most local studies are focused upon using the TFR as a distance indicator. They therefore impose very strict selection criteria, e.g., requiring undisturbed late-type spirals, in an effort to produce as strong a correlation as possible. Kannappan et al. (2002) give a detailed discussion of the sources of scatter in the local TFR. At high redshift we do not have the luxury of abundant data, and so cannot impose strict selection criteria. For example, it is harder to identify galaxies with slightly disturbed rotation curves and morphologies, making rejection of such objects impossible. In addition, corrections for known, locally-calibrated correlations, e.g., between TFR intercept and morphological type, are often applied to local samples. However, such corrections are not yet calibrated at high-redshift and so cannot be applied to our data. The variations caused by minor disturbances, differing sample selection, and varying corrections may be responsible for the entire increase in intrinsic scatter. However, physical effects, such as an increased stochasticity of star-formation, may also contribute.

4.2.2 TFR evolution with redshift

The slope of the TFR we measure for the whole field galaxy sample is very similar to that found locally by PT92, and consistent within our errors. Note that we have used a comparable fitting method to PT92, so this statement is valid. The precise slope measured is very much dependent on the fitting method employed, and may explain why some studies find apparently different slopes. Our fit suggests there is little change in the TFR slope with redshift. We can attempt to evaluate this further by fitting redshift sub-samples of our data.

As noted above, any difference in intercept between our sample and the local relation of PT92 may not be a real effect. However, by fitting redshift sub-samples we may investigate any evolution of this offset purely within our own sample.

In order to examine the intercept evolution we divide the sample in to five bins, each of 18 points (17 for the highest redshift bin). The TFR is fit for each bin using the usual method, but with the slope constrained to the PT92 value (and hence very similar to the value for our whole sample) to isolate the changes in intercept. In panel (a) of figure 4.2 we plot these results, as the M_B value of the best-fitting TFR at the median $V_{\rm rot}$ of the full sample. Also plotted is a conventional weighted least-squares fit to the points. There is reasonably clear evidence for a brightening of the TFR intercept with redshift of ~ 1 mag by $z = 1$, corresponding to a factor of ~ 2.5 in luminosity at a fixed rotation velocity.

At high redshift, however, we only sample the bright end of the galaxy luminosity function, and hence preferentially select objects which have been brightened. In particular we require a certain emission line flux to measure $V_{\rm rot}$, and hence the limiting emission-line luminosity of our sample will increase with redshift. As emission line luminosity increases with SFR, we will therefore sample galaxies with higher SFR at higher redshifts, which in turn implies brighter B-band magnitudes for the high-redshift galaxies. The evolution of the TFR intercept that we measure is therefore probably an upper limit on the true brightening.

To investigate any evolution in the TFR slope we divide the full sample into only three redshift bins, as the slope requires more points to constrain it. Each bin thus contains 30 points (29 for the highest redshift bin). A TFR was fit to each sub-sample in the same way as for the full sample, and the results are shown in panel (b) of figure 4.2. Due to the small numbers of points in each bin, the errors on the slope are quite large. Given these errors, and the restricted M_B range of the data in the highest redshift bin, no strong constraints can be inferred. However, the slope in each bin is consistent with no evolution of this parameter with redshift.

In order to further investigate changes in the intercept of the TFR via the offsets

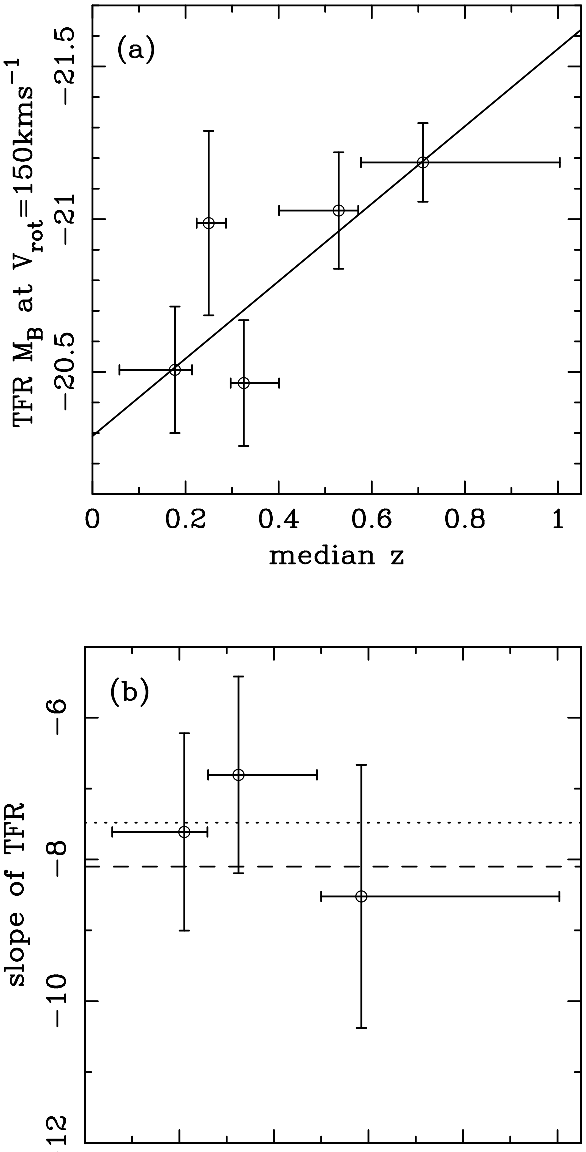

Figure 4.2. Plots showing the evolution of the slope and intercept of the best-fitting TFR in several redshift bins, indicated by the horizontal error bars. Panel (a) gives the intercept (at the median V_{rot} of the full sample) for TFR fits to five redshift subsamples of the data. Each redshift bin contains ~ 18 points. The line shows a weighted least-squares fit to the points. For these fits the slope was held fixed to the PT92 value. Panel (b) plots the slope for TFR fits to three redshift subsamples of the data. Each redshift bin contains $\sim$30 points. The horizontal lines show the local TFR slope of PT92 (dotted) and the slope from equation 4.6, the fit to our whole field TFR sample (dashed).

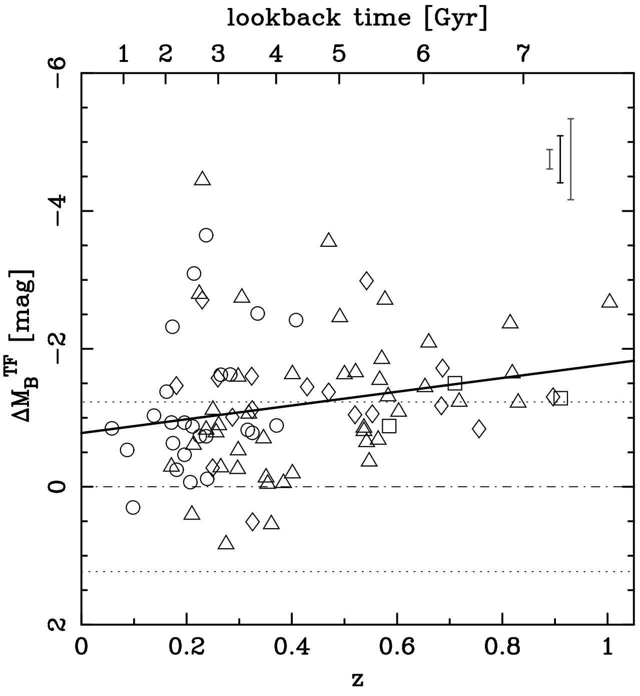

Figure 4.3. The residuals, $\Delta M_B{}^{\rm TF}$, from the fiducial PT92 TFR plotted against redshift and look-back time. Galaxies with $\mu_{R,\rm eff,abs} < -20.0$ are denoted by squares, those with $-20.0 < \mu_{R,\rm eff,abs} < -18.0$ are shown by triangles, circles denote those with $\mu_{R,\rm eff,abs} > -18.0$, and galaxies with no $\mu_{R,\rm eff,abs}$ measurement (i.e., those from the supplementary MS1054 data) are indicated by diamonds. The fiducial local relation of PT92 is again marked by the thin dot-dashed and dotted lines. A weighted least-squares fit to all the points is shown by the solid line, see the text for details. The error bars in the top right corner indicate the 10th-, 50th- and 90th-percentiles of the (broadly unimodal) distribution of uncertainties on the displayed points.

of individual galaxies, it is helpful to work with the residuals from the fiducial TFR:

$$\begin{aligned}\Delta M_B{}^{\rm TF} &= M_B - M_B^{\rm PT92}(V_{\rm rot}) \\ &= M_B - (-7.48 \log V_{\rm rot} - 3.37)\ . \end{aligned} \qquad (4.8)$$

We can evaluate an evolution of the TFR with redshift by looking at a plot of these residuals versus redshift, as shown in figure 4.3. A trend in $\Delta M_B{}^{\rm TF}$ with redshift, such that more distant galaxies are brighter for a given rotation velocity, is apparent. Fitting the data in a similar manner to that described for the TFR in section 4.2.1 (minimising residuals in $\Delta M_B{}^{\rm TF}$) produces the relation

$$\Delta M_B{}^{\rm TF} = (-1.0 \pm 0.5) \cdot z + (0.8 \pm 0.2)\ \rm mag \qquad (4.9)$$

with $\sigma_{\rm total} = 0.9$ mag and $\sigma_{\rm int} = 0.8$ mag. This is in good agreement with the more qualitative result from figure 4.2. Once again, however, this is most likely an upper limit on the true luminosity evolution experienced by giant spirals in the field, due to our preferential selection of the brightest objects at high redshift.

The luminosity evolution we find from consideration of the TFR is also in agreement with a simple comparison of the luminosity function of our field sample with that observed locally, as shown later in section 4.3.2.

In figure 4.3 there is clearly some asymmetric scatter to brighter offsets, which decreases with redshift. This may be due, at least in part, to the fact that there is a larger scatter in the TFR around $V_{\rm rot} \sim 100$ km s^{-1}. Only brighter galaxies, and hence those with $V_{\rm rot} \gtrsim 150$ km s^{-1} and thus lower TFR scatter, are observed at high redshifts. However, this does not seem able to account for the whole effect, and there is a hint that this reduction in scatter with redshift is real.

The points in figure 4.3 are shown using different symbols depending upon absolute surface brightness, $\mu_{R,\rm eff,abs}$. There appears to be no obvious difference in the $\Delta {M_B}^{\rm TF}$ distribution of high and low surface brightness galaxies at a given redshift. This argues against the variation in scatter being simply a consequence of sampling different surface brightness ranges at different redshifts. It also implies that the varying surface brightness selection function has relatively small impact on the evolution we measure.

As mentioned in the previous section, there is a systematic offset between our TFR and that of PT92, even when the evolution with redshift is taken into account (as indicated by the zero-point of equation 4.9 being inconsistent with zero). The earlier discussion of the uncertainties in the intercept of the PT92 TFR also applies here. Note that the 'cosmological' correction of −0.5 mag suggested in section 4.2.1 would bring the zero-points into much closer agreement. In addition, there are a variety of other possible explanations for the offset. For example, the asymmetric scatter to brighter M_B for a given $V_{\rm rot}$, seen particularly at lower redshifts, may influence the fit away from the PT92 relation. This scatter may be due to galaxies that would not have been included in the PT92 sample, for example due to interactions, or that are less prevalent locally. A more rapid evolution in the past ∼2 Gyr, which is not well constrained by our data, could also be responsible.

4.2.3 Comparison with other studies

The primary work with which we compare is that of Böhm et al. (2004, hereafter B04). This is a similar study of field spirals between $0.1 \lesssim z \lesssim 1$ with 36 'high quality' and 41 'low quality' rotation velocity measurements. The internal extinction correction applied is the same as in this paper. In figure 4.4 we plot our data together with those of B04[1]. We also plot TFR fits to our data and their 'high quality' and full samples. Our fit to the B04 'high-quality' data is

$$M_B = (-9.5 \pm 2.3) \cdot \log V_{\rm rot} \ + \ (0.2 \pm 5.1) \tag{4.10}$$

with $\sigma_{\rm total} = 1.2$ mag and $\sigma_{\rm int} = 1.0$ mag, while for their full sample we obtain

$$M_B = (-6.4 \pm 0.7) \cdot \log V_{\rm rot} \ + \ (-6.7 \pm 2.3)\ . \tag{4.11}$$

with $\sigma_{\rm total} = 1.0$ mag and $\sigma_{\rm int} = 0.8$ mag. Our Tully-Fisher relations are thus in reasonable agreement. This is surprising since we see no evidence for a flattening of the TFR slope, particularly when considering only the 'high-quality' data, while B04 claim to see a strikingly shallow slope. This may be in some part due to their interpretation of the correlation between $\Delta {M_B}^{\rm TF}$ and $V_{\rm rot}$, which is potentially entirely due to correlated errors rather than any underlying physical effect, as we will show in section 4.3. They also use a different method of fitting the TFR, a bisector fit. This may be more easily biased to flatter slopes, by the effect of TFR scatter combined with restrictions on the magnitude range, than our purely inverse

---

[1] obtained from the CDS catalogue archive

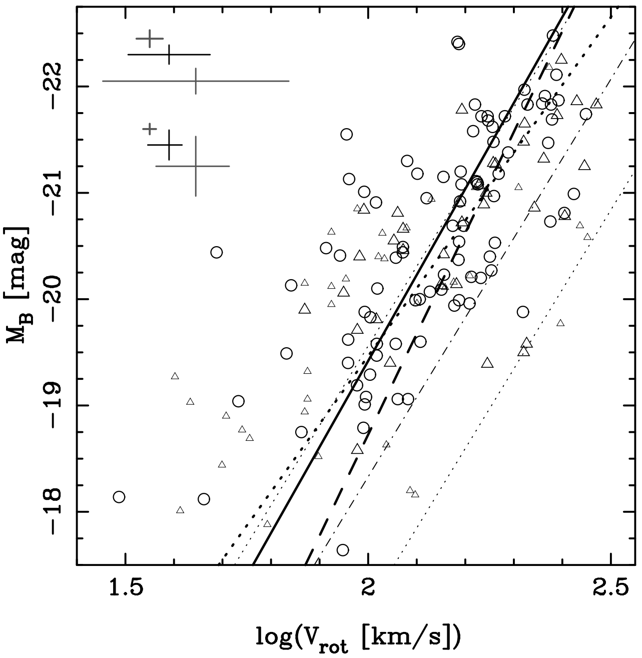

Figure 4.4. A comparison of our TFR with that of B04. The circular points and solid line are the same is in figure 4.1, as are the thin lines indicating the fiducial PT92 TFR. In addition the 'high quality' and 'low quality' points from B04 are marked by large and small triangles respectively. The dashed line is a fit to the 'high quality' points, and the dotted line is a fit to the full B04 sample. Both of these fits are performed using the same algorithm used to fit our data, as described in section 4.2.1. The upper set of error bars in the top left corner indicate the 10th-, 50th- and 90th-percentile uncertainties on the B04 'high quality' points, while the lower set give the same for our full TFR data set.

fit (see discussion in section 4.3).

Apart from the disagreement over the evolution of the TFR slope, our results are very much in accord with those of B04. In particular we find very similar modest evolutions in the TFR offset with redshift, of ∼1 mag by $z = 1$, also supported by the studies of Barden et al. (2003) and Nakamura et al. (2006).

Several other earlier studies of the Tully-Fisher relation at intermediate redshifts (e.g., Rix et al. 1997; Simard & Pritchet 1998) found significant luminosity evolution with redshift, in some agreement with our findings. However, Dalcanton, Spergel & Summers (1997) and Simard et al. (1999) argue that much, if not all, of the detected evolution is due to surface brightness selection effects. This is in agreement with the work of Vogt et al. (1996, 1997, 2002) who find little or, more recently, no significant evolution in the TFR out to $z = 1.3$, once surface brightness selection effects have been accounted for. Further details of this latter study's selection and analysis methods will hopefully shed light on the difference between our results and theirs. A discussion of the results from other field TFR studies can be found in section 1.2.2.

We will not attempt a more detailed analysis of the surface brightness selection effects in our study given the complexity of our selection. Nevertheless, for the above reasons and the arguments presented in section 4.2.2, we believe it is safe to take our measured luminosity evolution as an upper limit. In section 4.4 we will use this limit to constrain the evolution of the star-formation rate of bright field spiral galaxies.

Some evidence that the evolution we observe may be real, and non-zero, is provided by the local studies of Blanton et al. (2003) and Loveday (2004), which find evolution in the luminosity function with redshift. This corresponds to around -2 mag per unit redshift in the g-band, and even more evolution would be expected in the B-band, although they only measure the evolution over the range $0.0 < z < 0.3$. However, these studies integrate over the entire galaxy population, including galaxies with no significant ongoing star formation. Studies of the luminosity function evolution to $z \sim 1$ find evidence for a brightening of ~ 1 mag per unit redshift when considering just the blue galaxy population (Wolf et al. 2003; Faber et al. 2005; Willmer et al. 2005; Zucca et al. 2005).

None of these studies constrain the luminosity evolution at a given galaxy mass. Our upper limit on the luminosity evolution of individual star-forming galaxies is significantly smaller than that seen for the overall galaxy population, and more in line with that seen when considering just the blue population. This suggests that a mechanism which transforms massive galaxies from bright and star-forming to fainter and passive, rather than just a dimming of continuously star-forming objects, is responsible for the strong luminosity function evolution which is observed. Similar behaviour and conclusions are reached on consideration of our results along with measurements of evolution in the star formation density of the universe, as discussed in section 4.4.

4.3 Tully-Fisher residuals versus rotation velocity

It may be thought that plotting the TFR residuals, ${\Delta M_B}^{\rm TF}$, versus $V_{\rm rot}$ would provide a test for a change of slope. However, this must be treated very carefully, as the two variables are intrinsically correlated through the scatter in $V_{\rm rot}$. Böhm et al. (2004, hereafter B04) use this plot to argue that galaxies with lower $V_{\rm rot}$, and hence lower mass, are offset further from the local TFR than more massive galaxies. However, a correlation between ${\Delta M_B}^{\rm TF}$ and $V_{\rm rot}$ does not necessarily imply such a result. The fact that the two variables are not independent (cf. equation 4.8), combined with scatter in the TFR and restrictions on the magnitude range of the data, causes an intrinsic correlation, even in the absence of any true difference in TFR slope.

4.3.1 Simple arguments

In order to show this in more detail, figure 4.5 gives a pedagogical illustration of the effect of scatter and magnitude cuts on the distribution of points in the TFR and ${\Delta M_B}^{\rm TF}-\log V_{\rm rot}$ plots. Panels (a) and (b) show three corresponding lines in the TFR and ${\Delta M_B}^{\rm TF}-\log V_{\rm rot}$ plot, respectively. The thick solid line is an example ideal TFR, corresponding to the PT92 relation with a constant magnitude offset of -1.06 mag, the median ${\Delta M_B}^{\rm TF}$ of our data, in order to allow more direct comparison of the examples with our data. This example TFR is limited to the range $1.9 < \log V_{\rm rot} < 2.3$, and hence $-18.64 > M_B > -21.63$. The thick dashed and dotted lines indicate loci of constant M_B at the faint and bright limits of the example TFR, respectively. In panel (b), the plot of ${\Delta M_B}^{\rm TF}$ versus $\log V_{\rm rot}$, the example TFR becomes a (relatively short) horizontal line, while the loci of constant M_B are lines with a slope negative that of the example TFR, as is obvious from consideration of equation 4.8.

To show the transformation of distributions of points in the TFR plot to the

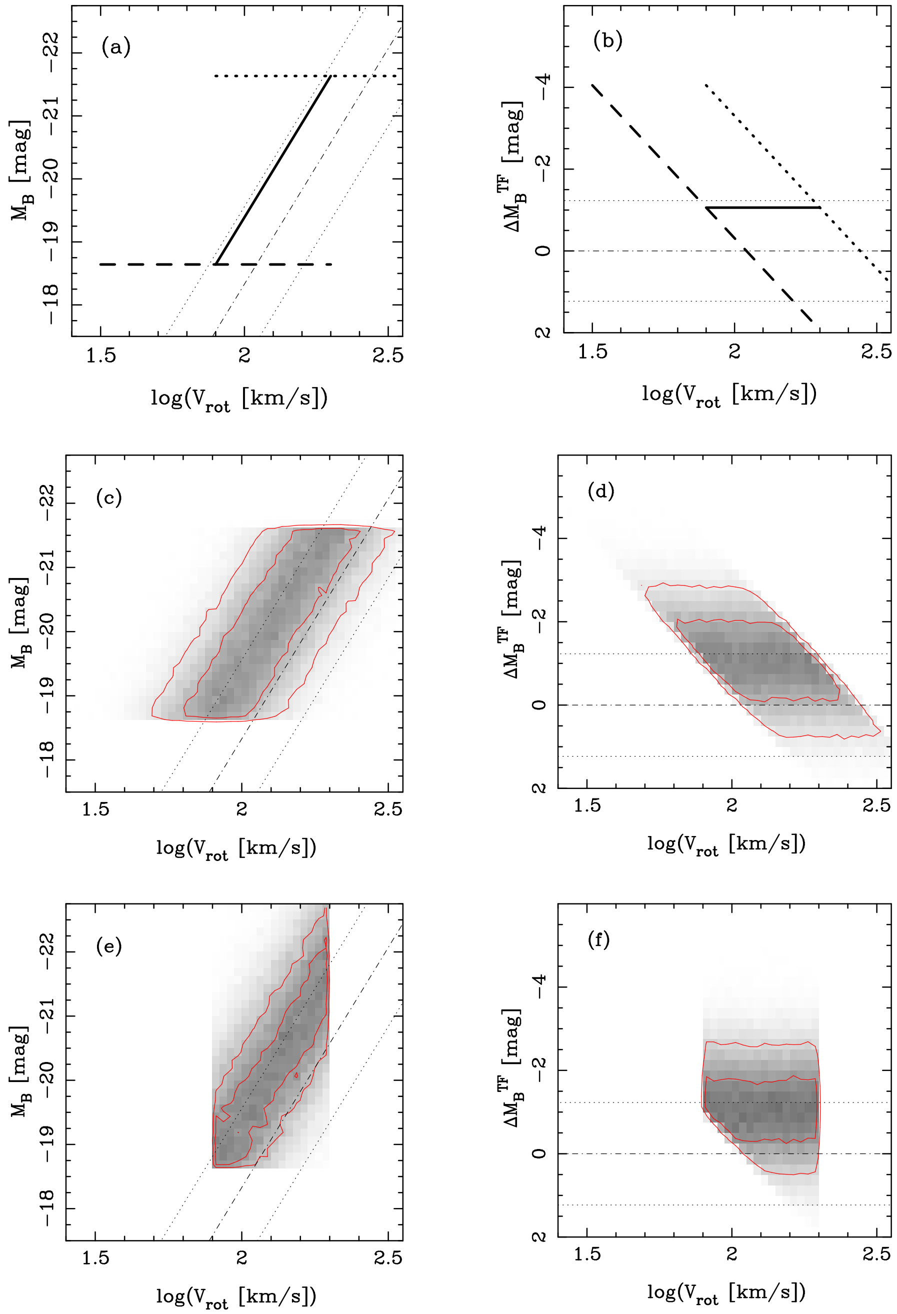

Figure 4.5. A simple demonstration of the intrinsic correlation between the TFR residuals from the fiducial PT92 TFR, ie., $\Delta M_B{}^{\mathrm{TF}}$, and V_{rot}. The fiducial local relation of PT92 is again marked by the thin dot-dashed and dotted lines. Panels (a) and (b) show instructive diagrams of the TFR and $\Delta M_B{}^{\mathrm{TF}}$ versus $\log V_{\mathrm{rot}}$ plot, respectively. Each line in panel (b) corresponds to the same style of line in panel (a). Panels (c) and (d) show the distribution of points, as greyscale and contours, for simulated galaxies with true $\log(V_{\mathrm{rot}})$ uniformly distributed on the range 1.9–2.3, true M_B assigned to each galaxy corresponding to the PT92 TFR, with a constant offset to make it more easily comparable to our intermediate redshift data. Gaussian scatter with 0.133 dex standard deviation (corresponding to 1.0 mag in terms of M_B assuming the PT92 TFR slope) has been added to generate the observed $\log V_{\mathrm{rot}}$. No scatter is added to the M_B values. Panels (e) and (f) show the distribution of simulated galaxies with true properties created in the same manner as the previous panels. However, in generating the observed values in this case, no scatter has been added to $\log V_{\mathrm{rot}}$, while Gaussian scatter with 1.0 mag standard deviation is added to the M_B. In addition, to demonstrate the effect of a magnitude cut, points with observed $M_B > -18.64$ have been removed from the sample. See the text for a more detailed discussion.

$\Delta M_B{}^{\mathrm{TF}} - \log V_{\mathrm{rot}}$ plane we construct samples of galaxies with simulated properties. These are designed to cover parameter ranges fairly similar to our data, but in order to keep our arguments straightforward, we initially keep these simulations highly simplified. More realistic simulations are considered later.

Each simulated galaxy is assigned a 'true' rotation velocity from a random uniform distribution in $\log V_{\mathrm{rot}}$ between 1.9 and 2.3, and a 'true' magnitude corresponding to this 'true' rotation velocity using the example TFR described above. The 'true' galaxy properties are thus uniformly randomly distributed on the solid line in panel (a) of figure 4.5. The distribution of 'true' properties is the same irrespective of whether the initial property assigned is $\log V_{\mathrm{rot}}$ or M_B. Scatter, in terms of measurement errors or intrinsic scatter in the TFR, may then be added to either the 'true' rotation velocities, magnitudes, or both, to produce simulated 'observed' values of the parameters.

The effects of measurement error and intrinsic scatter on the distribution of points are equivalent for these examples. Differences between the two can only arise as artifacts of the simulation method. Measurement error must always be applied after both parameters have been assigned, while intrinsic scatter may be applied between the production of the first parameter, e.g., $\log V_{\mathrm{rot}}$ and the assignment of the corresponding second parameter, e.g., M_B. If the intrinsic scatter is only applied to the value of the first-assigned parameter that is then used to generate the second parameter, then this is equivalent to a measurement scatter applied directly to the second parameter. If the intrinsic scatter is only applied to the first parameter after the second parameter has been generated, then this is equivalent to measurement error on the first parameter. Alternatively, if the intrinsic scatter is applied to the 'true' value of the first-assigned parameter, which is then used to generate the second parameter and also used as a basis for the 'observed' value of the first parameter, then this is effectively an alteration of the initial distribution from which the first parameter is derived, as well as the addition of a scatter in the second parameter which is indistinguishable from a measurement error. As we wish to be able to control the distribution of the 'true' parameters independently of the inclusion of scatter, we choose to implement intrinsic scatter as offsets applied following the generation of both 'true' parameters, in which case it is identical to a scatter due to measurement error. For the following simple examples we therefore do not distinguish between the two. All random scatters applied in these simulations are based on Gaussian distributions with the specified standard deviation.

In panel (c) of figure 4.5 we plot the distribution of 10^5 simulated points, as greyscale and contours, generated by the procedure described above, and with the inclusion of 0.133 dex of scatter in $\log V_{\mathrm{rot}}$ (corresponding to 1.0 mag in terms of M_B assuming the PT92 TFR slope). As no scatter has been added to the magnitude coordinates, the distribution is restricted to a sharply defined range of M_B. Panel (d) shows the corresponding distribution in the $\Delta M_B{}^{\mathrm{TF}} - \log V_{\mathrm{rot}}$ plane. The extension of the points parallel to the fiducial TFR produces a horizontal extension in this plot. The scatter in $\log V_{\mathrm{rot}}$ spreads the distribution in both the horizontal and vertical direction, along lines with slope equal to minus the TFR slope. The restrictions in M_B, due to the initial choice of the 'true' TFR points' distribution, translate into sharply defined sloping cut-offs in the $\Delta M_B{}^{\mathrm{TF}} - \log V_{\mathrm{rot}}$ plot, corresponding to the dashed and dotted lines shown in panels (a) and (b) of the same figure.

Panel (e) of figure 4.5 shows, in the same manner as panel (c), the distribution of another 10^5 simulated points. These points were generated by the same procedure, but this time with 1.0 mag of scatter in M_B, and none in $\log V_{\rm rot}$. In addition, in this panel we demonstrate the effect of a magnitude cut, by rejecting points with observed $M_B > -18.64$ (corresponding to the faint end of the simulated 'true' M_B distribution) from the sample. Without a magnitude cut, the edges of the distribution are defined by sharp vertical lines of constant $\log V_{\rm rot}$, due to the initial range of the simulated distribution, and by softer drop-offs parallel to the example TFR, due to the introduced scatter.

In the $\Delta M_B{}^{\rm TF}\!-\log V_{\rm rot}$ plot, shown in panel (f), this translates into a rectangle, the constant $\log V_{\rm rot}$ edges are obviously preserved, and the scatter is purely in the $\Delta M_B{}^{\rm TF}$ direction. However, the inclusion of a magnitude cut causes a slope at the corresponding edge of the $\Delta M_B{}^{\rm TF}\!-\log V_{\rm rot}$ distribution. For a more realistic, magnitude-limited sample, the range in $\log V_{\rm rot}$ would not be restricted as it is in this example, and so the entire low $\log V_{\rm rot}$ side of the $\Delta M_B{}^{\rm TF}$ versus $\log V_{\rm rot}$ distribution would be sloped. In addition, a realistic magnitude distribution would show a cut-off at the bright end due to the observed nature of the luminosity function. Magnitude errors in studies like this one do not typically exceed 0.2 mag, and so adopting 1.0 mag of M_B scatter would require intrinsic scatter in the TFR. However, assuming a uniform distribution of $\log V_{\rm rot}$ with this amount of intrinsic scatter is clearly at odds with the observed luminosity function.

With an unrestricted range of $\log V_{\rm rot}$ and magnitude cuts for $M_B > -18.64$ and $M_B < -21.63$ the distribution of points in the TFR and $\Delta M_B{}^{\rm TF}\!-\log V_{\rm rot}$ planes would look nearly identical to those shown in panels (c) and (d). Therefore, scatter in either M_B and/or $\log V_{\rm rot}$, in the form of intrinsic scatter or measurement errors, when combined with restrictions on the M_B range, whether due to the underlying luminosity function, selection effects or directly imposed, produces a correlation in a plot of $\Delta M_B{}^{\rm TF}$ versus $\log V_{\rm rot}$. As these restrictions only affect the edges of the $\Delta M_B{}^{\rm TF}\!-\log V_{\rm rot}$ distribution, the strength of the correlation, and its apparent slope, are related to the ratio of the total scatter to the M_B range covered. The correlation is strongest, with slope equal to minus that of the TFR, when the M_B range is smaller than the scatter, and weakens, with flatter slope, as the M_B range grows relative to the scatter.

Finally, note that the combination of a scatter with restrictions on the magnitude range leads to the measured slope of the simulated/observed TFR appearing flatter than the real underlying TFR, as can be seen in panel (c) of figure 4.5. (Likewise, restrictions in the rotation velocity range lead to a steepening of the apparent TFR.) However, this well known problem is greatly reduced by choosing a method to fit the TFR which minimises the residuals in $\log V_{\rm rot}$, rather than M_B (e.g., see Willick 1994), as is done throughout this paper.

While we have made the reasonable assumption of Gaussian scatter on $\log V_{\rm rot}$ and M_B in the above examples, the appearance of a correlation does not depend on the form of the scatter, merely that there is some broadening of the TFR. Clearly the detailed distribution in the $\Delta M_B{}^{\rm TF}\!-\log V_{\rm rot}$ plane will vary with the choice of the scatter distribution, but the existence of a significant correlation is robust.

4.3.2 Realistic simulations

The examples in figure 4.5 are relatively simple, in order to avoid confusing the effects of different simulation parameters. However, to compare more fairly, though still qualitatively, with our real data, we require a more detailed and realistic set of simulated data. To generate this data we use the following method. We assign each simulated galaxy a redshift, randomly drawn from a uniform distribution[2] on the range 0.0–1.0. Because of the varying volume elements enclosed by a given solid angle at different redshifts, we must preferentially include galaxies in our sample at a rate proportional to the comoving volume element at their redshift. To do this we calculate the ratio of the comoving volume element at the assigned galaxy redshift to that at redshift 1.0. If a random number between 0 and 1 is greater than this ratio, then we reject this galaxy from our sample and begin generating a new galaxy. This assumes that the comoving number density of galaxies is constant, which is true in the absence of mergers, and a reasonably good assumption at these redshifts. Changes in the number density at a given magnitude due to luminosity evolution are considered later.

If the galaxy is not rejected it is then assigned a true absolute magnitude, randomly drawn from a uniform distribution between -12.0 and -24.0. We model the effect of the luminosity function by calculating $\phi(M_B)$, normalised to be less than unity on the magnitude range considered, and rejecting the galaxy from our sample if a random number between 0 and 1 is greater than $\phi(M_B)$. The luminosity function assumed, $\phi(M_B)$, is a Schechter function (Schechter 1976) with parameters from the 2dF Galaxy Redshift Survey (2dFGRS) determined by Norberg et al. (2002), with M^* converted from the b_J-band to the B-band as described in section 2.4.1, i.e., $M^*_B = -20.3$ and $\alpha = -1.2$.

An added complication for comparing with the real data is evolution of the luminosity function. Without including any evolution, the bright end of the luminosity function of the simulated galaxies does not match that seen for our real sample. Although our data is not a complete sample, and is subject to complex selection effects, the bright magnitude cut-off should be reasonably close to that of the true underlying luminosity function. In section 4.2.2 we find evidence for luminosity evolution, at a given rotation velocity, of up to around -1 mag per unit redshift. Loveday (2004) and Blanton et al. (2003) find evolution in the r-band luminosity function from SDSS data, although with only $z \lesssim 0.3$, amounting to a change in M^* between -1 and -2 mag per unit redshift. Studies of the luminosity function at $z \sim 1$ find evidence for a brightening of the blue galaxy population by ~ 1 mag per unit redshift (Wolf et al. 2003; Faber et al. 2005; Willmer et al. 2005; Zucca et al. 2005).

Evolution of the luminosity function with redshift is therefore certainly plausible, and would have a most noticeable effect around the sharp cutoff at bright magnitudes. To account for this we apply an evolution of $M^*_B(z) = M^*_B(0) - 1.0\,z$ when calculating $\phi(M_B)$ for each simulated galaxy. This brings the luminosity function of the simulated galaxies into much better agreement with that of our real data. Figure 4.6 shows the luminosity function of the simulated data set, and demonstrates the effect of including luminosity evolution.

For the galaxies remaining, which now have the redshift distribution expected given the comoving volume of space sampled at each redshift, and an absolute magnitude distribution corresponding to a realistic, evolving luminosity function, we now generate apparent magnitudes, and apply a magnitude limit.

No intrinsic scatter is added to the magnitudes as we have already used a realistic observed luminosity function to generate the magnitudes. Adding intrinsic scatter to these values does not make sense, as it would change the assumed magnitude

---

[2] actually discrete values separated by 0.001 to improve the computational speed, by allowing redshift-dependent values to be calculated prior to the galaxy-generating loop

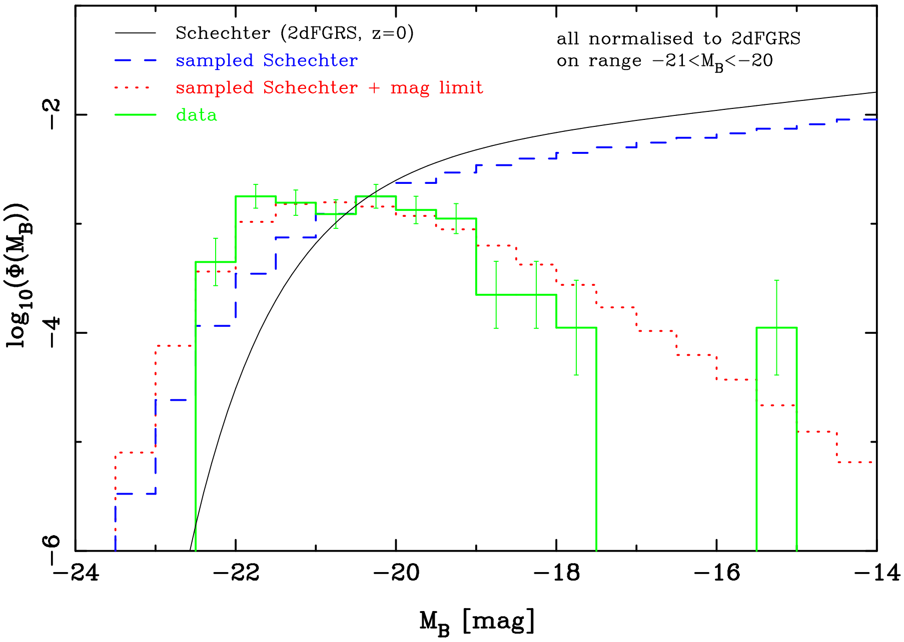

Figure 4.6. Plot showing the luminosity functions of the simulated datasets considered in this section, and comparing with the luminosity function of the field TFR sample. The 2dFGRS Schechter luminosity function, assumed in the simulations, is shown by the smooth black line. The dashed blue histogram shows a sampling of this function with 10^6 points, with the inclusion of a luminosity evolution of 1 mag per unit redshift. The dotted red histogram shows a similar sampling of the Schechter function, with the application of an apparent magnitude limit of 22.5 mag. This is the distribution of the simulated points used to construct the plots in figure 4.7. The luminosity function of the field TFR sample is shown by the solid green histogram with Poisson error bars. This is normalised to the 2dFGRS function over the range $-21 < M_B < -20$, and so may be shifted vertically.

distribution to be less representative of that observed. Any intrinsic scatter in the TFR must therefore be added to the rotation velocities.

To apply a realistic magnitude limit we first calculate ‘true’ apparent magnitudes from the absolute magnitudes using the distance modulus at each galaxy’s redshift. We then reject any galaxy with a ‘true’ apparent magnitude fainter than a specified limit. We apply a magnitude limit similar to that seen in our data, from examination of the plot of M_B versus z in figure 5.1 and comparison of the faint end of the luminosity functions for our simulated and real data. An apparent magnitude limit of 22.5 mag is thus adopted. Figure 4.6 demonstrates the effect of applying this magnitude limit on the luminosity function of the simulated data set.

Next, simulated ‘observed’ M_B are produced, by adding to the ‘true’ magnitudes values randomly drawn from a distribution with properties similar to the measurement uncertainties on our real data. Rather than over-complicate the simulation by allowing the measurement uncertainties to vary from galaxy to galaxy, we model the magnitude measurement scatter by a Gaussian distribution with a constant standard deviation of 0.15 mag, equal to the median magnitude uncertainty in our real data. Simulations with scatter based on more realistic, variable measurement uncertainties, including using the distribution of uncertainties from the real data, produce very similar results, with a slight broadening of the TFR and corresponding extension of the $\Delta M_B{}^{\mathrm{TF}}$ versus $\log V_{\mathrm{rot}}$ correlation, due to the tail of points with large uncertainties.

We apply the scatter due to measurement errors after the magnitude cut, as the magnitude limit is approximately due to our inability to measure the properties of galaxies with real magnitudes fainter than the limit, rather than a direct cut based on our observed apparent magnitudes.

'True' $\log V_{\rm rot}$ are generated for the simulated galaxies, using the 'true' M_B and the example TFR used throughout these simulations. These are converted into 'observed' $\log V_{\rm rot}$ by adding random offsets to mimic intrinsic scatter and measurement errors, both drawn from Gaussian distributions. The measurement error standard deviation used was the median $\log V_{\rm rot}$ uncertainty in our real data, 0.04 dex. The intrinsic scatter standard deviation used was 0.12 dex, corresponding to the 0.9 mag of intrinsic scatter determined in fitting our real field TFR (see equation 4.6).

The above procedure has been repeated to generate 10^6 simulated points. The resulting distribution of these simulated galaxies in the TFR plot is shown by panel (a) of figure 4.7. The distribution's properties are broadly similar to those of the simpler examples in figure 4.5 (c) and (d), but with a much more realistic appearance. Note that the sharp cut-off at the bright end of the luminosity function produces a fairly well defined edge to the top of the TFR, while the apparent magnitude limit causes a gentler drop-off at the bottom of the TFR. This is because the wide redshift range of the sample smears out this limit in terms of absolute magnitude.

Residuals of the simulated data points from the fiducial TFR are calculated in the same manner as for the real data. Panel (b) of figure 4.7 shows the distribution of the simulated galaxies in the ${\Delta M_B}^{\rm TF}\!-\log V_{\rm rot}$ plane. Note the clear correlation in this plot, despite the fact that the points were generated from a TFR parallel to the fiducial PT92 TFR, and with only symmetrical scatter in M_B and $\log V_{\rm rot}$. The well defined sloping top-right edge of this ${\Delta M_B}^{\rm TF}\!-\log V_{\rm rot}$ distribution is a consequence of the bright cut-off of the underlying luminosity function. Slightly less well-defined, but still clear, is the sloped edge defining the bottom-left limit of the distribution. This is due to the fairly gentle cut-off at the faint end of the TFR, itself a result of the apparent magnitude limit. As this cut-off is gentler than at the bright end of the TFR, the slope in the ${\Delta M_B}^{\rm TF}\!-\log V_{\rm rot}$ plot is flatter, and thus the distribution broadens slightly towards low $\log V_{\rm rot}$.

The ${\Delta M_B}^{\rm TF}\!-\log V_{\rm rot}$ plot of our real data is shown in panel (c) of figure 4.7. These points display a correlation very similar to that seen in the simulated data sets. Note the similarity with the detailed simulation in panel (b). The only significant difference could be argued to be the existence of a few points at lower $\log V_{\rm rot}$ and higher ${\Delta M_B}^{\rm TF}$ than the simulated distribution. However, remember that the error distribution in our simulation assumes a constant measurement uncertainty, whereas the real data shows a wide variation. Including a fraction of points with significantly larger measurement uncertainties causes the ${\Delta M_B}^{\rm TF}\!-\log V_{\rm rot}$ distribution to extend further, to lower $\log V_{\rm rot}$ and higher ${\Delta M_B}^{\rm TF}$.

The observed correlation of our data in the plot of ${\Delta M_B}^{\rm TF}$ versus $\log V_{\rm rot}$ can therefore be easily explained as a result of the intrinsic correlation between the two axes, combined with scatter in the TFR and restrictions on the magnitude range, particularly due to the underlying luminosity function. It is therefore clear that a correlation between ${\Delta M_B}^{\rm TF}$ and $V_{\rm rot}$ does not necessarily imply a physical effect, and in our case it appears to be entirely consistent with no $V_{\rm rot}$-dependent change in the TFR with redshift.

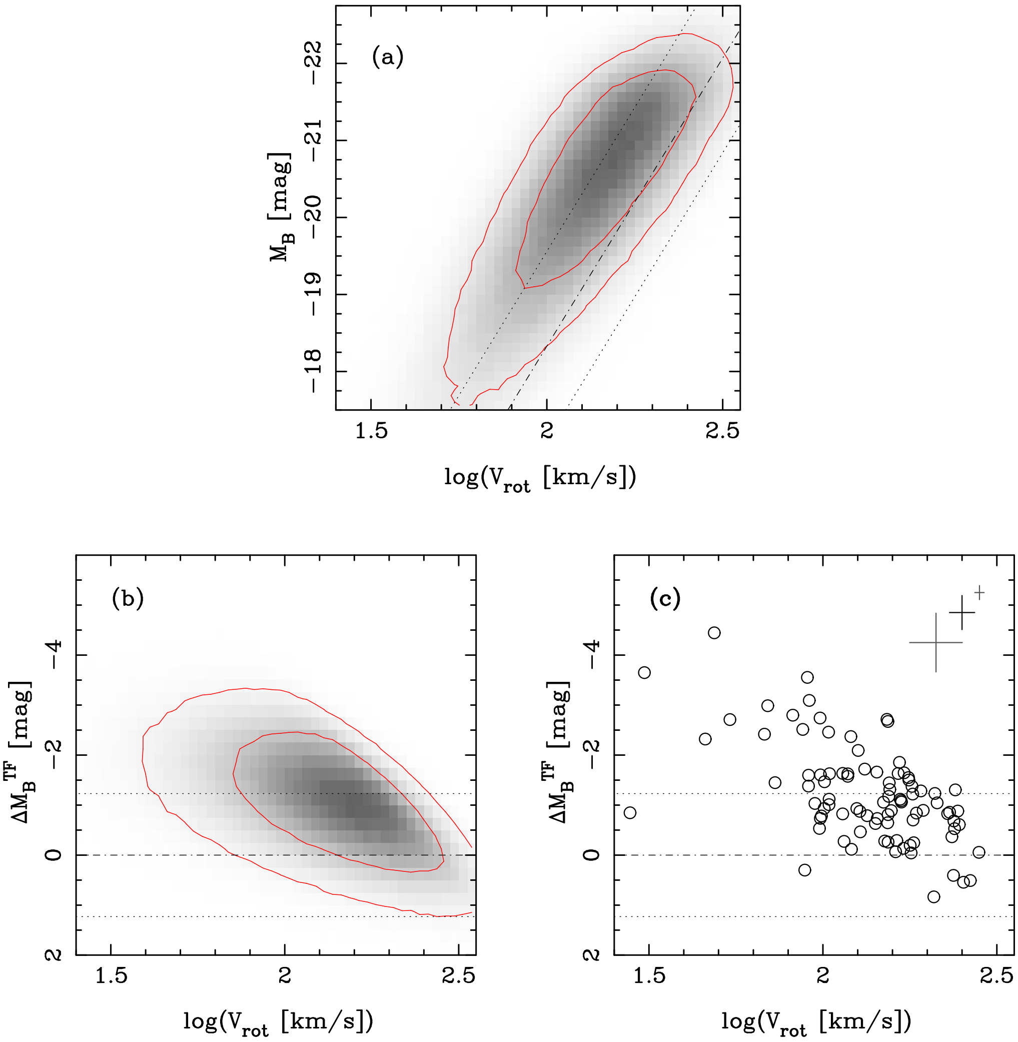

Figure 4.7. A more detailed demonstration of the intrinsic correlation between $\Delta M_B{}^{\mathrm{TF}}$ and V_{rot}. The fiducial local relation of PT92 is again marked by the thin dot-dashed and dotted lines. Panels (a) and (b) show the distribution of points in the TFR and $\Delta M_B{}^{\mathrm{TF}}$ versus $\log V_{\mathrm{rot}}$ plot, respectively, for a realistic simulated sample of galaxies, as described in the text. This may be compared with panel (c), a plot of $\Delta M_B{}^{\mathrm{TF}}$ versus $\log V_{\mathrm{rot}}$ for our real field TFR sample. Note the clear correlation, which, as shown by the simulations, may be explained purely by the intrinsic correlation between $\Delta M_B{}^{\mathrm{TF}}$ and $\log V_{\mathrm{rot}}$, along with the effect of scatter in the TFR combined with a restriction on the magnitude range of the data. This correlation, therefore, does not necessarily imply that the data prefers a slope of the TFR different to that of the chosen fiducial TFR, and is thus not adequate evidence for such a real, physical effect.

4.4 SFR evolution with redshift

We can consider what our best-fitting evolution in the TFR implies for the luminosity and star-formation evolution of field spirals. The implicit assumption in this section is that the B-band luminosity of spiral galaxies with a given rotation velocity evolves due to its star formation history only. For simplicity, we shall parameterise the luminosity and star-formation rate evolution as simple power-laws.

Let us assume that the rest-frame B-band luminosity of field spirals evolves as a power law in $(1+z)$. Then,

$$L_B(z) = L_B(0) \cdot (1+z)^{\beta} \tag{4.12}$$

and therefore

$$\Delta {M_B}^{\mathrm{TF}}(z) \equiv M_B(z) - M_B(0) = -2.5\beta \log(1+z). \tag{4.13}$$

In section 4.2.2 we find a best-fitting evolution of the TFR intercept with redshift dependence

$$\Delta {M_B}^{\mathrm{TF}}(z) \approx (-1.0 \pm 0.5) \cdot z \text{ mag}. \tag{4.14}$$

If we assume no evolution in the rotation velocities of field spirals, i.e., that all evolution is in terms of the stellar populations, this implies $\beta_{\mathrm{fit}} = 1.3 \pm 0.6$. Fitting directly with respect to $\log(1+z)$ gives the same value for β.

Before we proceed to compare with stellar evolution models, we need a way to relate $(1+z)$ to time. For the concordance cosmology,

$$(1+z) \approx \left(\frac{t}{t_0}\right)^{-0.813} \tag{4.15}$$

is an excellent approximation for $z < 1$ and sufficiently accurate for our purposes up to $z \sim 5$. For a galaxy of age t_{age}, which formed at t_{f} we thus have

$$(1+z) \approx \left(\frac{t_{\mathrm{f}} + t_{\mathrm{age}}}{t_0}\right)^{-0.813}. \tag{4.16}$$

Using equation 4.16 to convert $(1+z)$ to t_{age} for various t_{f} we can determine the expected value of β for any star-formation history using the stellar evolution models of Bruzual & Charlot (2003). We model the SFR as

$$SFR \propto \begin{cases} 0 & z > z_{\mathrm{f}} \\ (1+z)^{\alpha} \approx \left(\frac{t_{\mathrm{f}}+t_{\mathrm{age}}}{t_0}\right)^{-0.813\alpha} & z \leq z_{\mathrm{f}}. \end{cases} \tag{4.17}$$

For a galaxy with constant SFR ($\alpha = 0$) and $z_{\mathrm{f}} = 2$ we find $\beta_{\alpha=0} = -0.27$. This corresponds to a brightening of 0.2 mag between $z = 1$ and today. A galaxy with constant SFR is therefore fainter in the past, opposite to what we measure. We therefore require a model with a SFR which declines with time, i.e., $\alpha > 0$

The difference in the power-law index between our best-fitting evolution and the constant SFR models is

$$\Delta\beta_{\alpha=0} \equiv \beta_{\mathrm{fit}} - \beta_{\alpha=0} = 1.6 \pm 0.6. \tag{4.18}$$

Choosing $z_{\mathrm{f}} = 5$ only decreases this slightly to $\Delta\beta_{\alpha=0} = 1.5 \pm 0.6$. We therefore work with $z_{\rm f} = 2$ hereafter.

In order to have some idea of of what value of α corresponds to what is observed, we can assume that B-band luminosity is proportional to the current SFR,

$$\frac{L_B}{L_{B,\alpha=0}} = \frac{SFR}{SFR_{\alpha=0}} \tag{4.19}$$

which implies $\alpha = \Delta\beta_{\alpha=0} = 1.6 \pm 0.6$. Putting this form for the SFR (i.e., SFR $\propto (1+z)^{1.6}$) into the Bruzual & Charlot (2003) code gives

$$\beta_{\alpha=1.6} = 1.2 \;\Rightarrow\; \Delta\beta_{\alpha=1.6} = 0.1, \tag{4.20}$$

nearly but not quite zero, as equation 4.19 is not a perfect approximation. However, we can improve our estimate by a straightforward parameter search to determine the value of α which produces our observed $\beta_{\rm fit}$. We thus find $\alpha = 1.7 \pm 1.1$.

In this calculation we have assumed that the rotation velocities of the field galaxies under study has remained constant since $z \sim 1$. Perhaps more realistically, we could instead assume that as well as their star formation rates evolving, the galaxies have become more massive over this time, due to accretion. In this case the star formation evolution required by the TFR evolution is less. For the extreme case where all of the observed B-band TFR evolution is actually in rotation velocity, rather than M_B, then $\beta_{\rm fit} = 0.0$. This implies a significantly lower value for α (though still positive as $\beta_{\alpha=0} = -0.27$ from above). If dark matter and stellar mass grow in step, as implied by the constancy the baryonic TFR (e.g., Conselice et al. 2005; Flores et al. 2006), then β is still considerably lower, and hence so is α.

In summary, we find that SFR(z) $\propto (1+z)^{1.7\pm1.1}$ in our sample of relatively bright ($M_B \gtrsim M_B^*$) galaxies, assuming our measured TFR evolution is purely a luminosity effect. As we argued earlier, the luminosity evolution determined from our TFR evolution is likely to be an overestimate. In addition, any increase in the mass of the galaxies due to accretion or merging decreases the degree of luminosity, and hence SFR, evolution required to reproduce the TFR evolution. The above quoted SFR evolution is therefore probably an upper limit, and the evolution of the average SFR in luminous spirals is likely to be even slower. In contrast, studies of the SFR density of the Universe at low redshift (e.g., Gallego et al. 1995) and as a function of look-back time (e.g., Heavens et al. 2004) generally indicate a very strong evolution up to $z \sim 1$. The precise rate of this evolution is somewhat controversial, but most studies agree that, parameterising as SFR $\propto (1+z)^{\alpha}$, $\alpha \simeq 3$–4 (see Hopkins 2004 for a compilation of SFR density evolution measurements).

This disparity suggests that the rapid evolution in the SFR density of the universe, observed since $z \sim 1$, is *not* driven by the evolution of the SFR in individual bright spiral galaxies, like those in our sample. However, it should be noted that, given the size of our sample and the intrinsic scatter in the TFR, the derived constraints on the evolution of SFR in the bright spiral galaxy population are relatively weak. Nevertheless, this kind of approach seems very promising for future studies with samples of several hundred or even thousands of galaxies to $z \sim 1$.

4.5 Ionisation conditions, metallicities, star formation rates and internal extinctions

4.5.1 Local comparison sample

In order to examine the properties of our intermediate-redshift EW sample of field galaxies (as defined in section 3.2), it is useful to have a local sample with which to compare. For this we utilise the sample of Jansen et al. (2000), who observed the Nearby Field Galaxy Sample (NFGS) of about 200 galaxies. This galaxy sample was selected from the first CfA redshift catalogue (Huchra et al. 1983) to approximate the local galaxy luminosity function. The NFGS sample includes galaxies of all morphological types and spans 8 mag in luminosity and a broad range of environments. The spectra of NFGS sample galaxies are integrated over a significant fraction of each galaxy, and are thus similar to the spatially integrated spectra of the galaxies in our EW sample. Following Jansen et al. (2000), an additional correction for stellar absorption of 1.5Å (1.0Å) has been applied to the NFGS Hα (Hβ) equivalent widths.

To distinguish between galaxies dominated by emission from star formation and those with a significant AGN component we classified galaxies according to their position in [OIII]λ5007/Hβ versus [NII]/Hα and [OIII]λ5007/Hβ versus [SII]/Hα diagrams. The demarcation between star-forming galaxies and AGNs in both diagrams was taken from Kewley et al. (2001). We used the conservative requirement that a galaxy must be classified as a star-forming galaxy in both diagnostic diagrams in order to be retained in our local comparison sample.

The colour excess from obscuration by dust for NFGS sample galaxies was estimated from the observed ratio of Hα and Hβ line fluxes. We adopt the Milky Way interstellar extinction law of Cardelli et al. (1989), with $R_V = 3.1$. We assume an intrinsic ratio Balmer decrement of 2.85, corresponding to the case B recombination with a temperature of $T = 10^4$ K and a density of $n_e \sim 10^2$–10^4 cm^{-2} (Osterbrock 1989). All this is consistent with the analysis of our intermediate-redshift sample. Note that the various published extinction laws are similar in the optical, making the determination of the colour excess independent of the exact choice of extinction law.

Gas phase oxygen abundances were determined for the NFGS galaxies using the R$_{23}$ method (see next section), assuming they all lie on the high-metallicity branch of the $12 + \log(\mathrm{O/H})$ versus R$_{23}$ calibration, as used for the intermediate-redshift EW sample. The star formation rate of galaxies in the NFGS sample were estimated using extinction-uncorrected Hα luminosities following the calibration of Kennicutt (1998).

4.5.2 Basic spectral diagnostics

The distributions of redshift, B-band absolute magnitude, rotation velocity, and emission scalelength for galaxies in our field EW sample (see section 3.2) are shown in figure 4.8. Our sample of star-forming galaxies at intermediate redshifts is dominated by bright ($M_B \lesssim -19$), massive ($V_{\mathrm{rot}} \gtrsim 80$ km s^{-1}), and large ($r_{\mathrm{d,spec}} \gtrsim 2$ kpc) disc galaxies.

Figure 4.9 shows the relationship between the rest-frame equivalent widths of the [OII]λ3727 and Hβ emission-lines for our intermediate-redshift EW sample and the comparative local NFGS sample. This demonstrates that the overall distribution of [OII] and Hβ rest-frame equivalent widths for massive and luminous star-forming

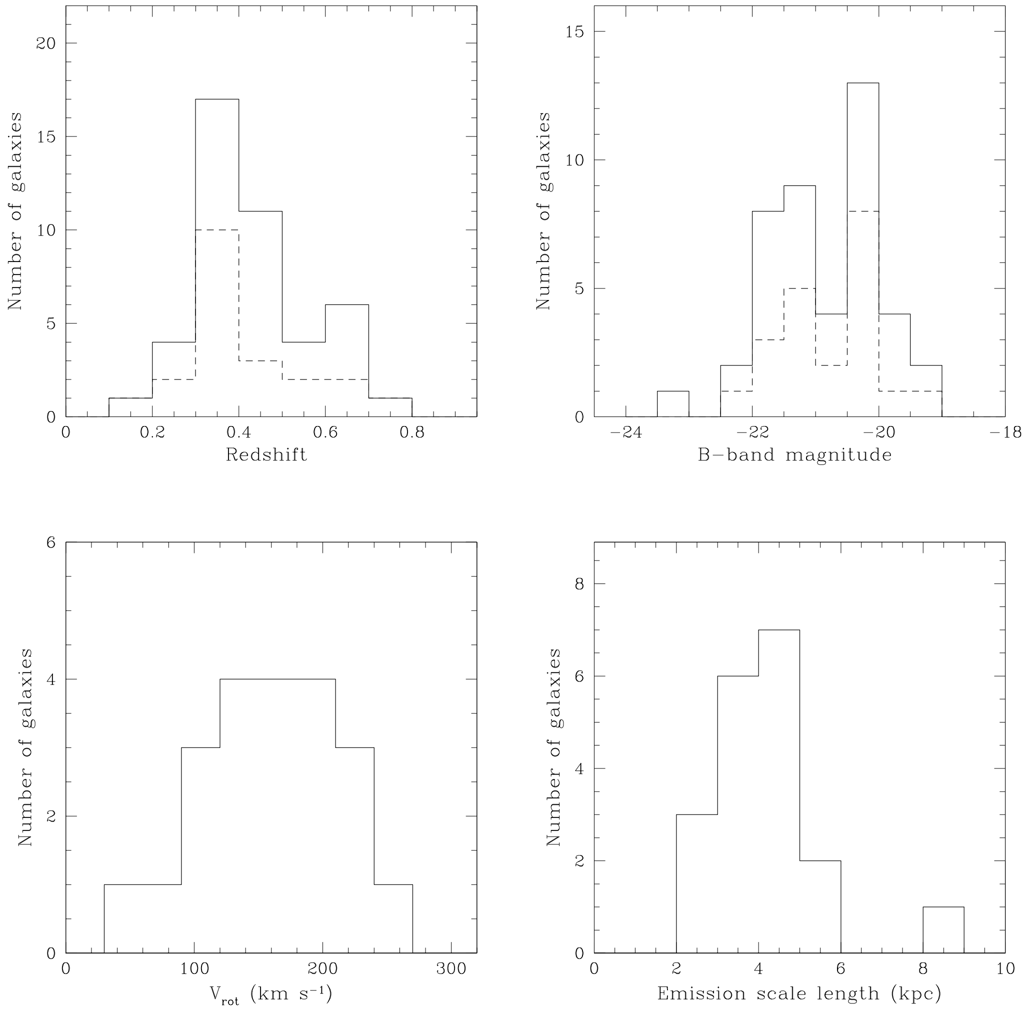

Figure 4.8. The redshift, B-band absolute magnitude, rotation velocity, and emission scalelength distributions for field galaxies in our EW sample. Dashed histograms show the distributions of galaxies with measured rotation velocities and emission scalelengths.

galaxies at intermediate redshifts is similar to the distribution for local star-forming galaxies.

The relationship between galaxy absolute rest-frame B-band magnitude and [OII] equivalent width is shown in figure 4.10. The local NFGS galaxies in this figure show the well-established correlation between galaxy luminosity and emission-line equivalent width, i.e., the bright end of the galaxy luminosity function at the present epoch is dominated by galaxies with low emission-line equivalent width (Salzer et al. 1989; Kong et al. 2002; Jansen et al. 2000). The galaxies in our intermediate-redshift EW sample cover a similar range of [OII] equivalent width to that observed locally, but over a much narrower luminosity range, i.e., ~ 2 mag in comparison to the ~ 7 mag covered by the NFGS sample. Strikingly, a fraction of the massive and luminous field galaxies at intermediate redshifts show large equivalent widths that are seen locally only for faint, i.e., $M_B \gtrsim -18$, (and metal-poor) galaxies (see also Lilly et al. 2003).

Locally, faint and metal-poor galaxies that show large emission-line equivalent

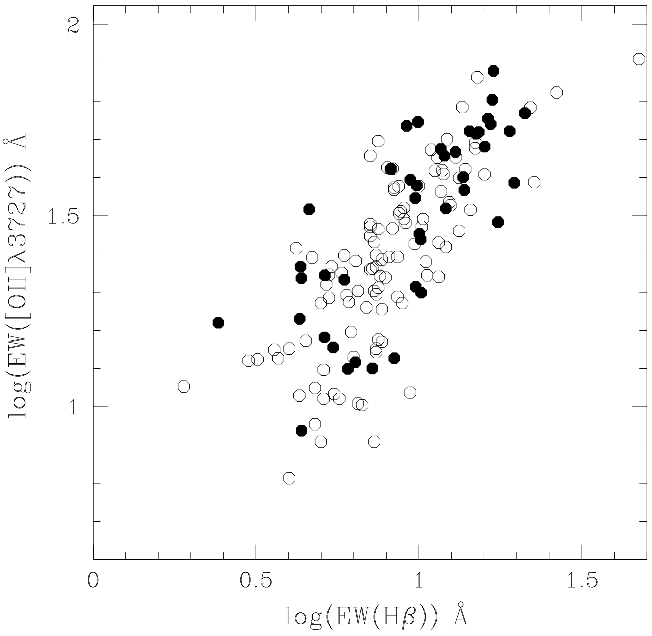

Figure 4.9. [OII]λ3727 versus Hβ equivalent widths for galaxies in our intermediate-redshift EW sample (filled circles), and for local galaxies from Jansen et al. (2000) (open circles).

widths tend to be highly ionised, while bright and metal-rich galaxies are characterised by low-ionisation parameters (e.g., McCall et al. 1985; Stasinska 1990; Mouhcine et al. 2005). Figure 4.11 shows the [OII] emission-line rest-frame equivalent width as a function of the diagnostic ratio $O_{32} = [OIII]\lambda4959, \lambda5007 / [OII]\lambda3727$, which is a function of both ionisation and metallicity (Kewley & Dopita 2002). To illustrate the effect of galaxy luminosity on O_{32}, we split the local sample of star-forming galaxies into faint ($M_B > -19.5$) and bright ($M_B \leq -19.5$) samples. The local NFGS galaxies are distributed along a well-defined luminosity-excitation sequence, with luminosity decreasing as the excitation parameter increases. The intermediate-redshift galaxies in our EW sample cover a similar range of O_{32} as is observed for local star-forming galaxies, and are generally distributed similarly in the [OII] equivalent width versus O_{32} diagram. Interestingly, however, a sub-sample of the luminous, star-forming, intermediate-redshift galaxies exhibit O_{32} values that are seen locally only for much fainter galaxies. This suggests that the physical parameters of the interstellar star-forming gas within these luminous galaxies, i.e., metallicity and ionisation conditions, might be similar to those observed for local faint and metal-poor star-forming galaxies.

Figure 4.12 shows the relationship between the abundance-sensitive parameter $R_{23} = ([OIII]\lambda4959, \lambda5007 + [OII]\lambda3727) / H\beta$ and absolute rest-frame B-band magnitude for both local star-forming galaxies from the NFGS sample and our EW sample of intermediate-redshift field galaxies. Again, the R_{23} parameter covers a similar range for both samples. However, our intermediate-redshift sample shows a large scatter of R_{23} parameter at a given galaxy luminosity. and, unlike the local galaxies, contains luminous and massive objects with large R_{23} parameters. Such R_{23} values are found locally only at lower luminosities, and are indicative of low oxygen abundances.

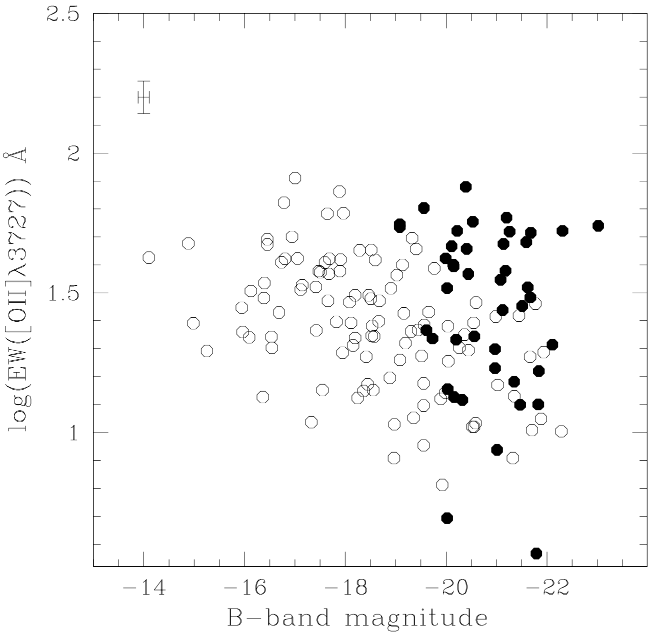

Figure 4.10. The relationship between [OII]λ3727 emission-line equivalent width and *B*-band absolute magnitude for field galaxies in our intermediate redshift EW sample (filled circles), and the NFGS sample of local star-forming galaxies (open circles).

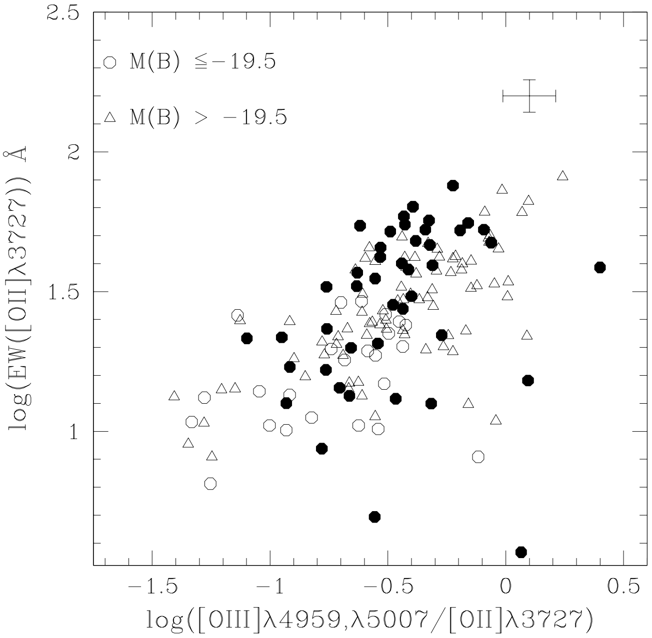

Figure 4.11. Equivalent width of [OII]λ3727 versus the ionisation sensitive ratio, O_{32} = [OIII]λ4959, λ5007 / [OII]λ3727. Field galaxies in our intermediate-redshift EW sample are indicated by filled circles. The NFGS sample of local star-forming galaxies is also plotted, with open triangles showing faint galaxies ($M_B > -19.5$) and open circles showing bright ($M_B \leq -19.5$) galaxies.

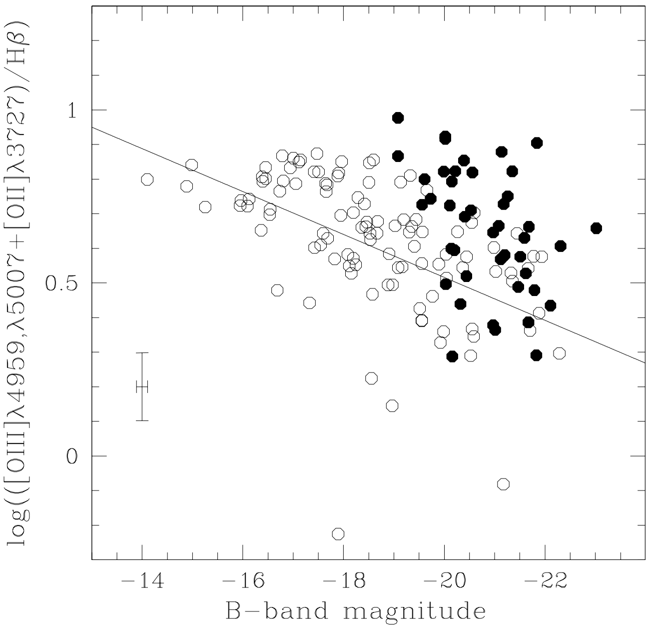

Figure 4.12. The relationship between the oxygen abundance sensitive parameter $R_{23} = ([\mathrm{OIII}]\lambda4959, \lambda5007 + [\mathrm{OII}]\lambda3727) / \mathrm{H}\beta$ and *B*-band absolute magnitude for field galaxies in our intermediate redshift EW sample (filled circles), and the NFGS sample of local star-forming galaxies (open circles). The solid line is the fit of Jansen et al. (2001).

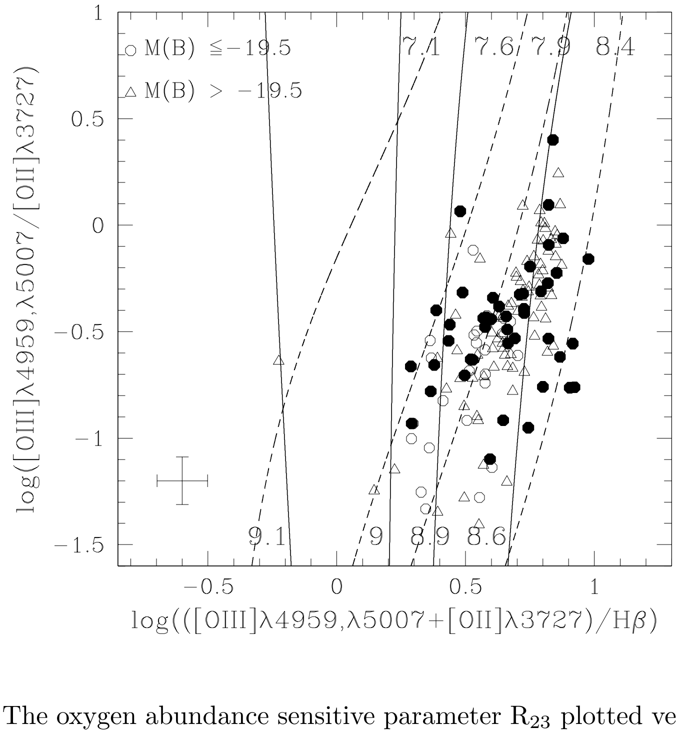

Figure 4.13. The oxygen abundance sensitive parameter R_{23} plotted versus the ionisation sensitive parameter O_{32}. Field galaxies in our intermediate-redshift EW sample are indicated by filled circles. The NFGS sample of local star-forming galaxies is also plotted, with open triangles showing faint galaxies ($M_B > -19.5$) and open circles showing bright ($M_B \leq -19.5$) galaxies. The oxygen abundance calibration of McGaugh (1991) is overlaid, showing tracks of constant metallicity. Models with $12 + \log(\mathrm{O/H}) > 8.5$ are shown by solid lines, while those with lower oxygen abundance are indicated by dashed lines.

The observed excitation- and abundance-sensitive diagnostic ratios for star-forming galaxies in our intermediate-redshift sample are similar to what is exhibited by local star-forming galaxies over much larger luminosity and abundance ranges, i.e., from faint/metal-poor to luminous/metal-rich galaxies. The observed large variation of the interstellar ionised gas properties within luminous field galaxies at intermediate redshift suggests that these galaxies do not represent a homogeneous population of galaxies in terms of the physical properties that shape emission-line galaxy spectra, e.g., the ionising stellar populations and the metal content. This indicates a sizeable evolutionary change of the properties of massive galaxies between $z \sim 0.5$ and the present epoch.

4.5.3 Metallicities

We can examine the difference between local and intermediate-redshift galaxies further by using estimated gas phase oxygen abundances, as described in section 3.2.3. Figure 4.13 shows the relationship between the R_{23} and O_{32} parameters for star-forming galaxies in both the intermediate-redshift and local samples. To show the effect of galaxy luminosity, faint ($M_B > -19.5$) and bright ($M_B \leq -19.5$) galaxies are plotted using different symbols. The McGaugh (1991) calibration of the relationship between R_{23} and O_{32} is over-plotted. Overall, the galaxies in each sample are distributed similarly. However, as shown above, a fraction of luminous intermediate-redshift field galaxies are located in a similar area as faint local star-forming galaxies, with intermediate values of O_{32} and R_{23}.

None of the intermediate-redshift galaxies in our sample have O_{32} significantly larger than unity, similar to the findings of Lilly et al. (2003) for a Hβ-selected galaxy sample and Liang et al. (2004) for a sample of luminous infrared galaxies. Such high O_{32} values are observed for some extragalactic HII regions in nearby galaxies (e.g., van Zee et al. 1998) and a few $z \gtrsim 2$ luminous galaxies (e.g., Kobulnicky & Koo 2000; Pettini et al. 2001; Lemoine-Busserolle et al. 2003). The sample of intermediate-redshift star-forming galaxies studied by Maier et al. (2004) does contain a few galaxies with O_{32} larger than unity. However, all these highly-ionised galaxies are 2–3 magnitudes fainter than the galaxies in our sample.

Figure 4.14 shows the relationship between galaxy B-band absolute magnitude and gas phase oxygen abundance, in terms of $12 + \log(\mathrm{O/H})$, for our EW sample of intermediate-redshift star-forming galaxies compared with several other studies. The comparison samples are the local relation defined by star-forming galaxies from the NFGS sample, and three intermediate redshift samples: the Hβ-selected sample of Lilly et al. (2003), a sample of star-forming galaxies drawn from the Deep Extragalactic Evolutionary Probe (DEEP) survey of Groth Strip galaxies (Kobulnicky et al. 2003), and the sample of intermediate redshift luminous infrared galaxies of Liang et al. (2004).

As expected from the earlier comparison of different diagnostic ratios observed for our sample galaxies with those for local star-forming galaxies, the estimated oxygen abundances for galaxies in our intermediate-redshift sample cover a large range, i.e., $8.4 \lesssim 12 + \log(\mathrm{O/H}) \lesssim 9$, similar to that seen for star-forming galaxies in the NFGS sample, with a mean of 8.7.

The upper-left panel of figure 4.14 shows the well-established correlation between luminosity and oxygen abundance for galaxies in the local universe (e.g., Melbourne & Salzer 2002; Lamareille et al. 2004; Tremonti et al. 2004). This has a large scatter, however, which could be related to the variety of star formation

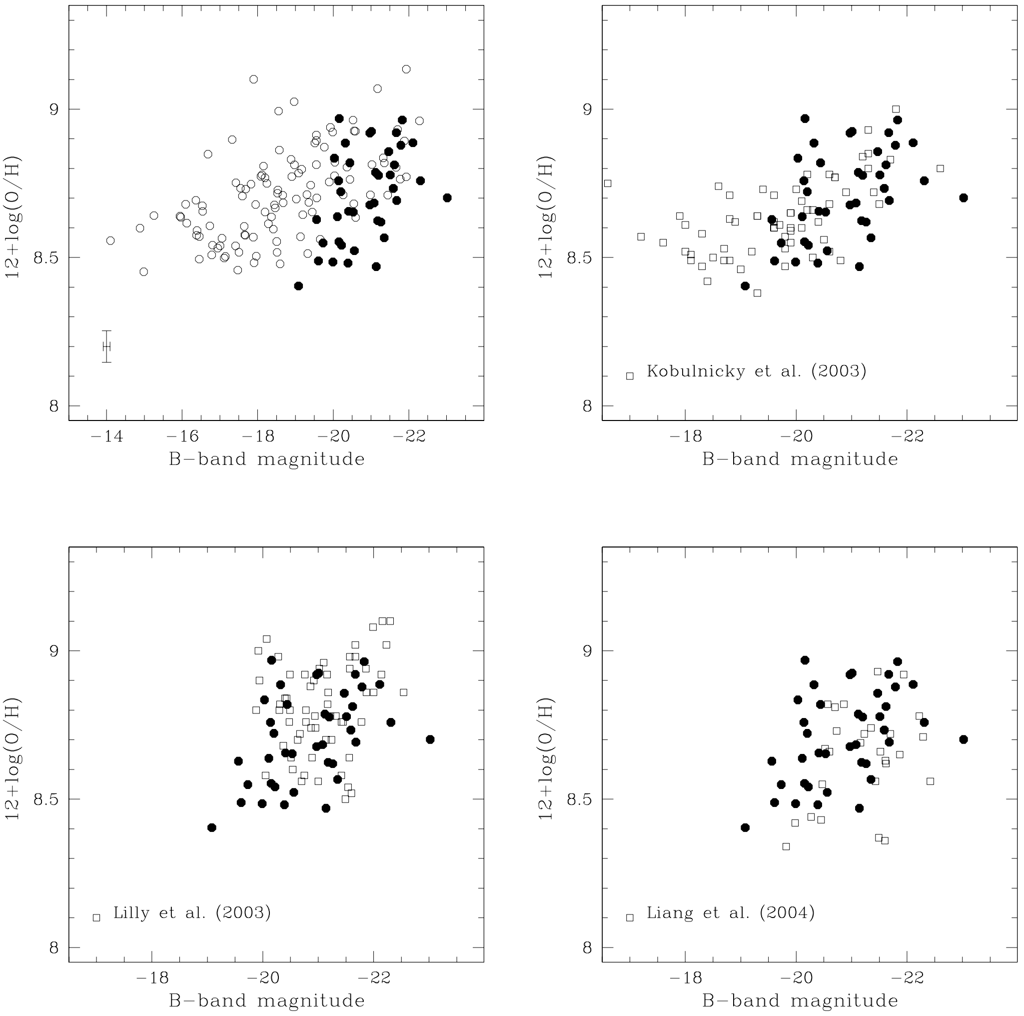

Figure 4.14. The luminosity–metallicity relation for our EW sample of intermediate-redshift star-forming field galaxies (filled circles), compared with several other studies. The comparison samples, shown with open symbols, are: (upper-left) local star-forming galaxies from the NFGS sample; (upper-right) intermediate redshift galaxies, with $0.4 < z < 0.82$, from Kobulnicky et al. (2003); (lower-left) the galaxy sample of Lilly et al. (2003), with $0.47 < z < 0.92$; and (lower-right) luminous infrared galaxies with $0.4 < z < 1.16$ from Liang et al. (2004).

histories in these galaxies (see e.g., Mouhcine & Contini 2002). In contrast, a clear correlation between galaxy luminosity and oxygen abundance is not observed for our sample of star-forming, intermediate-redshift, field galaxies. Rather, a broad range of oxygen abundances at any given galaxy luminosity is observed. Our sample contains luminous galaxies that exhibit oxygen abundances similar to those seen for bright galaxies at the present epoch, i.e., $12 + \log(\mathrm{O/H}) \sim 8.8$–$9$, suggesting that the chemical properties of this population of intermediate redshift galaxies will not evolve significantly to the present epoch. This is in agreement with other recent studies of the chemistry of luminous star-forming galaxies at intermediate redshifts (e.g., Kobulnicky & Kewley 2004).

However, a subsample of luminous, intermediate-redshift, star-forming galaxies show oxygen abundances lower than is observed for local galaxies with similar luminosities, i.e., $12 + \log(\mathrm{O/H}) \sim 8.4$–$8.6$. Given their rotation velocities and physical sizes, the population of metal-poor galaxies in our intermediate-redshift sample is likely to evolve into massive metal-rich galaxies in the local universe. Their evolution will be in metallicity (vertically) rather than luminosity (horizontally). Thus, these galaxies are in the process of building up their metal content. This is in agreement with the suggested scenario of Lilly et al. (2003), who argue, based on optical and near-infrared photometry, morphological properties and oxygen abundances, that bright intermediate-redshift galaxies with intermediate oxygen abundances are likely to evolve into metal-rich disc galaxies at the present epoch, through a progressive enrichment of their metal content, rather than fade into local dwarf galaxies. The appearance of a population of luminous and metal-poor galaxies at intermediate redshifts should affect the slope of the luminosity–metallicity relation at this redshift range, making it flatter than the relation observed locally (see e.g., Kobulnicky & Kewley 2004). The existence of a population of bright, metal-poor galaxies at intermediate redshifts corresponds well with the results of higher redshift studies. Shapley et al. (2005) measure metallicities for a small sample of galaxies at $z \sim 1$ and $z \sim 1.4$, finding them to have similar or lower metallicities at similar or higher luminosities than our intermediate-redshift, metal-poor galaxies.

The upper-right panel of figure 4.14 compares with the sample of Kobulnicky et al. (2003), with $0.26 < z < 0.82$. Note that this study used emission-line equivalent widths rather than fluxes to estimate oxygen abundances, similar to our procedure. The oxygen abundances of both samples cover similar ranges; however the sample of Kobulnicky et al. (2003) extends to fainter luminosities, and unlike our sample shows a trend between galaxy luminosity and oxygen abundance. The galaxies in our intermediate-redshift sample cover a wider range of oxygen abundance at a given luminosity. Overall the Kobulnicky et al. (2003) galaxies tend to be fainter at a given oxygen abundance. However, this difference simply reflects that our sample is limited to brighter galaxies than the rest-frame B-band selected sample from which their sample has been drawn (see also Liang et al. 2004).

The lower-left panel of figure 4.14 compares the luminosity–metallicity relation of our intermediate-redshift star-forming galaxies with a sample of Canada-France Redshift Survey galaxies with $0.47 < z < 0.92$ from Lilly et al. (2003). Both samples show similar luminosity–metallicity relations.

Liang et al. (2004) investigated the luminosity–metallicity relation for a sample of intermediate-redshift, luminous, infrared (15μm-selected) galaxies with $0.4 < z < 1.16$. The comparison between the luminosity–metallicity relation for their sample and for our intermediate-redshift field galaxies is shown in the lower-right panel of figure 4.14. Interestingly, both galaxy samples show similar relations, despite the fact that optically selected galaxy samples and mid-infrared selected galaxy samples tend to select different population of galaxies, i.e., luminous infrared galaxies in the Liang et al. (2004) sample tend to show on average larger internal dust obscuration and intrinsic star formation rates than galaxies in our sample (see section 4.5.4 for a discussion of the distribution of the star formation rate and colour excess for the galaxies in our sample). The similarity of the observed luminosity–metallicity relations might be due to luminous infrared galaxies at intermediate redshifts showing similar rest-frame optical and spectral properties to normal starburst galaxies, and suggests the differences in the selection procedure do not lead to a significant bias against a given class of galaxies (Hammer et al. 2005).

If the assembly of galaxy stellar mass, and subsequently its metal content, is related to the size of the dark matter halo in which it is located, the degree of the interstellar gas chemical evolution may be expected to correlate with the total mass of the galaxy, and hence its rotation velocity and size. The rotation velocity versus metallicity relation for our EW sample field galaxies is shown in the top panel of figure 4.15. No correlation is immediately obvious. However, if the galaxies with $V_{\rm rot} \lesssim 100~{\rm km\,s^{-1}}$are not considered, a reasonable correlation may be seen, such that galaxies with higher rotation velocities tend to be more metal-rich. Such a trend between gas phase oxygen abundance and rotation velocity has been found for local spiral galaxies by Zaritsky et al. (1994), and may be expected from the existence of the stellar mass–metallicity and the baryonic Tully-Fisher relations locally (e.g. Bell & de Jong 2001; Tremonti et al. 2004) and at higher redshifts (Shapley et al. 2005; Conselice et al. 2005). The existence of several systems with low rotation velocities ($V_{\rm rot} \lesssim 100~{\rm km\,s^{-1}}$) but high metallicities is puzzling, and suggests a wide range of star-formation histories for lower mass objects at high redshifts.

The rotation velocity–metallicity relation has been reproduced in chemical hydrodynamic simulations by Tissera et al. (2005). These were conducted in a cosmological, ΛCDM scenario, and find that the relation arises naturally as a consequence of hierarchical galaxy formation. Note that this study uses the stellar oxygen abundance, rather than the gas-phase value measured for our galaxies. However, they find these follow the same trends, though their gas-phase relations show more scatter. Their stellar metallicities require adjustment to match the gas-phase local relation of Tremonti et al. (2004). However, their simulated gas-phase metallicities are higher than the stellar values, and thus reproduce the Tremonti et al. (2004) relation *a priori*, though there are caveats regarding the metallicity being measured in different regions of the galaxies. From these simulations they predict the evolution of the rotation velocity–metallicity relation with redshift, which is shown in the bottom panel of figure 4.15 (figure 4 of Tissera et al. 2005). Given these caveats, our observed $z \sim 0.5$ relation matches the results of the simulations fairly well, though more data, and a wider redshift range, is required in order to test the simulation results quantitatively.

Metallicity is plotted versus size, in terms of the emission-line scalelength, for our EW sample field galaxies in figure 4.16. No convincing correlation is seen between these quantities in our data. For a given size, our intermediate-redshift galaxies exhibit a wide range of oxygen abundances. This is consistent with the lack of a correlation between gas phase oxygen abundance and I-band half-light radius for luminous intermediate-redshift star-forming galaxies reported by Lilly et al. (2003). This suggests that at least a fraction of large galaxies at intermediate redshifts

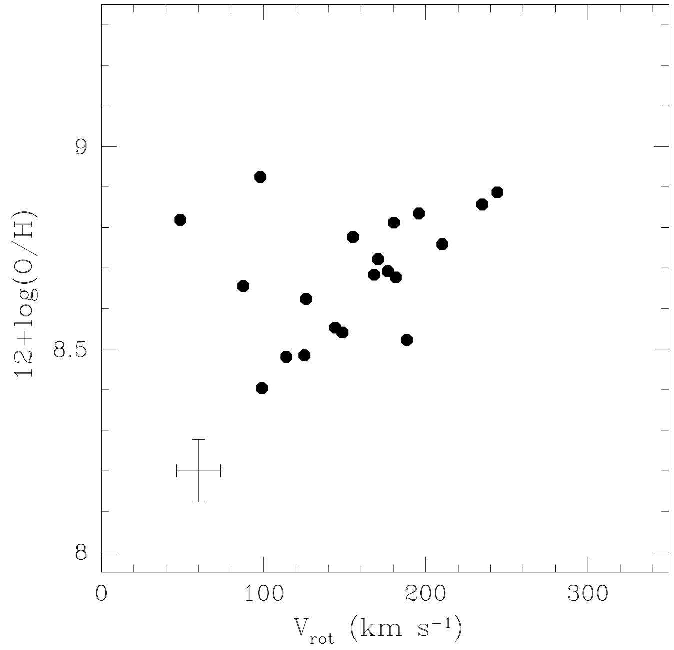

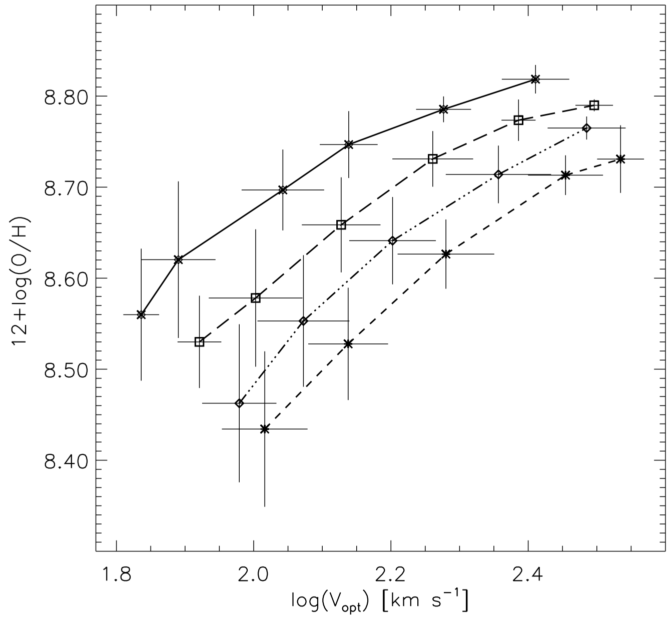

Figure 4.15. (Top) the rotation velocity–metallicity relation for our EW field sample of intermediate-redshift star-forming galaxies. (Bottom) the rotation velocity–metallicity relation, at $z = 3$ (short-dashed lines), $z = 2$ (dotted-dashed lines), $z = 1$ (long-dashed lines) and $z = 0$ (solid lines), from chemical hydrodynamical simulations by Tissera et al. (2005). This is a reproduction of figure 4 from that paper. Error bars correspond to the standard rms dispersion of their simulated relations. Note the different scales for the two plots.

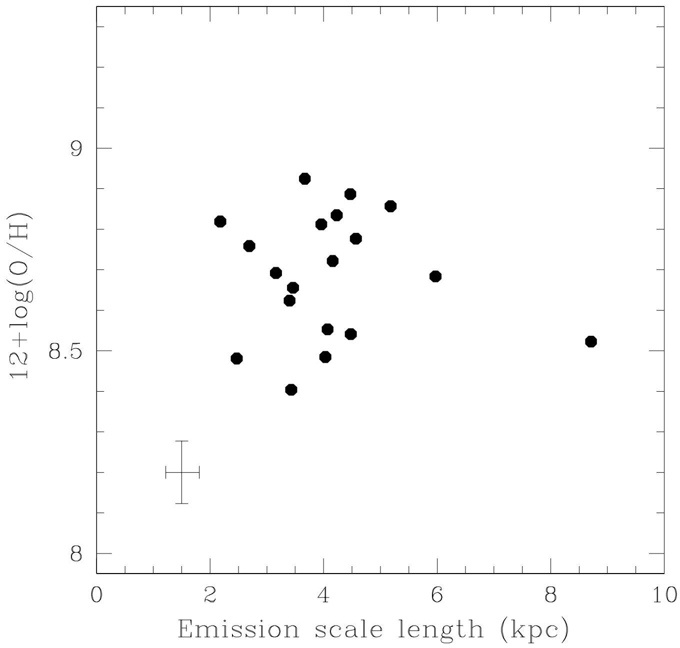

Figure 4.16. The emission scalelength versus metallicity relation for intermediate-redshift star-forming field galaxies in our EW sample.

continue the assembly of their chemical content after $z \sim 1$. Metal-rich and metal-poor galaxies cover similar ranges of rotation velocity and physical size, implying that both galaxy populations reside within similar halos, and that the size of the halo is not the only parameter that affects galactic chemical enrichment history.

4.5.4 Star formation rates and dust obscuration

We have found that luminous field galaxies at intermediate redshifts consist of a mixture of galaxies with different levels of chemical evolution and interstellar gas properties. This indicates that these galaxies have a variety of star formation histories, and thus could exhibit further differences in their intrinsic properties.

Figure 4.17 shows the relationship between gas phase oxygen abundance, in terms of $12 + \log(\mathrm{O/H})$, and the rest-frame equivalent width of the [OII] and Hβ emission-lines, respectively. There is a clear correlation between oxygen abundance and [OII] equivalent width, but no convincing trend is seen between oxygen abundance and Hβ equivalent width, as also found by Lilly et al. (2003) and Kobulnicky et al. (2003). This is intriguing, but could just be due to an unreliable correction of the underlying stellar Balmer absorption lines introducing extra scatter into the relation.

Emission-line equivalent widths can be considered as rough tracers of the current star formation rate relative to the total past-integrated star formation rate, i.e., the star formation rate per unit luminosity. Our intermediate-redshift and local star-forming galaxy samples are distributed similarly in the oxygen abundance versus emission-line rest-frame equivalent width diagrams. This suggests that massive, metal-poor field galaxies at intermediate redshifts might have similar relative star formation histories to local faint and metal-poor star-forming galaxies. The observed trend might be taken to suggest that systems with low metallicities on average show higher relative star formation rates than metal-rich galaxies. The absence of

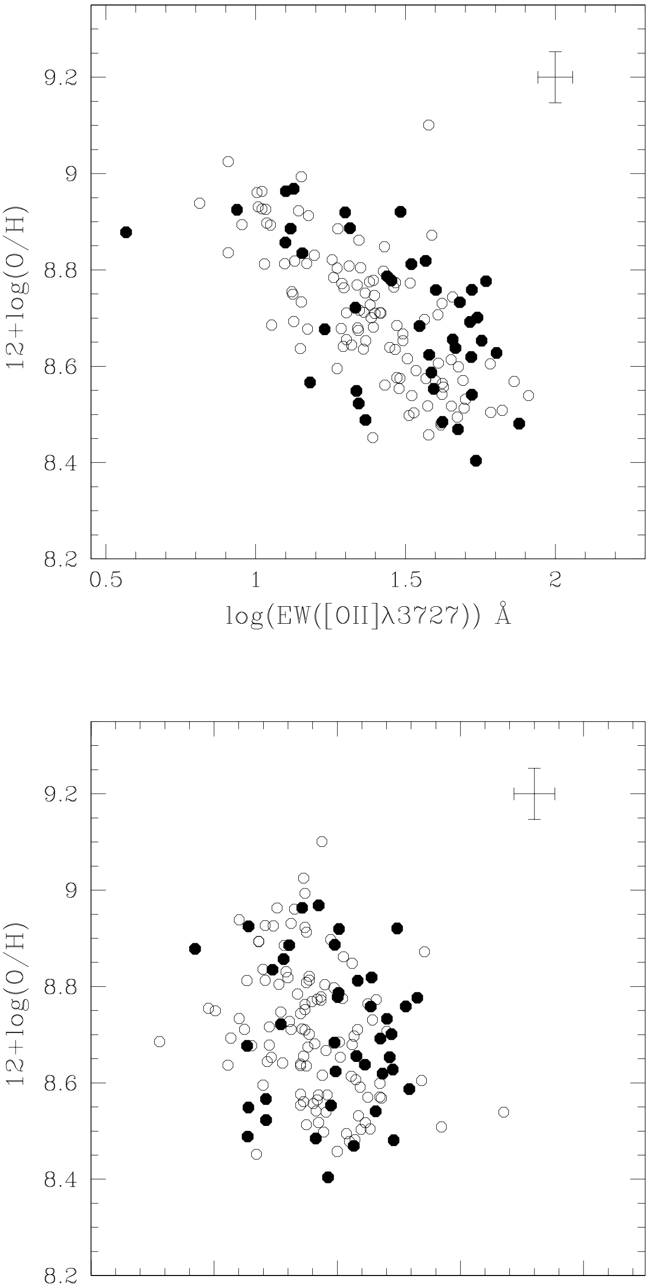

Figure 4.17. The relationship between oxygen abundance, $12 + \log(\mathrm{O/H})$, and *(left)* [OII]$\lambda3727$ and *(right)* Hβ equivalent widths for field galaxies in our intermediate redshift EW sample (filled circles), and the NFGS sample of local star-forming galaxies (open circles).

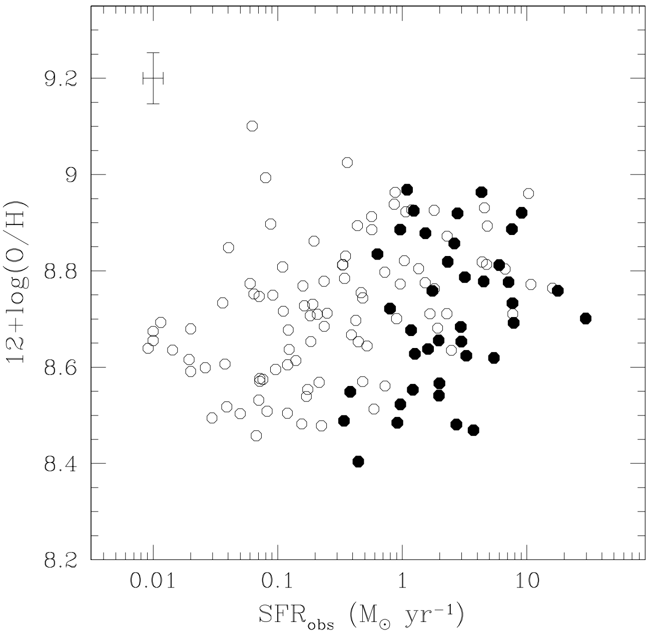

Figure 4.18. The relationship between oxygen abundance, $12 + \log(O/H)$, and star formation rate, derived from Hβ (uncorrected for extinction due to dust), for field galaxies in our intermediate redshift EW sample, shown as filled circles. Star formation rates for the NFGS sample of local star-forming galaxies, derived from Hα but also uncorrected for extinction, are indicated by open circles.

a correlation between oxygen abundance and rotation velocity suggests that this might be the case independent of the size of the galaxy halo.

Figure 4.18 shows oxygen abundance as a function of observed star formation rate for both the local NFGS comparison sample and our intermediate-redshift EW field galaxy sample (see section 3.2). The determination of these star formation rates are described in sections 4.5.1 and 3.2.4, respectively. These are not corrected for internal reddening, and thus must be considered as lower limits.

Local star-forming galaxies exhibit a correlation between the oxygen abundance of their interstellar gas and the extinction-uncorrected star formation rate, in the sense of higher oxygen abundances for galaxies with higher observed star formation rate, i.e., observed Balmer emission luminosity. However, no clear trend is obvious for our luminous, star-forming, intermediate-redshift galaxies: metal-poor and metal-rich galaxies cover a similar range of extinction-uncorrected star formation rate. The metal-rich intermediate-redshift galaxies show extinction-uncorrected star formation rates similar to their local counterparts. This could be the case if metal-rich luminous galaxies at intermediate redshift have star formation rates and internal dust obscuration similar to their counterparts at the present epoch. However, this could also be the case if they show both higher/lower Balmer intrinsic emission-line fluxes and lower/higher internal reddening than metal-rich star-forming galaxies locally. On the other hand, metal-poor luminous galaxies at intermediate redshift show, on average, larger extinction-uncorrected star formation rates than local galaxies with similar gas phase oxygen abundances. This suggests that metal-poor galaxies at intermediate redshift have higher intrinsic star formation rates

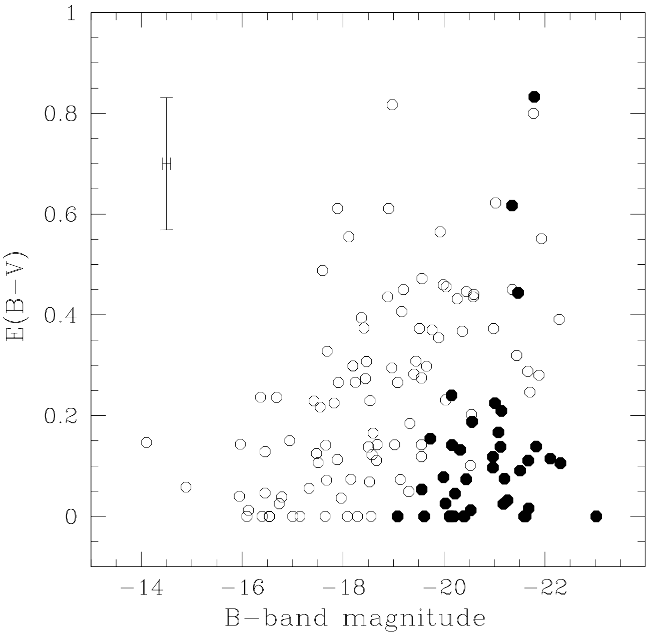

Figure 4.19. Colour excess versus absolute B band magnitude. Field galaxies in our intermediate redshift EW sample are shown by filled circles, while open circles indicate local star-forming galaxies from the NFGS sample.

and/or lower internal reddening than their local counterparts. To disentangle these possibilities, we can estimate the internal dust obscuration affecting the galaxies, as described in section 3.2.4.

Figure 4.19 shows the estimated colour excess as a function of luminosity for the field galaxies in our intermediate-redshift EW sample and the local NFGS comparison sample. The colour excesses for intermediate-redshift galaxies are distributed over a range similar to that seen across a large sample of local star-forming galaxies with $-14.0 \lesssim M_B \lesssim -22.0$. However, the mean colour excess for intermediate redshift galaxies in our sample, i.e., 0.16 ± 0.03 when excluding galaxies with $E(B-V) = 0$ and 0.12 ± 0.03 when all galaxies are included, is significantly lower than the observed average colour excess, $E(B-V) \sim 0.3$, for local star-forming galaxies (e.g., Nakamura et al. 2004; Hopkins et al. 2003; Kewley et al. 2004; Mouhcine et al. 2005). Bright, star-forming galaxies at intermediate redshifts show a wide variation in colour excess: a fraction have amounts of dust obscuration similar to what is observed for their local counterparts, while another subpopulation has low dust obscuration, similar to that observed locally only for much fainter galaxies.

Comparisons of different star formation rate indicators for local samples of star-forming galaxies have shown a clear trend for increasing dust obscuration with intrinsic star formation rate (e.g. Wang & Heckman 1996; Sullivan et al. 2001; Buat et al. 2002). The lower panel of figure 4.20 shows the relationship between the inferred Balmer decrement and the extinction-corrected star formation rate for both the local comparative sample and our EW sample of intermediate-redshift star-forming field galaxies. The distribution of local star forming galaxies in the NFGS sample agrees nicely with the local galaxy relationship from Hopkins et al. (2001); however

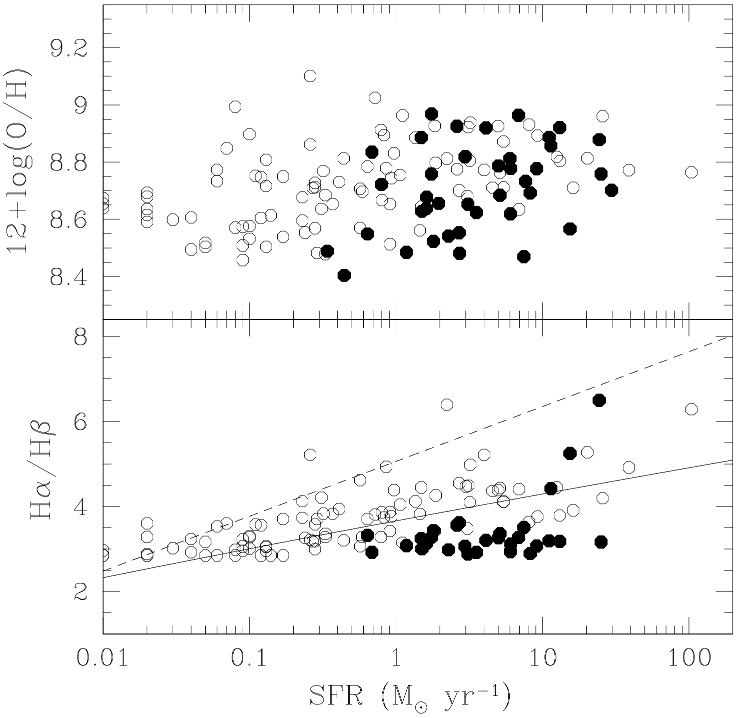

Figure 4.20. (Top) the relationship between oxygen abundance and extinction-corrected star formation rate for the sample of intermediate redshift star-forming galaxies (filled circles), and the local sample of star-forming galaxies from the NFGS sample (open circles). (Bottom) the relationship between Balmer decrement and extinction-corrected star formation rate. Symbols are the same as for the upper panel. The solid line represents the relationship derived by Hopkins et al. (2001) for a sample of local star-forming galaxies, while the dashed line indicates the relationship for a sample of radio-selected galaxies from Afonso et al. (2003).

they deviate significantly from the relationship observed for radio-selected galaxies by Afonso et al. (2003). This could be because radio-selected galaxy samples tend to be biased toward dustier galaxies than optically selected samples. The galaxies in our intermediate-redshift galaxy sample deviate systematically from the fit of Hopkins et al. (2001), especially those with star formation rates lower than ~10 M$_\odot$ yr^{-1}, indicating that for a given star formation rate, these galaxies show on average lower internal reddening than their local counterparts. Galaxies with star formation rates larger than ~10 M$_\odot$ yr^{-1} display Balmer decrements and a scatter similar to that observed for local star-forming galaxies.

The upper panel of figure 4.20 shows the relationship between gas phase oxygen abundance and extinction-corrected star formation rate for both the local comparison sample and our sample of intermediate-redshift galaxies. The trend observed locally between oxygen abundance and extinction-uncorrected star formation rate (see figure 4.18) is still visible after the extinction correction is performed. No convincing trend is observed for the intermediate-redshift galaxies. Metal-poor luminous galaxies at intermediate redshifts show higher extinction-corrected star formation rates than observed locally for galaxies with similar oxygen abundances, while metal-rich luminous galaxies show extinction-corrected star formation rates similar to those

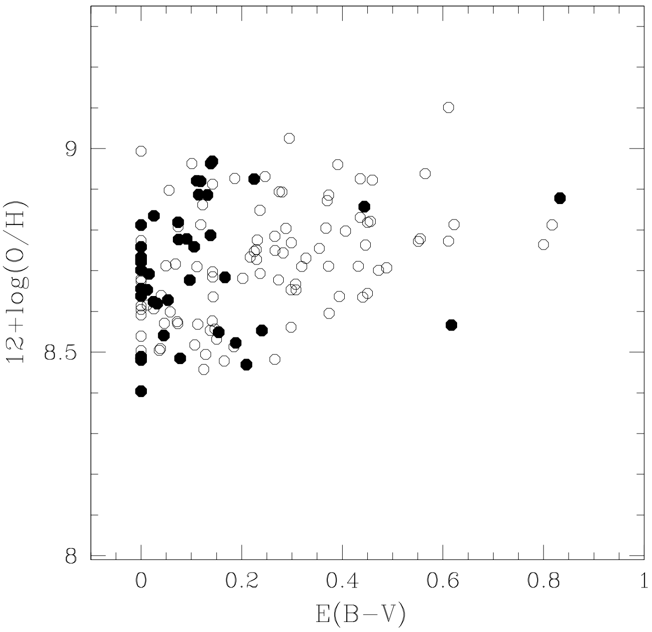

Figure 4.21. Colour excess versus oxygen abundance, $12 + \log(\mathrm{O/H})$. Field galaxies in our intermediate redshift EW sample are shown by filled circles, while open circles indicate local star-forming galaxies from the NFGS sample.

observed for their local counterparts. This agrees with the results reported recently for a sample of Canada-France Redshift Survey galaxies (Maier et al. 2005).

There have been contradictory claims regarding a possible correlation between dust obscuration and metallicity of galaxies in the local universe. Zaritsky et al. (1994) reported no clear evidence for a sensitivity of internal reddening to abundance in a sample of disc galaxies, suggesting that abundance and extinction are not necessarily linked. For other local samples, however, it has been found that the extinction derived from the Balmer decrement correlates with metallicity (e.g., Stasińska & Sodré 2001; Kong et al. 2002). The observed trends between galaxy luminosity, metallicity, dust extinction and star formation rate suggest that the main driver of the extinction in local star-forming galaxies is their mass, combined with their metallicity (and probably the presence of old stellar populations; Stasińska et al. 2004).

Figure 4.21 shows gas phase oxygen abundance as a function of colour excess for our sample of intermediate-redshift galaxies and the local comparison sample. Locally, a positive trend is apparent between oxygen abundance and colour excess, although with a large scatter (see Stasińska & Sodré 2001, and Kewley et al. 2004, who analysed the properties of the same local galaxy sample). In this diagram the luminous star-forming galaxies in our intermediate-redshift sample are distributed fairly similarly to the local star-forming galaxies in the NFGS sample, although they have lower $E(B - V)$ on average. Combining this with the absence of a correlation between galaxy luminosity and colour excess for our intermediate-redshift galaxies, one might conclude that the dust obscuration is primarily a function of the level of galaxy chemical enrichment rather than luminosity.

4.5.5 Discussion

We have thus found that the properties of the interstellar star-forming gas in luminous, massive, large field galaxies at intermediate redshifts cover a wide range. They extend from those observed for local bright, metal-rich, star-forming galaxies, i.e., weak emission-lines, low ionisation conditions, high oxygen abundances and high dust obscuration, to those of local metal-poor, star-forming dwarf galaxies, i.e., strong emission-lines, high ionisation conditions, low oxygen abundances, and low dust obscuration.

A fraction of massive field galaxies at intermediate redshifts have already undergone a significant chemical enrichment, as indicated by their high oxygen abundances. This suggests that this population of galaxies have already formed a large fraction of the stellar mass observed at the present epoch in massive, metal-rich galaxies. This is consistent with the reported mild evolution of the galaxy stellar mass function of the massive galaxy population since $z \sim 1$, implying that the evolution of these galaxies is essentially complete by this redshift (e.g., Brinchmann & Ellis 2000; Drory et al. 2004; Fontana et al. 2004; Bundy et al. 2005). In addition, the relationship between stellar mass and maximum rotation velocity, i.e., the baryonic Tully-Fisher relation, out to $z \sim 1$ seems to largely agree with the local relation (Conselice et al. 2005). These observations are consistent with the downsizing picture for galaxy evolution, in which star formation activity ceases for high mass galaxies at earlier cosmic epochs than for less massive galaxies (e.g., Cowie et al. 1997).

On the other hand, a sub-population of large, massive and luminous intermediate-redshift, star-forming galaxies appear to be at earlier stages of the assembly of their content of metals, as indicated by their low oxygen abundances. This suggests that they are probably also at earlier stages of assembling their stellar masses, as both stellar and metal contents of galaxies are thought to be linked. Metal-poor luminous galaxies at intermediate redshift would therefore be expected to deviate from the local baryonic Tully-Fisher relation.

Hammer et al. (2005) have presented a body of evidence to show that present-day intermediate stellar mass galaxies, i.e., with stellar masses of 3–30 × 10^{10} $M_\odot$, have built up half of their stellar mass since $z \sim 1$, and emphasise the importance of luminous infrared galaxies, thought to be starbursts resulting from merging at these masses. The star formation in luminous infrared galaxies accounts for most of the stellar mass growth in these galaxies since $z \sim 1$. They argue that recent merging and gas infall explain both star formation history and morphological changes in a hierarchical galaxy formation scheme, where more than 50 per cent of spiral galaxies experienced their last major merger event less than 8 Gyr ago. Intermediate redshift luminous infrared galaxies show oxygen abundances two times lower than local bright disc galaxies (Liang et al. 2004). The presence of a population of intermediate-redshift massive and luminous star-forming galaxies with oxygen abundances lower than those observed locally for similar galaxies, supports the scenario in which the assembly of intermediate stellar mass galaxies is still operating between $z \sim 1$ and $z = 0$.

Our observations suggest that in some ways both of these competing scenarios are correct, but for different populations. Rather than a smooth change in the star formation properties of the field galaxy population with redshift, we see evidence that the evolution is highly stochastic. Some galaxies appear to have already completed most of their star-formation and chemical evolution by $z \sim 0.5$, while others, inhabiting apparently similar haloes, are in the early stages of their development. This is broadly consistent with the findings of our Tully-Fisher study (described in section 4.2) and the star formation evolution inferred from it (in section 4.4), where we found fairly little evolution with redshift in the luminosity and star formation rate of galaxies at a given rotation velocity. This may be expected if different galaxies experience a range of star formation histories, both declining and initially increasing, between intermediate redshifts and today. If this behaviour depends on the mass of the host halo, then we would expect a change in slope of the TFR. However, although we do not constrain it well, we do not see any evidence for TFR slope evolution. This implies, in agreement with our chemical evolution findings, that it is the stellar mass of galaxies at a given time which determines their subsequent star formation evolution.

The sample studied in this paper is by no means complete. The implications of our findings for constraining galaxy assembly from $z \sim 1$ to the present epoch are thus only tentative. Additional work to determine the properties of metal-poor massive galaxies and their evolution, e.g., number density, stellar masses, and morphologies, is needed to help reveal the nature of star formation evolution over the last $\sim$8 Gyr. In the near future, further studies will be able to measure chemical properties and stellar masses of many more star-forming galaxies at intermediate redshifts, in order to tightly constrain the assembly of the stellar and metal content of present day galaxies. Large galaxy surveys like DEEP2 (Davis et al. 2003) and EDisCS (White et al. 2005) are promising, as they will observe large samples of galaxies distributed over a wide area and redshift range.

Chapter 5

Cluster results

The analysis and results described in this chapter which relate to the Tully-Fisher relation have been presented previously in Bamford et al. (2005). All of this work was directly performed by the author of this thesis, with advice from the coauthors of the paper, Alfonso Aragón-Salamanca and Bo Milvang-Jensen.

The work based on the spatially integrated spectral measurements is presented in Mouhcine et al. (2006a), and was principally done in collaboration with Mustapha Mouhcine. Note that despite not being first author of Mouhcine et al. (2006a), the author of this thesis played a highly significant role in determining the content of the entire paper, and wrote much of the text.

5.1 Overview

In this chapter we investigate the differences between luminous, star-forming, disc galaxies in rich, intermediate-redshift clusters and their counterparts in the coeval field. We do this by comparing their Tully-Fisher relations (TFRs), star-formation rates, metallicities, and extinctions. Our aim is to take a step towards determining which of the proposed star-formation histories plotted in figure 1.2 best describes the evolution of star-forming discs interacting with the cluster environment, and hence the dominant mechanism responsible for the apparent transformation of spirals to S0s in clusters. Emission-line luminosities and equivalent widths allow us to measure the instantaneous star-formation rate, and its level relative to past star formation, while B-band luminosities give an indication of the amount of recent star formation. Both of these allow us to probe the recent effects of any environmental interaction. However, it is important to check whether the cluster galaxies under study have long-term star formation histories that are intrinsically different to those in the field. The gas-phase metallicity of the galaxies should provide such an indication.

5.2 Tully-Fisher relation

Our target selection has been performed in a way designed to give easily comparable samples of field and cluster galaxies, however further efforts are required to ensure these samples are well matched. While the cluster galaxies are located at particular redshifts, between $0.30 \lesssim z \lesssim 0.85$, the field galaxies span a much wider range in redshift, and consequently in absolute magnitude. As the TFR may evolve with redshift, irrespective of environment (e.g., see section 4.2), care must be taken to avoid this complicating the comparison between cluster and field. In particular, the

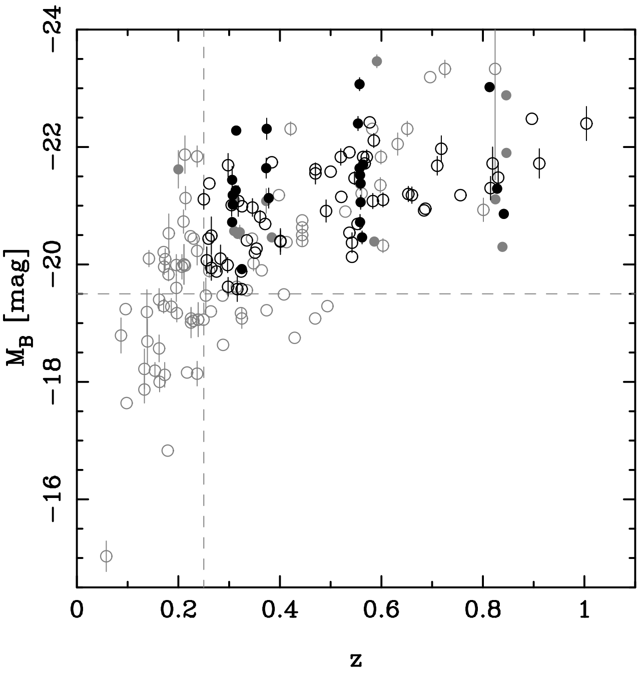

Figure 5.1. Absolute rest-frame B-band magnitude versus redshift for *all* our field (open points) and cluster (filled points) galaxies with emission-lines. Points in our final 'matched' TFR sample are black, while those not included are grey. Grey points thus denote galaxies for which no lines pass our quality criteria or which do not meet our M_B or z cuts. Error bars are not shown where they are smaller than the symbols. Adopted cuts for the 'matched' samples are shown by dashed lines.

evolution of low-luminosity galaxies, which are not represented in our sample at higher redshifts, is particularly unconstrained. We therefore impose cuts of $z \geq 0.25$ and $M_B \leq -19.5$ mag, simply chosen to better match the distribution of field galaxies to that of the cluster sample, as indicated in figure 5.1.

The 'matched' TFR sample used for the cluster−field comparison in this thesis thus contains a total of 80 galaxies, comprising 58 field and 22 cluster galaxies.

Now we have established samples of field and cluster galaxies over similar epochs and luminosity ranges, we can investigate whether the samples differ in other ways. The distributions of M_B, $V_{\rm rot}$, $r_{\rm d,spec}$ and $r_{\rm d,phot}$ are shown in figure 5.2, with the K-S test confidence levels that the parent distributions of the two samples are the same. Note from figures 5.2(a) and 5.1 that the cluster and field galaxies cover a very similar range in M_B, with a hint that the cluster galaxies extend to brighter magnitudes. There should be absolutely no difference in the selection of galaxies at the bright end of this distribution. This is therefore a first indication that cluster spirals may be brighter than those in the field.

The distributions of galaxy size, in terms of both photometric and spectroscopic scalelength (figure 5.2 panels (b) and (d)), are similar for the field and cluster samples. For $r_{\rm d,phot}$ they are practically identical, although it is worth noting that the cluster members do extend to larger values. On the other hand, the cluster $r_{\rm d,spec}$ distribution is restricted to lower values than the field.

The two samples cover the same range in $V_{\rm rot}$, although there is evidence that the cluster galaxies have a slightly broader distribution, possibly more skewed to lower values. This is considered further below. However, these differences are minor, and

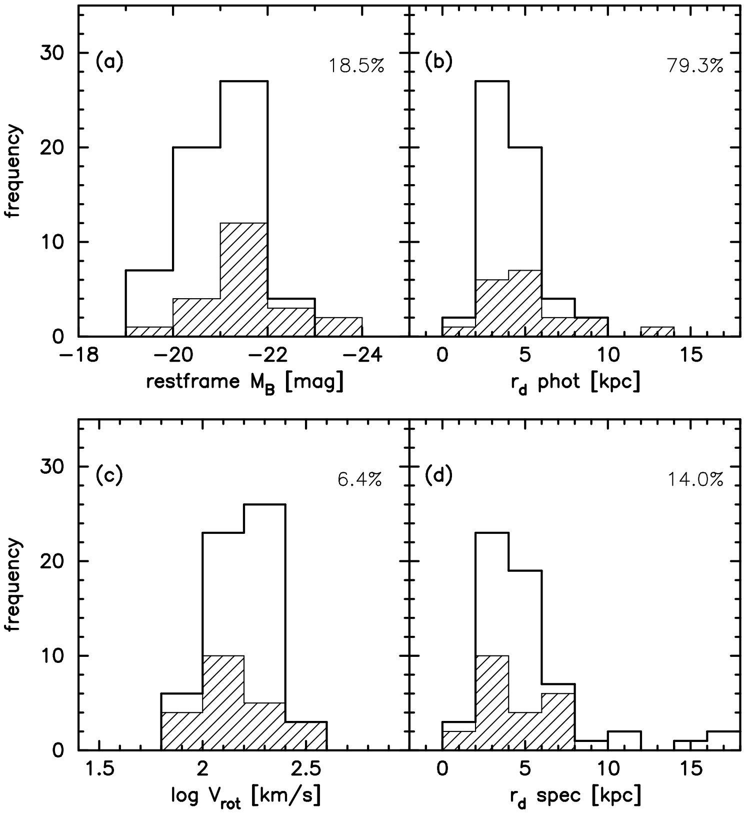

Figure 5.2. The distributions of (a) absolute rest-frame B-band magnitude (M_B), (b) photometric disc scalelength ($r_{\rm d,phot}$), (c) rotation velocity ($V_{\rm rot}$), and (d) spectroscopic emission scalelength ($r_{\rm d,spec}$) for the galaxies in our final 'matched' TFR sample. The empty histogram corresponds to field galaxies, while the hatched histogram corresponds to cluster members. The percentage in the top right corner of each panel indicates the confidence that the field and cluster samples are drawn from identical parent distributions, as given by a K-S test.

point at real characteristics of the galaxy population, rather than a selection bias.

5.2.1 Cluster versus field TFR

Figure 5.3 shows the TFR for our 'matched' samples of field and cluster galaxies. A fiducial local field TFR is indicated by the thin lines. This is derived from the TFR of Pierce & Tully (1992, hereafter PT92), with a zero-point adjustment because PT92, while otherwise using the internal extinction correction of Tully & Fouque (1985), do not include the 0.27 mag of face-on extinction that is applied to our data. The fiducial PT92 TFR, adapted to our internal extinction correction, is given by equation 4.7.

The thick solid line in figure 5.3 is a fit to the matched field sample. This is a weighted, least-squares fit, minimising the residuals in $V_{\rm rot}$ (referred to as an 'inverse' TFR fit) and incorporating an intrinsic scatter term, as described in more detail in section 4.2.1. The thick dotted and dashed lines are fits to the cluster sample, performed by the same method, except for the dashed line the slope was fixed to that of the fit to the matched field sample. The fit to the matched field

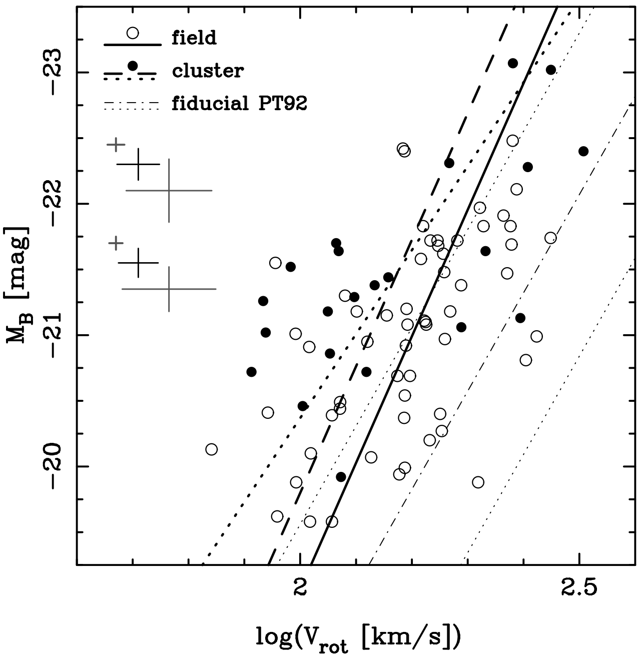

Figure 5.3. The Tully-Fisher relation for our 'matched' samples of field (open points) and cluster (filled points) galaxies. The fiducial local relation of Pierce & Tully (1992) is marked by the thin dot-dashed line, with its 3σ scatter delimited by thin dotted lines. Weighted least-squares fits to the matched field sample (solid line) and cluster sample (constrained to the field slope: dashed line, free slope: dotted line) are also marked. The two sets of error bars shown on the left indicate the 10th-, 50th- and 90th-percentile errors for field *(top)* and cluster *(bottom)* points.

sample, and cluster samples with free and fixed slopes, respectively give

$$\begin{aligned} M_B &= (-9.6 \pm 1.7) \cdot \log V_{\rm rot} + (0.2 \pm 3.8) \, , \\ M_B &= (-6.4 \pm 1.5) \cdot \log V_{\rm rot} + (-7.6 \pm 5.5) \, , \\ M_B &= -9.6 \cdot \log V_{\rm rot} + (-0.5 \pm 0.3) \, . \end{aligned} \tag{5.1}$$

The slope of the fit to the cluster sample is markedly shallower than that to the matched field sample. However, the slopes only differ by 1.4σ, so this not a significant result.

The weights ($w_{\rm TF}$) assigned to each galaxy in the above fits are given in table 3.1. These are calculated from the reciprocal of the sum of the squared uncertainties in $V_{\rm rot}$ and M_B and the intrinsic scatter. The best fit is determined iteratively, because of its dependence on the slope (used to convert the M_B error into one in $V_{\rm rot}$) and intrinsic scatter. The $w_{\rm TF}$ only differ by $\lesssim 0.001$ between the two alternative cluster fits; the values for the free-slope fit are given.

It can be seen that the field galaxies lie primarily along a reasonably tight relation, with similar slope to the local fiducial TFR, but with an offset to brighter magnitudes and/or lower rotation velocities. This is particularly clear when considering the full field sample, unrestricted in M_B, as in section 4.2. This overall, systematic offset from the fiducial local TFR is of little concern for this study. A comparison with the intercept of the PT92 TFR must consider the different manners in which the magnitudes and rotation velocities are measured for the two studies. It is also likely that the absolute calibration of the PT92 TFR is incorrect by ~0.5

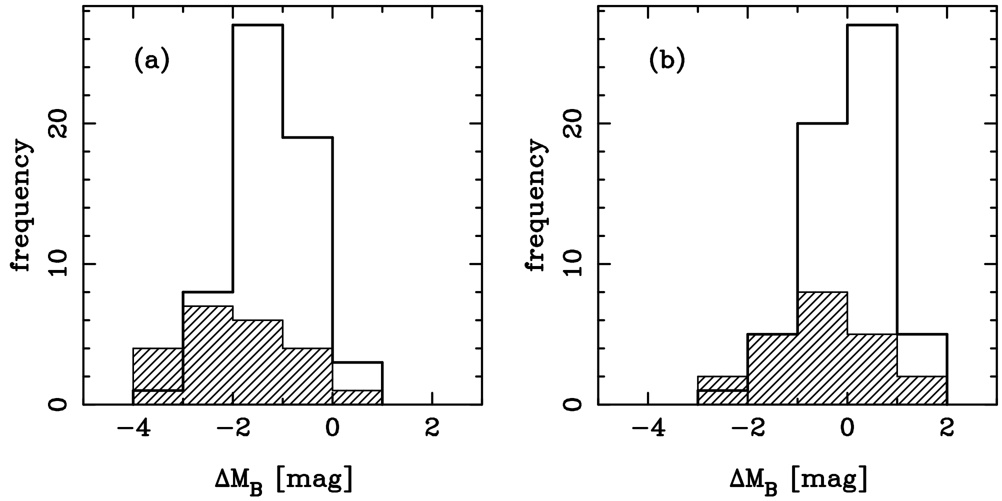

Figure 5.4. The offset from the fiducial Tully-Fisher relation of PT92 for our 'matched' samples of field (empty histogram) and cluster (shaded histogram) galaxies. Panel (a) shows the distributions of $\Delta M_B{}^{\mathrm{TF}}$, while in (b) $\Delta M_B{}^{\mathrm{TF}}$ has been corrected for the field evolution with redshift found in section 4.2.2. The K-S probabilities for the cluster and field distributions being the same are (a) 0.1% and (b) 0.8%.

mag, as discussed further in section 4.2.1. Correcting for this would bring the fiducial TFR into closer agreement with our field sample, particularly for the low redshift objects.

The cluster members are preferentially located above the field relation, particularly for galaxies with lower rotation velocities $\lesssim 150\ \mathrm{km\,s^{-1}}$, as also indicated by the shallower slope of their TFR fit. To help compare the field and cluster samples we can take out the slope and examine the residuals from the fiducial TFR (equation 4.8).

The difference between the cluster and field galaxies is particularly evident in a histogram of $\Delta M_B{}^{\mathrm{TF}}$, as shown in figure 5.4(a). The peaks of the distributions are clearly not aligned, such that cluster galaxies are generally brighter at a fixed rotation velocity. A K-S test gives the probability of the parent distributions being the same as 0.1%.

To assess this offset more quantitatively we can consider the mean and variance of $\Delta M_B{}^{\mathrm{TF}}$ for each of the samples. These are calculated in a similar manner to the TFR fitting method described in section 4.2.1. Weighted means and variances are calculated, with weights assigned from the measurement errors in combination with an iteratively-determined intrinsic scatter. The derived offset between the cluster and field samples is 0.7 ± 0.2 mag. A t-test gives the significance of this offset as 3σ.

It could be suggested that the offset we find between field and cluster galaxies is due to the combination of a general (field) trend with redshift and a difference between the redshift distribution of the field and cluster samples. In order to demonstrate that this is not the case we plot $\Delta M_B{}^{\mathrm{TF}}$ versus redshift in figure 5.5. Despite a possible trend in $\Delta M_B{}^{\mathrm{TF}}$ with redshift for the field population, as examined in section 4.2.2, the offset is clearly still present, with cluster galaxies consistently brighter for the same rotation velocity and redshift. The best-fitting field evolution from section 4.2.2 is

$$\Delta M_B{}^{\mathrm{TF}} = (-1.0 \pm 0.5) \cdot z + (0.8 \pm 0.2)\ \mathrm{mag} \tag{5.2}$$

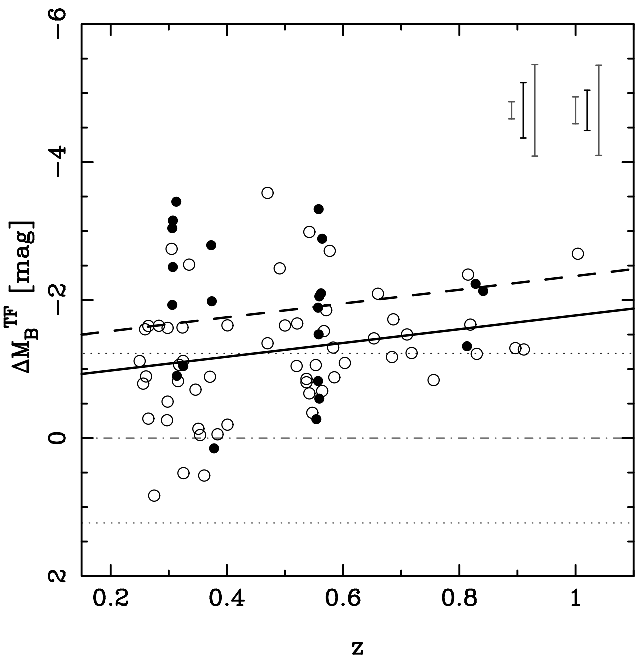

Figure 5.5. The residuals from the fiducial Tully-Fisher relation of PT92 for our matched TFR samples of field (open points) and cluster (filled points) galaxies, plotted versus redshift. The fiducial local relation of Pierce & Tully (1992) is marked by the thin dot-dashed line, with its 3σ scatter delimited by thin dotted lines. Weighted least-squares fits to the full field TFR sample from section 4.2.1 (solid line) and the cluster sample (constrained to the field slope: dashed line) are also marked. The two sets of error bars in the upper-right corner indicate the 10th-, 50th- and 90th-percentile errors for field *(left)* and cluster *(right)* points.

Subtracting this field evolution does not change either the size or significance of the cluster−field offset. This can also be seen in figure 5.4(b), a histogram of $\Delta M_B{}^{\mathrm{TF}}$ with the field evolution taken out, although the K-S significance declines slightly.

Note that we have selected cluster galaxies in each field simply from their redshifts coinciding with the targeted clusters. It is possible that a number of the galaxies we classify here as 'field' actually reside in separate high density regions. Unfortunately, our sample is not large enough to identify additional groups in our field. It will be interesting to see if the field scatter is reduced in future studies, when such groups can be excluded, and whether the group spirals inhabit the same region of the TFR as our cluster sample.

5.2.2 Origin of the TFR cluster−field offset

It is clear that there is a significant difference between the cluster and field galaxies in our sample. As the galaxies have all been selected, observed and analysed in the same manner, it is very likely this difference is real. Now we must consider the reasons for this disparity. The offset from the field TFR may be due to some effect causing cluster galaxies to appear brighter for a given rotation velocity, slower-rotating for a given magnitude, or a combination of both. Physically, both scenarios are possible, an enhancement of star-formation would lead to a brightening, while stripping of the dark matter halo by the cluster potential could, at least hypothetically, decrease the galaxy mass and hence lower V_{rot}.

Simulations by Gnedin (2003b, hereafter G03b) find that V_{rot} changes little ($\lesssim$

5% decrease), even when over half of a galaxy's dark-matter halo is stripped away. This is because the halo is truncated to a galactocentric radius that lies beyond the edge of the luminous disc. Within the region that the galaxy is luminous – and thus its rotation can be measured – the halo is mostly unaffected, the enclosed mass stays constant, and therefore $V_{\rm rot}$ remains the same.

G03b uses a pseudo-isothermal initial dark matter density profile. This is 'cored' (finite at the centre), as opposed to the 'cuspy' halo profiles generally produced by CDM simulations (Navarro et al. 1996; Moore et al. 1998). However, cored profiles (van Albada et al. 1985; Burkert 1995) seem to be required for galaxy haloes, from observations of individual rotation curve shapes (e.g. Gentile et al. 2004), and in order to solve the problem of reproducing the TFR zeropoint in a hierarchical universe (Navarro & Steinmetz 2000). If galaxy haloes are instead actually cuspy, it would be even harder to remove dark matter from their inner regions than found by G03b. From this point of view their result provides an upper limit on the feasible change in $V_{\rm rot}$ due to tidal interaction with a cluster.

However, higher resolution simulations using a different code, also performed by G03b, find slightly larger decreases in $V_{\rm rot}$ of $\sim 15\%$. Adopting the slope of the PT92 TFR, this corresponds to an apparent brightening at fixed rotation velocity of ~ 0.5 mag, comparable to the TFR offset we measure.

In addition, the G03b simulations discussed above are based on galaxies with $V_{\rm rot} = 250$ km s^{-1}. Less massive galaxies, with correspondingly less dense haloes, may well be more seriously affected. For example, G03 find that low surface brightness galaxies with comparable masses, but much more extended haloes, suffer decreases in $V_{\rm rot}$ of $\gtrsim 20\%$, while dwarf galaxies, with initial $V_{\rm rot} = 20$ km s^{-1}, are completely destroyed. This could explain why most of our cluster galaxies with large TFR offsets have low rotation velocities, $V_{\rm rot} \lesssim 150$ km s^{-1}. Further simulations would be helpful to establish how the effectiveness of tidal stripping depends upon the initial rotation velocity of infalling galaxies.

With our present data, and the uncertainties concerning the dark matter halo profile, we therefore cannot exclude tidal stripping of the galaxy dark matter haloes as an origin for the cluster–field TFR offset we measure.

The enhanced SFR hypothesis is supported by the increased fraction of galaxies with strong E+A spectra (EW(Hδ) $\gtrsim 5.0$Å) in intermediate redshift clusters (Poggianti et al. 1999; Tran et al. 2003), implying these galaxies have recently experienced a short star-burst prior to truncation of their star-formation. More direct evidence may be provided by a correlation between star-formation rate and offset from the fiducial TFR, as suggested by our MS1054 sample in Milvang-Jensen (2003). This is examined for our full TFR sample later, in section 5.5.

There may be a less straightforward reason why we observe lower rotation velocities for cluster galaxies. This could be a symptom of cluster galaxies having rotation curves or emission surface brightness profiles that are different from field galaxies. Both of these could cause a systematic divergence from the assumptions used in ELFIT2PY, thereby affecting the measured value of $V_{\rm rot}$. Vogt et al. (2004) find spirals in local clusters with truncated Hα emission and deficient in HI, presumably due to removal of gas from the outer regions of the disc through interactions with the cluster environment. If spirals in our cluster sample are significantly affected by this, then we may preferentially be observing emission from nearer the centre of these galaxies. This could potentially bias our $V_{\rm rot}$ measurements to lower values. To look for any differences in the extent, quality and shape of the rotation

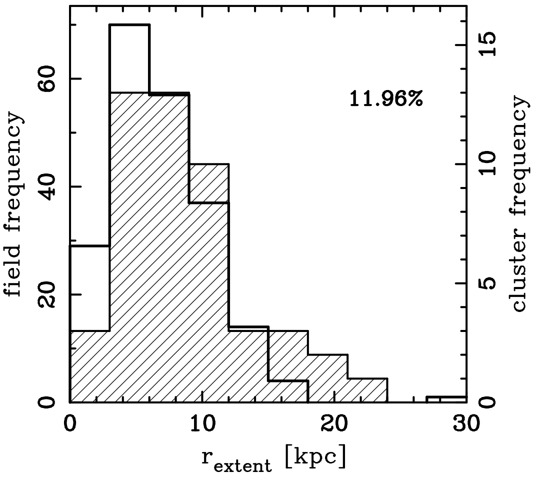

Figure 5.6. The r_{extent} distribution for the lines used to measure V_{rot} and $r_{\mathrm{d,spec}}$ of galaxies in the full TFR sample, in units of kpc. The field (empty line) and cluster (hatched) histograms have been scaled to the same area. The cluster galaxies have a similar distribution of extent compared with the field sample. Note that the cluster galaxy emission-lines can still often be traced out as far, or further, than for the field galaxies. The percentage in the top right corner indicates the confidence that the field and cluster samples are drawn from the same distribution, as given by a K-S test.

curves between the two samples, we can utilise the emission line 'traces' described in section 3.1.1.

Recall that r_{extent} is the spatial distance, from the line centre, to which we can reliably detect the emission above the background noise. This was determined by attempting to fit a Gaussian to the emission in each spatial row, repeating the fit with different noise realisations to determine uncertainties on the Gaussian parameters. The sanity of these parameters and their significance, as judged by the derived uncertainties, were then used to classify each average fit as 'good' or 'bad', according to whether the emission was reliably detected in that spatial row. In addition, isolated points, otherwise deemed to be 'good', but separated from other 'good' points by more than two spatial pixels, were also judged unreliable and hence classified as 'bad' points. The resultant values of r_{extent} are thus robust measurements of the extent to which the emission-lines can be reliably detected. The distributions of emission-line extent, r_{extent}, in units of kpc, for all lines used to measure V_{rot} for galaxies in the 'matched' samples, are shown in figure 5.6. It is clear that there is very little difference between the extent of the emission-lines for cluster and field galaxies, and hence no evidence of a bias that could affect the measured values of V_{rot} and $r_{\mathrm{d,spec}}$. If anything, figure 5.6 suggests that we can actually trace the emission out further in cluster galaxies than in field galaxies.

The distributions of the additional quality assessment quantities, χ^2_{r} and S/N are shown in figure 5.7. Again, there is no appreciable difference between the two samples, apart from a hint that the lines of cluster galaxies extend to higher S/N than those of the field galaxies. We therefore conclude that there is no significant difference in the extent or quality-of-fit of our cluster and field galaxy rotation curves.

In addition, even if there are differences in the r_{extent} and S/N distributions of our cluster and field samples, we find no correlation between V_{rot} and these quantities, so this cannot be responsible for the TFR offset we measure. This is demonstrated by figure 5.8, plots of the fractional deviation of the $V_{\mathrm{rot},j}$ of individual lines,

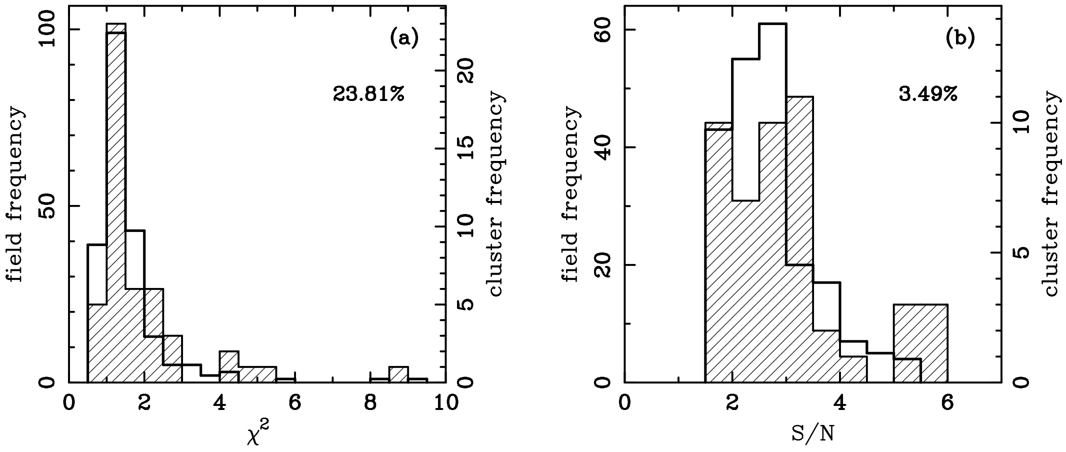

Figure 5.7. The distributions of (a) χ_r^2 and (b) S/N for the lines used to measure $V_{\rm rot}$ and $r_{\rm d,spec}$ of galaxies in the full TFR sample. The field (empty line) and cluster (hatched) histograms have been scaled to the same area. There are no significant differences between the matched cluster and field samples. The percentage in the top right corner indicates the confidence that the field and cluster samples are drawn from the same distribution, as given by a K-S test.

from the weighted mean of all the ‘good’ lines for that galaxy ($V_{\rm rot}$), versus $r_{\rm extent}$ and S/N. Note that the scatter increases with both decreasing $r_{\rm extent}$ and S/N, as one would expect.

Representative examples of our data, model lines and observed rotation curves, for both field and cluster galaxies, are shown in figures 5.9–5.11. For each galaxy, labelled above by cluster name and id number, two columns are given. Their contents, from top to bottom, are: *Left — example imaging data: (top)* the best HST or R-band image available with the spectroscopic slit overlaid, *(middle)* GIM2D model (greyscale) of the above image with ellipses overlaid indicating $3r_{\rm d,phot}$ (black line) and the bulge effective radius (grey line, dashed if bulge fraction < 0.1), *(bottom)* data$-$model residual image, *(text)* band of the shown image, absolute rest-frame B-band magnitude, photometric disc scalelength, adopted inclination and redshift. *Right — example spectroscopic data: (top)* the emission-line contributing most to the $V_{\rm rot}$ measurement, *(middle)* ELFIT2PY model of the above emission-line, *(bottom)* data$-$model residual image, *(plot)* the observed rotation curve (filled points) and model rotation curve (as observed, open points), including the effects of inclination, seeing, etc., from a combination of all the available emission-lines, *(text)* wavelength of the example line, (rest-frame) rotation velocity and spectroscopic emission scalelength (possibly combined from fits to multiple lines), S/N and χ_r^2 for the example line.

The plotted rotation curves have been measured by the tracing method described in section 3.1.1, combined by weighted averages of the reliable points in the case of multiple lines for a single galaxy. Only points with at least one ‘good’ measurement are plotted, thereby showing the extent to which we can reliably trace the line. The model lines have been traced, and ‘good’ points determined, in exactly the same way, so that the extent of the model line shows the distance to which it can be reliably traced assuming the same pixel errors as the real data. Note that $V_{\rm rot}$ is not measured using this method, but rather by comparison with model 2D spectra in the Metropolis parameter search of ELFIT2PY. Visually there is no difference in the

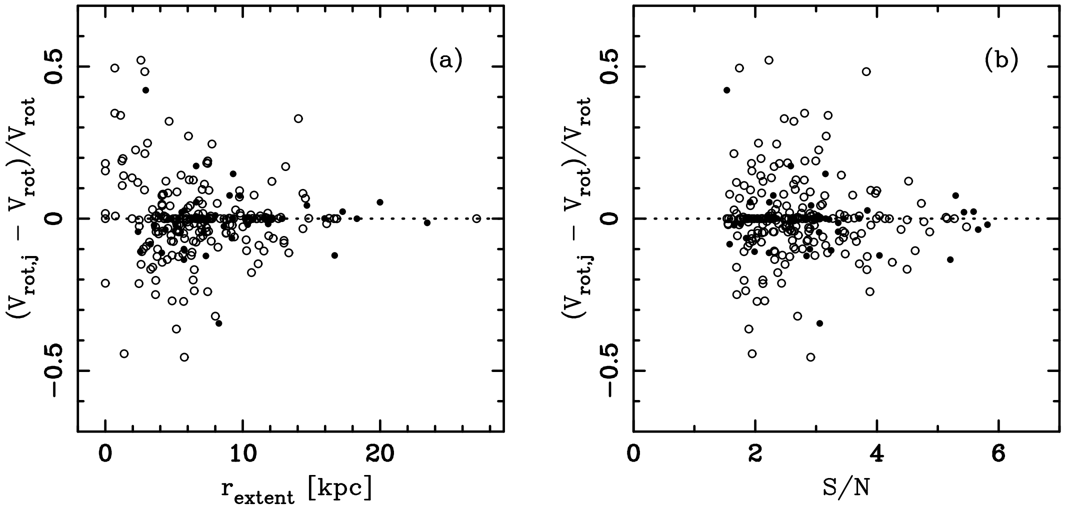

Figure 5.8. The fractional deviation of the $V_{\mathrm{rot},j}$ of individual lines, from the weighted mean of all the 'good' lines for that galaxy (V_{rot}), plotted versus (a) r_{extent} and (b) S/N. Filled points correspond to emission lines from cluster galaxies, while open points are from field galaxies. Points on the dotted line have a fractional deviation of zero, usually because only one emission-line is available for that galaxy. Note that while the scatter varies, the plots indicate no correlation between the rotation velocity measured from a line and that line's r_{extent} or S/N.

form and quality of the emission-lines and rotation curves between the two samples. We therefore assert that the offset between the TFR of the two samples is due to real, physical differences in M_B and/or V_{rot}.

Note that the objects in our sample are giant galaxies, which must have emission-lines bright enough for us to be able to fit and hence measure V_{rot}. Our results therefore apply to massive ($V_{\mathrm{rot}} \gtrsim 80$ km s^{-1}), luminous ($M_B > -19.5$) galaxies, with significant active star-formation in the disc. No conclusions may be drawn concerning the population of fainter disc galaxies or those with little or no ongoing star-formation.

5.2.3 Comparison with other studies

In contrast to our result, the study of Ziegler et al. (2003) finds no difference between the TFR of 13 spirals in three clusters at $0.3 \lesssim z \lesssim 0.5$ and that determined for the FORS Deep Field by Böhm et al. (2004). This is puzzling, and may point to real differences in TFR offsets between individual clusters. However, this question must wait to be addressed by larger studies which can examine TFR offsets, along with SFRs and colours, as a function of cluster properties.

It seems difficult to attribute the conflict between our results and those of Ziegler et al. (2003) to a difference in sample selection. This was performed in a fairly similar manner, generally giving preference to galaxies based on luminosity, spiral morphology, known emission-lines, and cluster membership (see Jäger et al. 2004). However, both studies have rather heterogeneous selection procedures, based upon the availability of disparate prior data in the literature. Additional, higher quality data for four more clusters are expected soon from this group, which should help confirm which result is correct.

A study of 15 spirals in the cluster CL0024+1654 at $z = 0.4$ by Metevier et al.

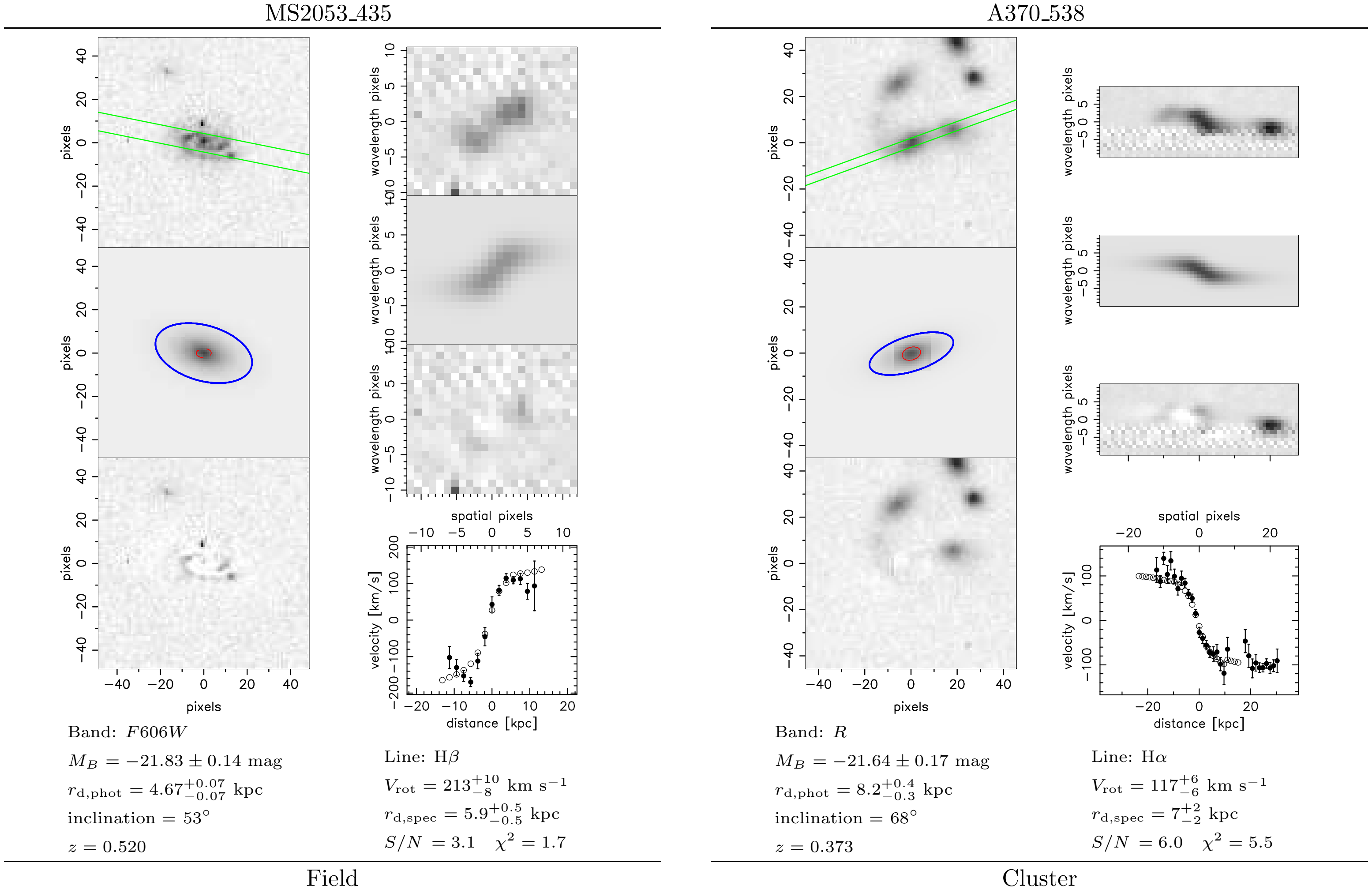

Band: $F606W$

$M_B = -21.83 \pm 0.14$ mag

$r_{\rm d,phot} = 4.67^{+0.07}_{-0.07}$ kpc

inclination $= 53^\circ$

$z = 0.520$

Line: Hβ

$V_{\rm rot} = 213^{+10}_{-8}$ km s^{-1}

$r_{\rm d,spec} = 5.9^{+0.5}_{-0.5}$ kpc

$S/N = 3.1 \quad \chi^2 = 1.7$

Band: R

$M_B = -21.64 \pm 0.17$ mag

$r_{\rm d,phot} = 8.2^{+0.4}_{-0.3}$ kpc

inclination $= 68^\circ$

$z = 0.373$

Line: Hα

$V_{\rm rot} = 117^{+6}_{-6}$ km s^{-1}

$r_{\rm d,spec} = 7^{+2}_{-2}$ kpc

$S/N = 6.0 \quad \chi^2 = 5.5$

Figure 5.9. Representative examples of our data, models and observed rotation curves. This figure shows galaxies with low $V_{\rm rot}$ errors (10th-percentile $\sigma_{V_{\rm rot}}$) in each of the field *(left)* and cluster *(right)* TFR samples. See the text for a description of the contents.

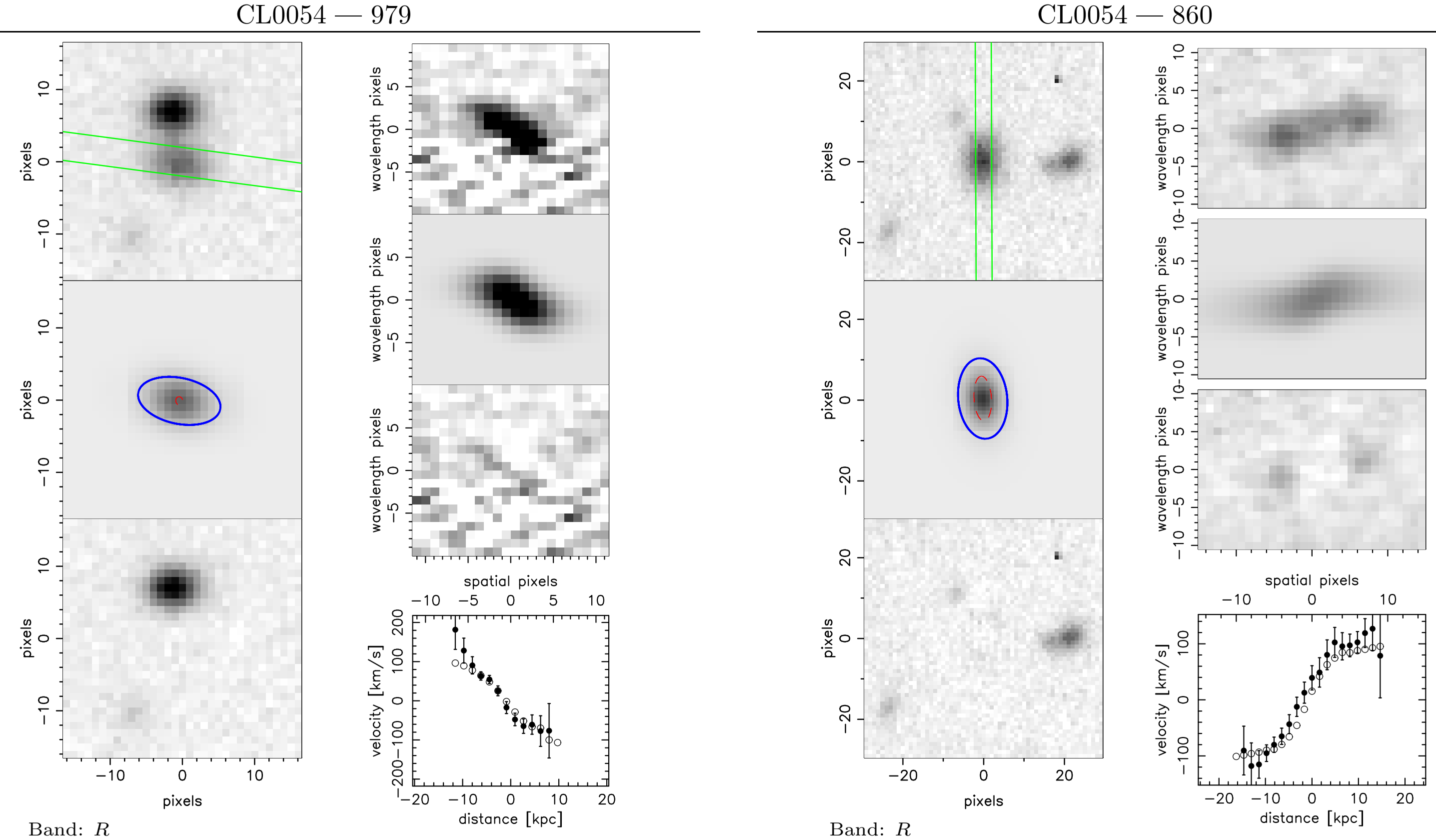

Band: R

$M_B = -21.18 \pm 0.14$ mag

$r_{\rm d,phot} = 3.4^{+0.3}_{-0.3}$ kpc

inclination = 57°

$z = 0.660$

Line: Hβ

$V_{\rm rot} = 126^{+12}_{-12}$ km s^{-1}

$r_{\rm d,spec} = 3.4^{+0.2}_{-0.2}$ kpc

$S/N = 2.8 \quad \chi^2 = 1.1$

Field

Band: R

$M_B = -21.38 \pm 0.11$ mag

$r_{\rm d,phot} = 5.4^{+0.2}_{-0.2}$ kpc

inclination = 53°

$z = 0.559$

Line: [OII]λ3727

$V_{\rm rot} = 136^{+13}_{-11}$ km s^{-1}

$r_{\rm d,spec} = 8^{+1}_{-1}$ kpc

$S/N = 2.6 \quad \chi^2 = 1.3$

Cluster

Figure 5.10. Representative examples of our data, models and observed rotation curves. This figure is the same as figure 5.9, but shows galaxies with median $V_{\rm rot}$ errors (50th-percentile $\sigma_{V_{\rm rot}}$) in each of the field *(left)* and cluster *(right)* TFR samples.

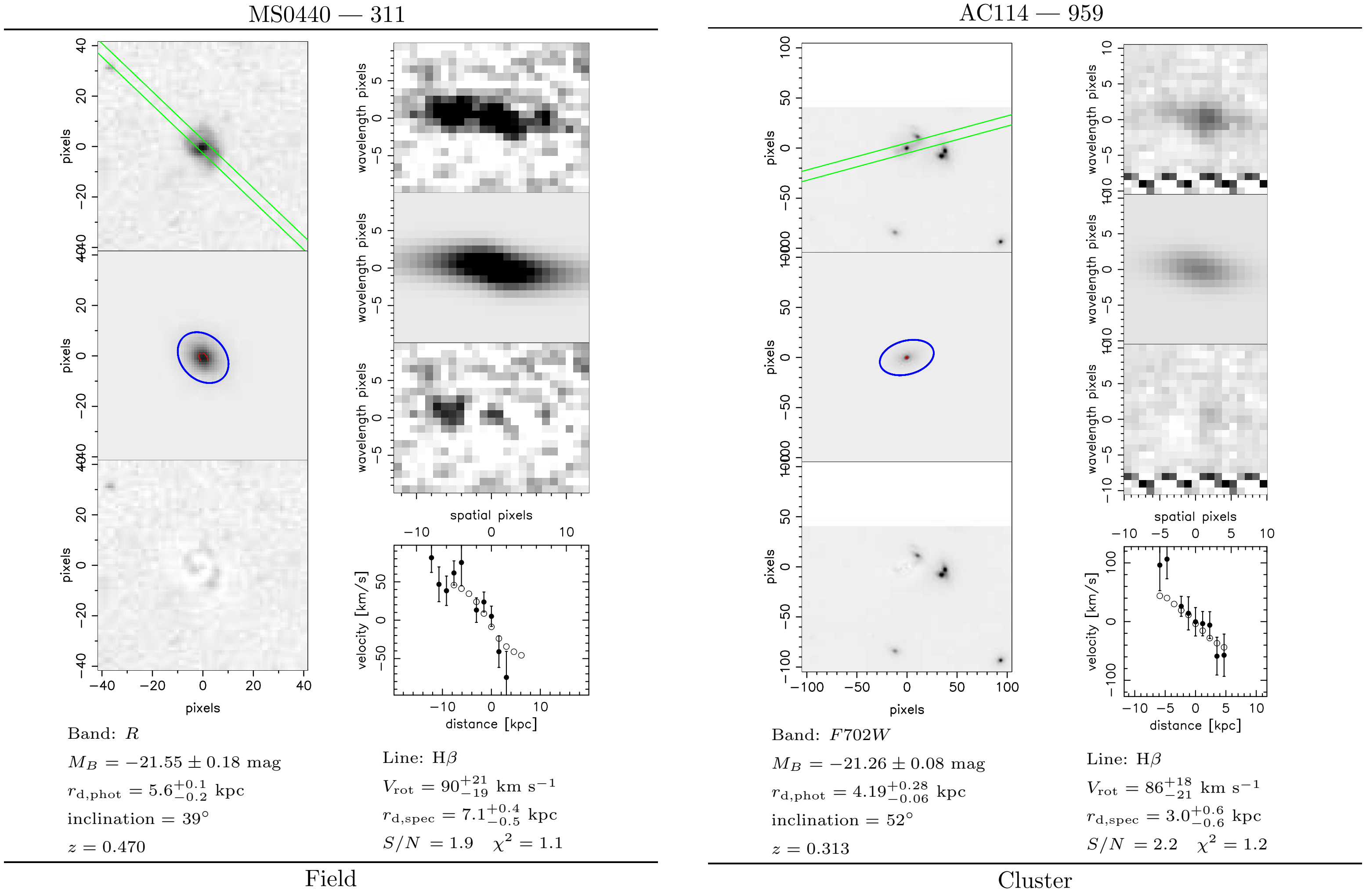

Band: *R*

$M_B = -21.55 \pm 0.18$ mag

$r_{\mathrm{d,phot}} = 5.6^{+0.1}_{-0.2}$ kpc

inclination = 39°

$z = 0.470$

Line: Hβ

$V_{\mathrm{rot}} = 90^{+21}_{-19}$ km s^{-1}

$r_{\mathrm{d,spec}} = 7.1^{+0.4}_{-0.5}$ kpc

$S/N = 1.9 \quad \chi^2 = 1.1$

Band: *F702W*

$M_B = -21.26 \pm 0.08$ mag

$r_{\mathrm{d,phot}} = 4.19^{+0.28}_{-0.06}$ kpc

inclination = 52°

$z = 0.313$

Line: Hβ

$V_{\mathrm{rot}} = 86^{+18}_{-21}$ km s^{-1}

$r_{\mathrm{d,spec}} = 3.0^{+0.6}_{-0.6}$ kpc

$S/N = 2.2 \quad \chi^2 = 1.2$

Figure 5.11. Representative examples of our data, models and observed rotation curves. This figure is the same as figure 5.9, but shows galaxies with high V_{rot} errors (90th-percentile $\sigma_{V_{\mathrm{rot}}}$) in each of the field *(left)* and cluster *(right)* TFR samples.

(2006) finds that these galaxies are ~ 0.5 mag *fainter* at a given rotation velocity than the *local* field TFR. When combined with the potential ~ 0.4 mag of field galaxy brightening which may be expected at this redshift from the results of section 4.2.2, this suggests a fairly large difference between cluster and field spirals at $z \sim 0.4$. In order to perform the comparison of their $z = 0.4$ measurements with previous local TFRs, Metevier et al. (2006) has attempted to take into account the systematic measurement differences between these various studies. While instructive, a direct comparison of cluster and field galaxies at intermediate redshift using identical techniques, as performed in this thesis, would be more reassuring.

An interesting difference between the Metevier et al. (2006) study and other work is their use of a rotation curve of the form

$$V(r) = \frac{2V_{arc}}{\pi} \arctan\left(\frac{r}{r_{to}}\right), \tag{5.3}$$

where V_{arc} is the maximum velocity, which is then corrected to match various local rotation velocity measures for comparison purposes, and r_{to} is the 'turnover' radius, and controls the radial scale of the rotation curve. However, note that $V(r_{to}) = 0.50V_{arc}$, and this function rises and asymptotes fairly slowly, for example $V(3r_{to}) = 0.80V_{arc}$. Therefore r_{to} is not well very described as the 'turnover' radius.

In contrast, the flat and URC functions used in this thesis are discontinuous (rise instantly), and reach V_{rot} at $r \leq 2.2r_{\mathrm{d,spec}}$. Furthermore, the function used by Böhm et al. (2004), and favoured by the comparison of local rotation curves by Courteau (1997), is

$$V(r) = \frac{V_{max}r}{(r^{\alpha} + r_0^{\alpha})^{(1/\alpha)}}, \tag{5.4}$$

where V_{max} is the maximum velocity, α controls the shape of the transition from the linearly rising to flat regime, and r_0 controls the slope at small r and the approximate location of the 'turnover'. A disadvantage of this latter expression is the addition of another free parameter compared with the arctan function, and two parameters compared with the simple flat or URC functions. For $\alpha \approx 1.1$ this form is similar to the arctan function. However, Courteau (1997) find a range of best-fitting α for local rotation curves (0.25–10), although with $\alpha \approx 0.5$–2 most common.

Böhm et al. (2004) find $\alpha = 5$ generally fits their rotation curves of bright intermediate-redshift galaxies well, and used this fixed value in their final rotation velocity fits. With this α, $V(r_0) = 0.87V_{max}$ and $V(3r_0) = 0.9992V_{max}$. Böhm et al. (2004) also fix r_0 to the same value as the scalelength of the line emission, which they in turn fix by $rdspec = (2 - z/2)r_{\mathrm{d,phot}}$. The redshift dependence of this relation accounts for the variable rest-frame wavelength their observed I-band scalelengths correspond to.

While Böhm et al. (2004) try to minimise the number of free parameters they fit, Metevier et al. (2006) attempt to simultaneously fit V_{arc}, r_{to} and $r_{\mathrm{d,spec}}$, amongst other parameters. Their best-fitting r_{to} shows fairly wide variation with respect to *rdspec*, but is generally smaller, as one might expect given the arctan function's slow rise. However, the model r_{to} is of the same order as $r_{\mathrm{d,spec}}$, and therefore must continue rising well beyond the measured region, as can be seen from the example images. This leaves the possibility that the maximum rotation velocity is overestimated. On the other hand, such slowly rising rotation curves may be real, in which case the more rapidly rising models of this thesis, Böhm et al. (2004), Vogt (1999), etc. may underestimate the true rotation velocity to a greater or lesser extent. In this case however, it will be hard to be sure of rotation velocities measured with any method, as detecting the flat region of the rotation curve will be difficult.

It is perhaps telling that intermediate-redshift TFR studies that use discontinuous, rapidly- and slowly-rising rotation curves, find TF offsets that are negative, roughly zero and positive respectively. Which form of rotation curve is most appropriate for intermediate-redshift galaxies is clearly an important outstanding issue.

The study by Nakamura et al. (2006, hereafter N05) compares the TFR for samples of intermediate redshift cluster and field galaxies, and is similar to the TFR analysis performed in this thesis. In contrast to our result, however, no evidence is found for an offset between cluster and field galaxies in the TFR, nor in terms of their $(B - V)$ colour. N05 do find that their clusters contain a considerably higher proportion of spiral galaxies with no current star formation, compared with the field. This is possible evidence for an overall suppression of star formation in cluster environments. However, they see no significant difference between star-forming galaxies in clusters and those in the field. This disparity between N05 and the results of this thesis may simply be a result of stochastic variance in the clusters targeted. Data for many more intermediate-redshift clusters will be provided soon by the EDisCS collaboration, see section 6.2.2, which will allow us to judge the extent of such cluster-cluster variances.

Alternatively, the contrasting results between N05 and this thesis may be due to differing sample properties. While the target selection has been performed in a very similar way for both, the N05 TFR sample is considerably smaller, partly because of the initial number of emission-line galaxies observed (77 versus 184), but also due to an apparently more aggressive emission-line quality control process. N05 reject the two-dimensional fits of all emission lines for 57% of their galaxies, while our study rejects only 40%. While one must be careful to remove galaxies for which the measurements will be unreliable, excessively removing those which are likely to be well fit reduces the statistical power of the study. In addition, there is a distinct possibility that it is those galaxies which show minor kinematical or morphological disturbances, the latter possibly just due to star formation asymmetries, which are the most interesting from an evolutionary point-of-view. If the rotation velocity of such galaxies can still be reliably measured, we should endeavour to include them in our sample. However, it is unfortunately still unclear where to draw the line, and the quality control procedure remains somewhat subjective. Clearly this issue needs further attention, and a study with the aim of improving upon the current situation is discussed in section 6.2.1.

More general studies of the correlation between SFR and local galaxy density by Lewis et al. (2002) and Gómez et al. (2003), using the 2dF and SDSS datasets respectively, both find the existence of a critical local galaxy density (of ~ 1 galaxy with $M_b \lesssim -19$ per Mpc^2). At densities greater than this, the average SFR decreases with density. At lower densities there is no significant correlation. These results imply that the global SFR of the universe may be influenced by environmental effects at quite low densities, outside of the boundaries of rich clusters, and therefore its variation is not simply due to a general, internal evolution of the SFR in individual galaxies.

How does the finding that groups may be the dominant site of star-formation suppression today compare with our result, that we also find this process occurring – accompanied by a SFR *enhancement* – in rich clusters at intermediate redshift? Firstly, the fact that suppression of SFR happens at low densities locally does not rule out it also occurring in cluster environments. Rather, the linearity of the SFR–density correlation implies that the efficiency of SFR suppression increases with density.

Furthermore, Balogh et al. (2004) find that the environmental dependence of the volume averaged SFR is due to changing proportions of the star-forming and passive galaxy populations, rather than a shift in the mean SFR of star-forming galaxies. This suggests that the process responsible for reducing the average SFR in groups is *stochastic*. When the process occurs it causes a halt in star-formation, and hence a transformation from a galaxy in the star-forming population into the passive population. However, in order to preserve the smooth correlation between SFR and local density, this process must occur randomly, with a frequency related to the local density. This suggests mergers as the responsible mechanism for SFR suppression in groups. However, in local rich clusters very few star-forming galaxies are found, yet mergers are less likely due to the large relative galaxy velocities. In this case it may be that a more all-encompassing mechanism, such as ram-pressure stripping, is at work, finishing the job started in groups.

Another finding by Balogh et al. (2004), that star-forming galaxies in dense environments have an EW(Hα) distribution indistinguishable from that for low-density environments, appears at first to be inconsistent with the present study's results. However, the necessarily short time-scale for any SFR enhancement, combined with the simultaneous existence of galaxies with declining SFR, may make detecting such an effect difficult using the EW(Hα) distribution.

A further explanation may be one of pre-processing. It seems likely that galaxies falling into rich clusters today have spent a longer time subjected to group conditions than those entering similar clusters at $z \sim 0.5$. If, as is suggested above, the probability for star-formation suppression increases with both local density and the length of time which the galaxy has been subjected to the environment, we would therefore expect clusters to be the site of star-formation truncation at intermediate redshifts, but no longer today – at least for massive galaxies, which are preferentially located in denser regions. However, to assert this will require a consideration of cosmological simulations beyond the scope of this thesis.

There has been surprisingly little direct study of the local ($z \sim 0$) dependence of the TFR on environment, although this is perhaps because a lack of any dependence is apparent in more general studies. An investigation by Biviano et al. (1990) finds no evidence for a difference between the TFR of spirals in clusters and those in a sample taken from groups and the field. This provides some evidence that any difference between cluster and field spirals that may have existed in the past, has now diminished, at least for those spirals which retain significant quantities of HI. Studies of asymmetry, truncation and HI deficiency in cluster spirals have also been performed for local clusters (Dale et al. 2001; Vogt et al. 2004), finding evidence for the stripping of disc gas through some process related to galaxy infall.

The variation of galaxy properties with environment, as investigated by the studies mentioned above, suggests a similar examination of TFR offset with respect to clustercentric distance and local density for our data. We plan to undertake a such a detailed 'geographical' study of our VLT and Subaru intermediate-redshift clusters in the future.

Table 5.1. The offsets between our cluster and field 'matched' samples, measured with respect to the fiducial relations and the best-fitting field relations, for the various relations of $r_{\rm d,phot}$, $r_{\rm d,spec}$ versus $V_{\rm rot}$, and M_B.

Relation			cluster−field offset w.r.t. fiducial relation	cluster−field offset w.r.t. field fit
$r_{\rm d,phot}$–$V_{\rm rot}$:	$\Delta\log(r_{\rm d,phot})$	=	0.13 ± 0.04	0.10 ± 0.04
$r_{\rm d,phot}$–M_B :	$\Delta\log(r_{\rm d,phot})$	=	0.03 ± 0.04	0.03 ± 0.04
$r_{\rm d,spec}$–$V_{\rm rot}$:	$\Delta\log(r_{\rm d,spec})$	=	-0.06 ± 0.06	-0.06 ± 0.06
$r_{\rm d,spec}$–M_B :	$\Delta\log(r_{\rm d,spec})$	=	-0.14 ± 0.05	-0.14 ± 0.06

5.3 Stellar versus emission-line scalelengths

As well as the TFR, several other relations are available which may shed light upon the nature of the cluster−field offset. These include $V_{\rm rot}$ and M_B versus measures of the stellar and emission-line scalelength, $r_{\rm d,phot}$ and $r_{\rm d,spec}$, respectively. These relations are plotted in figure 5.12. From these plots it can been seen that cluster and field galaxies lie on similar relations in $r_{\rm d,phot}$–M_B and $r_{\rm d,spec}$–$V_{\rm rot}$. However, they differ in their $r_{\rm d,phot}$–$V_{\rm rot}$ relation such that cluster galaxies have higher $r_{\rm d,phot}$ and/or lower $V_{\rm rot}$, and in their $r_{\rm d,spec}$–M_B relation such that cluster galaxies have lower $r_{\rm d,spec}$ and/or are brighter in M_B. These offsets echo those suggested more tentatively by the MS1054 data considered alone (Milvang-Jensen 2003). To quantify the offsets we subtract a fiducial relation and measure the weighted mean and variance using the same method as for the $\Delta {M_B}^{\rm TF}$–z relation in section 5.2.1. The fiducial $r_{\rm d,phot}$–$V_{\rm rot}$ relation used here is that of Vogt (1995) (as read from figure 5 of Vogt 1999):

$$\log(r_{\rm d,phot}) = 0.95\log(V_{\rm rot}) - 1.55. \tag{5.5}$$

Combining this with the local TFR of PT92 gives

$$\log(r_{\rm d,phot}) = -0.127M_B - 1.98, \tag{5.6}$$

used as a consistent fiducial $r_{\rm d,phot}$–M_B relation. These relations are indicated by the dashed lines in figure 5.12, and included in the $r_{\rm d,spec}$ panels for reference. The cluster−field offsets are given in table 5.1.

For comparison we also fit the field sample, using the same method used for the TFR above, shown by solid lines in figure 5.12. We additionally determine the cluster–field offsets with respect to these field relations, also given in table 5.1. We determine the following field fits,

$$\log(r_{\rm d,phot}) = (0.347 \pm 0.167)\log(V_{\rm rot}) - (0.175 \pm 0.368), \tag{5.7}$$

$$\log(r_{\rm d,phot}) = (-0.125 \pm 0.024)M_B - (2.034 \pm 0.504), \tag{5.8}$$

$$\log(r_{\rm d,spec}) = (0.696 \pm 0.214)\log(V_{\rm rot}) - (0.877 \pm 0.470), \tag{5.9}$$

$$\log(r_{\rm d,spec}) = (-0.139 \pm 0.037)M_B - (2.266 \pm 0.768). \tag{5.10}$$

The two simplest possibilities admitted by our results are: (1) $V_{\rm rot}$ and $r_{\rm d,spec}$ are lower for cluster galaxies, while M_B and $r_{\rm d,phot}$ are unchanged, or (2) M_B is lower (brighter) and $r_{\rm d,phot}$ higher for cluster galaxies, while $V_{\rm rot}$ and $r_{\rm d,spec}$ remain similar to field galaxies. A combination of these two effects could also explain the observed offsets. A lower $r_{\rm d,spec}$ for cluster galaxies is plausible, as ram-pressure stripping is

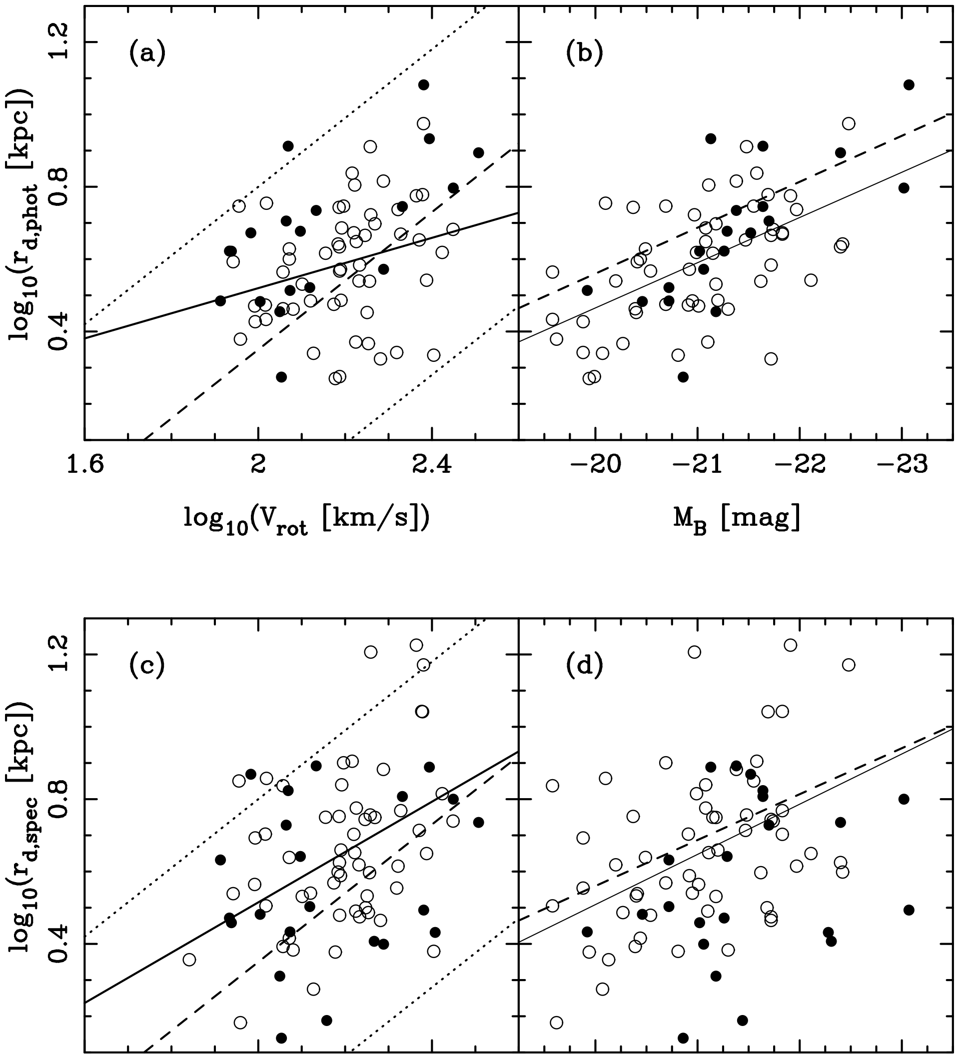

Figure 5.12. The (a) $V_{\rm rot}$–$r_{\rm d,phot}$, (b) M_B–$r_{\rm d,phot}$, (c) $V_{\rm rot}$–$r_{\rm d,spec}$ and (d) M_B–$r_{\rm d,spec}$ relations for our matched TFR samples. Only the subsample of galaxies with reliable $r_{\rm d,phot}$ measurements are shown in (a) and (b). The fiducial relations described in the text are plotted by dashed lines, with the 3σ scatter indicated by the dotted lines where known. Weighted least-squares fits to the field sample are indicated by the solid line in each panel.

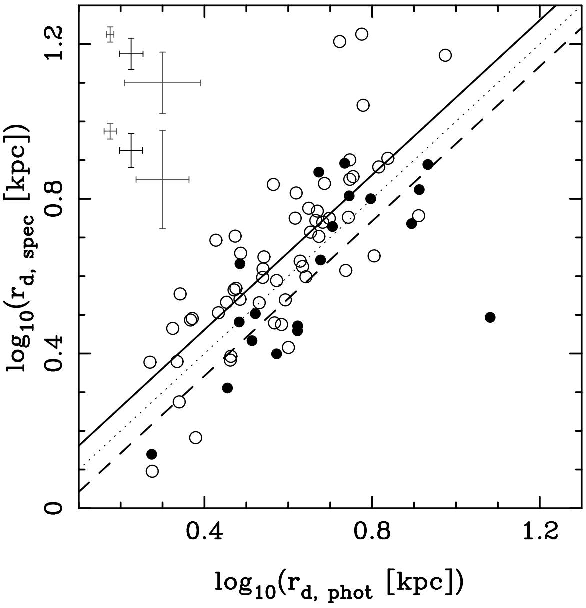

Figure 5.13. A plot of $r_{\rm d,spec}$ versus $r_{\rm d,phot}$ for our 'matched' field (open points) and cluster (filled points) TFR samples. The one-to-one relation is indicated by a dotted line. Fixed slope fits to the field (solid line) and cluster (dashed line) data are shown.

expected to truncate the gas in the outer regions of the disc. Similarly, M_B may be brighter for cluster galaxies due to an enhancement of their star-formation. Deciding which of the two possibilities dominates therefore comes down to determining which of decreasing $V_{\rm rot}$ or increasing $r_{\rm d,phot}$ is more plausible. The distributions of these four variables, shown in figure 5.2, are consistent with a combination of both the above scenarios. Note that the evidence in panel (c) of this figure, for an excess of cluster galaxies with low rotation velocities compared with the field, does not require a real difference in $V_{\rm rot}$. This effect could rather be caused by a brightening of cluster galaxies leading to a higher proportion of low-$V_{\rm rot}$ galaxies in the cluster sample.

The relationship between $r_{\rm d,spec}$ and $r_{\rm d,phot}$, plotted in figure 5.13, is also consistent with the possibilities listed above. Fits indicate that

$$\left(\frac{r_{\rm d,spec}}{r_{\rm d,phot}}\right)_{\rm field} = 1.15 \pm 0.05 \quad \text{and} \quad \left(\frac{r_{\rm d,spec}}{r_{\rm d,phot}}\right)_{\rm cluster} = 0.88 \pm 0.08. \tag{5.11}$$

The cluster−field offset is thus

$$\Delta \log(r_{\rm d,spec}) = -0.12 \pm 0.04 \text{ dex} \tag{5.12}$$

and comparable to that seen for the relations in figure 5.12 and table 5.1. For the field galaxies, star formation appears to be more uniform with radius than the current stellar profile. In contrast, star formation in our cluster galaxies is generally more centrally concentrated.

Interestingly the $r_{\rm d,spec}$–$r_{\rm d,phot}$ relations we find in our intermediate-redshift samples are very similar to those seen locally by Koopmann et al. (2006), who find

$$\left(\frac{r_{\rm d,spec}}{r_{\rm d,phot}}\right)_{\rm field} = 1.14 \pm 0.07 \quad \text{and} \quad \left(\frac{r_{\rm d,spec}}{r_{\rm d,phot}}\right)_{\rm cluster} = 0.79 \pm 0.06. \tag{5.13}$$

for local field and Virgo cluster galaxies, respectively (both using their preferred fits, over the range 1–3$r_{\rm d,phot}$).

5.4 Metallicities, ionisation conditions, star formation rates and internal extinctions

We take another step toward quantifying environmental variation in galaxy properties at intermediate redshifts by comparing the integrated spectral properties of our cluster galaxies with those of the field galaxies discussed in section 4.5. Both of these samples of intermediate redshift galaxies were selected and analysed in an identical manner, and have comparable redshift distributions (see section 3.2.1). We also compare against the Nearby Field Galaxy Sample (NFGS) of Jansen et al. (2000), as used in section 4.5 and specifically described in section 4.5.1.

The distributions of [OII]λ3727 and Hβ equivalent width, O_{32} and R_{23} parameters, M_B, star formation rate derived from Hβ, oxygen abundance, and colour excess are shown for our intermediate redshift cluster and field samples in figure 5.14. In addition to the visual comparison between our cluster and field samples afforded by these histograms, we have quantitatively compared the parameters. This has been done primarily by estimating the difference between the parameters' parent distribution means and evaluating the significance of this difference. The results are given in table 5.2. The figures presented in this table are from a comparison utilising the robust biweight estimates of location and scale (e.g., Beers et al. 1990). The probability that the parent distributions have the same mean is evaluated by a robust t-test, which does not assume that the distributions have equal variances (Welch 1937). Similar results are found using canonical statistics, both unweighted and with weights corresponding to the measurement errors with the inclusion of an intrinsic dispersion term. An exception is $\mathrm{SFR}_{\mathrm{H}\beta}$, for which the less robust statistics find a less significant difference between the cluster and field samples. Table 5.2 also lists the probability that the parent cluster and field distributions are the same as given by a Kolmogorov-Smirnov (KS) test.

The most striking differences are displayed by the equivalent widths of [OII] and Hβ, for which the cluster and field galaxy means differ at a $\gtrsim 99.99\%$ significance level. The KS-test does not appear to be as powerful at discriminating between the two distributions, but still finds differences at a $> 98\%$ significance level. The equivalent widths of [OII] and Hβ are on average significantly lower for cluster galaxies than for field galaxies in our samples, both by a factor of $\sim 0.52 \pm 0.09$. If there is no variation in broad-band luminosities between these galaxy samples, these equivalent width ratios imply similar emission-line luminosity ratios. Star formation rate is proportional to Hβ and, upto a metallicity and ionisation dependence, [OII] luminosity. We therefore expect the star formation rates of our cluster galaxies to be on average lower than those in our field sample, by a similar factor. Indeed, we find this to be true, by a factor of 0.6 ± 0.1. However, this result is less significant than that based solely upon the equivalent widths. The robust statistics presented in table 5.2 find the difference to be $\sim 98\%$, but canonical statistics and the KS-test find no significant difference. Also, if the comparison is performed in the log-regime, which may be more appropriate, no significant difference is found. This reduction in significance is probably due to broad-band luminosity variations. The spread in luminosity (~ 2 mag, therefore a factor of ~ 6 in luminosity) is comparable to the spread in equivalent width, and appears to blur out the differences between

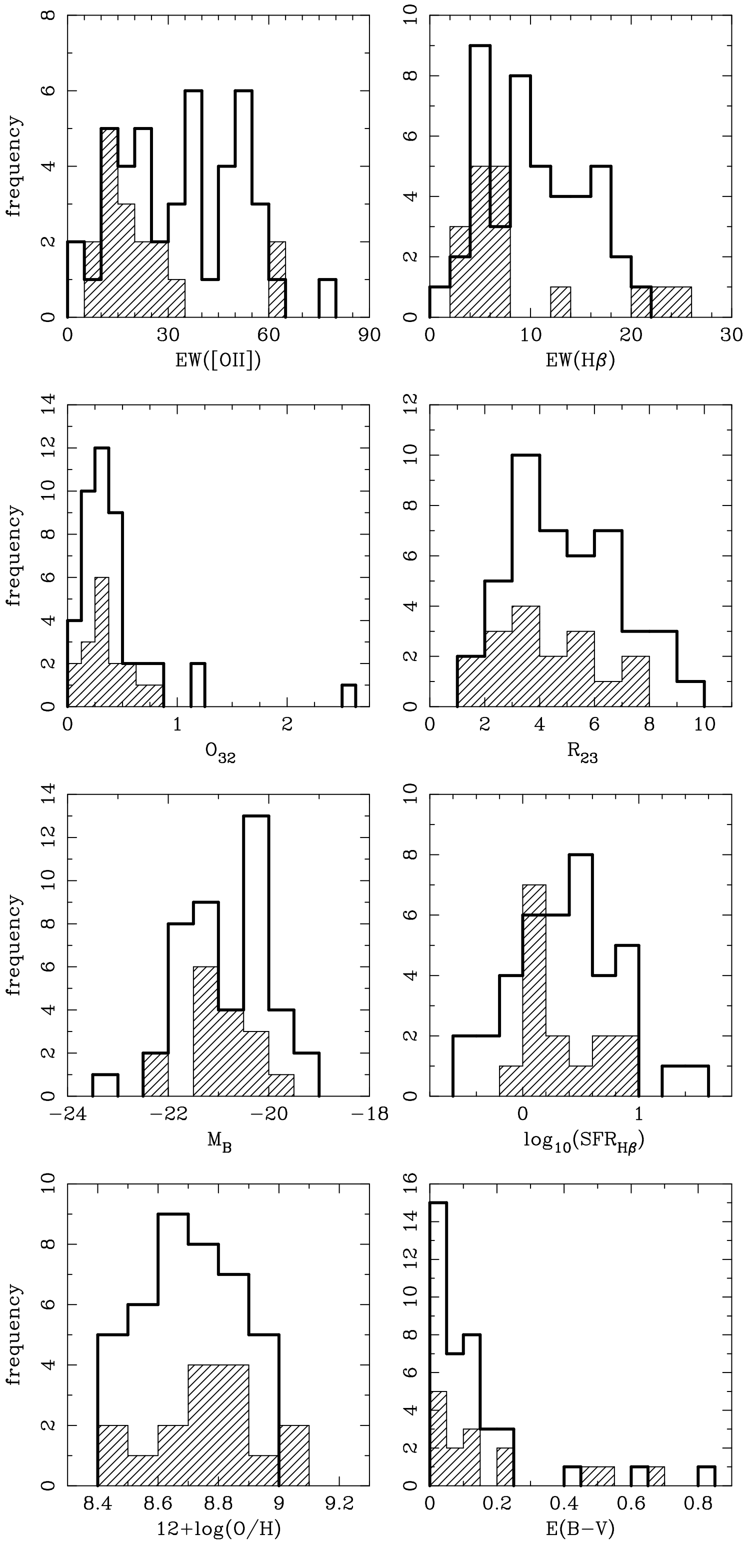

Figure 5.14. The distributions of [OII] and Hβ equivalent width, the O_{32} and R_{23} parameters, M_B, star formation rate derived from Hβ (shown as $\log_{10}(\mathrm{SFR}_{\mathrm{H}\beta})$ to aid comparison), oxygen abundance, and colour excess for galaxies in our intermediate redshift cluster (hatched, thin line) and field (thick line) samples.

Table 5.2. Statistical comparison of our cluster and field EW samples. For each parameter (x), the columns give the number of cluster and field objects (n_{cl} and n_{f} respectively), the robust mean of that parameter for cluster and field objects ($\overline{x}_{\mathrm{cl}}$ and $\overline{x}_{\mathrm{f}}$ respectively), the cluster−field difference in the means ($\Delta(\overline{x}_{\mathrm{cl}} - \overline{x}_{\mathrm{f}})$), an estimate of the size of cluster−field difference that would be required in order to discriminate between the two at the 3σ-level (Δ_{dis}), the probability that the cluster and field populations have the same mean ($P(\mu_{\mathrm{cl}} = \mu_{\mathrm{f}})$), and the KS-test probability that the cluster and field population distributions are the same ($P(\mathrm{KS})$).

x	n_{cl}	n_{f}	$\overline{x}_{\mathrm{cl}}$	$\overline{x}_{\mathrm{f}}$	$\Delta(\overline{x}_{\mathrm{cl}} - \overline{x}_{\mathrm{f}})$	Δ_{dis}	$P(\mu_{\mathrm{cl}} = \mu_{\mathrm{f}})$ %	$P(\mathrm{KS})$ %
EW([OII]) (Å)	17	44	17.55 ± 2.68	33.86 ± 2.82	-16.31	11.68	0.013 [a]	0.991
EW(Hβ) (Å)	17	44	5.35 ± 0.65	10.24 ± 0.82	-4.90	3.14	0.002 [a]	1.826
O_{32}	17	44	0.35 ± 0.05	0.33 ± 0.03	0.02	0.17	75.63	96.53
R_{23}	17	44	4.13 ± 0.48	4.87 ± 0.30	-0.75	1.71	19.19	44.96
M_B (mag)	16	43	-20.90 ± 0.15	-20.79 ± 0.14	-0.11	0.61	57.34	19.87
SFR ($\mathrm{M}_{\odot}\,\mathrm{yr}^{-1}$)	15	39	1.34 ± 0.23	2.37 ± 0.38	-1.03	1.32	2.242 [b]	46.45
$12 + \log(\mathrm{O/H})$	16	40	8.77 ± 0.05	8.71 ± 0.03	0.06	0.17	25.09	50.55
E(B−V) (mag)	15	39	0.10 ± 0.05	0.08 ± 0.01	0.03	0.16	61.53	74.35

[a] highly significant, [b] significant, but see discussion in text for caveats.

the cluster and field samples, reducing the significance of the difference, but not particularly affecting its magnitude.

However, these statistics do not tell the whole story. While most cluster galaxies have equivalent widths on the low side of the field distribution, there are several objects (10–20%) which have equivalent widths as high as any of the field galaxies. This bimodality is also visible in the plot of [OII] equivalent width versus B-band magnitude in the top panel of figure 5.15. It also remains in the star formation rate distribution, with the majority of our cluster galaxies having star formation rates at the low end of the field distribution, but with several objects ($\sim 20\%$) having SFRs higher than any of the field galaxies with the same broad-band luminosity. This is shown clearly by a plot of star formation rate versus magnitude, as given in figure 5.16. These results tentatively imply that distant cluster galaxies have a star formation rate per unit luminosity that is lower than the average for coeval field galaxies, with the exception of a subsample of $\sim 20\%$ cluster galaxies, which have star formation rates per unit luminosity that are higher than those usually seen in the field. We do not find evidence for bimodalities in the distribution histograms for any of the other parameters measured for our distant field and cluster galaxies.

Locally, the strength of emission-lines is known to correlate with galaxy properties, i.e., luminosity, metallicity, and ionisation conditions (e.g., McCall et al. 1985; Stasinska 1990; Kewley & Dopita 2002; Mouhcine et al. 2005). On average faint/metal-poor galaxies tend to be highly ionised, while bright/metal-rich galaxies are characterised by low-ionisation parameters. The top panel of figure 5.15 shows the relationship between galaxy B-band magnitude and [OII] rest-frame emission-line equivalent width. Our cluster galaxies are shown as filled triangles, our sample of intermediate-redshift field galaxies is shown by filled circles, and the local star-forming galaxies in the NFGS sample are shown as open circles. The NFGS galaxies in this figure display the well-established correlation between galaxy luminosity and emission-line equivalent width (e.g., Salzer et al. 1989; Kong et al. 2002; Jansen et al. 2000). As discussed in section 4.5, distant field galaxies cover a similar range of [OII] rest-frame emission-line equivalent width to that observed locally, but over a much narrower luminosity range, that is, ~ 2 mag in comparison to the ~ 7 mag covered by the NFGS sample. Strikingly, intermediate redshift cluster galaxies seem to be mostly located in a similar region to local bright galaxies, while [OII] equivalent widths for galaxies in the field extend to values observed locally only at much lower luminosities. As mentioned earlier, an exception to this trend is provided by two cluster galaxies with [OII] equivalent widths higher than nearly all of our distant field galaxies.

The bottom panel of figure 5.15 shows the variation of [OII] emission-line rest-frame equivalent width as a function of the ionisation-sensitive diagnostic ratio O_{32}. Intermediate redshift cluster and field galaxies are shown as in the top panel of the figure. To illustrate the effect of galaxy luminosity on O_{32}, we split the local sample of star-forming galaxies into faint ($M_B > -19.5$) and bright ($M_B \leq -19.5$), samples. As discussed in section 4.5, the bright, star-forming field galaxies at intermediate redshifts tend to be located in the same region as *faint* local star-forming galaxies, and show higher O_{32} values than are seen locally in galaxies with comparable luminosities. However, our distant, star-forming cluster galaxies preferentially inhabit the same region as local field galaxies with similar, bright, luminosities. Exceptions to this are the same two high [OII] equivalent width galaxies discussed previously, and a population of high-O_{32} cluster galaxies. While the O_{32} distributions of our

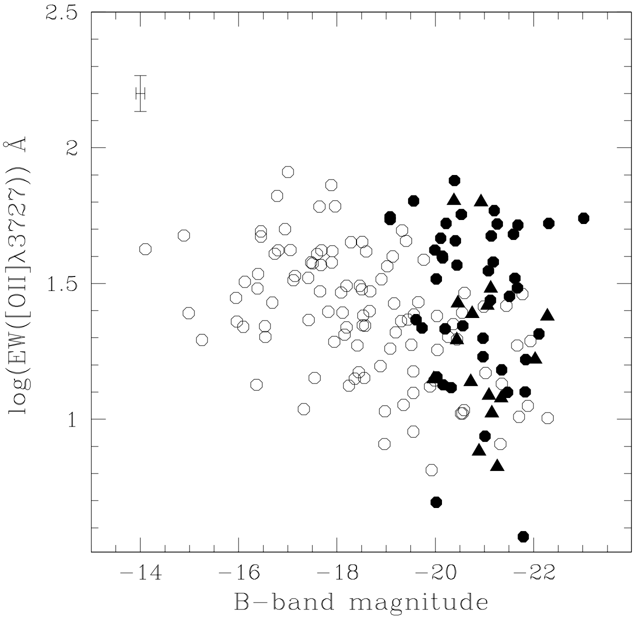

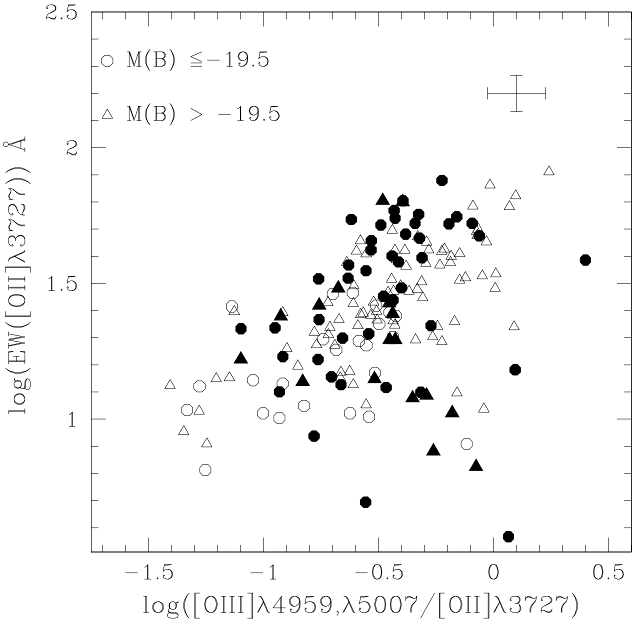

Figure 5.15. (Top) The relationship between rest-frame [OII]λ3727 emission-line equivalent width and absolute rest-frame B-band magnitude for our EW samples of intermediate redshift bright, star-forming galaxies (field galaxies as filled circles, and cluster members as filled triangles), and the NFGS sample of local star-forming galaxies (open circles). (Bottom) Rest-frame [OII]λ3727 emission line equivalent width as a function of the excitation-sensitive diagnostic ratio O_{32}. Field star-forming galaxies at intermediate redshifts are shown as filled circles, and cluster members as filled triangles, open triangles show faint ($M_B > -19.5$) NFGS galaxies, and open circles show bright ($M_B \leq -19.5$) NFGS galaxies.

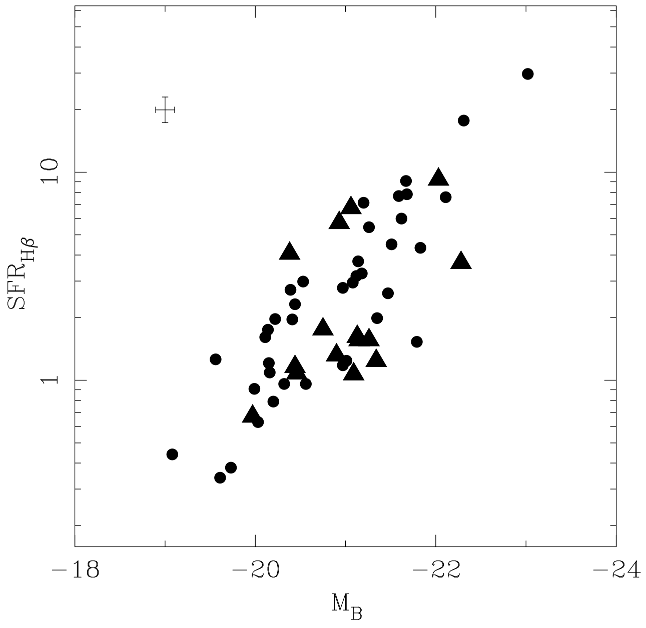

Figure 5.16. Absolute B-band magnitude versus star formation rate, derived from Hβ, for our EW samples of field (circles) and cluster (triangles) galaxies. Representative errors are shown by the error bars in the top left corner.

distant field and cluster galaxies are similar (see figure 5.14), the [OII] equivalent widths display a strong difference. The galaxies most responsible for this difference appear to be those with $O_{32} \gtrsim 0.4$. This combination of high O_{32} and low [OII] equivalent width is rather more unusual in both our distant and local field samples.

The broad similarity between the observed rest-frame emission-line equivalent widths and diagnostic ratios for bright, star-forming galaxies in the local field and those in intermediate-redshift clusters, suggests that the two samples span the same range of HII region physical parameters, in terms of ionising flux, ionisation parameter, and metallicity. This also indicates that the R_{23} versus $12 + \log(O/H)$ local calibration should be valid for converting line ratios measured for distant cluster galaxies in our sample into oxygen abundances, without introducing any systematic biases.

Figure 5.17 shows the relationship between galaxy luminosity and oxygen abundance for our sample of distant star-forming cluster galaxies compared with the distant field and local galaxy samples. The local sample shows the well-established luminosity–metallicity relation (e.g., Skillman et al. 1989; Lamareille et al. 2004; Tremonti et al. 2004). As expected from figure 5.14, our distant cluster and field galaxies are distributed similarly.

The panels of figure 5.18 show the relationship of gas phase oxygen abundance versus the rest-frame equivalent width of the [OII] emission line and extinction-corrected star formation rate. Both distant cluster and field galaxies follow similar relations between oxygen abundance and [OII] equivalent width (an indication of star formation rate per unit luminosity) as the local sample. However, as seen above, the intermediate redshift cluster galaxies tend to have lower [OII] equivalent widths at a given oxygen abundance than the distant field galaxies. This is most noticeable at low oxygen abundances, but does not necessarily imply a difference in slope, as we may be missing high oxygen abundance cluster galaxies with very

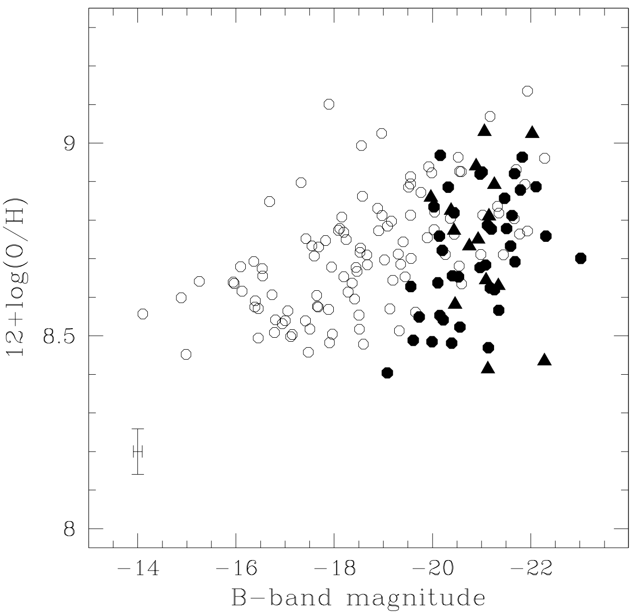

Figure 5.17. Luminosity–metallicity relation for our EW samples of intermediate-redshift star-forming cluster (filled triangles) and field (filled circles) galaxies, and local star-forming galaxies from the NFGS sample (open circles).

low [OII] equivalent widths. As anticipated from figure 5.14, there is only subtle evidence for a difference in the distributions of our intermediate redshift cluster and field galaxies in the oxygen abundance versus star formation rate diagram.

To summarise, our comparison between these distant cluster galaxies and their counterparts in the coeval field reveals that the properties of the interstellar gas are broadly similar for both samples. The primary difference is that the emission-line equivalent widths of the cluster galaxies are, on average, significantly lower than for the field galaxies. However, a fraction of the distant cluster galaxies appear to have much higher emission-line equivalent widths, comparable to the highest seen in the field. This tentatively implies a bimodality in the star formation rates per unit luminosity of distant cluster galaxies. Our luminous, star-forming, intermediate-redshift field galaxies, on the other hand, have broad, unimodal distributions, which extend smoothly to ranges observed locally only for much fainter galaxies (see section 4.5).

The hint of a bimodality in the star formation rates per unit luminosity of distant cluster galaxies, with the majority being suppressed, but some apparently enhanced, lends support to a mechanism for galaxy evolution in clusters which causes a temporary increase in the star formation rate of infalling galaxies prior to a decline in their star formation. Indications of this were also found in the consideration of the Tully-Fisher relation of cluster and field samples in section 5.2.1.

We have examined the oxygen abundances for our galaxies, but are unable to discriminate between our cluster and field samples in terms of their chemical properties. This may be due to a true lack of a difference between the two samples, perhaps because the star-forming galaxies in distant clusters have recently entered the cluster environment from the field. Alternatively, it could be that this study lacks the required statistical power to measure the difference, due to our small sample size. However, we have established some upper limits on the possible differences between

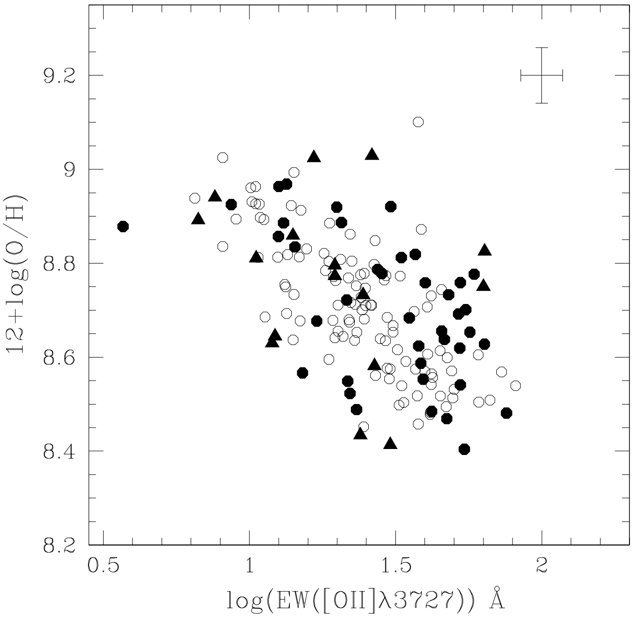

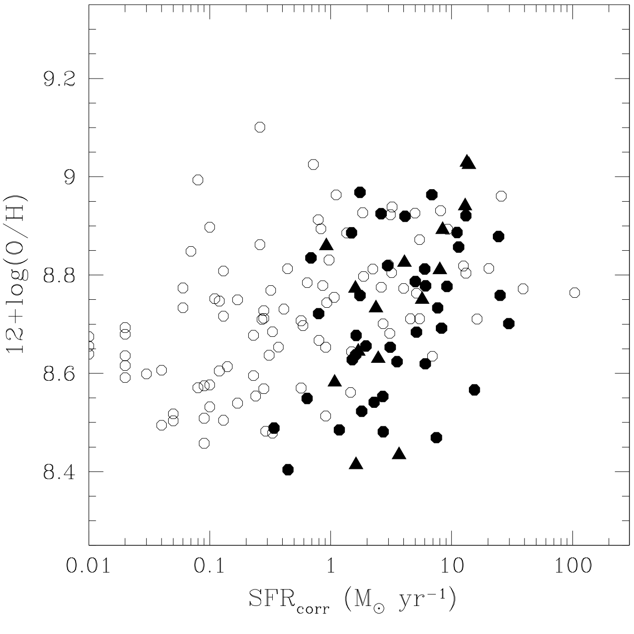

Figure 5.18. Plots showing the relationships between *(top)* oxygen abundance and rest-frame [OII] equivalent width, and *(bottom)* extinction-corrected star formation rate. Intermediate redshift star-forming cluster/field galaxies are shown as filled triangles/circles, and the NFGS sample of local star-forming galaxies is marked by open circles.

the samples. Any differences are thus small, and do not imply large differences in the star formation histories of cluster and field galaxies. They should therefore have no serious effect on the conclusions drawn from our Tully-Fisher study.

5.5 Tully-Fisher residuals versus star formation

As briefly mentioned in section 5.2.2, we can attempt to test whether Tully-Fisher residuals really do reflect differences in the recent star formation activity of galaxies by plotting these TFR residuals against indicators of current star formation. We can, perhaps, thereby add support to the interpretation of the TFR offset between cluster and field samples as being due to a recent enhancement of star formation in cluster galaxies. We may also be able to find support for interpreting the field TFR evolution with redshift, found in section 4.4, as driven by changes in star formation rate.

In figures 5.19 and 5.20 we plot the equivalent width and luminosity, respectively, of the [OII]λ3727 and Hβ emission lines versus TFR residuals ($\Delta {M_B}^{\rm TF}$). The emission-line luminosities are approximately proportional to the galaxies' current star formation rate (see section 3.2.4), while the equivalent widths indicate the current star formation rate relative to the total luminosity of the galaxy (and hence its integrated past star formation). For both the cluster and field samples a 'wedge'-shaped distribution is seen: galaxies with low emission-line luminosities span the full range of $\Delta {M_B}^{\rm TF}$, while higher emission-line luminosity galaxies display only intermediate values of $\Delta {M_B}^{\rm TF}$. Galaxies with high emission-line luminosities are not found with either low or high TFR residuals. No clear correlation is observed, although field galaxies are seen to be more numerous near the bottom edge of the wedge, while cluster galaxies tend to lie towards the top edge. A similar distribution is seen in the equivalent width plots.

This distribution can be explained by considering the evolutionary path of galaxies in this plot, along with the time spent at each region of this path. Consider a galaxy starting at $\Delta {M_B}^{\rm TF} \sim 0$, with a small emission-line luminosity due to a low level of ongoing star formation, and subsequently experiencing a burst of star formation. The emission-line and B-band luminosities will immediately increase, roughly in proportion. A factor of 6 increase in luminosity corresponds to -1.9 magnitudes. The rotation velocity is presumably unaffected. This, therefore, defines the sloping lower edge of the distribution, blurred by intrinsic scatters in both the TFR and initial star formation rate. After the burst, the star formation rate returns to a low, or zero, level. The emission-line luminosity is dominated by very massive stars, so immediately follows the star formation rate, and the galaxy thus moves back to the left of the plot. However, the B-band luminosity includes a significant contribution from less-massive stars, and therefore declines on a longer timescale. The galaxy thus remains at a higher (more negative) value of $\Delta {M_B}^{\rm TF}$ than originally, filling in the wedge-distribution. The top slope of the wedge may be explained by the constraint that larger starbursts must, in general, occur on shorter timescales as they use up the available gas faster. Therefore, galaxies with very strong bursts of star formation, which have an evolutionary track that reaches to high emission-line luminosities and $\Delta {M_B}^{\rm TF}$, spend very little time in this position. They must quickly move back to the left of the diagram, while remaining for a while at very negative TFR residuals. The sloping top edge of the distribution thus arises naturally.

While the above argument is not as obvious a connection between SFR and B-

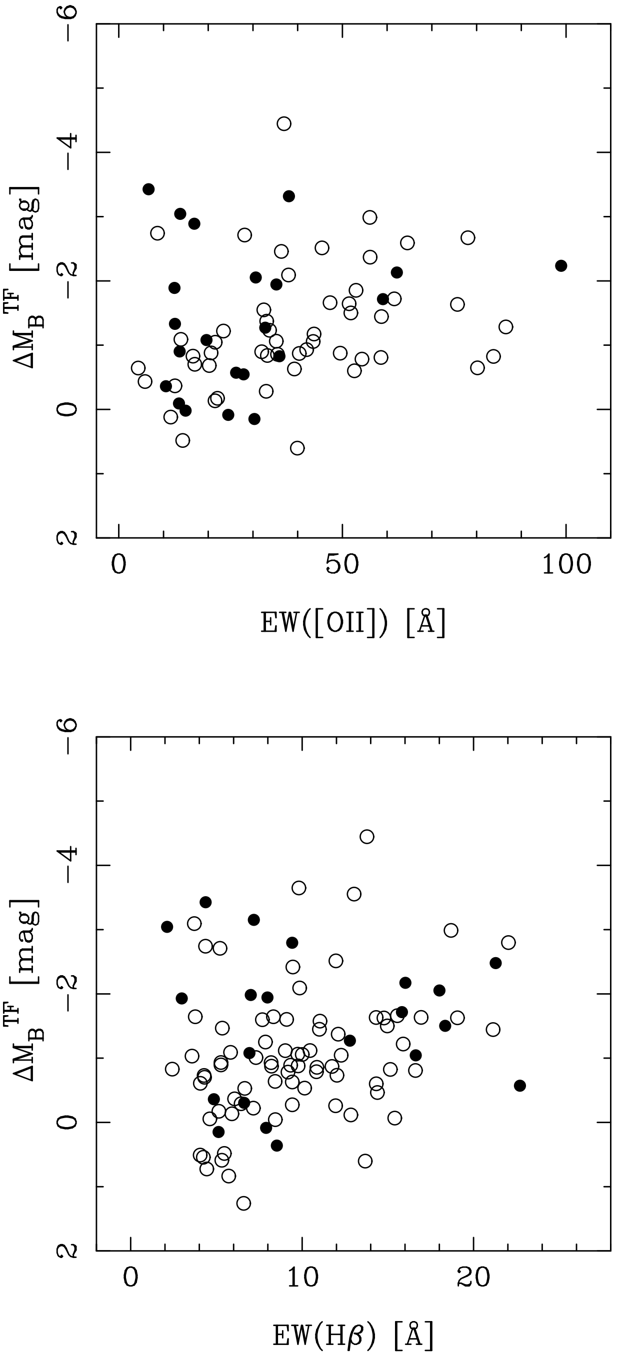

Figure 5.19. Equivalent widths of the *(top)* [OII]λ3727 and *(bottom)* Hβ emission lines, plotted versus residuals from the fiducial TFR of PT92, for all the galaxies for which we observe the respective line in our full TFR sample and including the TFR data of Nakamura et al. (2006). Cluster galaxies are indicated by filled symbols, while field galaxies are plotted with open symbols.

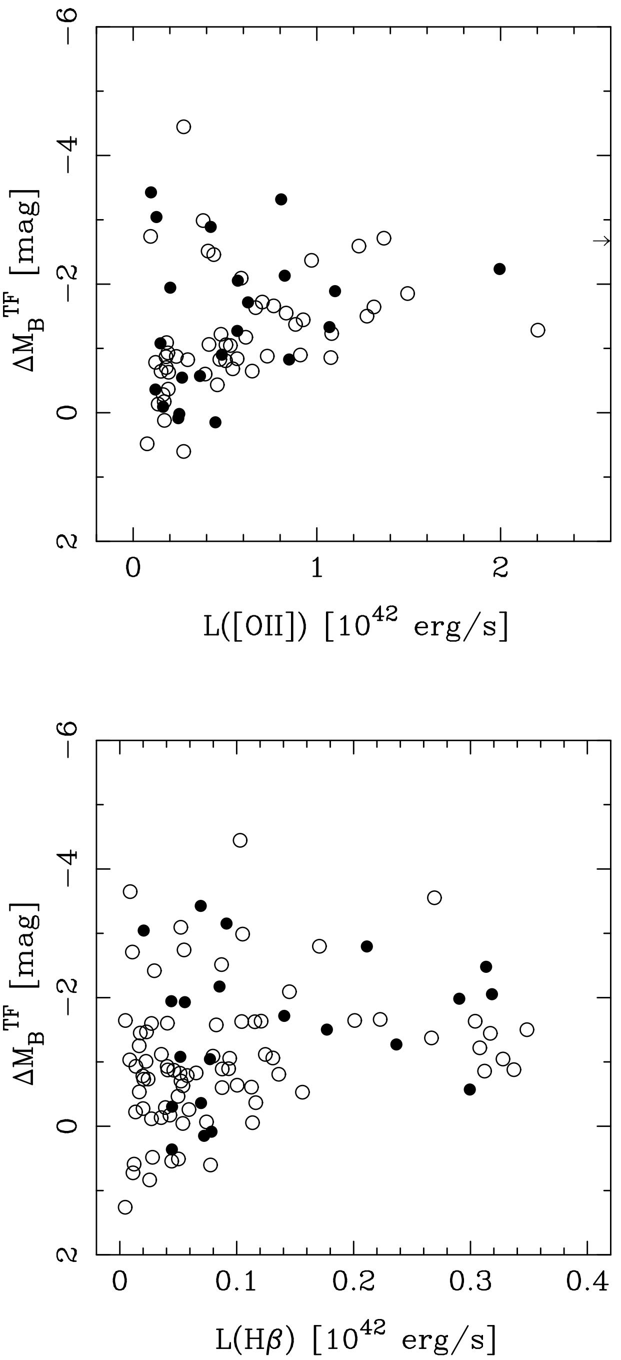

Figure 5.20. Luminosity of the *(top)* [OII]λ3727 and *(bottom)* Hβ emission lines, plotted versus residuals from the fiducial TFR of PT92, for all the galaxies for which we observe the respective line in our full TFR sample and including the TFR data of Nakamura et al. (2006). Cluster galaxies are indicated by filled symbols, while field galaxies are plotted with open symbols.

band magnitude as, say, a simple correlation, it does provide significant support for such a connection, with the crucial point that the B-band TFR residuals allow one to probe star formation activity on longer timescales than the usual current-SFR indicators. Without $\Delta M_B{}^{\mathrm{TF}}$ being related to the recent SFR it is hard to see how such a 'wedge'-shaped distribution could come about. These figures thus support the interpretation of the TFR offset between cluster and field galaxies as due to differences in their recent star formation activity, as proposed in section 5.2.2. Galaxies along the top of this distribution, and hence offset to more negative TFR residuals, are currently undergoing, or have recently experienced, a period of enhanced star formation. That this characteristic distribution is also present in the field sample lends support to the interpretation of evolution in the TFR residuals with redshift as due to star formation rate evolution, in section 4.4. This argument potentially implies a bursty mode for star formation in the field, but this will require further consideration.

Chapter 6

Conclusions and further work

6.1 Conclusions

We have analysed spectroscopic data for a large sample of luminous disc galaxies inhabiting both rich clusters and the field over the redshift range $0.1 \lesssim z \lesssim 1.0$. From these data we have determined reliable rotation velocities for 111 galaxies, as well as estimates of metallicity for 56 and star formation rate for 54 galaxies. These measurements have been used to construct several samples, in order to use both the Tully-Fisher relation (TFR) and various spectral properties to study evolution with both redshift and environment. A summary of each of these studies' conclusions is presented below.

6.1.1 Field evolution

Using all 89 field galaxies with measured rotation velocities we have investigated the evolution of the TFR with redshift. These galaxies cover the redshift range $0.1 \lesssim z \lesssim 1$, with a median of $\langle z \rangle = 0.33$. The best-fitting TFR for the full sample has a slope which is entirely consistent with that found locally by PT92. There is an intercept offset of ~ 1 mag, such that our galaxies are brighter for a given rotation velocity. However, it is likely that this is a least partly due to both the differing methods employed to measure the magnitudes and rotation velocities, and uncertainties in the distance scale used to normalise the PT92 TFR. We therefore only evaluate evolution in the TFR by making internal comparisons of our data.

Fitting sub-samples binned by redshift indicates that the TFR intercept evolves by ~ 1 mag between $z = 1$ and today, in the sense that more distant galaxies are brighter for a given rotation velocity. Plotting the residuals of our data from a local fiducial TFR against redshift confirms this trend in TFR intercept: higher-redshift galaxies are offset to brighter magnitudes. Fitting this correlation we find an evolution of -1.0 ± 0.5 mag by $z = 1$, which we argue is an upper limit due to the selection effects present in our sample.

We find no significant evidence for a change in TFR slope with redshift. Previous studies have used an observed correlation between the TFR residuals and rotation velocity to argue that low mass galaxies have evolved significantly more than those with higher mass. However, we have demonstrated that such a correlation may be due solely to an intrinsic coupling between rotation velocity scatter and TFR residuals, and thus does not necessarily indicate a physical difference in the evolution of galaxies with different rotation velocities.

Using stellar population models we have interpreted our observed TFR luminosity evolution in terms of a star formation rate (SFR) evolution. If the SFR in spiral galaxies had remained constant since $z \sim 1$, their B-band luminosity should have increased with time. However, we find the opposite trend, indicating that the SFR in these galaxies was larger in the past. We estimate $\mathrm{SFR}(z) \propto (1+z)^{1.7\pm1.1}$ for our sample. We argue that, given the likely selection effects, this is an upper limit on the SFR increase with look-back time. Our results therefore suggest that the rapid evolution in the SFR density of the universe observed since $z \sim 1$ is not driven by evolution of the SFR in individual, bright spiral galaxies.

Even though we cannot yet place strong constraints on the evolution of the SFR in the bright spiral galaxy population, due to our relatively small sample and the intrinsic scatter in the TFR, our approach could be successfully applied to ongoing and future surveys. A study with similar quality data for a sample of $\sim$600 galaxies would be needed to provide a clear ($\sim 3\sigma$) rejection of the hypothesis that the SFR density of the universe and the SFR of the average spiral galaxy evolve at the same rate.

For our 44 luminous ($M_B \lesssim -19$) disc field galaxies with reliable measurements of the equivalent widths of [OII]λ3727, Hβ and [OIII]λ5007, we examine the current star formation and chemical properties of galaxies at intermediate redshifts ($z = 0.2$–0.8, $\langle z \rangle = 0.45$). Emission-line equivalent widths and excitation- and metallicity-sensitive diagnostic ratios of these luminous galaxies cover similar ranges to those observed for local emission-line galaxies over a wide range of luminosities, i.e., $-14 \lesssim M_B \lesssim -22$. In particular, the properties for a subsample of these bright, intermediate-redshift galaxies are similar to those observed for faint and metal-poor galaxies, with moderate excitation-sensitive diagnostic ratios, at the present cosmic epoch.

We have estimated the oxygen abundance of the interstellar emitting gas for 40 of these bright, intermediate-redshift, field galaxies, finding it to cover the range $8.4 \lesssim 12 + \log(\mathrm{O/H}) \lesssim 9.0$. Our sample galaxies exhibit a luminosity–metallicity relation different from that of local galaxies. A subsample of our galaxies show oxygen abundances that are consistent with what is observed locally for their local couterparts. However, a fraction of the massive, star-forming galaxies in our sample have low oxygen abundances that are observed locally only for much fainter galaxies. Oxygen abundances are not found to correlate with the emission scale length size of the galaxy, and the rotation velocity–metallicity relation, while perhaps present, is unclear.

Metal-rich luminous and large field galaxies at intermediate redshifts show extinction-uncorrected and intrinsic star formation rates similar to their local counterparts. However, lower-metallicity systems are ~ 2 mag brighter, and have star formation rates an order of magnitude higher, compared with similar metallicity galaxies today. This suggests that the luminosity evolution measured using the TFR above, and inferred from measurements of the intermediate redshift luminosity function for blue galaxies (e.g., Wolf et al. 2003; Faber et al. 2005; Willmer et al. 2005; Zucca et al. 2005), is due to combination of substantial evolution in a subsample of field disc galaxies and very little evolution in the remainder. This may shed some light on the difficulties in unambiguously determining this evolution using the TFR, and the differences between various studies. For example, the galaxies which are rapidly forming stars at intermediate redshifts may be rejected from some studies' samples due to their non-regular colours, morphologies, etc.

These results can be considered along with the finding, by the same luminosity function studies listed above, of very little number density evolution for blue galaxies, but a rapid increase with time for red galaxies. This agrees well with a speculative scenario combining downsizing, whereby more massive galaxies form their stars earlier, due to the early suppression of star formation in lower-mass haloes, with a mechanism to truncate star-formation in galaxies which have reached a given threshold of their stellar-to-total mass ratio. These old galaxies, which consequently become red and cease line emission, thereby leave the blue luminosity function and Tully-Fisher samples. They are, however, replaced by younger galaxies, which rapidly form stars at later times. Whether this picture is plausible in reality will require extensive further testing.

The nebular extinction of our intermediate-redshift, star-forming galaxies, as derived from the ratio of the extinction-uncorrected star formation rates based on [OII]λ3727 and Hβ, is found to span a similar range to that measured for star-forming galaxies at the present epoch, but has a lower mean than is observed locally for optically-selected galaxy samples. At intermediate redshifts, luminous metal-rich galaxies exhibit similar internal reddening to local luminous metal-rich galaxies, while luminous metal-poor galaxies show lower internal reddening, similar to what is observed locally for faint, metal-poor galaxies. However, across the whole sample the dust extinction is generally less than seen locally. This suggests that the dust content of galaxies is related to their gas-phase metal content, but perhaps takes a longer time to develop.

6.1.2 Cluster evolution

From the galaxies for which we have measured reliable rotation velocities, we have constructed matched samples of 22 cluster and 58 field galaxies. These samples cover similar ranges in redshift ($0.25 \leq z \leq 1.0$) and luminosity ($M_B \leq -19.5$ mag), and are selected in an identical manner. Comparing the TFR for these two samples, we find an offset, such that galaxies in clusters are on average 0.7 ± 0.2 mag brighter than those in the coeval field, at a given rotation velocity. The reality of this offset is significant at a 3σ confidence level, and remains, with similar significance, even if a global evolution in the field population is taken into account. This result applies only to the bright, massive, star-forming, disc galaxies which form the sample considered. However, we do find a marginal indication that the galaxies in our sample with lower rotation velocities ($\lesssim 150\ \mathrm{km\,s^{-1}}$) contribute most to our measured offset.

There is a concern that the measured TFR offset could be due to biases in the fitting procedure, resulting from differences in the extent of emission, signal-to-noise, or rotation curve shape between cluster and field galaxies. In order to check this, we have extensively compared the emission-lines of the field and cluster samples, within our ability given the limited resolution of the data. We find no difference to which we could attribute the TFR offset. We consider the most likely explanation for this offset to be that the cluster galaxies have been brightened by their initial interaction with the intra-cluster medium. This is presumably due to an initial enhancement of their star-formation rate, before further interaction has suppressed it. However, at this point we cannot rule out the possibility of a change in rotation velocity due to stripping of the dark matter haloes of cluster galaxies.

We have examined the [OII]λ3727, Hβ and [OIII]λ5007 emission-line equivalent widths, and resultant diagnostic diagrams, oxygen abundances and extinction-corrected star formation rates, for a sample of 16 bright ($M_B \lesssim -20$), star-forming, mostly disc, cluster galaxies at intermediate redshifts ($0.3 \lesssim z \lesssim 0.6$, $\langle z \rangle = 0.42$). The comparison between these distant cluster galaxies and 44 of their counterparts in the coeval field, reveals that both samples have generally similar properties for their interstellar gas. However, the cluster galaxies have emission-line equivalent widths that are, on average, significantly lower than for the field galaxies. A contrasting fraction of the distant cluster galaxies, though, appears to have much higher emission-line equivalent widths, comparable to the highest seen in the field. This tentatively implies a bimodality in the star formation rates per unit luminosity of distant cluster galaxies, which is not present for our field sample.

The hint of a bimodality in the specific star formation rates of distant cluster galaxies, with the majority being suppressed but some apparently enhanced, lends support to the scenario described above, motivated by the comparison of the TFR for our cluster and field samples, whereby spiral galaxies entering intermediate-redshift clusters experience a temporary increase in their star formation rate, prior to a decline. A similar bimodal behaviour is seen in the total star formation rates. A variety of plausible physical mechanisms have been proposed which could be responsible for such an evolution, see section 1.3.2. However, more work is necessary before the roles and dominance of the various suggested mechanisms can be established.

We are unable to discriminate between our cluster and field samples in terms of their chemical properties. This may be due to a true lack of a difference between the two samples, perhaps because the star-forming galaxies in distant clusters have recently entered the cluster environment from the field. Alternatively, it could be that this study lacks the required statistical power to measure the difference, due to our small sample size. However, we have established some upper limits on the possible differences between the samples. These suggest that the long-term star formation histories of luminous, intermediate-redshift, star-forming, disc galaxies do not differ substantially between cluster and field environments.

Taken alone, a general reduction in the specific star formation rates of our cluster galaxies implies a B-band dimming of these galaxies. However, from our TFR study we find that these cluster galaxies are actually on average brighter than similar-redshift field galaxies, at a given rotation velocity. Combining these findings implies that the B-band luminosities of our cluster galaxies have been previously increased, either by star-formation at a rate higher than typically seen in the field, or by their forming stars over a longer period of time. As only a relatively small fraction of cluster galaxies are seen to have current star-formation rates in excess of the field average ($\sim$10–20%), our cluster galaxies must have established their increased star formation history prior to entering the cluster environment, or it must be a result of a recent, short-lived, phase of enhanced star formation. However, the lack of a difference in the metallicity and dust content of cluster and field galaxies argues against long term differences in their star formation histories. The scenario of a recent, short burst of star formation, followed by a decline, is thus preferred.

There is a remaining possibility that the TFR offset could be due to changes in the rotation velocity of cluster galaxies, rather than an enhancement of their luminosity. However, without an earlier phase of enhanced star-formation, the dimming associated with the lower star formation rates that are observed requires an even more considerable rotation velocity change to produce the measured TFR offset. This scenario thus becomes even less feasible when compared with the results of simulations (e.g., Gnedin 2003b), which do not find such substantial changes in the rotation velocities of cluster galaxies with stripped dark matter haloes, even for extreme cases.

Beyond looking for a simple difference between galaxies in clusters and those in the field, one would like to determine the detailed trends of galaxy star formation histories with respect to quantitative indicators of their environment. An expectation for the relationship between environment and the chemical evolutionary status of galaxies, an indicator of long-term star formation history, may be inferred from the trends observed for current star formation rates. The total star formation rate per cluster mass (Finn et al. 2005), the fraction of star-forming cluster galaxies, and the star formation rates of individual cluster galaxies (Poggianti et al. 2006) correlate strongly with cluster mass, in the sense that clusters with larger velocity dispersions tend to have systematically lower star-formation activity, and are populated by more passive galaxies (but see also Kodama et al. 2004). In addition, an anti-correlation between the cluster X-ray luminosity and the total star formation rate per cluster mass (Homeier et al. 2005) offers support for the dependence of the normalized star formation rate on cluster mass. The correlation between star formation activity and cluster mass seems to be traced by both high and low redshift clusters, as suggested by Lewis et al. (2002) and Gómez et al. (2003). However, the picture is complicated by Goto (2005) which finds, using a sample of low redshift clusters drawn from the Sloan Digital Sky Survey, that the fraction of late-type galaxies and the mass-normalized star formation rate do not significantly depend on cluster mass.

However, considering current star formation rates leaves open the question of whether galaxies in higher-mass clusters are more advanced in their evolutionary state, because they have formed stars for longer, or faster at earlier times, or whether they are less evolved, because their star formation activity has been more suppressed. In our study, we are unable to discern a difference in the metallicity of bright cluster and field star-forming galaxies. This implies that star-forming cluster galaxies are recent entrants from the field. Therfore, the chemical properties of the passive galaxy population must be considered in order to address this issue as a function of cluster mass.

To fully quantify the effect of environment on the chemical evolution of galaxies, future studies must thus overcome the degenerate effects of cluster mass and redshift on galaxy properties, and investigate all of the galaxy populations present. They will therefore require considerably larger samples than are considered here, spanning a range of cluster masses at a variety of redshifts.

Finally, a missing piece of this puzzle is the behaviour of faint galaxies. In our sample we consider only the brightest galaxies, with $M_B \lesssim -20$. The effect of environment on the chemical evolution of galaxies as a function of galaxy luminosity and mass is unknown at intermediate redshifts. Investigating this topic must be postponed until intermediate redshift field and cluster galaxy samples are available with large quantities of star-forming galaxies spanning a range of galaxy luminosity.

6.2 Further work

6.2.1 Tests and improvements of the two-dimensional emission-line fitting method

Tests for biases in the two-dimensional emission-line fitting procedure have been previously made, finding none (e.g., Simard & Pritchet 1999). However, these tests have not been particularly comprehensive. We would like to be more sure of the level of such potential biases over the full range of parameter combinations encountered, and their dependence on signal-to-noise. For example, concern has been expressed that galaxies with scalelengths comparable to the seeing may result in underestimated rotation velocities, although we have seen no clear evidence for this. We therefore plan to perform a large series of tests to evaluate these issues in detail.

The reliability of our rotation velocity and emission-line scalelength measurements is dependant upon the degree to which the assumptions made in the fitting process match the properties of the galaxies under consideration. For example, an exponential surface brightness profile is used to produce the model emission-lines. However, the true emission-line surface brightness profile may be different, perhaps with a nuclear component or displaying truncation. This makes comparing the model and real emission-lines less valid, and may introduce biases in the resulting fit parameters.

In this thesis we have attempted to deal with galaxies which contravine the model assumptions by removing them from the sample using a combination of quantitative cuts and visual inspection. However, this procedure is limited by the data quality, and we are unable to identify and remove all the galaxies which do not match our assumptions, particularly when the deviations are not substantial. In addition, we would also like to be able to measure parameters, particularly the rotation velocity, for galaxies with deviating surface brightness profiles. These are potentially the most interesting objects in terms of galaxy evolution, but current TFR studies must reject them from consideration.

It would therefore be preferable for the fitting procedure to be capable of adapting to more varied surface brightness profiles, so that this variation, including our lack of knowledge about it, can be accounted for in the fitting procedure. The rejection of such objects would thus not be necessary, and reliable rotation velocities could be measured for them.

In order to assess the seriousness of departures from the assumed surface brightness profile and intrinsic rotation curve on the results of the emission-line fitting method, we plan to perform another large series of simulations. For these we will produce model lines with varied surface brightness profiles and intrinsic rotation curves, add noise, and attempt to recover the input parameters by fitting using our usual assumptions. We will also add the improvements to our fitting method suggested above, for example the inclusion of a nuclear emission component. These improved procedures will be tested to ascertain if they can improve the reliability of our fits in both the presence of departures from our usual assumptions and in cases where the usual assumptions are valid.

6.2.2 The European Distant Cluster Survey

The ESO Distant Cluster Survey (EDisCS; White et al. 2005) is a study of galaxies in and around ~ 20 clusters at $0.4 \leq z_{\rm cl} \leq 1.0$ (White et al. 2005). These clusters were optically selected using the Las Campanas Distant Cluster Survey (LCDCS; Gonzalez et al. 2001), and thus have a wide range of properties. For each cluster a wealth of imaging and spectroscopy data has been obtained, much of this using the VLT and NTT, through the survey's status as an ESO large programme. Many projects are underway using these data, including studies of morphology, luminosity functions, colour-magnitude diagrams, cluster substructure, velocity distributions, lensing masses and stellar populations.

From the spectra we will soon measure rotation velocities, in the same manner as discussed in section 3.1. We will thus be able to perform detailed investigations into the evolution of various galaxy properties with respect to this useful baseline. With more than five times as many galaxies, we will have the statistical power to vastly improve upon the studies presented in this thesis. The addition of HST morphologies, homogeneous colours, spectral indices and a variety of clusters with well characterised properties, will allow unprecedented studies of disc galaxy evolution with environment and redshift.

6.2.3 IFU observations of E+A cluster disc galaxies

A useful alternative to slit-based spectroscopy is provided by integral field units (IFUs). These sample light from the whole galaxy, rather than just a narrow slit, and can thus provide a more detailed picture of the velocity field. This allows kinematical disturbances to be identified more easily, and potentially more accurate rotation velocity measurements.

However, the main drawback of IFUs at this time is a much reduced multiplexing ability. Most integral field spectrographs are only capable of observing a single object at a time (e.g., GMOS). While some instruments can have a relatively wide field-of-view, this comes at the expense of spatial and/or spectral resolution, and is still rather too small to observe many intermediate-redshift emission-line galaxies simultaneously (e.g., VIMOS). Currently, the only instrument with a true multiplexing ability is FLAMES/GIRAFFE on the VLT, which has 15 deployable $3'' \times 2''$, 20 element IFUs. This is still significantly less than the typical 26 slits on each of our FORS2 masks, and a factor of ten less than is possible using the multi-slit mode of VIMOS.

An important consideration for using IFUs to observe high-redshift galaxies is that they can access the near-infrared. Such a capability is provided by instruments such as CIRPASS and SPIFFI. Another significant breakthrough is the coupling of IFUs with adaptive optics, a purpose for which SPIFFI is designed.

IFUs are already being used to measure the rotation velocities of galaxies at $z \sim 1$, e.g., Smith et al. (2004), and are now being used to construct samples for high-redshift Tully-Fisher studies (Flores et al. 2004), that are more kinematically reliable than slit-based work.

In order to further investigate the interaction of disc galaxies with cluster environments, we are conducting an examination of E+A discs in AC114, a rich $z \sim 0.3$ cluster. For this study we have successfully obtained very deep (14h integration) integral field spectroscopy for a magnitude-limited sample of 12 disky E+A galaxies, using the deployable IFUs of the FLAMES/GIRAFFE instrument on the VLT. E+A spectra display strong Balmer absorption lines, tracing young stars, as well as metal lines from the older stellar population. Such E+A discs are potentially galaxies in the critical intermediate stage of the transformation from spiral to S0. By examining spectra over the entire galaxy (rather than a narrow slit as with conventional spectroscopy), we will be able to perform a detailed comparison of the distribution and dynamics of these constituent stellar populations. From this we aim to firmly test the hypothesis of disky E+A galaxies as an evolutionary link between spirals and S0s and, in particular, constrain the mechanisms responsible for the their observed properties.

A very similar study has been performed recently by Pracy et al. (2005), although they only examine the relative distributions of the two stellar populations. We intend to perform a more detailed analysis of our data and theirs combined, in order to hopefully gain further insight from the dynamics.

6.2.4 Interactions of distant star-forming galaxies as a function of environment

Recent work by members of the EDisCS collaboration clearly demonstrates that galaxy evolution is closely linked to environment at intermediate redshifts. Poggianti et al. (2006) shows that the fraction of star-forming galaxies (as indicated by [OII] emission) is a strong function of environment, and that this relationship evolves with redshift in a complex manner. Even poor groups have some effect on their constituent galaxies, and the trends with environment are not straightforward, e.g., there is a significant presence of rich cluster galaxies with large [OII] equivalent widths, opposing the general trend.

Galaxies can evolve through internal processes and through interactions with their environment, including other galaxies. In the hierarchical picture galaxy-galaxy interactions, particularly mergers, are the dominant process in determining the properties of the galaxy population (e.g., Cole et al. 2000). While most frequent at high redshift, mergers are still prevalent at intermediate-redshifts and are not uncommon today. In addition to spectacular major mergers there are a range of more subtle galaxy-galaxy interactions, minor mergers and close encounters, which can still have significant effects on the galaxies involved. The absolute and relative frequencies of these galaxy-galaxy interactions are expected to change with environment, due to variation in the number density and relative velocities. Dense environments also present other interactions, including ram-pressure due to the intracluster medium and tidal forces. While these are often expected to only be significant in rich clusters, there is evidence that they may also be at work in groups (Balogh et al. 2004).

As an extension of the studies presented in this thesis, and those we will be undertaking with EDisCS, we plan to obtain IFU observations for a subset of $\sim$ 90 galaxies in our EDisCS sample, covering a range of environments. An ideal field comparison sample of ~ 100 galaxies, selected and observed in a very similar manner, is provided by another ESO large programme. Using these we aim to get a clear picture of the variety and frequency of galaxy interactions as a function of environment, and relate this to the resultant star-formation and morphological evolution. We will thus improve our knowledge of which evolutionary mechanisms dominate as a function of environment, and their role in the observed trends of galaxy properties with environment and redshift.

In addition, this study will allow us to determine the robustness of our, more efficiently obtained, slit-based results, and any biases present in such studies. The lack of certainty concerning these systematic effects is a significant weakness of current work. A thorough knowledge of any biases, or lack thereof — together with the simulation study described above — will strengthen or refute previous results, as well as providing a solid grounding for future work.

Bibliography

Aaronson M., Huchra J., Mould J., 1979, ApJ, 229, 1

Abadi M. G., Moore B., Bower R. G., 1999, MNRAS, 308, 947

Afonso J., Hopkins A., Mobasher B., Almeida C., 2003, ApJ, 597, 269

Allende Prieto C., Lambert D. L., Asplund M., 2001, ApJ, 556, L63

Alloin D., Collin-Souffrin S., Joly M., Vigroux L., 1979, A&A, 78, 200

Aragón-Salamanca A., Ellis R. S., Couch W. J., Carter D., 1993, MNRAS, 262, 764

Böhm A., et al., 2004, A&A, 420, 97

Böhm A., Ziegler B. L., 2006, ApJ submitted (astro-ph/0601505)

Baker J. G., Menzel D. H., 1938, ApJ, 88, 52

Baldwin J. A., Phillips M. M., Terlevich R., 1981, PASP, 93, 5

Balogh M., et al., 2004, MNRAS, 348, 1355

Bamford S. P., Milvang-Jensen B., Aragón-Salamanca A., Simard L., 2005, MNRAS, 361, 109

Bamford S. P., Aragón-Salamanca A., Milvang-Jensen B., 2006, MNRAS, 366, 308

Barden M., Lehnert M. D., Tacconi L., Genzel R., White S., Franceschini A., 2003, unpublished (astro-ph/0302392)

Barnes J., Efstathiou G., 1987, ApJ, 319, 575

Beers T. C., Flynn K., Gebhardt K., 1990, AJ, 100, 32

Bekki K., 1998, ApJ, 502, L133

Bekki K., 1999, ApJ, 510, L15

Bekki K., Couch W. J., 2003, ApJ, 596, L13

Bekki K., Couch W. J., Shioya Y., 2002, ApJ, 577, 651

Bell E. F., de Jong R. S., 2001, ApJ, 550, 212

Bell E. F., McIntosh D. H., Katz N., Weinberg M. D., 2003, ApJS, 149, 289

Bell E. F., et al., 2005, ApJ, 625, 23

Bertin E., Arnouts S., 1996, A&AS, 117, 393

Biviano A., Giuricin G., Mardirossian F., Mezzetti M., 1990, ApJS, 74, 325

Blanton M. R., et al., 2003, ApJ, 592, 819

Bond J. R., Cole S., Efstathiou G., Kaiser N., 1991, ApJ, 379, 440

Bonnell I. A., Vine S. G., Bate M. R., 2004, MNRAS, 349, 735

Borgani S., Governato F., Wadsley J., Menci N., Tozzi P., Quinn T., Stadel J., Lake G., 2002, MNRAS, 336, 409

Bower R. G., 1991, MNRAS, 248, 332

Bower R. G., Lucey J. R., Ellis R. S., 1992, MNRAS, 254, 601

Bower R. G., Benson A. J., Malbon R., Helly J. C., Frenk C. S., Baugh C. M., Cole S., Lacey C. G., 2005, MNRAS in press (astro-ph/0511338)

Brinchmann J., Ellis R. S., 2000, ApJ, 536, L77

Bromm V., Larson R. B., 2004, ARA&A, 42, 79

Bruzual G., Charlot S., 2003, MNRAS, 344, 1000

Buat V., Boselli A., Gavazzi G., Bonfanti C., 2002, A&A, 383, 801

Bundy K., Ellis R. S., Conselice C. J., 2005, ApJ, 625, 621

Burkert A., 1995, ApJ, 447, L25

Burstein D., Bender R., Faber S., Nolthenius R., 1997, AJ, 114, 1365

Butcher H., Oemler A., 1978, ApJ, 219, 18

Cardelli J. A., Clayton G. C., Mathis J. S., 1989, ApJ, 345, 245

Carilli C. L., Rawlings S., 2004, New Astronomy Review, 48, 979

Ciardi B., Ferrara A., 2005, Space Science Reviews, 116, 625

Cole S., Aragon-Salamanca A., Frenk C. S., Navarro J. F., Zepf S. E., 1994, MNRAS, 271, 781

Cole S., Lacey C. G., Baugh C. M., Frenk C. S., 2000, MNRAS, 319, 168

Conselice C. J., Bundy K., Ellis R. S., Brichmann J., Vogt N. P., Phillips A. C., 2005, ApJ, 628, 160

Couch W. J., Sharples R. M., 1987, MNRAS, 229, 423

Couch W. J., Barger A. J., Smail I., Ellis R. S., Sharples R. M., 1998, ApJ, 497, 188

Courteau S., 1997, AJ, 114, 2402

Cowie L. L., Hu E. M., Songaila A., Egami E., 1997, ApJ, 481, L9

Croton D. J., Springel V., White S. D. M., De Lucia G., Frenk C. S., Gao L., Jenkins A., Kauffmann G., Navarro J. F., Yoshida N., 2006, MNRAS, 365, 11

Crowl H. H., Kenney J. D. P., van Gorkom J. H., Vollmer B., 2005a, AJ, 130, 65

Crowl H. H., Kenney J. D. P., van Gorkom J. H., Vollmer B., 2005b, in ASP Conf. Ser. 331: Extra-Planar Gas p. 281

Dalcanton J. J., Spergel D. N., Summers F. J., 1997, ApJ, 482, 659

Dale D. A., Giovanelli R., Haynes M. P., Scodeggio M., Hardy E., Campusano L. E., 1997, AJ, 114, 455

Dale D. A., Giovanelli R., Haynes M. P., Campusano L. E., Hardy E., 1999, AJ, 118, 1489

Dale D. A., Giovanelli R., Haynes M. P., Hardy E., Campusano L. E., 2001, AJ, 121, 1886

Davis M., et al., 2003, in Guhathakurta, P., ed., Proc. SPIE Vol. 4834. pp 161–172

de Jong R. S., 1996, A&A, 313, 45

De Lucia G., Kauffmann G., Springel V., White S. D. M., Lanzoni B., Stoehr F., Tormen G., Yoshida N., 2004, MNRAS, 348, 333

Denicoló G., Terlevich R., Terlevich E., 2002, MNRAS, 330, 69

Dessauges-Zavadsky M., Pindao M., Maeder A., Kunth D., 2000, A&A, 355, 89

Douglas N. G., Gerssen J., Kuijken K., Merrifield M. R., 2000, MNRAS, 316, 795

Dressler A., 1980, ApJ, 236, 351

Dressler A., Gunn J. E., 1982, ApJ, 263, 533

Dressler A., Gunn J. E., 1983, ApJ, 270, 7

Dressler A., Gunn J. E., 1992, ApJS, 78, 1

Dressler A., et al., 1997, ApJ, 490, 577

Dressler A., Smail I., Poggianti B. M., Butcher H., Couch W. J., Ellis R. S., Oemler A. J., 1999, ApJS, 122, 51

Drory N., Bender R., Feulner G., Hopp U., Maraston C., Snigula J., Hill G. J., 2004, ApJ, 608, 742

Drory N., Salvato M., Gabasch A., Bender R., Hopp U., Feulner G., Pannella M., 2005, ApJ, 619, L131

Efstathiou G., Frenk C. S., White S. D. M., Davis M., 1988, MNRAS, 235, 715

Eggen O. J., Lynden-Bell D., Sandage A. R., 1962, ApJ, 136, 748

Ellison S. L., Kewley L. J., Mallén-Ornelas G., 2005, MNRAS, 357, 354

ESO 2002, Szeifert T., ed., FORS1+2 User Manual (Issue 2.5). European Southern Observatory. Available from http://www.eso.org/instruments/fors/doc

Faber S. M., et al., 2005, submitted to ApJ (astro-ph/0506044)

Fall S. M., Efstathiou G., 1980, MNRAS, 193, 189

Fasano G., Poggianti B. M., Couch W. J., Bettoni D., Kjærgaard P., Moles M., 2000, ApJ, 542, 673

Ferrari C., Benoist C., Maurogordato S., Cappi A., Slezak E., 2005, A&A, 430, 19

Finn R. A., Zaritsky D., McCarthy D. W., Poggianti B., Rudnick G., Halliday C., Milvang-Jensen B., Pelló R., Simard L., 2005, ApJ, 630, 206

Flores H., Puech M., Hammer F., Garrido O., Hernandez O., 2004, A&A, 420, L31

Flores H., Hammer F., Puech M., Amram P., Balkowski C., 2006, A&A in press (astro-ph/0603563)

Fontana A., Pozzetti L., Donnarumma I., Renzini A., Cimatti A., Zamorani G., Menci N., Daddi E., Giallongo E., Mignoli M., Perna C., Salimbeni S., Saracco P., Broadhurst T., Cristiani S., D'Odorico S., Gilmozzi R., 2004, A&A, 424, 23

Forbes D. A., Phillips A. C., Koo D. C., Illingworth G. D., 1996, ApJ, 462, 89

Fukugita M., Shimasaku K., Ichikawa T., 1995, PASP, 107, 945

Gallego J., Zamorano J., Aragón-Salamanca A., Rego M., 1995, ApJ, 455, L1

Gebhardt K., et al., 2003, ApJ, 597, 239

Gentile G., Salucci P., Klein U., Vergani D., Kalberla P., 2004, MNRAS, 351, 903

Gioia I. M., Shaya E. J., Le Fevre O., Falco E. E., Luppino G. A., Hammer F., 1998, ApJ, 497, 573

Girardi M., Mezzetti M., 2001, ApJ, 548, 79

Gnedin O. Y., 2003a, ApJ, 582, 141

Gnedin O. Y., 2003b, ApJ, 589, 752

Gómez P. L., et al., 2003, ApJ, 584, 210

Gonzalez A. H., Zaritsky D., Dalcanton J. J., Nelson A., 2001, ApJS, 137, 117

Goto T., 2005, MNRAS, 356, L6

Goto T., et al., 2003, PASJ, 55, 757

Gunn J. E., Gott J. R. I., 1972, ApJ, 176, 1

Hammer F., Flores H., Elbaz D., Zheng X. Z., Liang Y. C., Cesarsky C., 2005, A&A, 430, 115

Hawkins E., et al., 2003, MNRAS, 346, 78

Haynes M. P., Giovanelli R., Herter T., Vogt N. P., Freudling W., Maia M. A. G., Salzer J. J., Wegner G., 1997, AJ, 113, 1197

Heavens A., Panter B., Jimenez R., Dunlop J., 2004, Nature, 428, 625

Henriksen M., Byrd G., 1996, ApJ, 459, 82

Hoekstra H., Franx M., Kuijken K., van Dokkum P. G., 2002, MNRAS, 333, 911

Homeier N. L., et al., 2005, ApJ, 621, 651

Hopkins A. M., 2004, ApJ, 615, 209

Hopkins A. M., Connolly A. J., Haarsma D. B., Cram L. E., 2001, AJ, 122, 288

Hopkins A. M., Miller C. J., Nichol R. C., Connolly A. J., Bernardi M., Gómez P. L., Goto T., Tremonti C. A., Brinkmann J., Ivezić Ž., Lamb D. Q., 2003, ApJ, 599, 971

Huchra J., Davis M., Latham D., Tonry J., 1983, ApJS, 52, 89

Hummer D. G., Storey P. J., 1987, MNRAS, 224, 801

Jäger K., Ziegler B. L., Böhm A., Heidt J., Möllenhoff C., Hopp U., Mendez R. H., Wagner S., 2004, A&A, 422, 907

Jansen R. A., Fabricant D., Franx M., Caldwell N., 2000, ApJS, 126, 331

Jansen R. A., Franx M., Fabricant D., 2001, ApJ, 551, 825

Kannappan S. J., Fabricant D. G., Franx M., 2002, AJ, 123, 2358

Kauffmann G., White S. D. M., Guiderdoni B., 1993, MNRAS, 264, 201

Kay S. T., Thomas P. A., Jenkins A., Pearce F. R., 2004, MNRAS, 355, 1091

Kelson D. D., 2003, PASP, 115, 688

Kennicutt R. C., 1998, ApJ, 498, 541

Kennicutt R. C., Tamblyn P., Congdon C. E., 1994, ApJ, 435, 22

Kennicutt R. C., Bresolin F., Garnett D. R., 2003, ApJ, 591, 801

Kewley L. J., Dopita M. A., 2002, ApJS, 142, 35

Kewley L. J., Heisler C. A., Dopita M. A., Lumsden S., 2001, ApJS, 132, 37

Kewley L. J., Geller M. J., Jansen R. A., 2004, AJ, 127, 2002

Kobulnicky H. A., Koo D. C., 2000, ApJ, 545, 712

Kobulnicky H. A., Phillips A. C., 2003, ApJ, 599, 1031

Kobulnicky H. A., Kewley L. J., 2004, ApJ, 617, 240

Kobulnicky H. A., Kennicutt R. C., Pizagno J. L., 1999, ApJ, 514, 544

Kobulnicky H. A., et al., 2003, ApJ, 599, 1006

Koda J., Sofue Y., Wada K., 2000, ApJ, 531, L17

Kodaira K., 1989, ApJ, 342, 122

Kodama T., Balogh M. L., Smail I., Bower R. G., Nakata F., 2004, MNRAS, 354, 1103

Kong X., Cheng F. Z., Weiss A., Charlot S., 2002, A&A, 396, 503

Koopmann R. A., Haynes M. P., Catinella B., 2006, AJ, 131, 716

Lamareille F., Mouhcine M., Contini T., Lewis I., Maddox S., 2004, MNRAS, 350, 396

Lemoine-Busserolle M., Contini T., Pelló R., Le Borgne J.-F., Kneib J.-P., Lidman C., 2003, A&A, 397, 839

Lewis I., et al., 2002, MNRAS, 334, 673

Liang Y. C., Hammer F., Flores H., Gruel N., Assémat F., 2004, A&A, 417, 905

Lilly S. J., Le Fevre O., Hammer F., Crampton D., 1996, ApJ, 460, L1

Lilly S. J., Carollo C. M., Stockton A. N., 2003, ApJ, 597, 730

Loveday J., 2004, MNRAS, 347, 601

Madgwick D. S., et al., 2002, MNRAS, 333, 133

Maier C., Meisenheimer K., Hippelein H., 2004, A&A, 418, 475

Maier C., Lilly S. J., Carollo C. M., Stockton A., Brodwin M., 2005, ApJ, 634, 849

Maier C., Lilly S. J., Carollo C. M., Meisenheimer K., Hippelein H., Stockton A., 2006, ApJ, 639, 858

Mathieu A., Merrifield M. R., Kuijken K., 2002, MNRAS, 330, 251

McCall M. L., Rybski P. M., Shields G. A., 1985, ApJS, 57, 1

McGaugh S. S., 1991, ApJ, 380, 140

McGaugh S. S., 1994, ApJ, 426, 135

Melbourne J., Salzer J. J., 2002, AJ, 123, 2302

Metevier A. J., Koo D. C., Simard L., Phillips A. C., 2006, ApJ in press (astro-ph/0601671)

Metropolis N., Rosenbluth A., Rosenbluth M., Teller A., Teller E., 1953, J. Chem. Phys., 21, 1087

Mihos J. C., Hernquist L., 1994, ApJ, 425, L13

Milvang-Jensen B., 2003, PhD thesis, University of Nottingham

Milvang-Jensen B., Aragón-Salamanca A., Hau G. K. T., Jørgensen I., Hjorth J., 2003, MNRAS, 339, L1

Mo H. J., White S. D. M., 1996, MNRAS, 282, 347

Mo H. J., White S. D. M., 2002, MNRAS, 336, 112

Moore B., Governato F., Quinn T., Stadel J., Lake G., 1998, ApJ, 499, L5

Moore B., Lake G., Quinn T., Stadel J., 1999, MNRAS, 304, 465

Mouhcine M., Bamford S. P., Aragón-Salamanca A., Nakamura O., 2006a, MNRAS, 368, 1871

Mouhcine M., Bamford S. P., Aragón-Salamanca A., Nakamura O., 2006b, MNRAS in press (astro-ph/0603639)

Mouhcine M., Contini T., 2002, A&A, 389, 106

Mouhcine M., Lewis I., Jones B., Lamareille F., Maddox S. J., Contini T., 2005, MNRAS, 362, 1143

Nakamura O., Aragón-Salamanca A., Milvang-Jensen B., Arimoto N., Ikuta C., Bamford S. P., 2006, MNRAS, 366, 144

Nakamura O., Fukugita M., Brinkmann J., Schneider D. P., 2004, AJ, 127, 2511

Narlikar J. V., Padmanabhan T., 2001, ARA&A, 39, 211

Navarro J. F., Frenk C. S., White S. D. M., 1996, ApJ, 462, 563

Navarro J. F., Steinmetz M., 2000, ApJ, 538, 477

Norberg P., et al., 2002, MNRAS, 336, 907

Osterbrock D. E., 1989, Astrophysics of gaseous nebulae and active galactic nuclei. Mill Valley: Univ. Sci.

Owen F. N., Ledlow M. J., Keel W. C., Wang Q. D., Morrison G. E., 2005, AJ, 129, 31

Pagel B. E. J., Edmunds M. G., Blackwell D. E., Chun M. S., Smith G., 1979, MNRAS, 189, 95

Pei Y. C., Fall S. M., 1995, ApJ, 454, 69

Persic M., Salucci P., 1991, ApJ, 368, 60

Pettini M., Shapley A. E., Steidel C. C., Cuby J.-G., Dickinson M., Moorwood A. F. M., Adelberger K. L., Giavalisco M., 2001, ApJ, 554, 981

Pierce M. J., 1994, ApJ, 430, 53

Pierce M. J., Tully R. B., 1992, ApJ, 387, 47

Pierini D., Tuffs R. J., 1999, A&A, 343, 751

Pilyugin L. S., 2001, A&A, 374, 412

Poggianti B. M., Smail I., Dressler A., Couch W. J., Barger A. J., Butcher H., Ellis R. S., Oemler A. J., 1999, ApJ, 518, 576

Poggianti B. M., Bridges T. J., Komiyama Y., Yagi M., Carter D., Mobasher B., Okamura S., Kashikawa N., 2004, ApJ, 601, 197

Poggianti B. M., et al., 2006, ApJ, 642, 188

Ponman T. J., Cannon D. B., Navarro J. F., 1999, Nature, 397, 135

Postman M., et al., 2005, ApJ, 623, 721

Pracy M. B., Couch W. J., Blake C., Bekki K., Harrison C., Colless M., Kuntschner H., de Propris R., 2005, MNRAS, 359, 1421

Press W. H., Schechter P., 1974, ApJ, 187, 425

Quilis V., Moore B., Bower R., 2000, Science, 288, 1617

Reed D., Gardner J., Quinn T., Stadel J., Fardal M., Lake G., Governato F., 2003, MNRAS, 346, 565

Rix H.-W., Guhathakurta P., Colless M., Ing K., 1997, MNRAS, 285, 779

Rola C. S., Terlevich E., Terlevich R. J., 1997, MNRAS, 289, 419

Saha P., Williams T. B., 1994, AJ, 107, 1295

Salzer J. J., MacAlpine G. M., Boroson T. A., 1989, ApJS, 70, 479

Schechter P., 1976, ApJ, 203, 297

Schlegel D. J., Finkbeiner D. P., Davis M., 1998, ApJ, 500, 525

Shapley A. E., Coil A. L., Ma C.-P., Bundy K., 2005, ApJ, 635, 1006

Sheth R. K., Mo H. J., Tormen G., 2001, MNRAS, 323, 1

Silk J., 1997, ApJ, 481, 703

Silk J., 2003, Ap&SS, 284, 663

Simard L., Pritchet C. J., 1998, ApJ, 505, 96

Simard L., Pritchet C. J., 1999, PASP, 111, 453

Simard L., Koo D. C., Faber S. M., Sarajedini V. L., Vogt N. P., Phillips A. C., Gebhardt K., Illingworth G. D., Wu K. L., 1999, ApJ, 519, 563

Simard L., et al., 2002, ApJS, 142, 1

Skillman E. D., Kennicutt R. C., Hodge P. W., 1989, ApJ, 347, 875

Smail I., Dressler A., Couch W. J., Ellis R. S., Oemler A. J., Butcher H., Sharples R. M., 1997, ApJS, 110, 213

Smith J. K., et al., 2004, MNRAS, 354, L19

Sofue Y., Rubin V., 2001, ARA&A, 39, 137

Somerville R. S., Primack J. R., 1999, MNRAS, 310, 1087

Spergel D. N., et al., 2003, ApJS, 148, 175

Springel V., Di Matteo T., Hernquist L., 2005, ApJ, 620, L79

Springel V., et al., 2005, Nature, 435, 629

Stasinska G., 1990, A&AS, 83, 501

Stasińska G., Sodré L., 2001, A&A, 374, 919

Stasińska G., Mateus A., Sodré L., Szczerba R., 2004, A&A, 420, 475

Steinmetz M., Bartelmann M., 1995, MNRAS, 272, 570

Stocke J. T., Morris S. L., Gioia I. M., Maccacaro T., Schild R., Wolter A., Fleming T. A., Henry J. P., 1991, ApJS, 76, 813

Sullivan M., Mobasher B., Chan B., Cram L., Ellis R., Treyer M., Hopkins A., 2001, ApJ, 558, 72

Swinbank M., Bower R., Smith G. P., Smail I., Kneib J. ., Ellis R., Stark D., Bunker A., 2006, MNRAS in press (astro-ph/0603042)

Tegmark M., et al., 2004, ApJ, 606, 702

Tissera P. B., De Rossi M. E., Scannapieco C., 2005, MNRAS, 364, L38

Tran K.-V. H., Franx M., Illingworth G., Kelson D. D., van Dokkum P., 2003, ApJ, 599, 865

Tran K. H., Franx M., Illingworth G. D., van Dokkum P., Kelson D. D., Magee D., 2004, ApJ, 609, 683

Tremaine S., et al., 2002, ApJ, 574, 740

Tremonti C. A., et al., 2004, ApJ, 613, 898

Tully R. B., Fisher J. R., 1977, A&A, 54, 661

Tully R. B., Fouque P., 1985, ApJS, 58, 67

Tully R. B., Pierce M. J., 2000, ApJ, 533, 744

Tully R. B., Pierce M. J., Huang J., Saunders W., Verheijen M. A. W., Witchalls P. L., 1998, AJ, 115, 2264

van Albada T. S., Bahcall J. N., Begeman K., Sancisi R., 1985, ApJ, 295, 305 van Dokkum P. G., Franx M., Fabricant D., Illingworth G. D., Kelson D. D., 2000, ApJ, 541, 95

van Zee L., Salzer J. J., Haynes M. P., O'Donoghue A. A., Balonek T. J., 1998, AJ, 116, 2805

Veilleux S., Osterbrock D. E., 1987, ApJS, 63, 295

Verheijen M. A. W., 2001, ApJ, 563, 694

Vitvitska M., Klypin A. A., Kravtsov A. V., Wechsler R. H., Primack J. R., Bullock J. S., 2002, ApJ, 581, 799

Vogt N. P., 1995, PhD thesis, Cornell University

Vogt N. P., 1999, in ASP Conf. Ser. 193: The Hy-Redshift Universe: Galaxy Formation and Evolution at High Redshift p. 145

Vogt N. P., 2001, in ASP Conf. Ser. 240: Gas and Galaxy Evolution p. 89

Vogt N. P., Forbes D. A., Phillips A. C., Gronwall C., Faber S. M., Illingworth G. D., Koo D. C., 1996, ApJ, 465, L15

Vogt N. P., et al., 1997, ApJ, 479, L121

Vogt N. P., et al., 2002, Bulletin of the American Astronomical Society, 34, 703

Vogt N. P., Haynes M. P., Giovanelli R., Herter T., 2004, AJ, 127, 3300

Vogt N. P., et al., 2005, ApJS, 159, 41

Wang B., Heckman T. M., 1996, ApJ, 457, 645

Welch B. L., 1937, Biometrika, 29

White S. D. M., et al., 2005, A&A, 444

Willick J. A., 1994, ApJS, 92, 1

Willmer C. N. A., et al., 2005, ApJ in press (astro-ph/0506041)

Wolf C., Meisenheimer K., Rix H.-W., Borch A., Dye S., Kleinheinrich M., 2003, A&A, 401, 73

Wyithe J. S. B., Loeb A., 2003, ApJ, 595, 614

Yang Y., Zabludoff A. I., Zaritsky D., Lauer T. R., Mihos J. C., 2004, ApJ, 607, 258

Zaritsky D., Kennicutt R. C., Huchra J. P., 1994, ApJ, 420, 87

Ziegler B. L., Böhm A., Jäger K., Heidt J., Möllenhoff C., 2003, ApJ, 598, L87

Zucca E., et al., 2005, A&A in press (astro-ph/0506393)